

Die approbierte Originalversion dieser Dissertation ist in der Hauptbibliothek der Technischen Universität Wien aufgestellt und zugänglich.

<http://www.ub.tuwien.ac.at>



The approved original version of this thesis is available at the main library of the Vienna University of Technology.

<http://www.ub.tuwien.ac.at/eng>



TECHNISCHE
UNIVERSITÄT
WIEN

VIENNA
UNIVERSITY OF
TECHNOLOGY

DISSERTATION

Beam dynamics and optics studies for the LHC injectors upgrade

ausgeführt zum Zwecke der Erlangung des akademischen Grades
eines Doktors der technischen Naturwissenschaften

unter der Leitung von
Priv. Doz. Dr. Michael Benedikt
Dr. Yannis Papaphilippou

E141, Atominstitut der österreichischen Universitäten

eingereicht von
HANNES BARTOSIK
e0026240

Wien, Oktober 2013

Abstract

The Large Hadron Collider (LHC) upgrade, which aims at reaching significantly higher luminosities at the experiment sites, requires the existing injector chain to provide proton beams with unprecedented beam intensity and brightness. The required beam parameters are out of reach for the CERN accelerator complex in its present state. Therefore, upgrade possibilities of the existing injectors for mitigating their performance limitations or their partial replacement by new machines have been studied.

The transition energy plays a central role for the performance of synchrotrons. Designing a lattice with negative momentum compaction (NMC), i.e. imaginary transition energy, allows avoiding transition crossing and thus the associated performance limitations. In the first part of this thesis, the properties of an NMC cell are studied. The limits of betatron stability are evaluated by a combination of analytical and numerical calculations. The NMC cell is then used for the design study of a new synchrotron called PS2, which has been proposed to replace the existing CERN Proton Synchrotron (PS) in the LHC injector chain. Two lattice options are presented, the baseline race-track lattice and the alternative option based on a threefold symmetry. They are compared with respect to their tuning flexibility as well as their linear and nonlinear properties. The effect of machine imperfections on the dynamic aperture is studied in detailed tracking simulations.

The direct impact of the transition energy and the phase slip factor on the performance of an operating synchrotron is described in the second part of this thesis. The intensity thresholds for the instabilities, that are presently limiting the performance of the LHC-type proton beams in the Super Proton Synchrotron (SPS), scale linearly with the slip factor. A new optics for the SPS is presented, which provides lower transition energy and thereby a three times higher slip factor at injection energy. The resulting increase of the intensity threshold for the transverse mode coupling instability at injection is demonstrated in experimental and simulation studies. Furthermore, numerical simulations show that the electron cloud density at which bunches become unstable is twice higher in the new optics. In addition to that, the expected improvement of longitudinal beam stability at higher energies is confirmed by a series of measurements. Finally, a reduction of the incoherent space charge tune shift by about 15% is achieved due to the larger dispersion function in the arcs, which helps minimizing incoherent emittance growth at the injection plateau for high brightness beams. Since fall 2012, the new optics is being successfully used for LHC filling in routine operation providing improved beam characteristics compared to the nominal SPS optics.

Kurzfassung

Der Ausbau des Large Hadron Collider (LHC) hat das Ziel höhere Luminositäten an den Kollisionpunkten zu erreichen, wofür die LHC Injektorkette zukünftig Protonenstrahlen von noch nie dagewesener Intensität und Brillanz zur Verfügung stellen muss. Nachdem der CERN Beschleunigerkomplex in seiner derzeitigen Form nicht in der Lage ist die geforderten Strahlparameter zu erbringen, wurden Möglichkeiten untersucht die Leistungsfähigkeit der bestehenden Beschleuniger zu erweitern oder diese durch neue Maschinen zu ersetzen.

Für die Leistungsfähigkeit eines Synchrotrons spielt die Übergangsenergie eine zentrale Rolle. Das Design einer Strahloptik mit "Negative Momentum Compaction" (NMC) und somit imaginärer Übergangsenergie erlaubt es, das Überschreiten der Übergangsenergie und die damit verbundenen Limitierungen zu vermeiden. Im ersten Teil dieser Arbeit werden die Eigenschaften einer NMC-Struktur untersucht. Die Grenzen der Betatron Stabilität werden mit Hilfe einer Kombination aus analytischen und numerischen Methoden analysiert. Die NMC-Struktur wird anschließend für die Designstudie des PS2 Synchrotrons verwendet, welches als Ersatz für das existierende CERN Proton Synchrotron (PS) vorgeschlagen wurde. Zwei Optionen für die Strahloptik werden vorgestellt: Die Basisvariante mit zweifacher Symmetrie und eine Alternative mit dreifacher Symmetrie. Diese werden einander gegenübergestellt. Ihre Abstimmungsmöglichkeiten sowie ihre linearen und nichtlinearen Eigenschaften werden verglichen. Der Einfluss von Maschinenimperfectionen auf die dynamische Apertur wird in detaillierten Trackingsimulationen untersucht.

Der direkte Einfluss der Übergangsenergie und des Slipfaktors auf die Leistungsfähigkeit eines laufenden Synchrotrons wird im zweiten Teil dieser Arbeit beschrieben. Die Intensitätsgrenzwerte für die Instabilitäten, die die derzeitigen Limitierungen für die LHC Protonstrahlen im Super Proton Synchrotron (SPS) darstellen, skalieren linear mit dem Slipfaktor. Eine neue Strahloptik für das SPS wird vorgestellt, die eine niedrigere Übergangsenergie zur Folge hat und somit einen dreifach höheren Slipfaktor bei Injektionsenergie erreicht. Der resultierende Anstieg der Intensitätsgrenzwerte für die "transverse mode coupling"-Instabilität bei Injektion wird anhand von Experimenten und Simulationen gezeigt. Numerische Simulationen zeigen darüber hinaus, dass die Elektronenwolken-dichte ab welcher der Strahl in der neuen Strahloptik instabil wird zweimal höher ist. Außerdem wird die erwartete Verbesserung der longitudinalen Strahlstabilität in einer Reihe von Messungen bestätigt. Durch die erhöhte Dispersionsfunktion wird weiters eine Reduktion der inkohärenten Raumladungsdefokussierung um 15% erreicht, was von Vorteil ist um das inkohärente Anwachsen der Emittanz am Injektionsplateau für Strahlen mit hoher Brillanz zu minimieren. Die neue Strahloptik wird seit Herbst 2012 erfolgreich für das Befüllen des LHC im Routinebetrieb verwendet und erzielt bessere Strahlparameter im Vergleich zur nominellen SPS Strahloptik.

Contents

1. Introduction	1
2. Momentum compaction and transition energy	5
2.1. General definition and considerations	5
2.2. Transition energy in the FODO lattice	7
2.3. Negative momentum compaction lattice	10
3. PS2 as potential replacement of the CERN PS	19
3.1. Introduction	19
3.2. PS2 baseline lattice	22
3.2.1. Linear optics	24
3.2.2. Physical aperture	26
3.2.3. Tuning flexibility	28
3.2.4. Working point considerations	30
3.2.5. Chromaticity correction	31
3.2.6. Correction of misalignment and closed orbit errors	35
3.2.7. Multipole field errors	39
3.2.8. Dynamic aperture without synchrotron motion	40
3.2.9. Dynamic aperture including all errors and synchrotron motion	49
3.3. Alternative PS2 lattice with threefold symmetry	51
3.3.1. Linear optics	51
3.3.2. Physical aperture	54
3.3.3. Tuning flexibility	54
3.3.4. Working point considerations	56
3.3.5. Chromaticity correction	57
3.3.6. Correction of misalignment and closed orbit errors	58
3.3.7. Multipole field errors	59
3.3.8. Dynamic aperture without synchrotron motion	60
3.3.9. Dynamic aperture including all errors and synchrotron motion	65
3.4. Lattice comparison	66
3.5. Consolidation and upgrade of the existing PS complex	67
4. SPS optics with low transition energy	69
4.1. Intensity limitations for LHC beams in the SPS	69
4.2. Motivation for lower transition energy in the SPS	71
4.3. Nominal and low transition energy optics of the SPS	72
4.3.1. Reducing transition energy in the SPS	72

4.3.2.	Implications of using lower transition energy in the SPS	76
4.4.	SPS nonlinear model	89
4.4.1.	Nonlinear chromaticity	89
4.4.2.	Tune scans	93
4.5.	High intensity single bunch beams	96
4.5.1.	Transverse mode coupling instability	96
4.6.	LHC-type beams in the SPS	106
4.6.1.	Longitudinal instabilities in the SPS	107
4.6.2.	Space charge studies with 50 ns beam	115
4.6.3.	Electron cloud effects with 25 ns bunch spacing	121
4.7.	Low gamma transition optics - operational deployment	134
4.7.1.	Overview	134
4.7.2.	Operational performance	136
4.8.	Outlook	139
4.8.1.	Future studies	139
4.8.2.	Split tunes	139
5.	Summary and conclusions	143
	Appendix	147
A.	Transverse particle motion	147
A.1.	Equations of motion	148
A.2.	Solution of Hill's equation	149
A.3.	Solution for off-momentum particles	153
A.4.	Normalized dispersion and dispersion action	154
A.5.	Linear magnet imperfections	155
A.6.	Non-linear beam dynamics	158
B.	Longitudinal particle motion	168
B.1.	Acceleration in longitudinal electric field	168
B.2.	Momentum compaction and phase-slip factor	169
B.3.	Longitudinal equations of motion	170
B.4.	Small amplitude synchrotron oscillations in the adiabatic regime	171
B.5.	Bucket area	173
C.	Collective effects	175
C.1.	Transverse plane	175
	Bibliography	183
	Nomenclature	197
	Acknowledgements	201

1. Introduction

The Large Hadron Collider (LHC) [1] at CERN, the European Organization for Nuclear Research, is presently the most powerful particle collider in the world. The LHC physics program started in March 2010 with colliding proton beams at an energy of 3.5 TeV per proton. After the physics run in 2011, the collision energy was raised to 4 TeV per proton for the run in 2012. The combined analysis of collision events recorded in 2011 and in 2012 led to the discovery of a Higgs like particle, as announced by the two main LHC experiments ATLAS [2] and CMS [3].

Apart from the beam energy, the key parameter describing the performance of a collider such as the LHC is the machine luminosity, which measures the ability to produce collision events. For Gaussian particle distributions and round beams colliding head-on, the luminosity \mathcal{L} can be written as (see for example [1], Chapter 3.1)

$$\mathcal{L} = \frac{N^2 n_b f_0 \beta \gamma}{4\pi \varepsilon_n \beta^*}, \quad (1.1)$$

where N denotes the intensity per bunch, n_b the number of bunches per beam, f_0 the revolution frequency, γ the Lorentz factor, β the normalized velocity, ε_n the normalized transverse emittance and β^* the betatron amplitude function at the collision point. Geometric reduction factors have been neglected. A high luminosity is required in order to allow for the measurement of rare processes. Hence, a staged upgrade program [4] for increasing the luminosity of the LHC after a few years of running has been anticipated already in the early stage of the project.

The LHC performance depends on the beam characteristics provided by its injectors, in particular the intensity per bunch N and the transverse emittance ε_n . A schematic view of the present accelerator complex at CERN is shown in Fig. 1.1. Protons are extracted from a Duoplasmatron source and accelerated to 50 MeV kinetic energy in the linear accelerator Linac2 before injected into the Proton Synchrotron Booster (PSB). In the four vertically stacked synchrotron rings of the PSB, the protons are accelerated to 1.4 GeV kinetic energy and extracted to the CERN Proton Synchrotron (CPS or simply PS), which is the oldest machine of the LHC injector complex. The PS plays a central role in the preparation of the LHC beam, in particular by creating the required bunch train structure in a series of RF manipulations. The beam is extracted at a momentum of 26 GeV/c and then brought to the Super Proton Synchrotron (SPS) through the TT2 and TT10 transfer lines. The SPS is the last accelerator in the LHC injector chain. It accelerates the beam to a momentum of 450 GeV/c before injection into the two rings of the LHC through the transfer lines TT60/TI2 (beam 1) and TT40/TI8 (beam 2).

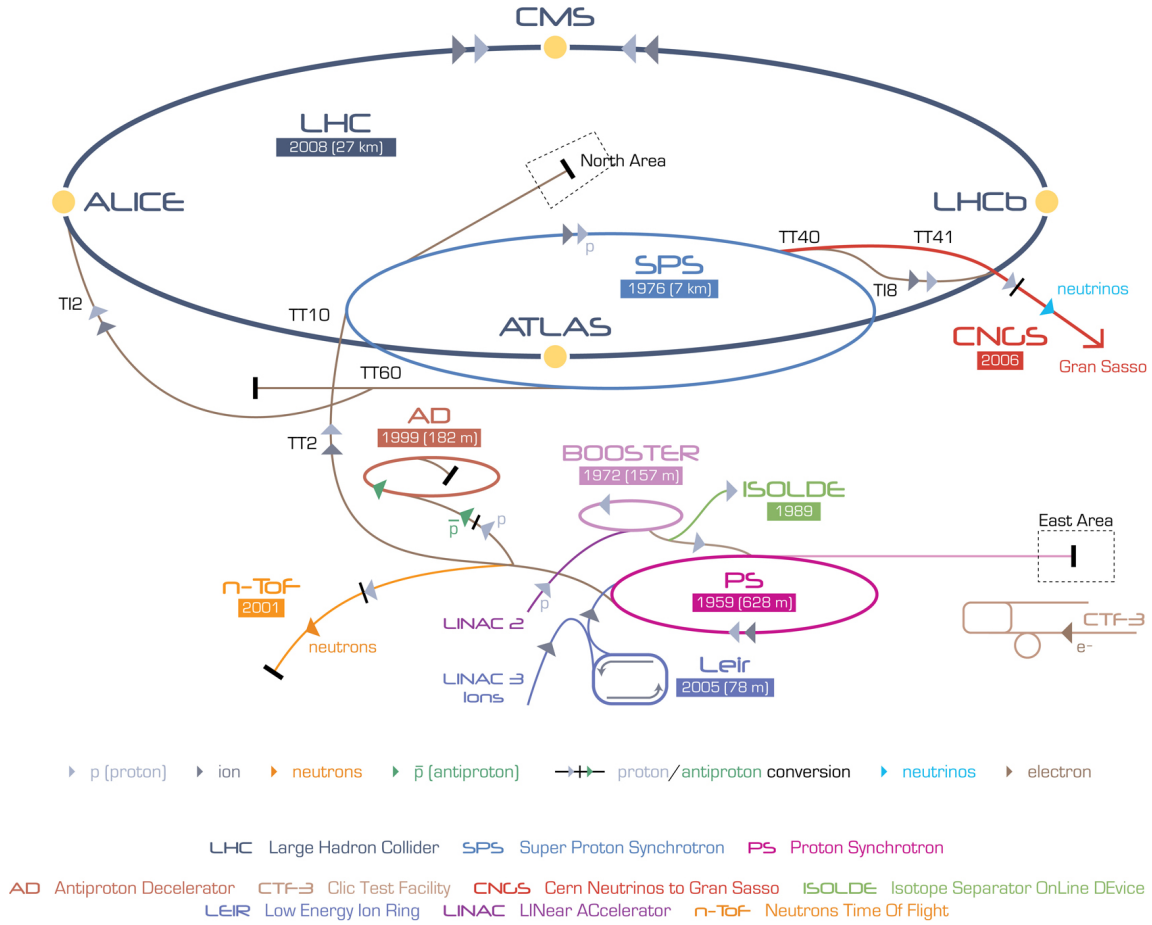


Figure 1.1: Schematic view of the present CERN accelerator complex. The year of commissioning and the circumference of circular machines is indicated in the boxes. The particle types in each machine and transfer line are indicated by the small arrows, with the color code explained in the figure. ©CERN.

In order to fully exploit the potential of the LHC and its future upgrades for higher luminosity, the injectors will have to deliver proton beams with significantly higher beam intensity and beam brightness N/ε_n compared to the current operation. Since the required beam parameters are out of reach for the present complex, the LHC injectors have to be upgraded [5]. As outcome of the working group on “Proton Accelerators for the Future” [6], the first stage of the injectors upgrade consists of a new linear accelerator for H^- -ions called Linac4 [7], which is presently under construction. Furthermore, it was proposed to replace the PSB and the PS by a new superconducting linear accelerator called SPL and a new synchrotron called PS2 [6, 8]. In this scenario Linac4 would serve as a front-end for the SPL, which would accelerate the H^- -ions up to 4 GeV kinetic energy before they would be injected into PS2 using a H^- charge exchange

injection scheme [9, 10]. This would allow for generating proton beams with the high brightness N/ε_n required for the LHC upgrades. Furthermore, the anticipated energy of 50 GeV at the transfer from PS2 to the SPS would mitigate some of the performance limitations due to high intensity effects in the SPS. The lattice optimization for the PS2 design study was performed as first part of this thesis.

The CERN strategy for the upgrades of the LHC complex was changed in 2010 [11]. The activities concerning the luminosity upgrade of the LHC itself are since then incorporated in the High Luminosity LHC (HL-LHC) project [12] and the upgrade of the injector complex is subject of the LHC Injectors Upgrade (LIU) project [13]. In particular, the LIU project aims at consolidating and upgrading the existing injector synchrotrons in the CERN complex instead of building new machines. The injection energy in the PSB will be raised from the present 50 MeV to 160 MeV with the connection of Linac4, which mitigates space charge effects and thus allows for twice higher beam brightness compared to present operation. Furthermore, it is planned to raise the extraction energy in the PSB to 2 GeV, in order to compensate the enhanced space charge tune shift at PS injection due to the higher beam brightness available with Linac4. After the upgrade of the PSB and the PS, the main performance limitations of the LHC injector complex are beam instabilities and high intensity effects in the SPS. They are studied in the second part of this thesis. In particular, mitigation of beam instabilities by changing the beam optics of the SPS have been demonstrated both in simulations and experiments. This new SPS optics is now part of the baseline upgrades of the LIU project.

The structure of this work is the following. Chapter 2 starts with a general introduction about the momentum compaction factor and transition energy. The beam physics phenomena encountered at transition crossing in the acceleration cycle of the PS are discussed briefly. These effects motivate the design of the PS2 lattice with negative momentum compaction for avoiding transition crossing (due to imaginary transition energy). The momentum compaction factor is derived analytically first for a simple FODO cell. It is shown how to design a lattice with negative momentum compaction factor. The properties of such a lattice are studied by a combination of analytical and numerical calculations.

These results are used for the PS2 design study presented in Chapter 3, in particular concerning the optimization of the linear lattice. Two lattice options were developed, the baseline option having a racetrack shape and an alternative option based on a threefold symmetry. For both lattice variants, studies on the tuning flexibility were performed with a systematic numerical scan of all possible lattice solutions. Furthermore, sextupole schemes for chromaticity correction are compared with respect to their impact on nonlinear dynamics and off-momentum beta-beating. The sensitivity of the negative momentum compaction lattice to closed orbit errors and magnet misalignments and the efficiency of an orbit correction scheme are investigated. The impact of higher order multipole errors on the nonlinear chromaticity and in particular on the dynamic aperture are presented.

The performance limitations of LHC beams in the SPS are discussed in the second part of this thesis, i.e. Chapter 4. The motivation for lowering the transition energy in the SPS and the expected gain of beam stability is summarized. A new optics for the SPS with lower transition energy is presented. Calculations and simulation studies show that no hardware modifications are needed for its implementation in the machine. A series of measurements and experimental studies demonstrate a clear performance gain with the new optics, with respect to single bunch transverse instabilities, electron cloud instabilities and longitudinal instabilities. This chapter concludes with an overview of the beam parameters achieved in 2012 with the new optics in routine operation and future perspectives.

A short summary of the main results and the conclusions are presented in Chapter 5. Further results and specific aspects relevant for this work are listed in the Appendix.

2. Momentum compaction and transition energy

2.1. General definition and considerations

In circular accelerators such as synchrotrons, the revolution period T of a particle with momentum p and velocity v is given by $T = C/v$, where C is the circumference of the machine. The fractional change of the revolution period $\Delta T/T$ between particles with reference momentum p_0 and particles with momentum offset $\Delta p = p - p_0$ is then calculated as (cf. [14], Chapter 2-IV.3)

$$\frac{\Delta T}{T} = \frac{\Delta C}{C} - \frac{\Delta v}{v} = \left(\alpha_c - \frac{1}{\gamma^2} \right) \frac{\Delta p}{p}, \quad (2.1)$$

where ΔC is the change in path length around the machine, Δv the change in velocity and γ is the relativistic Lorentz factor. The momentum compaction factor α_c is defined as the variation of the path length with momentum. To first order in $\delta \equiv \Delta p/p$, α_c is determined by the integral of the dispersion function $D_x(s)$ (cf. Appendix A.3) in the bending magnets,

$$\alpha_c = \frac{\Delta C/C}{\Delta p/p} = \frac{1}{C} \oint \frac{D_x(s)}{\rho(s)} ds, \quad (2.2)$$

where $\rho(s)$ is the bending radius. The momentum compaction factor defines the γ at transition $\gamma_t \equiv 1/\sqrt{\alpha_c}$, at which the phase slip factor η ,

$$\eta = \alpha_c - \frac{1}{\gamma^2} = \frac{1}{\gamma_t^2} - \frac{1}{\gamma^2}, \quad (2.3)$$

changes its sign. Below transition ($\gamma < \gamma_t$), the time of arrival at a given location in the ring is dominated by the particle velocity. Particles with a positive momentum offset have a shorter revolution period than synchronous particles and $\eta < 0$. Above transition ($\gamma > \gamma_t$), the difference in velocity is smaller than the change in path length. Thus, particles with higher momentum will have a larger revolution period and $\eta > 0$.

As shown in Appendix B.4, the synchrotron motion is slowing down when approaching transition energy ($\gamma \approx \gamma_t$ and $\eta \approx 0$) due to the dependence on η . At the same time, the bunch length is decreasing and the momentum spread is becoming larger, see Eqs. (B.166). During transition crossing numerous unfavourable effects are encountered (see [15], Chapter 4.9):

- Close to transition, the synchrotron motion enters a nonadiabatic regime [16] and the longitudinal particle motion cannot follow the rapid change of the RF

bucket shape. At transition, the bunch length is reducing to a minimum but not reaching zero because of the nonadiabatic synchrotron motion. On the other hand the momentum spread of the beam reaches a maximum, which can be so large that it exceeds the available momentum aperture of the machine resulting in particle loss.

- Due to nonlinearities and higher order components of the momentum compaction factor [17], particles with different momenta may cross transition at different moments in time which can lead to distortion of the longitudinal phase space distribution and beam loss.
- Longitudinal space charge (or the inductive part of the longitudinal broadband impedance) causes a longitudinal mismatch at transition [16, 18], which results in bunch length oscillations after transition crossing and emittance blow-up if not damped.
- Since the synchrotron frequency spread within the bunch is very small close to transition, there is almost no Landau damping of the microwave instability, which are induced by longitudinal space charge (“negative mass instability”) [19]. This can result in emittance blow-up and again particle loss.
- Chromaticity has to be adjusted from negative values below transition to positive values above transition in order to avoid head-tail instability [20]. Furthermore, the stability condition for the longitudinal motion requires the RF stable phase ϕ_s to be shifted to $\pi - \phi_s$.

In machines where transition crossing cannot be avoided, transition jump schemes [21] are used to minimize the time close to transition: fast pulsing quadrupoles, installed in dispersive areas around the ring, are used to dynamically change γ_t such that the transition crossing is much faster than it would be with constant γ_t . This technique was first applied at the CERN PS [22]: since 1973, 16 quadrupoles are grouped to doublets (and triplets) in order to generate a large γ_t jump with almost zero tune-shift [23, 24]. This γ_t -jump scheme is inevitable for efficient transmission of high intensity beams in the PS [25].

Transition crossing can be avoided by designing a lattice with negative momentum compaction factor, as originally proposed by Teng [26]. In this case, γ_t is imaginary and transition crossing is eliminated as the slippage factor remains always negative. The concept of imaginary γ_t was already successfully applied to the design of the J-PARC main ring [27]. A similar strategy is followed for the PS2 design study presented in the first part of this thesis.

In the next section, the transition energy as function of the phase advance for the FODO lattice in thin lens approximation will be reviewed using the well established matrix formalism for describing the linear beam transport. The result for the FODO lattice will then be generalized to the negative momentum compaction (NMC) lattice as used for the PS2 design study.

2.2. Transition energy in the FODO lattice

The transition energy is defined through the dispersion function in the bending magnets. As derived in the Appendix (section A.3), the dispersion function $D_x(s)$ satisfies the second order inhomogeneous differential equation

$$D_x(s)'' + K_x(s)D_x(s) = 1/\rho, \quad (2.4)$$

where the focusing term $K_x = \frac{1}{\rho^2} + \frac{1}{B\rho} \frac{\partial B_y}{\partial x}$ is composed of the weak focusing and the quadrupole focusing. The solution for Eq. (2.4) can be represented using the matrix formalism (cf. section A.3)

$$\begin{pmatrix} D_x(s_2) \\ D'_x(s_2) \\ 1 \end{pmatrix} = \begin{pmatrix} M_x(s_2|s_1) & \bar{d}_x \\ 0 & 1 \end{pmatrix} \begin{pmatrix} D_x(s_1) \\ D'_x(s_1) \\ 1 \end{pmatrix} = \mathcal{M}_x \begin{pmatrix} D_x(s_1) \\ D'_x(s_1) \\ 1 \end{pmatrix}, \quad (2.5)$$

where M_x is the 2×2 betatron transfer matrix. Imposing the closed orbit conditions $D_x(s_2) = D_x(s_1)$ and $D'_x(s_2) = D'_x(s_1)$, the 3×3 matrix \mathcal{M}_x for a *symmetric* cell becomes

$$\mathcal{M}_x = \begin{pmatrix} \cos \phi_x & \beta_x \sin \phi_x & (1 - \cos \phi_x) D_x \\ -\frac{1}{\beta_x} \sin \phi_x & \cos \phi_x & \frac{1}{\beta_x} \sin \phi_x D_x \\ 0 & 0 & 1 \end{pmatrix}, \quad (2.6)$$

where ϕ_x denotes the horizontal phase advance along the structure and β_x is the horizontal beta function.

A simple FODO cell consists of a focusing quadrupole, two sector bending magnets and a defocusing quadrupole. This FODO cell can be represented as

$$\left\{ \frac{1}{2} Q_{F_1} \text{ B } Q_{D_2} \text{ B } \frac{1}{2} Q_{F_1} \right\},$$

where Q_{F_1} and Q_{D_2} denote the focusing and defocusing quadrupoles, respectively, and B stands for a sector bending magnet. The 3×3 transfer matrix \mathcal{M}_x for this FODO cell in thin lens and small angle approximation is then obtained by matrix multiplication of the individual transfer matrices (cf. section A.2 and section A.3)

$$\mathcal{M}_x = \begin{pmatrix} 1 & 0 & 0 \\ -\frac{1}{2f_1} & 1 & 0 \\ 0 & 0 & 1 \end{pmatrix} \begin{pmatrix} 1 & L & \frac{L\theta}{2} \\ 0 & 1 & \theta \\ 0 & 0 & 1 \end{pmatrix} \begin{pmatrix} 1 & 0 & 0 \\ \frac{1}{f_2} & 1 & 0 \\ 0 & 0 & 1 \end{pmatrix} \begin{pmatrix} 1 & L & \frac{L\theta}{2} \\ 0 & 1 & \theta \\ 0 & 0 & 1 \end{pmatrix} \begin{pmatrix} 1 & 0 & 0 \\ -\frac{1}{2f_1} & 1 & 0 \\ 0 & 0 & 1 \end{pmatrix}, \quad (2.7)$$

where the beginning of the structure is chosen at the symmetry point in the center of the focusing quadrupole. The independent focal lengths of the focusing and defocusing quadrupoles are denoted as f_1 and f_2 , respectively. The bending magnets are characterized by a length L and a bending angle θ . For simplicity, they are assumed to cover the entire space between the thin lens quadrupoles such that the total length of the

FODO cell is $2L$. The closed orbit condition is given by

$$\begin{pmatrix} D_x \\ D'_x \\ 1 \end{pmatrix} = \begin{pmatrix} 1 + \frac{(f_1 - f_2 - L/2)L}{f_1 f_2} & (2 + \frac{L}{f_2})L & (2 + \frac{L}{2f_2})L\theta \\ \frac{(2f_1 - L)(2f_1 - 2f_2 - L)}{4f_1^2 f_2} & 1 + \frac{(f_1 - f_2 - L/2)L}{f_1 f_2} & \frac{2f_1 L - 4f_2 L + 8f_1 f_2 - L^2}{4f_1 f_2} \theta \\ 0 & 0 & 1 \end{pmatrix} \begin{pmatrix} D_x \\ D'_x \\ 1 \end{pmatrix}. \quad (2.8)$$

The first element of the matrix \mathbf{M}_x in Eq. (2.8) determines the phase advance in the horizontal plane ϕ_x by comparison with Eq. (2.6). The vertical phase advance ϕ_y follows by inverting the signs of the focal lengths f_1 and f_2 . Hence it follows that

$$\cos \phi_x = 1 - \frac{L}{f_1} + \frac{L}{f_2} - \frac{L^2}{2f_1 f_2}, \quad (2.9a)$$

$$\cos \phi_y = 1 + \frac{L}{f_1} - \frac{L}{f_2} - \frac{L^2}{2f_1 f_2}. \quad (2.9b)$$

Writing L/f_2 as a function of $\cos \phi_x$ and $\cos \phi_y$, and inserting this expression into Eq. (2.8) gives by comparison with Eq. (2.6) the beta function at the center of the focusing quadrupole (beginning of the structure) $\beta_{x,F}$,

$$\beta_{x,F} = \left(\underbrace{2 + \frac{\cos \phi_x - \cos \phi_y}{4} + \sqrt{\left(\frac{\cos \phi_x - \cos \phi_y}{4}\right)^2 + 2 - \cos \phi_x - \cos \phi_y}}_{L/f_2} \right) L / \sin \phi_x, \quad (2.10)$$

and similarly by replacing f_2 with $-f_1$ one obtains the beta function $\beta_{x,D}$ at the center of the defocusing quadrupole $\beta_{x,D}$,

$$\beta_{x,D} = \left(\underbrace{2 - \frac{\cos \phi_y - \cos \phi_x}{4} - \sqrt{\left(\frac{\cos \phi_y - \cos \phi_x}{4}\right)^2 + 2 - \cos \phi_y - \cos \phi_x}}_{-L/f_1} \right) L / \sin \phi_x. \quad (2.11)$$

As the center of the focusing quadrupole is a symmetry point in the periodic solution, it follows that the derivate of the dispersion in the center of the focusing quadrupole $D'_{x,F} = 0$ and in the center of the defocusing quadrupole $D'_{x,D} = 0$. For the general case of $f_1 \neq f_2$, the dispersion functions at the center of the quadrupoles are obtained similar to the beta functions by comparison with Eq. (2.6), which yields

$$D_{x,F} = \left(4 + \frac{\cos \phi_x - \cos \phi_y}{4} + \sqrt{\left(\frac{\cos \phi_x - \cos \phi_y}{4}\right)^2 + 2 - \cos \phi_x - \cos \phi_y} \right) \frac{L\theta}{4 \sin^2 \frac{\phi_x}{2}}, \quad (2.12)$$

$$D_{x,D} = \left(4 - \frac{\cos \phi_y - \cos \phi_x}{4} - \sqrt{\left(\frac{\cos \phi_y - \cos \phi_x}{4}\right)^2 + 2 - \cos \phi_y - \cos \phi_x} \right) \frac{L\theta}{4 \sin^2 \frac{\phi_x}{2}}. \quad (2.13)$$

A particularly simple case is obtained if the quadrupoles have equal focusing strength, i.e. $f_1 = f_2 = f$. Then, the phase advance is identical in both planes¹ $\phi_x = \phi_y = \phi$. Using the identity $\sin^2 \frac{\phi}{2} = \frac{1 - \cos \phi}{2}$, the above relations reduce to

$$\sin \frac{\phi}{2} = \frac{L}{2f}, \quad \beta_F = \frac{2L(1 + \sin \frac{\phi}{2})}{\sin \phi}, \quad \beta_D = \frac{2L(1 - \sin \frac{\phi}{2})}{\sin \phi}, \quad (2.14)$$

and the dispersion in the center of the quadrupoles becomes

$$D_{x,F} = \frac{(1 + \frac{1}{2} \sin \frac{\phi}{2})}{\sin^2 \frac{\phi}{2}} L\theta, \quad D_{x,D} = \frac{(1 - \frac{1}{2} \sin \frac{\phi}{2})}{\sin^2 \frac{\phi}{2}} L\theta. \quad (2.15)$$

In good approximation, the average dispersion function in the bending magnets of the FODO cell is just the arithmetic mean of $D_{x,F}$ and $D_{x,D}$. Thus, the momentum compaction factor as defined in Eq. (2.2) can be calculated using the general expressions for the dispersion function found in Eqs. (2.12)-(2.13). For a machine built entirely of such FODO cells, this yields [17]

$$\begin{aligned} \alpha_c &= \frac{1}{C} \oint \frac{D_x(s)}{\rho(s)} ds \approx \frac{1}{C} \sum_i \langle D_x \rangle_i \theta \approx \frac{(D_{x,F} + D_{x,D})}{2L} \theta = \frac{1 + (\cos \phi_x - \cos \phi_y)/16}{\sin^2 \frac{\phi_x}{2}} \theta^2 \\ &\approx \frac{\theta^2}{\sin^2 \frac{\phi_x}{2}} \approx \frac{\theta^2}{(\frac{\phi_x}{2})^2} = \frac{1}{Q_x^2}, \end{aligned} \quad (2.16)$$

where the weak dependence on the vertical phase advance ϕ_y was omitted and the last equation follows from the definitions of the phase advance and the betatron tune (cf. Appendix A.2) and the fact that a pure FODO lattice without straight sections was considered. Thus, the momentum compaction factor is determined mainly by the horizontal tune Q_x and the transition energy γ_t in a FODO lattice is approximately given by

$$\gamma_t \approx \frac{\sin \frac{\phi_x}{2}}{\theta} \approx Q_x, \quad (2.17)$$

i.e. in a pure FODO lattice, the transition energy γ_t is in first approximation equal to Q_x . Figure 2.1 shows the optics functions obtained by MADX [28] for the basic FODO cell considered in the calculations above. In this case, the bending angle for each of the two dipoles is set to $\theta = \pi/30$, so that a closed ring would consist of 30 cells. As the phase advance per cell in this example is matched to $\phi_x = \phi_y = \pi/2$, the transition energy can be estimated using Eq. (2.17) as $\gamma_t \approx \sin \frac{\phi_x}{2} / \theta \approx 6.75$. In comparison to that, the calculation of MADX gives $\gamma_t = 6.9$.

¹Due to the the small angle approximation, the sector bending magnet behaves like a drift space since the weak focusing is neglected.

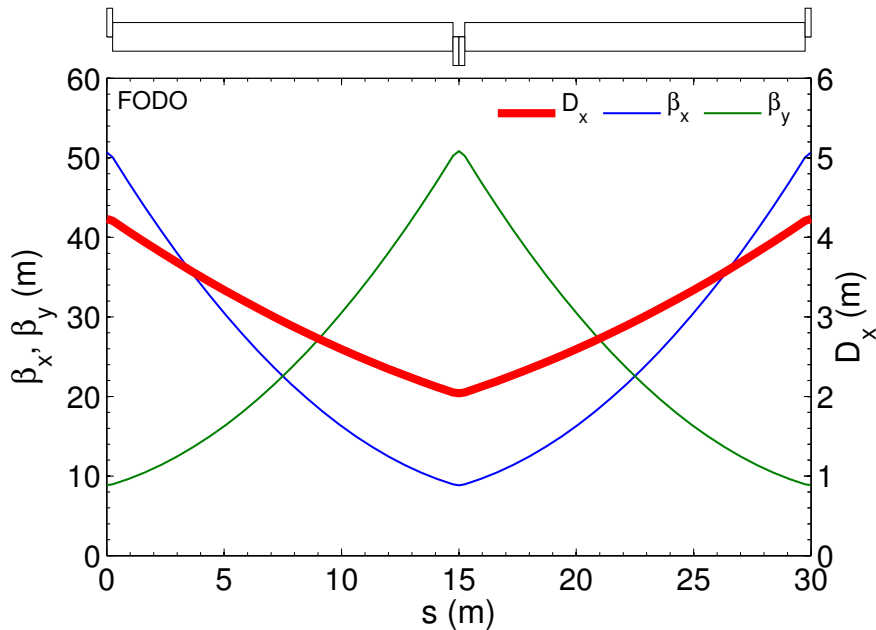


Figure 2.1: Optics functions for a basic FODO cell. The long rectangular boxes in the plot header represent the dipole magnets. The small boxes correspond to the focusing (shifted upwards) and the defocusing (shifted downwards) quadrupoles.

2.3. Negative momentum compaction lattice

In the previous section it was shown that the transition energy of a pure FODO lattice scales like the horizontal tune. As already mentioned above, a negative momentum compaction factor can be achieved by special lattice design. In this case, γ_t is imaginary and transition crossing is avoided as the phase slip factor remains always negative. Considering the definition of the momentum compaction factor as given in Eq. (2.2), α_c becomes negative if the average dispersion function in the bending magnets becomes negative. Teng [26] was the first to design lattices where the dispersion function became negative in parts of a circular machine. As proposed by Trbojevic *et al.* [29], this can be achieved by a modular approach for a so-called flexible momentum compaction (FMC) lattice. The idea is to design modules with a prescribed negative dispersion at their entrance. A matching section in the center of the cell is then used to achieve periodicity of the (symmetric) module. This approach was then extended by Lee *et al.* [30] showing how to minimize dispersion in these flexible momentum compaction lattices. However, in their analysis the betatron stability criterion for these NMC cells was not shown. In the following, a basic FMC module as described by Lee *et al.* will be discussed. The dependence of the momentum compaction factor on the phase advances and the dispersion at the entrance of the module will be investigated. As extension to the results of Lee *et al.*, the stability criterion will be included.

As described in [30] and [14], a basic FMC module can be built of two FODO cells with a quadrupole doublet insertion for matching in between them. The basic structure of this module can be represented as

$$M_a \left\{ \frac{1}{2} Q_{F_1} \text{ B } Q_{D_2} \text{ B } \frac{1}{2} Q_{F_1} \right\} M_b \left\{ Q_{F_3} \text{ O}_1 \text{ } Q_{D_4} \text{ O}_2 \right\} M_c + \text{mirror reflection},$$

where M_a, b, c represent marker locations, O_1 and O_2 are drift spaces of length L_d and L_{d2} , respectively. The quadrupoles of the matching section are denoted as Q_{F_3} and Q_{F_4} with focal lengths f_3 and f_4 , respectively.

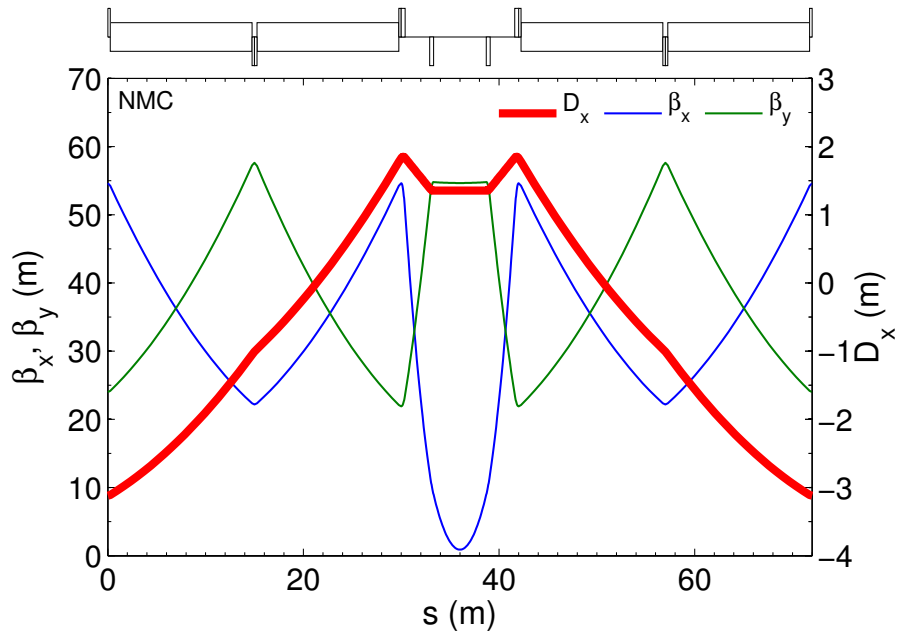


Figure 2.2: Optics functions for a basic NMC cell. The optical elements are represented by small boxes in the figure header.

Figure 2.2 shows a plot of the optical functions obtained with MADX for a basic NMC cell as considered in the presented analysis. Note the negative dispersion at the entrance of the module. The (doublet) insertion connecting the two FODO cells is needed for matching the dispersion function to periodic conditions. As the dispersion function is on average negative in the dipole regions, a negative momentum compaction factor is achieved. For this particular case shown here, the MADX calculation yields $\alpha_c = -0.0056$ and $\gamma_t = 13.3i$ with tunes $\nu_{x,\text{NMC}} \approx 0.72$ and $\nu_{y,\text{NMC}} \approx 0.31$ in the horizontal and vertical plane, respectively.

The analytical treatment of the basic NMC cell starts from a *matched* FODO cell. Although the assumption of a matched FODO cell is not a necessary condition for the analysis, it simplifies the following calculations. As shown in section 2.2, the 3×3

transfer matrix for the periodic FODO cell is given by

$$\mathcal{M}_{x,FODO} = \begin{pmatrix} \cos \phi_x & \beta_{x,F} \sin \phi_x & D_{x,F}(1 - \cos \phi_x) \\ -\frac{1}{\beta_{x,F}} \sin \phi_x & \cos \phi_x & \frac{D_{x,F}}{\beta_{x,F}} \sin \phi_x \\ 0 & 0 & 1 \end{pmatrix}, \quad (2.18)$$

where $\beta_{x,F}$ and $D_{x,F}$ are the horizontal beta function and the dispersion at the center of the focusing quadrupole as derived in Eqs. (2.10) and (2.12), respectively, and ϕ_x is the horizontal phase advance in the FODO cell. In the following, the dispersion function at the entrance of the FODO cell, denoted as $D_{x,a}$, will be prescribed with a negative value in order to achieve negative momentum compaction. As the NMC module under consideration is symmetric, it is required that the dispersion derivative at the entrance of the cell $D'_{x,a} = 0$. Transporting these initial condition through the FODO cell using the transfer matrix in Eq. (2.18) gives the dispersion $D_{x,b}$ and its derivative $D'_{x,b}$ at marker location M_b ,

$$D_{x,b} = D_{x,F} - (D_{x,F} - D_{x,a}) \cos \phi_x, \quad D'_{x,b} = \frac{D_{x,F} - D_{x,a}}{\beta_{x,F}} \sin \phi_x. \quad (2.19)$$

In thin lens approximation, the 3×3 transfer matrix $\mathcal{M}_{x,b \rightarrow c}$ for the matching section from the end of the FODO part (marker location M_b) to the center of the NMC cell (marker location M_c) is obtained as

$$\mathcal{M}_{x,b \rightarrow c} = \begin{pmatrix} 1 + \frac{L_{d2}f_3 - L_d f_4 - L_{d2}f_4 - L_d L_{d2}}{f_3 f_4} & \frac{L_d f_4 + L_{d2} f_4 + L_d L_{d2}}{f_4} & 0 \\ \frac{f_3 - f_4 - L_d}{f_3 f_4} & 1 + \frac{L_d}{f_4} & 0 \\ 0 & 0 & 1 \end{pmatrix} \quad (2.20a)$$

$$= \begin{pmatrix} \sqrt{\frac{\beta_{x,c}}{\beta_{x,F}}} \cos \Phi_x & \sqrt{\beta_{x,c} \beta_{x,F}} \sin \Phi_x & 0 \\ -\frac{1}{\sqrt{\beta_{x,F} \beta_{x,c}}} \sin \Phi_x & \sqrt{\frac{\beta_{x,F}}{\beta_{x,c}}} \cos \Phi_x & 0 \\ 0 & 0 & 1 \end{pmatrix}, \quad (2.20b)$$

where Φ_x denotes the horizontal phase advance in the matching section. Note that Eq. (2.20b) is the betatron transfer matrix (cf. Eq. (A.32) in the Appendix) with the symmetry condition $\alpha_x = 0$ at the beginning and the end of the matching section. Using this generic transfer matrix and the expressions in Eq. (2.19), the derivate of dispersion at the center of the NMC module $D'_{x,c}$ is calculated as

$$D'_{x,c} = \frac{(1 - \zeta) \sin(\phi_x + \Phi_x) - \sin \Phi_x}{\sqrt{\beta_{x,F} \beta_{x,c}}} \quad (2.21)$$

where the parameter $\zeta = D_{x,a}/D_{x,F}$ was introduced. Note that $D'_{x,c}$ and $D_{x,c}$ do not depend on the actual structure of the matching section but on the phase advance Φ_x .

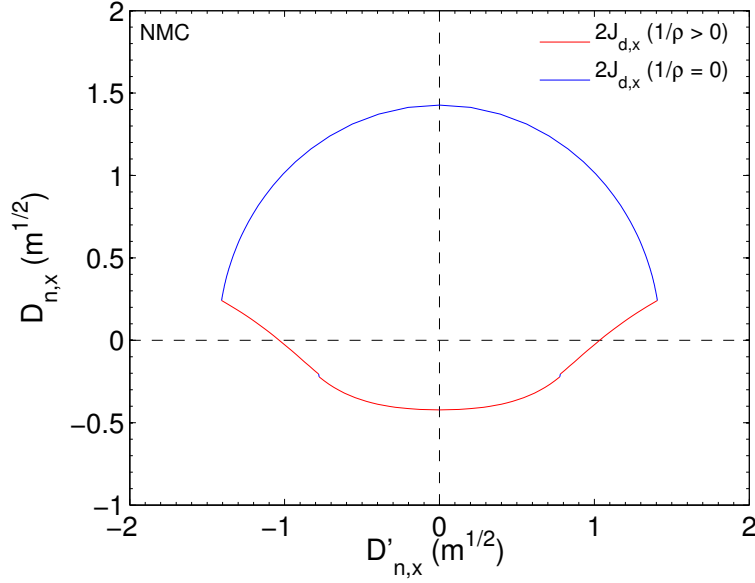


Figure 2.3: Plot of the normalized dispersion phase-space for the basic NMC cell shown in Fig. 2.2. The dispersion action $2J_{d,x}$ in dipole regions is indicated by red lines, while the blue lines indicate regions with zero curvature.

As symmetry requires $D'_{x,c} = 0$, the dispersion matching condition becomes [14]

$$\tan \Phi_x = \frac{(1 - \zeta) \sin \phi_x}{1 - (1 - \zeta) \cos \phi_x}. \quad (2.22)$$

Thus, the phase advance in the matching section Φ_x is not a free parameter, since it is determined by the choice of the phase advance in the FODO cell ϕ_x and the prescribed dispersion $D_{x,a}$ through the parameter ζ . The principle of dispersion matching is demonstrated instructively in the *normalized dispersion* phase-space (cf. [14], Chapter IV), as described in the following. The normalized dispersion coordinates for the horizontal plane are defined as

$$\begin{cases} D_{n,x} = \frac{1}{\sqrt{\beta_x}} D_x = \sqrt{2J_{d,x}} \cos \psi_{d,x}, \\ D'_{n,x} = \sqrt{\beta_x} D'_x + \frac{\alpha_x}{\sqrt{\beta_x}} D_x = -\sqrt{2J_{d,x}} \sin \psi_{d,x}, \end{cases} \quad (2.23)$$

where $J_{d,x}$ is the horizontal dispersion action, and $\psi_{d,x}$ is the horizontal dispersion phase advance. Further details on the definition of the dispersion action and its properties can be found in Appendix A.4. Figure 2.3 shows the normalized dispersion phase-space coordinates for the case of the NMC cell discussed above. The beginning of the cell corresponds to the negative value of $D_{n,x}$ (as negative dispersion was imposed) and $D'_{n,x} = 0$ (as α_x and $D'_x = 0$). The dispersion action $J_{d,x}$ is increased continuously

through the bending magnets as shown by the red lines up to the end of the FODO cell. As $J_{d,x} = \text{const.}$ in bending-free regions, the matching section corresponds to the big blue part of the line lying on a circle and transporting the dispersion to the first bending magnet of the second FODO cell. This is achieved by matching the horizontal phase advance Φ_x in the doublet insertion.

As the phase advance Φ_x in the matching section is determined by Eq. (2.22), f_3 and f_4 are obtained by comparison of Eqs. (2.20a) and (2.20b). It follows that

$$f_4 = \frac{L_d(L_d + 2L_{d2} + \sqrt{L_d^2 + 2L_{d2}\beta_{x,F}\sin 2\Phi_x})}{\beta_{x,F}\sin 2\Phi_x - 2(L_d + L_{d2})}, \quad (2.24)$$

where a second solution for f_4 yielding negative values is disregarded, as it corresponds to an inversion of the defocusing quadrupole in the center of the matching section. Thus, it is found that

$$f_3 = \frac{L_d\beta_{x,F}(L_d \cos 2\Phi_x - \beta_{x,F}\sin 2\Phi_x - \sqrt{L_d^2 + 2L_{d2}\beta_{x,F}\sin 2\Phi_x})}{2\beta_{x,F}(L_{d2} + L_d \cos 2\Phi_x) + (L_d - \beta_{x,F})(L_d + \beta_{x,F})\sin 2\Phi_x}. \quad (2.25)$$

At this point, the focal lengths of all four quadrupoles are defined, which determines the horizontal beta function in the center of the NMC module to

$$\beta_{x,c} = \frac{L_{d2}\beta_{x,F}\sin 2\Phi_x + L_d(L_d + \sqrt{L_d^2 + 2L_{d2}\beta_{x,F}\sin 2\Phi_x})}{2\beta_{x,F}\sin^2 \Phi_x}. \quad (2.26)$$

For the NMC module analyzed here, the momentum compaction factor can be determined in first approximation by the values of dispersion in the center of the bending magnets. Using the appropriate transfer matrices, it is obtained that

$$\begin{aligned} D_{x,B_1} &= \left(1 - \frac{L}{4f_1}\right) D_{x,a} + \frac{1}{8}L\theta, \\ D_{x,B_2} &= \left(1 - \frac{3L}{4f_1} + \frac{L}{2f_2} - \frac{L^2}{4f_1f_2}\right) D_{x,a} + \left(\frac{9}{8} + \frac{L}{4f_2}\right) L\theta, \end{aligned} \quad (2.27)$$

where D_{x,B_1} and D_{x,B_2} denote the dispersion in the center of the first and the second dipole, respectively. For simplicity it will be assumed in the following that the focal lengths in the FODO part are equal, i.e. $f_1 = f_2 = f$ and thus $\phi_x = \phi_y = \phi$ within the small angle approximation². In this case, Eq. (2.27) can be rewritten using the expressions in Eq. (2.14) such that

$$\begin{aligned} D_{x,B_1} &= D_{x,a} \left(1 - \frac{1}{2}\sin \frac{\phi}{2}\right) + D_{x,F} \frac{\sin^2 \frac{\phi}{2}}{8 + 4\sin \frac{\phi}{2}}, \\ D_{x,B_2} &= D_{x,a} \left(1 - \frac{1}{2}\sin \frac{\phi}{2} - \sin^2 \frac{\phi}{2}\right) + D_{x,F} \frac{(9 + 4\sin \frac{\phi}{2})\sin^2 \frac{\phi}{2}}{8 + 4\sin \frac{\phi}{2}}. \end{aligned} \quad (2.28)$$

²In small angle approximation the weak focusing of the sector bending magnet is neglected.

Similar to Eq. (2.16), the transition energy and the momentum compaction factor of the NMC cell are approximately given by

$$\alpha_c = \frac{1}{\gamma_t^2} \approx \frac{D_{x,B_1} + D_{x,B_2}}{L_M/2} \theta = \frac{D_{x,F} \theta}{L_M/2} \left[(2 - \sin \frac{\phi}{2} - \sin^2 \frac{\phi}{2}) \zeta + \frac{(5 + 2 \sin \frac{\phi}{2}) \sin^2 \frac{\phi}{2}}{4 + 2 \sin \frac{\phi}{2}} \right], \quad (2.29)$$

where the total length of the NMC module is obtained as $L_M = 2(2L + L_{d1} + L_{d2})$. Hence, the choice of the dispersion function at the entrance of the module $D_{x,a}$ is essential for determining the momentum compaction factor (or transition energy) and the dispersion excursion. In the bending free matching section, the dispersion action is invariant, i.e.

$$J_{d,c} = J_{d,b} = \frac{1}{2} \left[\frac{D_{x,b}^2}{\beta_{x,F}} + \beta_{x,F} D_{x,b}'^2 \right] = J_{d,F} [1 - 2(1 - \zeta) \cos \phi + (1 - \zeta)^2], \quad (2.30)$$

where $J_{d,b}$ and $J_{d,c}$ denote the values of the horizontal dispersion action at marker locations M_b and M_c , respectively. $J_{d,F}$ is the horizontal dispersion action of a pure FODO cell in the center of the focusing quadrupole given by

$$J_{d,F} = \frac{1}{2} \frac{D_{x,F}^2}{\beta_{x,F}} = \frac{1}{2} \left[L \theta^2 \frac{\cos \frac{\phi}{2} (1 + \frac{1}{2} \sin \frac{\phi}{2})^2}{\sin^3 \frac{\phi}{2} (1 + \sin \frac{\phi}{2})} \right], \quad (2.31)$$

under the assumption of equal phase advances in both planes for a FODO cell in thin lens approximation. As pointed out by Lee *et al.* [30], the form of Eq. (2.30) may tempt to conclude that small phase advances ϕ are preferable for minimizing the dispersion action in the matching section. However, according to Eq. (2.31) $J_{d,F}$ is inversely proportional to $\sin^3 \frac{\phi}{2}$ and it increases with smaller ϕ . Lee *et al.* concluded that a compromise choice for smallest dispersion action is obtained for ϕ_x between $\pi/3$ and $2\pi/5$. It is interesting to note that choosing a low beta insertion for the matching cell helps to reduce the excursion of the dispersion function in the center of the NMC cell and to shorten the length of the matching section (and consequently of the entire module).

Up to now, only conditions for the matching of the NMC module in the horizontal plane were discussed. However, not all quadrupole settings that are found to match the optical functions in the horizontal plane yield stable solutions in the vertical plane. Since the analysis was based on the assumption of a matched FODO cell, the focal lengths of the two quadrupoles in the matching section are determined by the choice of the prescribed dispersion function $D_{x,a}$. Therefore, a given set of parameters for the NMC module can be easily checked for stability in the vertical plane. As the module is symmetric, the periodicity condition requires the derivative of the beta function to be zero at the entrance and in the center of the cell, i.e. $\alpha_{y,a} = \alpha_{y,c} = 0$. Thus, for stability the 2×2 transfer matrix $M_{y,a \rightarrow c}$ for half the NMC module in the vertical plane has to

take the form

$$M_{y,a \rightarrow c} = \begin{pmatrix} \sqrt{\frac{\beta_{y,c}}{\beta_{y,a}}} \cos \mu_y & \sqrt{\beta_{y,c} \beta_{y,a}} \sin \mu_y \\ -\frac{1}{\sqrt{\beta_{y,a} \beta_{y,c}}} \sin \mu_y & \sqrt{\frac{\beta_{y,a}}{\beta_{y,c}}} \cos \mu_y \end{pmatrix}, \quad (2.32)$$

where $\beta_{y,a}$ and $\beta_{y,c}$ are the vertical beta functions at marker locations M_a and M_c , respectively, and μ_y denotes the vertical phase advance along half the module. It should be emphasized here that in general, $\beta_{y,a} \neq \beta_{y,F}$, i.e. the vertical beta function at the entrance of the NMC module is in general not equal to the periodic solution of the pure FODO cell. For stability of the NMC cell, the phase advance μ_y has to be real or equivalently $0 < \sin^2 \mu_y \leq 1$. This criterion can be applied numerically by multiplying the off-diagonal elements of the transfer matrix $M_{y,a \rightarrow c}$ for a set of quadrupole focal lengths as determined by the dispersion matching in the horizontal plane.

In the following, such an analysis is presented for a specific case of a basic NMC module where the length of each bending magnet is chosen as $L = 15$ m with a bending angle of $\theta = \pi/30$ and the lengths of the drift spaces in the matching section are $L_{d1} = L_{d2} = 3$ m. Very similar parameters were also chosen for the optics calculation shown in Fig. 2.2. For reducing the parameter space, the focal lengths of the quadrupoles in the FODO cell are set to identical values, i.e. $f_1 = f_2 = f$. It should be emphasized that the analysis could also be performed without this assumption. For pairs of numerical values for the phase advance in the FODO cell $\phi_x = \phi$ and for the prescribed dispersion $D_{x,a}$ the focal lengths of all four quadrupoles are calculated using the corresponding matching conditions. For these values, the vertical phase advance μ_y is then determined as described above.

The *stable solutions* as found by this technique are shown in various color plots in Fig. 2.4. In the graph on the top left they are shown as a function of the horizontal tune in the FODO cell $\nu_{x,\text{FODO}} = \phi/2\pi$ and the prescribed dispersion $D_{x,a}$, where the color code indicates the vertical tune of the entire NMC module $\nu_{y,\text{NMC}} = 2\mu_y/2\pi$. Note that the stable solutions are grouped to a complicated structure of islands, which are bounded by lines at which the vertical tune is equal to a multiple of 0.5, i.e. $\nu_{y,\text{NMC}} = n \cdot 0.5$ with $n = 1, 2, 3, 4$. This is a direct consequence of the stability criterion. Within the presumed parameter set, a big part of the possible solutions are unstable in the vertical plane. On the top right plot, the color code indicates the momentum compaction factor as calculated using Eq. (2.29). For a sufficiently small horizontal tune $\nu_{x,\text{FODO}}$ and negative dispersion $D_{x,a}$, the momentum compaction factor α_c becomes negative. The boundary between positive and negative α_c can be observed even more clearly on the bottom left graph of Fig. 2.4, as γ_t is changing from large real values to large imaginary numbers. From a lattice design point of view, the most interesting solutions with negative momentum compaction are located on the stable island with $\nu_{x,\text{FODO}} < 0.2$ and $D_{x,a} < 0$. For these cases, the vertical tunes of the NMC module are found as $\nu_{y,\text{NMC}} < 0.5$ and the vertical beta function is varying smoothly along the NMC cell,

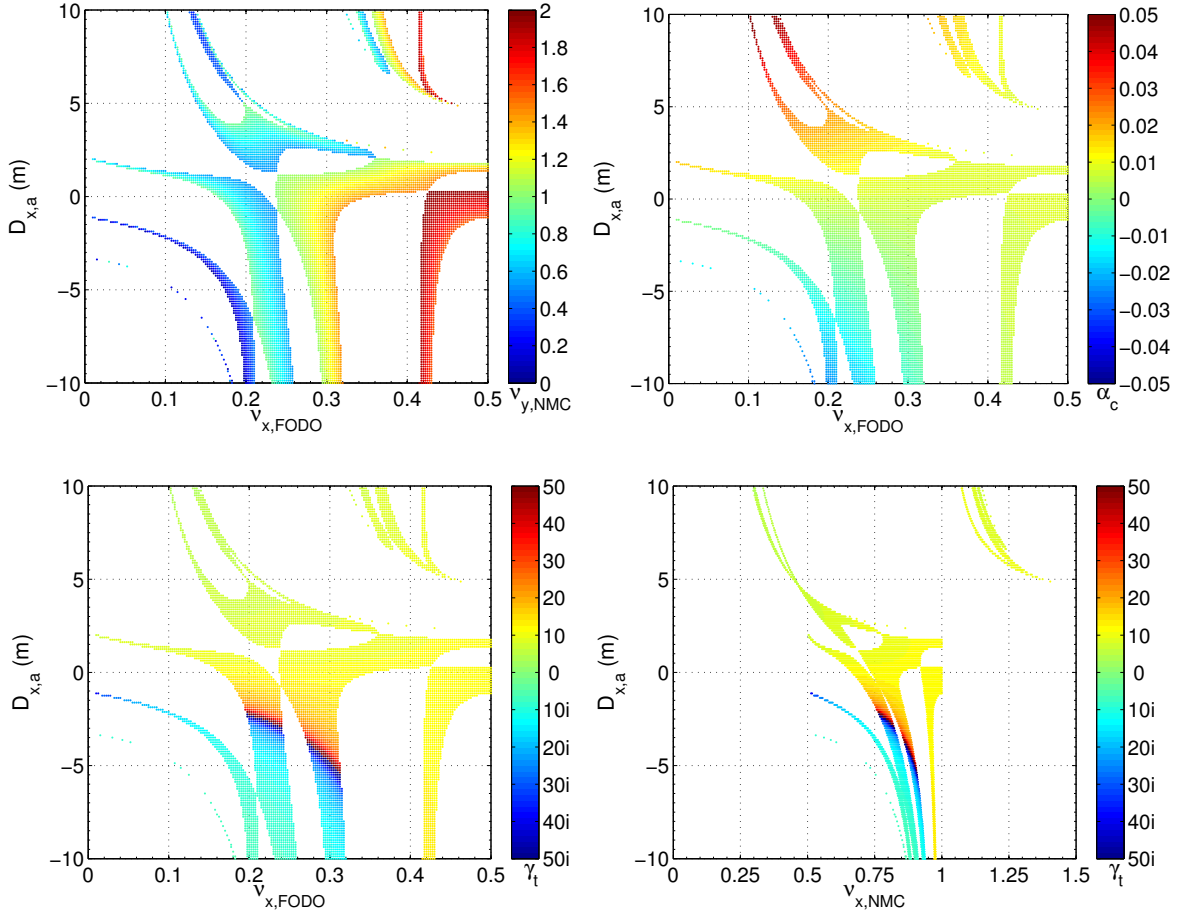


Figure 2.4: Results of a numerical analysis of the NMC cell stability: stable solutions are indicated by dots, where the color code indicates the vertical tune of the module $\nu_{y,\text{NMC}}$ (top left), the momentum compaction factor α_c (top right) and the transition energy γ_t (bottom left and bottom right). They are plotted as function of the tune in the FODO cell $\nu_{x,\text{FODO}}$ or the tune of the NMC module $\nu_{x,\text{NMC}}$, respectively and the prescribed dispersion $D_{x,a}$.

similar to the example shown in Fig. 2.2. Moderate dispersion excursion is sufficient for achieving negative momentum compaction and a minimum of the dispersion action in the matching section is obtained for $\nu_{x,\text{FODO}} \approx 1/6$. Finally, the transition energy is shown as function of the horizontal tune of the NMC module $\nu_{x,\text{NMC}} = (2\phi + 2\Phi_x)/2\pi$ and the prescribed dispersion $D_{x,a}$ on the lower right plot of Fig. 2.4. Due to the dispersion matching condition derived in Eq. (2.22), the stable islands for imaginary γ_t are squeezed to a dense region of $\nu_{x,\text{NMC}}$ values. Thus, it is possible to tune the momentum compaction factor for a given value of $D_{x,a}$ by adjusting the horizontal phase advance along the NMC module.

The analysis shows that the matching of the NMC cell is not trivial. In particular, taking into account that quite some simplifications and approximations were applied, the relations between parameters are rather complex. As the focal lengths f_1 and f_2 were assumed to be equal, the vertical tune of the module $\nu_{y,\text{NMC}}$ is not a free parameter and is determined entirely by the matching in the horizontal plane. A more general treatment of the NMC module should account for the fact that the focal lengths in the FODO cell can assume different values. It is worth pointing out that this can be implemented easily in the analysis as performed above by replacing the simplified expressions in Eqs. (2.28) by the corresponding general expressions for calculating the dispersion in the dipoles according to Eqs. (2.27). Then, the additional degree of freedom can be used to adjust $\nu_{y,\text{NMC}}$. A further artificial constraint was imposed by the fact that the matching as followed here starts from a periodic solution of the FODO cell, i.e. $\alpha_x = \alpha_{x,b} = 0$ at the end of the FODO cell. This condition was introduced here in order to achieve a simple analytically closed form based on the results of the FODO cell as discussed in section 2.2. Omitting this constraint enlarges the stable area in the parameter space and allows to further adjust the NMC cell to the desired properties. For practical purposes, the matching of an NMC lattice is performed using optics codes such as MADX in combination with systematic parameter scans. This will be discussed in the following chapter.

3. PS2 as potential replacement of the CERN PS

3.1. Introduction

The performance reach of the LHC depends to a large extent on the beam quality provided by the injectors, in particular on the beam intensity and the beam brightness. In order to fully profit from the potential of the LHC and its future luminosity upgrades, the LHC injectors have to be upgraded [5]. Therefore, a working group on “Proton Accelerators for the Future” [6] has been created in 2005 for planning the upgrade of the CERN accelerator complex.

In a first stage, the existing 50 MeV proton linac, Linac2, will be replaced by a new 160 MeV H^- linac called Linac4 [7], which is presently under construction. This will remove the space charge bottleneck for LHC beams at injection into the PSB. In particular, the incoherent space charge tune spread in a machine with smooth lattice functions can be estimated by (cf. Appendix C.1)

$$\Delta Q_{x,y} \propto \frac{N}{\varepsilon_n \beta \gamma^2}, \quad (3.1)$$

where β, γ are the relativistic velocity and mass factors, respectively, N/ε_n is the beam brightness with N the number of protons per bunch and ε_n the normalized transverse emittance of a round beam. Since an increase of the injection energy from 50 MeV to 160 MeV corresponds to a twice larger relativistic factor $\beta\gamma^2$, the brightness in the PSB at injection can be doubled while keeping the same incoherent space charge tune spread. This higher brightness is expected to be conserved during acceleration by optimizing the painting of the three dimensional particle distribution in the PSB acceptance during the H^- charge-exchange injection.

In a second stage [8], it was proposed to build a superconducting proton linac SPL [31] for injecting into a new 50 GeV synchrotron called PS2, replacing the 1.4 GeV PSB and the 26 GeV PS. In this scenario, Linac4 is used as a front-end for the SPL, which in the low power option (LPSPL) injects an H^- beam at a repetition rate of 2 Hz into PS2. Limiting the incoherent space charge tune spread to $\Delta Q_y < 0.2$ for an intensity of 4×10^{11} p/b at normalized emittances of $\varepsilon_n = 3.5 \mu\text{m}$ in PS2 requires a kinetic energy of 4 GeV at injection. The PS2 extraction energy of 50 GeV is expected to mitigate beam instabilities and collective effects on the SPS flat bottom and to reduce losses during beam transfer. A substantial upgrade program for the SPS [32] in preparation for the higher injection energy and the higher beam intensity was foreseen. The main design goals of the PS2 for LHC operation are significantly increased beam brightness, flexibility for generating different bunch patterns and spacings, sufficient

Table 3.1: PS2 beam parameters (for $\gamma_t = 25.7i$)

Injection	LHC 25 ns	LHC 50 ns	FT SPS/PS2	Ions
Kinetic energy, E_{kin} (GeV)	4.0	4.0	4.0	0.1354
Energy, E (GeV)	4.938	4.938	4.938	221.16
Beam rigidity, $B\rho$ (Tm)	16.172	16.172	16.172	6.67
Relativistic factor, γ	5.26	5.26	5.26	1.15
Revolution freq., f_{rev} (kHz)	218.6	218.6	218.6	108.4
Particles per bunch	4.2×10^{11}	3.1×10^{11}	6.3×10^{11}	1.1×10^8
Emittance, $\varepsilon_{n,x}/\varepsilon_{n,y}$ (μm)	3/3	3/3	9/6	0.7/0.7
Harmonic number, h	180	180	180	172
Long. emittance, ε_l (eVs)	0.4	0.3	0.4	4.0
Full mom. spread, $2\hat{\delta}$	0.00653	0.00482	0.00653	0.00276
Bunching factor	0.47		0.47	
Full bunch length, $4\sigma_l$ (ns)	17.8	17.8	17.8	37.5
RF voltage, V_{RF} (MV)	0.658	0.370	0.658	0.481
Synchrotron tune, Q_s	0.0122	0.00915	0.0122	0.102
Number of bunches	168	168	128-168	8
Particles per pulse	7.1×10^{13}	5.2×10^{13}	$8.1-11 \times 10^{13}$	9×10^8
Total beam power (kW)	23	17	27-35	0.011
Energy per pulse (kJ)	56	41	64-84	0.032
Total beam current (A)	2.5	1.8	2.8-3.7	0.001
Extraction	LHC 25 ns	LHC 50 ns	FT SPS/PS2	Ions
Kinetic energy, E_{kin} (GeV)	50	50	50	12.23
Energy, E (GeV)	50.938	50.938	50.938	2757
Beam rigidity, $B\rho$ (Tm)	169.88	169.88	169.88	169.88
Relativistic factor, γ	54.28	54.28	54.28	14.28
Revolution freq., f_{rev} (kHz)	222.6	222.6	222.6	222.1
Particles per bunch	4.0×10^{11}	5.9×10^{11}	6.0×10^{11}	1.2×10^8
Emittance, $\varepsilon_{n,x}/\varepsilon_{n,y}$ (μm)	3/3	3/3	9/6	0.7/0.7
Harmonic number, h	180	90	180	90
Long. emittance, ε_l (eVs)	0.6	0.7	0.6	10
Full mom. spread, $2\hat{\delta}$	0.00375	0.00405	0.00375	0.00129
Full bunch length, $4\sigma_l$ (ns)	4.0	4.33	4.0	3.6
RF voltage, V_{RF} (MV)	1.5	1.5	1.5	1.5
Synchrotron tune, Q_s	0.00125	0.00125	0.00125	0.00165
Number of bunches	168	84	128-168	4
Particles per pulse	6.7×10^{13}	5.0×10^{13}	$7.7-10 \times 10^{13}$	4.8×10^8
Bunch spacing (ns)	25	50	0	100
Total beam power (kW)	230	170	263-346	0.076
Energy per pulse (kJ)	548	404	627-823	0.212
Total beam current (A)	2.4	1.8	2.7-3.6	0.001

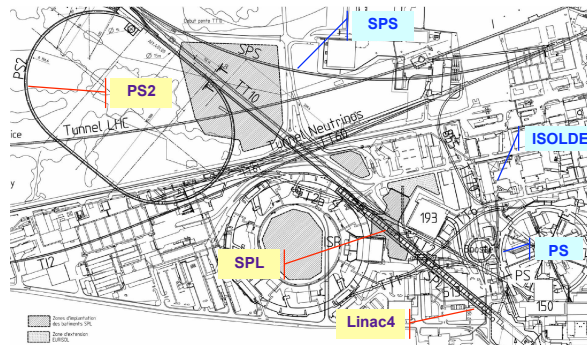


Figure 3.1: Integration of the PS2 and SPL in the existing accelerator complex at CERN [8]. Existing machines are indicated by blue labels while machines under construction (Linac4) or in study are indicated by yellow labels.

margin for fully exploiting the potential of the LHC and simplified operation compared to the existing PS machine. For reliability, the design of the PS2 is based on normal conducting magnets. Hence, achieving a top energy of 50 GeV requires a roughly twice larger circumference compared to the PS. The PS2 circumference determines the filling strategy for the subsequent SPS and thus plays an important role for the operation of the overall complex. With a twice larger circumference compared to the PS, only half the number of PS2 pulses are needed to fill the SPS for the LHC. This reduces the required length of the SPS injection plateau from the present 10.8 s for the injection of four PS batches to around 2.4 s for the injection of two PS2 batches while minimizing the filling time of the LHC [33]. The fixed target beams for the SPS will be extracted from PS2 using a resonant five turn extraction [10]. An optimized filling of the SPS in a single pulse requires therefore a ratio between the PS2/SPS circumferences of slightly less than 1/5. Considerations on rf-synchronization for the LHC beams determine the optimum circumference of the PS2 as 15/77 of the SPS circumference (i.e. 1346.4 m) [34]. The beam will be extracted from PS2 with a 40 MHz bunch structure (harmonic number $h = 180$) and a 4 ns total bunch length to be compatible with the SPS 200 MHz RF bucket. Since the LPSPL injector provides chopping at 40 MHz, any bunch pattern can be generated already at injection into PS2. Therefore, elaborate longitudinal gymnastics and bunch splitting schemes as presently used in the PS can be avoided, thus minimizing equipment and impedance of the machine. In addition to the challenging proton beams for LHC, the PS2 as replacement of the PS has to provide beam for a competitive fixed-target physics program. Furthermore, it is also required to deliver ion beams to the LHC and to physics users. In this case, PS2 will receive ion beams from the low energy ion ring LEIR. A summary of the beam parameters at injection and extraction from the PS2 complex is given in Table 3.1. Note that two bunch spacings are considered for the LHC proton beams, namely 25 ns and 50 ns. Ion beams considered here are made of Pb^{54+} ions.

Integrating the PS2 and its injector SPL in the existing CERN accelerator complex should be achieved with a minimum length of high-energy transfer line to the SPS and reusing the existing SPS injection channel. Small bending radii should be avoided in the H^- injection line from SPL to PS2 in order to minimize losses due to Lorentz stripping. Furthermore, transporting the ion beam from LEIR should be achieved with a minimum length of transfer lines from the existing TT10 line to PS2. An optimal solution is thus found by locating the PS2 injection and extraction channels in a single straight section in line with the SPL. This suggests a racetrack shape for the PS2 machine. A possible integration in the existing CERN accelerator complex is shown in Fig. 3.1. The main PS2 design parameters are summarized in Ref. [35].

3.2. PS2 baseline lattice

As part of the injector chain of the CERN accelerator complex, PS2 has to provide flexibility for accelerating a variety of different beams with high intensities. Prototypes of the PS2 lattice based on a simple FODO structure with missing dipoles at the arc extremities for suppressing dispersion in the long straight sections have been described in Ref. [36]. Given the circumference and the energy range of the machine, transition has to be crossed when using a regular FODO lattice. A γ_t -jump scheme (cf. Section 2.1) has been studied for mitigating beam instabilities during transition crossing. For the intensities envisaged for PS2 and assuming the impedance of the PS, a total $\Delta\gamma_t$ of around 3 within a duration of 1 ms would be required for beam stability [37]. This was found to be at the limit of what can be achieved with acceptable optics distortion. As a consequence of that and for avoiding the operational complication of a γ_t -jump scheme and limitations due to transition crossing, it was decided to design the PS2 lattice with negative momentum compaction (NMC) leading to a imaginary γ_t . PS2 lattice candidates based on this approach were reported in [38] and [39], and their properties with respect to orbit and chromaticity correction was studied [40]. Towards a more realistic lattice design, tighter space constraints between the magnets were imposed in order to reserve sufficient empty space for beam instrumentation and vacuum equipment. In this context, the layout of the long straight sections (LSSs) was changed from the FODO structure used in early designs to a shorter structure based on quadrupole doublets [41]. This new layout based on quadrupole doublets has the additional advantage of avoiding the crossing of transfer-lines of the previous design. PS2 lattice variants with racetrack shape based on the doublet straight section were reported in [42] and compared to higher symmetric options [43].

The baseline option for the PS2 lattice with racetrack shape is presented in the following. A list of the corresponding machine parameters is given in Table 3.2. Figure 3.2 shows a layout of the lattice. An alternative option with threefold symmetry and resonant arcs will be discussed in Section 3.3.

Table 3.2: Machine parameters of the baseline PS2

Basic parameters	
Circumference, C (m)	1346.4
Superperiodicity	2
Maximum beam rigidity, $\hat{B}\rho$ (Tm)	169.9
Optics parameters	
Betatron tune, Q_x/Q_y	11.76/6.70
Maximum beta function, $\hat{\beta}_x/\hat{\beta}_y$ (m)	60/60
Minimum/maximum dispersion, \hat{D}_x (m)	-3/+3.3
Natural chromaticity, Q'_x/Q'_y	-21.5/-11
Specific natural chromaticity, ξ_x/ξ_y	-1.8/-1.6
Gamma at transition, γ_t	25.7 <i>i</i>
Dipole magnets	
Number of dipoles	170
Bending radius, ρ (m)	99.9
Bending angle, θ (mrad)	36.95
Length (m)	3.69
Minimum drift space between dipoles (m)	0.8
Gap height (mm)	84
Full aperture (cm)	12.6×6.5
Quadrupole magnets	
Number of quadrupoles	116
Number of independent families	15
Number of types, arc	3
Length, arc (m)	0.8, 1.6, 2.2
Maximum normalized quadrupole gradient, arc (m^{-2})	0.094
Minimum drift space around quadrupoles (m)	1.3
Pole radius, arc (mm)	65
Full aperture, focusing quadrupoles (cm)	12.6×6.5
Full aperture, defocusing quadrupoles (cm)	11×7.5
Number of types, LSS	1
Pole radius, LSS (mm)	82
Length, LSS (m)	2.4
Chromatic sextupole magnets	
Number of sextupoles	84
Number of independent families	4
Number of types	1
Length (m)	0.4
Maximum normalized sextupole strength (m^{-3})	0.8

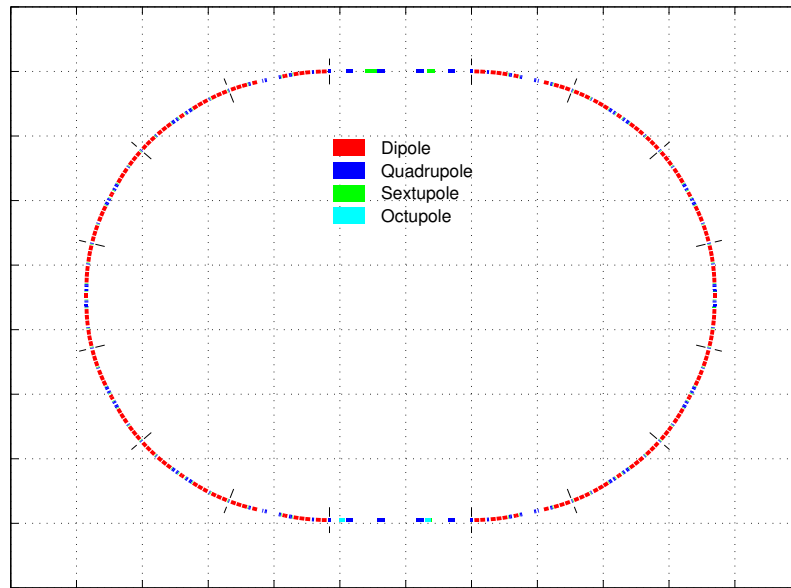


Figure 3.2: Layout of the racetrack PS2 lattice. The grid lines are spaced by 50 m.

3.2.1. Linear optics

The optics of the long straight sections in the PS2 lattice have to meet stringent requirements on the phase advances between beam transfer elements. Therefore, the arcs have to provide not only negative dispersion for achieving imaginary γ_t , but also need to be flexible for tuning the machine. In the baseline PS2 lattice, each of the arcs consists of five negative momentum compaction (NMC) cells and two dispersion suppressor modules for matching to the dispersion-free long straight sections. Operational reliability and flexibility is provided by normal conducting, separated function magnets. The PS2 lattice is built of 170 dipoles each with a length of 3.7 m, a bending radius of $\rho = 100$ m and a maximum field of 1.7 T at top energy. The 116 quadrupole magnets are grouped to 15 families.

The design of the PS2 lattice is based on the assumption that all beam transfer elements are located in a single long straight section. In particular, three different extraction modes have to be accommodated: fast extraction to the SPS for LHC type beams, multi-turn (five-turn) extraction to the SPS for fixed target physics and resonant slow extraction for potential physics directly from PS2. A compact design of the straight section compatible with these requirements is achieved by using a quadrupole doublet structure [41]. In order to allow large beam excursion during beam transfer, the quadrupole magnets in the straight sections have enlarged aperture. Each of the mirror symmetric LSSs has a length of about 108 m. The stripping foil for the H^- charge exchange injection is placed in the center of the LSS, surrounded by four chicane magnets for steering the closed orbit during the multi-turn phase-space painting. Ions are injected in a classical single turn injection close to the arc. The LSS on the opposite

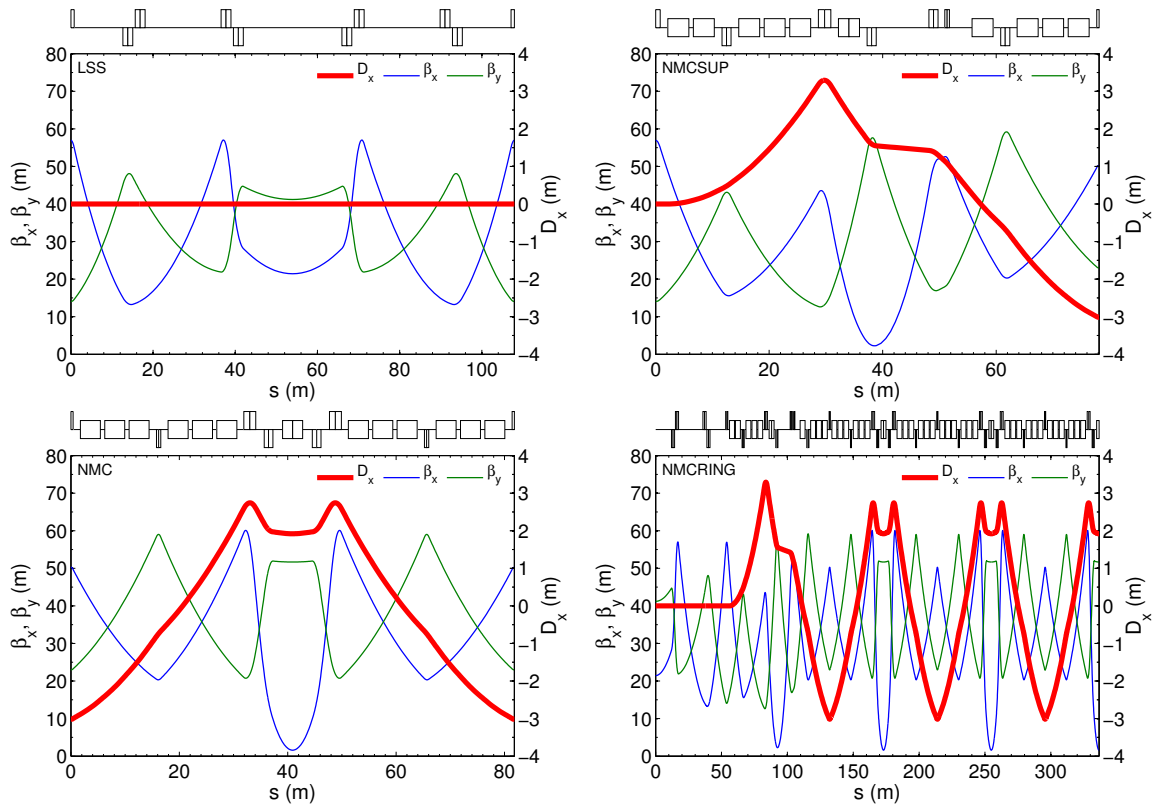


Figure 3.3: Optics functions in the base-line PS2 lattice, with the zero dispersion long straight section (LSS) on the top left, the dispersion suppressor module on the top right and the PS2 negative momentum compaction (NMC) cell on the bottom left. The plot on the bottom right shows a quarter of the PS2 ring.

side of the ring will accommodate the collimation system and the RF cavities. Figure 3.3 shows plots of the optics functions in the baseline PS2 lattice with betatron tunes $(Q_x, Q_y) = (11.76, 6.70)$ and $\gamma_t = 26i$. The backbone of the PS2 arcs are the NMC cells. The layout of these cells is based on two FODO cells linked by a central insertion of quadrupole doublets [30]. A high packing factor is achieved by 13 dipole magnets, three of them placed in each FODO half cell and one in the center of the doublet insertion. As discussed in Section 2.3 for a similar NMC module, wide tuning flexibility can be achieved using four independent families of quadrupoles. Optimizing their maximal gradients to 16 T/m yields three different types of quadrupoles for the four families with corresponding lengths of 0.8 m, 1.6 m and 2.2 m. The magnet-to-magnet drift spaces of 0.8 m between dipoles and 1.3 m around quadrupoles are reserved for the installation of chromaticity sextupoles, orbit correctors, beam position monitors, vacuum pumps and beam instrumentation. The PS2 basic NMC cell has a total length of 81.8 m. The optics functions are matched to the LSSs with the dispersion suppressor modules on either side of the NMC arcs. Their length is fixed by the machine circumference to 78.1 m. The first and the last quadrupole is shared with the LSS and the adjacent NMC

cell, respectively. Ten dipole magnets and six independent quadrupole families based on the same types of magnets as used in the arc cells are needed to achieve the matching constraints. The dispersion matching can be illustrated by plotting the dispersion action $J_{d,x}$ in the normalized dispersion phase-space (cf. Appendix A.4), as shown in Fig. 3.4. The zero dispersion straight sections are represented by a dot in the origin (zero dispersion action). From there, the dispersion suppressor module is building up the dispersion action $J_{d,x}$ in several bending magnets as represented by red lines. The phase advance is adjusted in order to match the dispersion function to the negative value at the entrance of the NMC arc module. This point corresponds to the minimum of $D_{n,x}$ and $D'_{n,x} = 0$. The dispersion action is then transported through the arc following the closed line. The dispersion suppressor on the other side of the arc is not shown in the plot. Note that most of the dipoles are located in regions where $D_{n,x} < 0$, as required for achieving negative momentum compaction. However, especially in the dispersion suppressor, quite a few bending magnets contribute with positive dispersion and therefore increase the momentum compaction factor of the overall lattice.

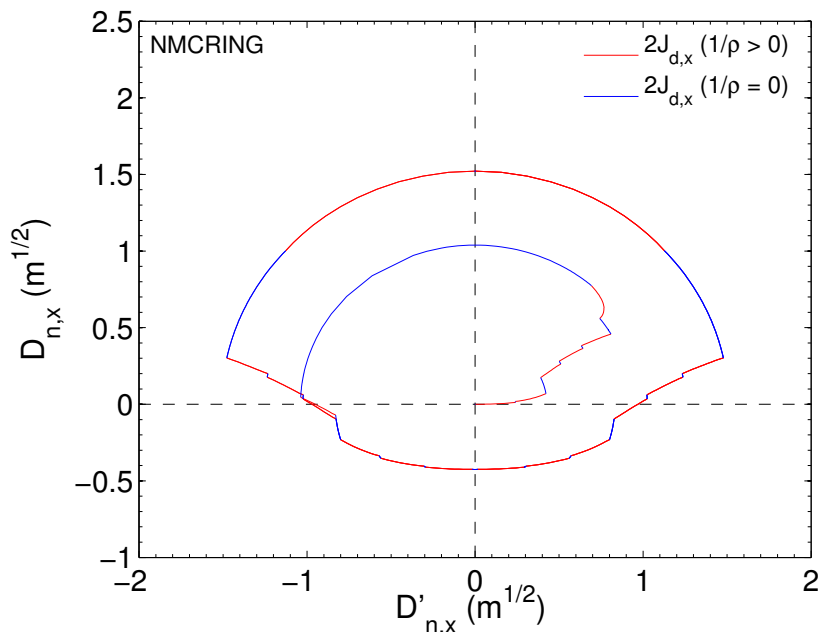


Figure 3.4: Dispersion action $J_{d,x}$ in the normalized dispersion phase-space coordinates $D_{n,x}$ and $D'_{n,x}$ for the PS2 ring.

3.2.2. Physical aperture

For optimizing the geometric acceptance of the PS2 ring, two major types of vacuum chambers will be used in the arcs. They have a superelliptical shape described by the

relation

$$\left(\frac{x}{a}\right)^g + \left(\frac{y}{b}\right)^g = 1, \quad (3.2)$$

where a and b are the maximum half sizes of the vacuum chamber in the horizontal and vertical plane, respectively, and g is the parameter defining the geometric shape ($g = 2$ corresponding to a true ellipse, while $g = \infty$ yields a rectangle). For calculating the actual beam size around the machine, the dispersive orbit as well as closed orbit errors and beta-beating have to be taken into account. Chromatic effects in the orbit are estimated by the parametric dispersion $\mathcal{D}_{x,y}$ defined as

$$\mathcal{D}_{x,y}(s) = (1+k_\beta) \left[|D_{x,y}(s)| + k_D \frac{\hat{D}_{x,y}}{\sqrt{\hat{\beta}_{x,y}}} \sqrt{\beta_{x,y}(s)} \right] \hat{\delta}, \quad (3.3)$$

where \hat{D} and $\hat{\beta}$ denote the peak values of dispersion and beta functions, k_β is the beta-beat factor, k_D is a factor accounting for parasitic dispersion and $\hat{\delta}$ is the maximum momentum spread as given by the RF-bucket height. The available aperture $a_u(s)$ in terms of rms beam size $\sigma_{x,y} = (1+k_\beta) \sqrt{\beta_{x,y} \varepsilon_{x,y}}$ around the ring can be calculated as³ (Chapter 4.3)

$$a_u(s) = \frac{A_u(s) - \left[u_{\text{co}}(s) + \Delta \hat{u}_{\text{co}} \sqrt{\beta_u(s)/\hat{\beta}_u} + (1+k_\beta) \left(|D_u(s)| + k_{D_u} \hat{D}_u \sqrt{\beta_u(s)/\hat{\beta}_u} \right) \hat{\delta} \right]}{(1+k_\beta) \sqrt{\beta_u(s) \varepsilon_u}}, \quad (3.4)$$

where $u_{\text{co}}(s)$ is the reference closed orbit offset (which is normally zero), Δu_{co} accounts for closed orbit distortion and u stands for either x or y . The available machine aperture can be expressed by a single parameter n_A referring to the number of rms beam sizes $\sigma_{x,y}$ that fit into the vacuum chamber in both planes all around the ring, i.e. $n_A = \min(a_x(s), a_y(s))$. The corresponding optics parameters for the PS2 lattice are $\hat{D}_x \approx 3.5$ m, $\hat{\beta}_{x,y} \approx 60$ m and $u_{\text{co}}(s) = 0$ in the arcs (deliberate closed orbit bumps are created only in the LSS during injection). The errors are estimated by a closed orbit uncertainty $\Delta \hat{u}_{\text{co}} = 1$ mm, parasitic dispersion $k_D = 0.1$ (i.e. 10%) and beta-beat $k_\beta = 0.1$ (i.e. 20%). In terms of aperture, the most demanding beam for the PS2 is the high intensity fixed target beam at injection, where $\hat{\delta} = 0.0035$ and normalized emittances of $\varepsilon_{n,x} = 9 \mu\text{m}$ and $\varepsilon_{n,y} = 6 \mu\text{m}$ are expected (cf. Table 3.1). The PS2 vacuum chambers [44] have geometries of $(a, b) = (63, 32.5)$ mm in the focusing quadrupoles and in the dipoles, and $(a, b) = (55, 37.5)$ mm in the defocusing quadrupoles. Both types of chambers are based on an elliptical shape with $g = 3$. The geometries of the main vacuum chambers are designed for providing a machine aperture of $n_A(\sigma_{\text{FT}}) = 3.5$ in units of the rms beam size of the fixed target beam (denoted as σ_{FT}) around the

³A similar concept was used for the calculation of the available aperture of the primary (n_1) and secondary beam halo (n_2) in the LHC vacuum chambers[1]

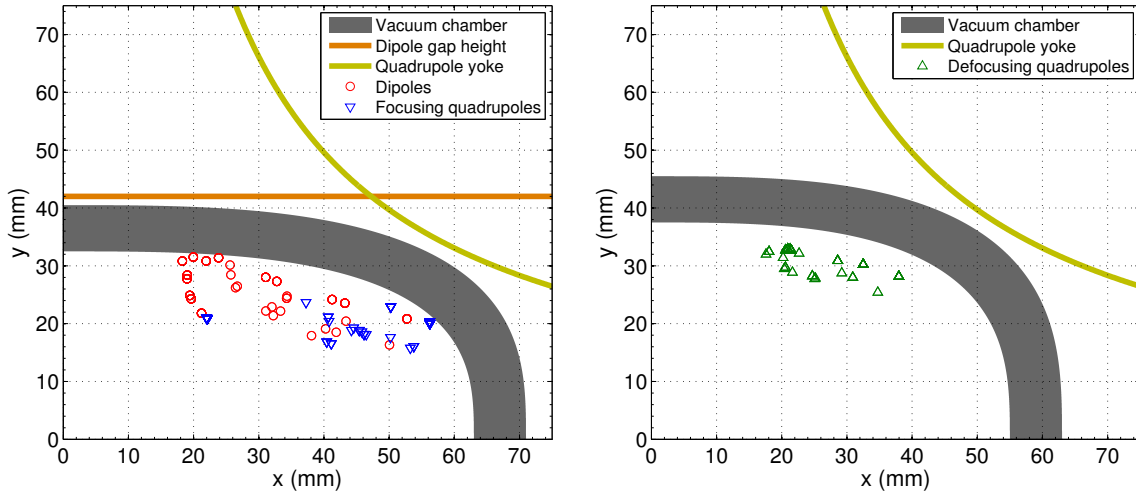


Figure 3.5: Physical aperture for the two types of PS2 vacuum chambers, for dipoles and focusing quadrupoles (left) and for defocusing quadrupoles (right). The beam size in all the different main magnets indicated by the markers correspond to $n_A(\sigma_{FT}) = 3.5$ times the rms beam size of the fixed target beam including the discussed errors.

machine. However, it should be emphasized here that the particles are painted into the transverse phase space at injection allowing for a more uniform-like distribution without large beam tails and so relaxing the requirements on the acceptance. The effective use of the available physical aperture is shown in Fig. 3.5. The rms beam size of the fixed target beam multiplied by $n_A(\sigma_{FT}) = 3.5$ is calculated for each of the main magnets taking into account the parametric dispersion, the closed orbit uncertainty and beta-beating. The yoke of the quadrupoles and the dipole gap height are indicated by lines outside the corresponding vacuum chambers. It should be emphasized that the two types of vacuum chambers differ only slightly in their dimensions, which is very attractive for minimizing the impedance of the machine and gaining margin for beam instabilities [45], [46]. The vacuum chamber in the LSSs will be adopted to the beam transfer requirements. Note that, in comparison with the fixed target beam, the available aperture for LHC-type beams is in general larger as their emittances are significantly smaller in both transverse dimensions.

3.2.3. Tuning flexibility

The rather stringent constraints on the phase advance between beam transfer elements limit the achievable tuning range in the LSSs. Thus, the working point of the machine is adjusted by changing the phase advances in the NMC arc cells and matching the dispersion suppressor module to the optics of the LSS. It was shown in section 2.3, that the achievable phase advance range of an NMC module as used in the arc of the PS2 is explored best by numerical methods. A very powerful tool for optimizing the

linear optics of highly periodic lattices as typically used in synchrotron light sources was developed by D. Robin *et al.* [47]. In particular, the parameter space of the independent quadrupole families of a synchrotron is scanned systematically in small steps within the limits of the corresponding power supplies. For each possible configuration providing stable betatron motion (i.e. the trace of the 2×2 transfer matrix is smaller than 2 in both planes), lattice properties of interest are calculated and stored in a database. As the search for possible solutions is systematic in the given parameter space, the technique is called “GLobal scan of All Linear Stable Settings” (GLASS). In the following, a similar approach is applied to the NMC cell of the PS2 arc using MADX for checking stability and calculating lattice properties. In fact, the method is even extended in the sense that for each stable solution of the NMC module, a MADX routine is launched for matching the dispersion suppressor to the nominal optics of the LSS. This procedure allows to obtain a global picture of the available tuning range of the PS2 lattice.

Global scan of All Linear Stable Settings - PS2 arcs

The normalized gradients of the four NMC quadrupole families are varied systematically in a MADX script. For each configuration yielding stability of the NMC module, the dispersion suppressor is matched to the standard optics of the LSSs. If this matching is successful, basic lattice parameters are calculated and together with the quadrupole settings stored in a database. In addition, the available aperture for the fixed target beam is computed as described in Section 3.2.2, where the actual geometry of each vacuum chamber is assigned to the main magnets accordingly. Machine errors are estimated in terms of 20% beta-beat, 10% parasitic dispersion and maximal closed orbit errors of 1 mm in both planes. A set of valid solutions are obtained by extracting the cases where the gradients in the arc quadrupoles are below the maximum of 16 T/m without changing sign and the available aperture is at least $n_A(\sigma_{FT}) = 3.5$.

Figure 3.6 shows all valid solutions found by scanning the 4 quadrupole gradients of the NMC module in steps of $\Delta K = 0.001 \text{ m}^{-2}$, where the color code indicates the transition energy γ_t (left) and the available aperture (right). The total tuning range of the arcs is about 2.5 units in both planes. This may be extended by modifying the optics of the LSSs while keeping phase advances between injection/extraction elements within specified ranges. Due to the half-integer stop band for configurations of the basic NMC cell with a vertical phase advance close to π , only a small density of solutions is found in the region around $Q_y \approx 8$. It should be emphasized that the ring is finally composed of a series of matched modules. Thus, in the absence of machine errors, the calculation of lattice parameters is not very sensitive to the optical resonances. This explains why the solutions close to the integer and half-integer tunes seem not affected by stop-bands. However, these solutions are of course unstable and of little interest for operating the machine.

The global scan of stable solutions reveals a clear dependence of γ_t on the horizontal tune. The smallest reachable value of $\gamma_t = 16i$ is obtained for $Q_x \approx 12.9$, while γ_t goes

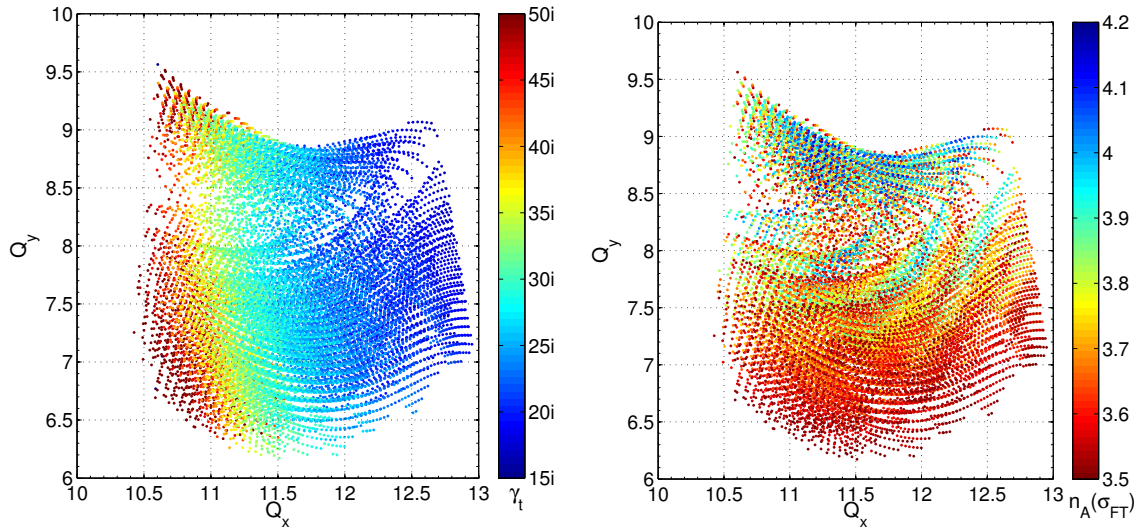


Figure 3.6: Transition energy (left) for a global scan of optics solutions in the tune diagram. The color-code indicates the value of γ_t as function of the betatron tunes, with values above $50i$ represented by dark red. For the same solutions, the available aperture is shown in units of beam sizes of the fixed target beam (right).

up to $80i$ for tunes around $Q_x \approx 10.5$. It should be emphasized however that γ_t can be adjusted by a few units for most of the working points, as different sets of solutions are found for a given region in the tune diagram. Note that a very similar dependence of γ_t on the horizontal phase advance in the NMC module was also found in the semi-analytical treatment in Section 2.3 for a region in the parameter space with moderate values of dispersion at the entrance of the module $D_{x,a}$. Concerning the available aperture, a large number of solutions is found with $n_A(\sigma_{FT})$ between 3.5 and 3.8. Peak values of $n_A(\sigma_{FT}) \approx 4.2$ are reached for higher vertical phase advances. A clear structure of the stable solutions can be explained by overlapping layers of stable islands with similar behaviour. Significantly larger acceptance is obtained for LHC-type beams as they have a smaller emittance in both transverse dimensions.

3.2.4. Working point considerations

The working point should be located in an area of the tune diagram avoiding low order resonances. Figure 3.7 shows the relevant part of the tune diagram accessible by the tuning range of the PS2 lattice. A medium value of γ_t is obtained for a horizontal tune Q_x between 11.5 and 12.5. Considering the incoherent space charge tune spread, it is preferred to stay below the structure resonance at $Q_x = 12$ and below the diagonal. In order to avoid large off-momentum beta-beat, it is advantageous to avoid the half integer stop-band of the basic NMC cell. The nominal working point is thus chosen as $(Q_x, Q_y) = (11.76, 6.70)$ with $\gamma_t = 26i$, where the phase advance per NMC cell is around $(\phi_{x,\text{NMC}}, \phi_{y,\text{NMC}}) \approx (0.75, 0.375) \times 2\pi$. Since the third order resonance in the

horizontal plane at $Q_x = 11.66$ is non-structural, high efficiency for the resonant slow extraction can be expected. Depending on the stop band width of the integer resonance at $Q_x = 12$, it may become necessary to move the working point of the machine closer to the half integer at $Q_x = 11.5$. Alternative working points can be found around $(Q_x, Q_y) = (11.76, 7.7)$ and $(Q_x, Q_y) = (11.25, 7.20)$. However, it should be emphasized that the structural resonance at $Q_x = 11.33$ may compromise the resonant slow extraction, in case the working point is chosen below $Q_x = 11.5$.

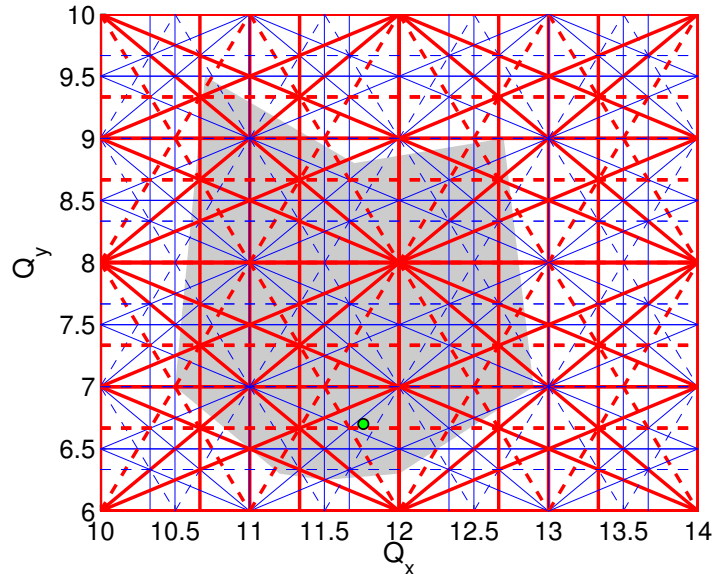


Figure 3.7: Tune diagram with resonances up to 3rd order. Red and blue lines indicate systematic and random resonances, respectively, where solid lines correspond to systematic and dashed lines to non-systematic resonances. The tuning range of the lattice is indicated by the grey area and the working point is marked by a green dot.

3.2.5. Chromaticity correction

Chromaticity control is enabled through the installation of sextupole magnets in dispersive regions of the arcs. In order to minimize their contribution to nonlinear effects, chromatic sextupoles are preferably positioned in high dispersive areas of the ring where the beta functions reach maximal values, i.e. close to the quadrupoles in the arc cells. As chromaticity is corrected by a large number of sextupoles in the arcs, the off-momentum beta-beat amplitude depends on the distribution of sextupoles with respect to their phase advance and their strength around the ring. Since the acceptance of the PS2 is a critical parameter, chromatic beta-beating should be minimized. Minimal off-momentum optics distortion is achieved with sextupole magnets installed in each of the NMC cells as well as in the dispersion suppressor modules. Comparably weak sextupolar fields are sufficient for correcting chromaticity in the PS2 lattice due to the large beta functions and large dispersion in the location of the sextupoles.

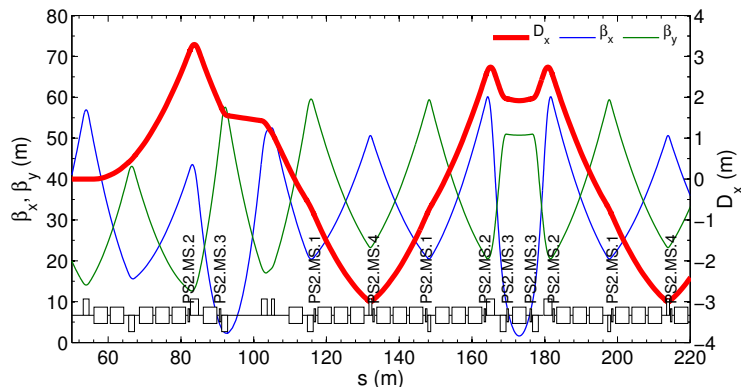


Figure 3.8: Chromaticity correction sextupoles in the dispersion suppressor and the basic NMC cell of the PS2 ring. The sextupole families are repeated periodically with the NMC cell up to the center of the arc, where the arrangement is mirrored.

The chromaticity correction scheme of the PS2 is based on four independent families with a total of 84 magnets, each with a length of 0.4 m. Figure 3.8 shows the positions of the magnets in the dispersion suppressor modules and in the NMC arc cells. The distribution of sextupoles is mirror-symmetric with respect to the center of the PS2 arcs. The most effective families for correcting chromaticity are MS.2 and MS.3 due to their large number of members (24), respectively, and the high local dispersion function. Each of the ten NMC cells in the arcs contains two members of the MS.2 family located close to the outer quadrupoles of the doublet insertion and two members of the MS.3 family installed around the central dipole magnet. Both of these families are extended by four sextupoles installed at locations in the dispersion suppressor modules with corresponding optics functions and phase advances. These two sextupole families will be referred to as the 2 family scheme in the following.

Due to the large phase advance per module and the odd number of modules per arc, the usual procedure of splitting two families into four or six families cannot be applied easily. The PS2 chromaticity correction scheme relies therefore on the installation of the two additional chromatic sextupole families MS.1 and MS.4 in the PS2 arcs. The 24 members of the MS.1 family are located close to the central quadrupole of the FODO channels of the NMC modules and the corresponding position in the dispersion suppressor modules. The 12 members of the MS.4 family are distributed symmetrically around the center of the arcs on either the entrance or the exit of the NMC cells. The two additional sextupole families can be used to control nonlinear effects like second order chromaticity, off-momentum beta-beat or first order detuning with amplitude.

As the PS2 is designed with negative momentum compaction and will thus always stay below transition, stable beam operation requires slightly negative chromaticity. However, at the stage of lattice design it is convenient to fully correct the linear chromaticity. Therefore, first order chromaticity is always corrected to zero in what follows unless stated otherwise. The MADX-PTC matching module is used to determine the

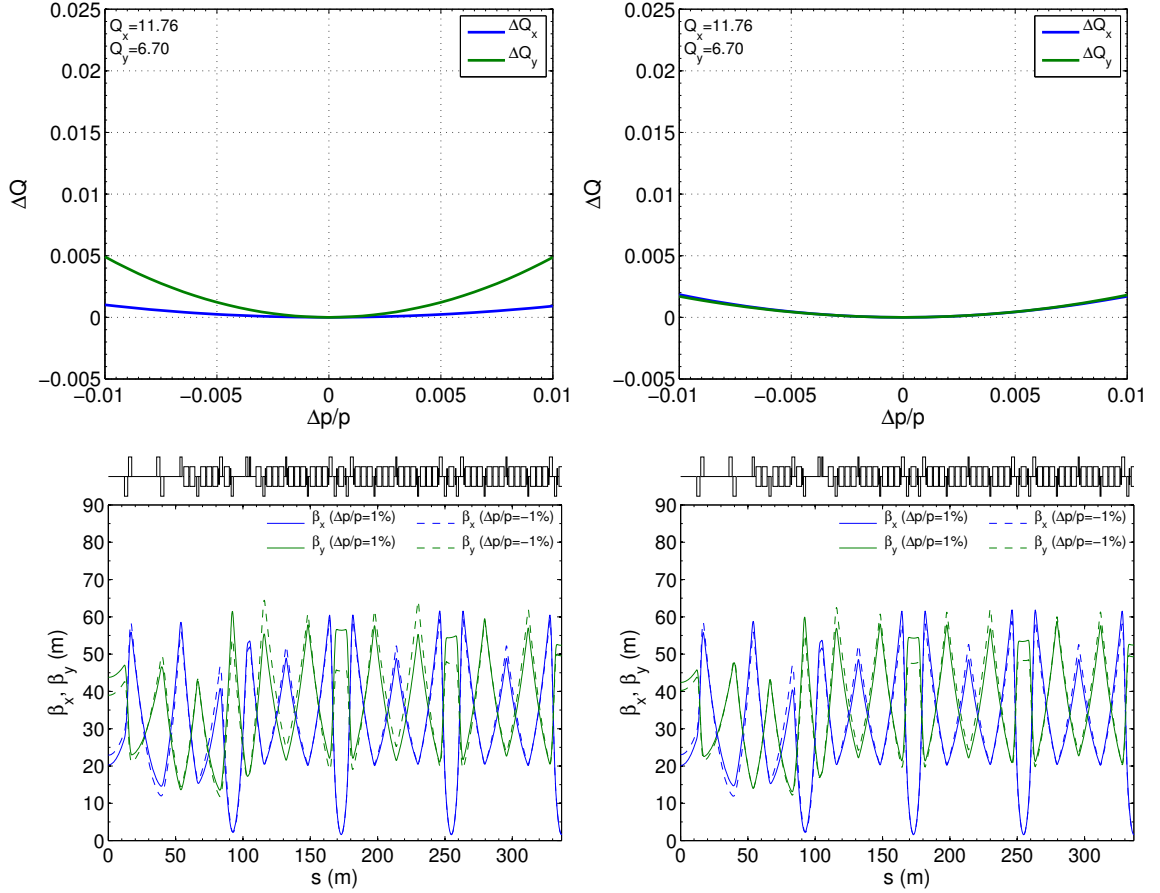


Figure 3.9: Off-momentum beta functions for one quarter of the PS2 lattice with $\Delta p/p \pm 1\%$ (bottom) and non-linear chromaticity (top) for the nominal working point $(Q_x, Q_y) = (11.76, 6.70)$ with 2 sextupole families (left) and 4 sextupole families (right). In the case of the 4 family scheme, the sextupoles are tuned to minimize Q_x'' and Q_y'' .

sextupole strengths for chromaticity correction. First order chromaticity can be set to zero by both the 2 and the 4 family sextupole scheme. Figure 3.9 shows the off-momentum optics functions for $\Delta p/p = \pm 1\%$ and the remaining nonlinear chromaticity for the 2 family scheme (left) and the 4 family scheme (right), at the nominal working point of the PS2. Note that the bare lattice nonlinearities induced by the fringe fields and chromatic sextupoles create a Q'' component (cf. Appendix A.6) in both planes. For the 2 family scheme, the Q'' component is larger in the vertical plane compared to the horizontal plane. As a result, the off-momentum beta-beat is stronger in the vertical plane. Although a beta-beat of 10% as obtained with the 2 family scheme is tolerable, a better correction can be achieved using all four sextupole families. By minimizing Q_y'' , the residual maximum off-momentum beta-beat is reduced below a few percent. This can be observed for example at the injection point in the center of the LSS (corresponding to $s = 0$ in the plot). A working point with higher vertical tune seems

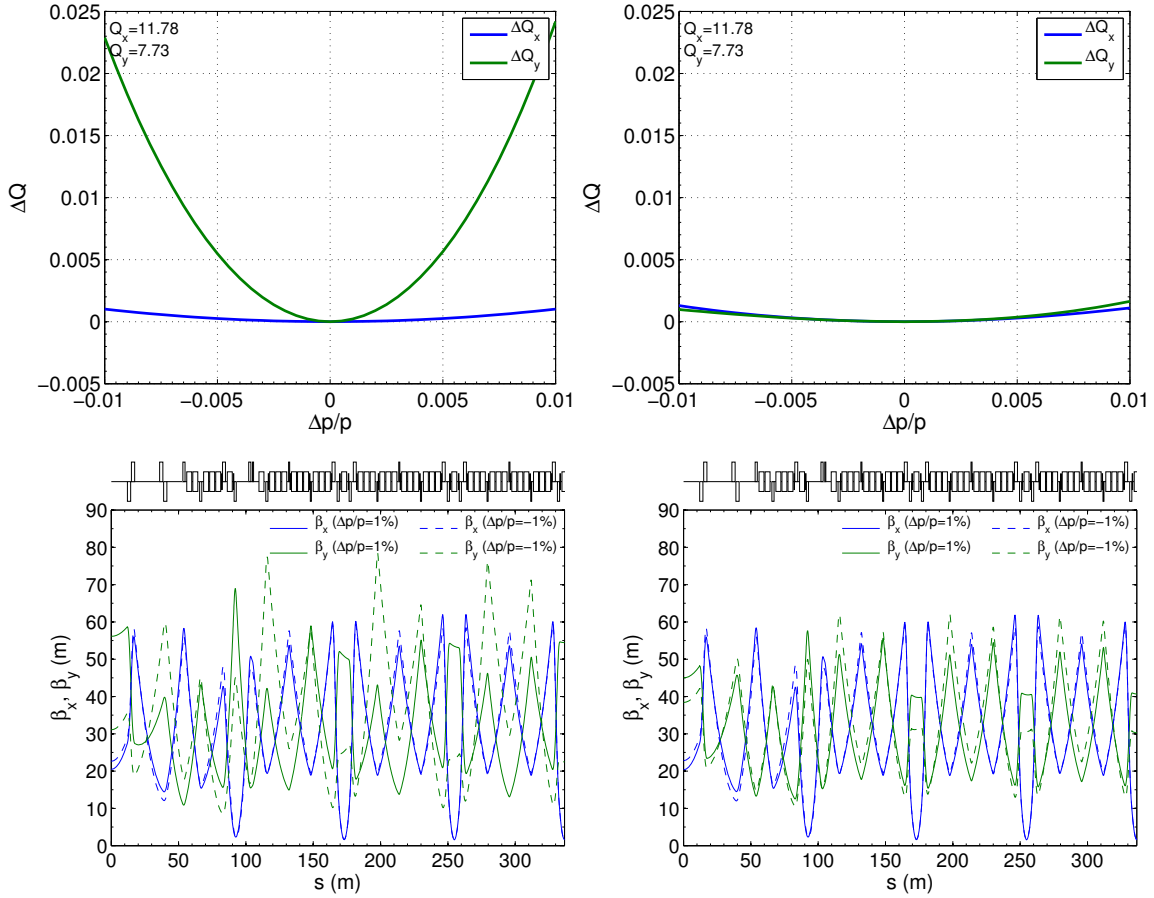


Figure 3.10: Off-momentum beta functions for one quarter of the PS2 lattice with $\Delta p/p \pm 1\%$ (bottom) and non-linear chromaticity (top) for the nominal working point $(Q_x, Q_y) = (11.78, 7.73)$ with 2 sextupole families (left) and 4 sextupole families (right). In the case of the 4 family scheme, the sextupoles are tuned to minimize Q''_x and Q''_y .

favourable with respect to the available aperture (cf. Fig. 3.6) while providing similar values of imaginary γ_t . In the following, the nominal working point as studied above will be compared to an optics solution for the working point $(Q_x, Q_y) = (11.78, 7.73)$, where the available aperture is about $n_A \approx 3.75 \sigma_{FT}$ assuming a beta-beat of 20%. Figure 3.10 shows the nonlinear chromaticity and the off-momentum optics functions for the 2 family and the 4 family sextupole scheme for this case. A large second order chromaticity Q''_y is obtained with only 2 chromatic sextupole families, causing significant optics distortion in the vertical plane (beyond 20%). In particular, the maximal beta functions reach up to $\hat{\beta}_y \approx 80$ m for $\Delta p/p = -1\%$ ⁴. Note also the extremely large variation of β_y with momentum in the center of the LSS. As before, a correc-

⁴A momentum deviation of $\Delta p/p = \pm 1\%$ is chosen here for the purpose of demonstration only. The maximal momentum spread in the PS2 will not exceed $\Delta p/p = \pm 0.4\%$ at injection energy.

Table 3.3: Chromatic and amplitude terms for different working points of the PS2

Sextupoles scheme	Q_x/Q_y	Q'_x/Q'_y	Q''_x/Q''_y	a_{xx}	a_{xy}	a_{yy}
bare lattice	11.76/6.70	-21.3/-10.9	110.1/46.0	34.0	39.4	24.1
2 sextupole families	11.76/6.70	0/0	19.2/97.5	11.7	44.4	69.2
4 sextupole families	11.76/6.70	0/0	35.5/35.1	-43.2	172.2	50.0
bare lattice	11.78/7.73	-21.7/-11.0	111.9/42.8	35.5	33.2	19.1
2 sextupole families	11.78/7.73	0/0	20.4/436.3	39.7	59.5	54.8
4 sextupole families	11.78/7.73	0/0	23.8/26.0	-26.0	72.5	229.3

tion of the off-momentum optics distortion is achieved by correcting Q'' using the 4 chromatic sextupole families. A very regular optics modulation with momentum is restored with only a few percent off-momentum beta-beat. Thus, the 4 family scheme is very powerful for controlling the chromatic dependence of the optics functions in the PS2, especially for working points in certain regions of the tune diagram, and is of great importance for the preservation of the aperture. A summary of the nonlinear chromatic terms for different working points comparing the 2 family with the 4 family chromaticity correction scheme is given in Table 3.3, including the amplitude detuning terms (cf. Appendix A.6). Note that already the 2 family scheme is compensating part of the Q''_x induced by the bare lattice nonlinearities of the magnet fringe fields. The 4 family scheme with the chosen settings results in larger amplitude detuning terms.

3.2.6. Correction of misalignment and closed orbit errors

The closed orbit correction in the PS2 lattice is achieved using 60 correctors for the vertical plane and 48 for the horizontal plane in combination with 108 bi-planar beam position monitors (BPMs). They are located close to the main quadrupole magnets in order to profit from the local maxima of the beta functions. The distortion of the closed orbit due to random magnet errors is studied for the following machine imperfections: misalignment of dipole, quadrupole and sextupole magnets with a Gaussian distribution cut at 3σ and errors in the main field component of dipoles and quadrupoles with a cut at 2σ . The corresponding rms values of these errors are summarized in Table 3.4. Figure 3.11 (top) shows the sensitivity of the closed orbit excursion to the individual error sources without any correction as obtained from MADX. It appears

Table 3.4: Assumed machine imperfections (rms values).

Type	Dipoles	Quadrupoles	Sextupoles
Relative field error	$5 \cdot 10^{-4}$	$5 \cdot 10^{-4}$	0
Transverse shift (mm)	0.3	0.2	0.2
Longitudinal shift (mm)	1	1	1
Tilt (mrad)	0.3	0.3	0.3

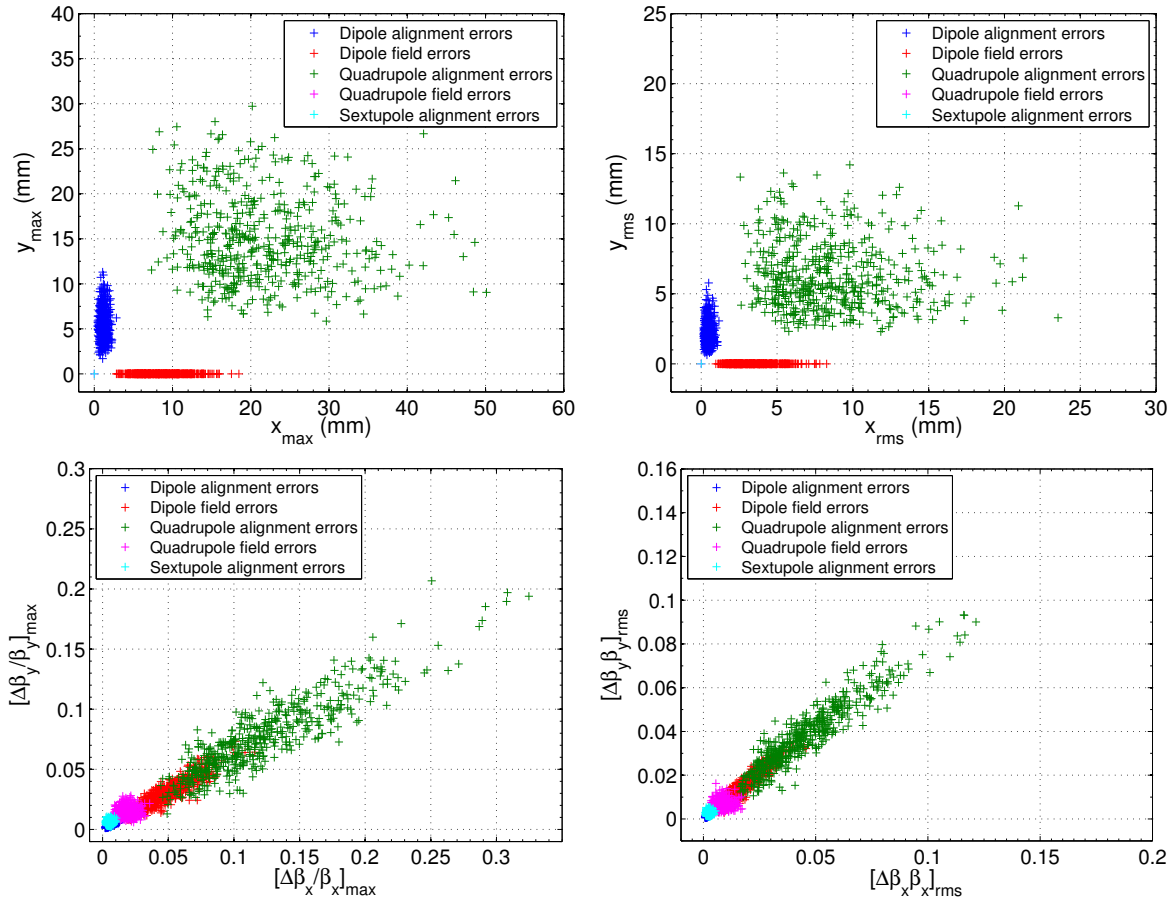


Figure 3.11: Sensitivity of the PS2 lattice to machine imperfections with respect to closed orbit (top) and beta-beat (bottom) in terms of maximal (left) and rms-values (right) for a sample of 500 seeds.

that the most critical errors with respect to closed orbit distortion in the PS2 lattice are feed-down effects due to quadrupole misalignment, which in some of the cases cause a maximal orbit excursion comparable to the physical aperture. Tilted dipoles induce mainly vertical and dipole field errors purely horizontal orbit distortion. As expected, quadrupole field errors and sextupole alignment errors can be neglected.

Figure 3.11 (bottom) shows the sensitivity of the PS2 lattice to optics distortion (beta-beat) caused by alignment and field errors of the main magnets. Local deviations of the beta functions of up to 30% are observed in some cases, while the rms-values are usually about half. It is interesting to note that an important contribution to beta-beating comes from the feed-down effects (cf. Appendix A.5) due to large closed orbit excursion in the sextupole magnets, as caused by the quadrupole alignment and dipole field errors. A significant reduction of the optics distortion can thus be expected after closed orbit correction. Apart from these alignment errors, the main sources for beta-beat are the errors in the quadrupole gradients. However, they are not causing

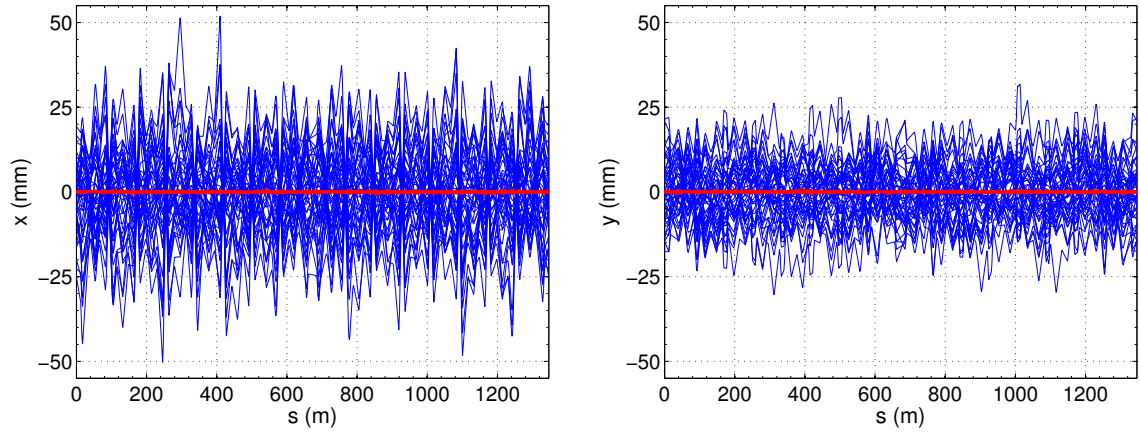


Figure 3.12: Closed orbit before (blue lines) and after the orbit correction algorithm (red lines) in the horizontal (left) and the vertical plane (right) for 50 error seeds.

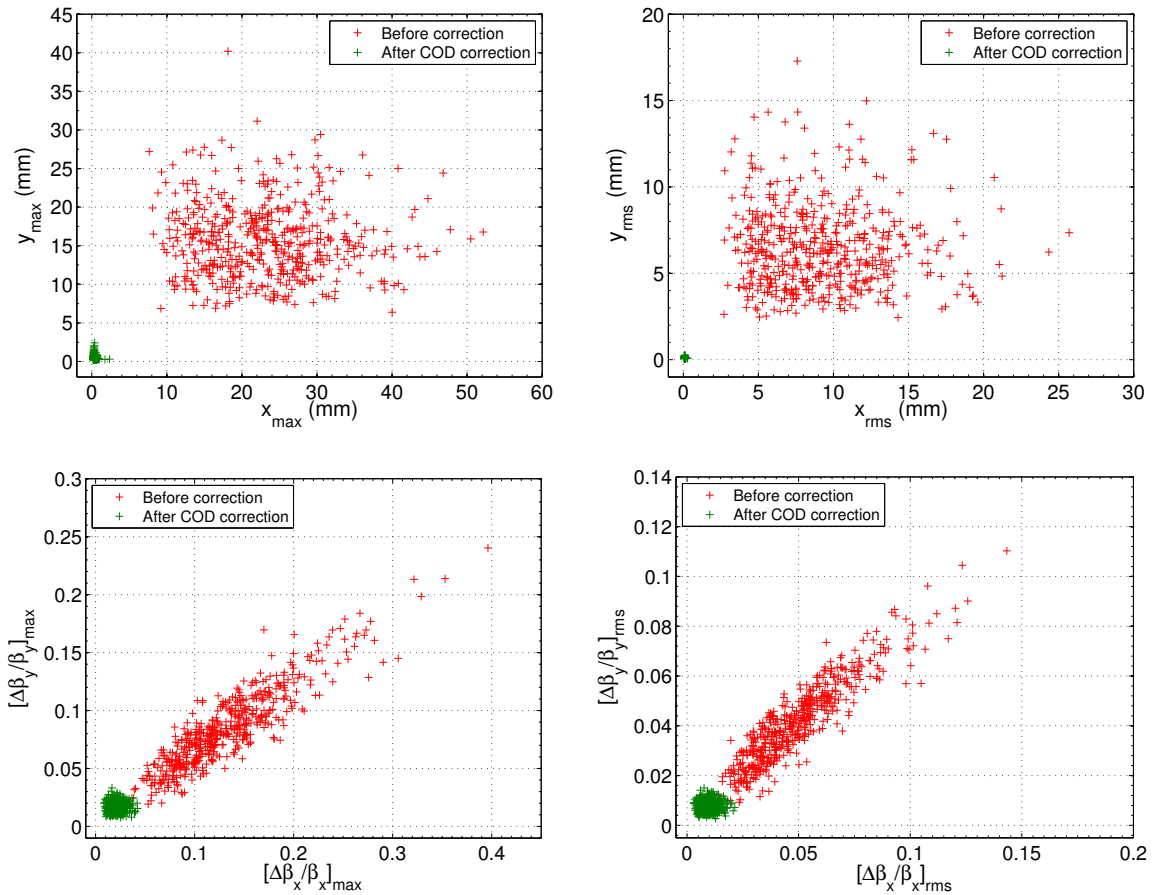


Figure 3.13: Distribution of the closed orbit distortion (top) and beta-beat (bottom) before and after two iterations of the correction algorithm in terms of maximal (left) and in terms of rms-values (right) for 500 error seeds.

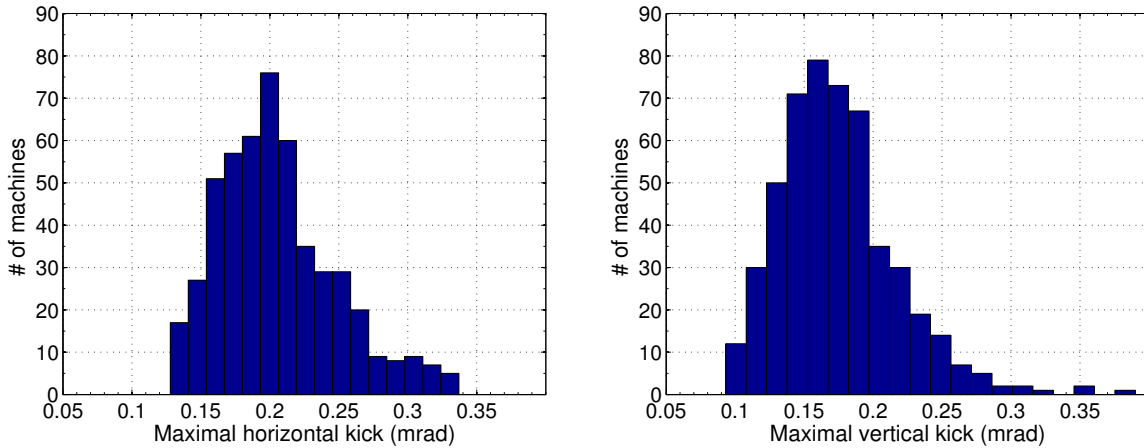


Figure 3.14: Distribution of the maximum corrector kicks needed for the closed orbit correction in the horizontal (left) and vertical (right) plane for a sample of 500 error seeds.

more than 5% relative change of the optics functions. Pure sextupole alignment errors are of minor importance.

The combined effect of these machine imperfections on the closed orbit distortion (COD) is studied for a sample of 500 random error seeds using MADX. In the simulation, two iterations of orbit correction are performed using the MICADO algorithm. Assuming that not all correctors may be available in real operation and especially during commissioning, only a random subset of 40 correctors in the horizontal and 52 correctors in the vertical plane are used for the correction. Similarly, a subset of 95% of the BPMs are considered to be functional. Figure 3.12 shows a few randomly chosen samples of the closed orbit before and after correction in the horizontal (left) and vertical plane (right). The distribution of the maximal and the rms orbit errors before and after the correction of the full set of 500 error seeds is presented in Fig. 3.13 (top). On average, the orbit is corrected by more than a factor 20 so that a remaining maximum orbit excursion of about 1 mm can be expected in both planes. Furthermore, none of the machine samples exceed 3 mm maximum orbit distortion after correction and average rms values are kept below 0.4 mm. The induced beta-beat before and after the correction is plotted in Fig. 3.13 (bottom). As pointed out earlier, the major part of the optics distortion is induced by feed-down effects due to orbit errors in the sextupole magnets. Thus, a significant reduction of the beta-beating to below 10% is achieved by the closed orbit correction. It is therefore concluded that no additional measures seem necessary for restoring the optical functions' variation. As shown in Fig. 3.14, maximum corrector strengths of typically 0.2 mrad are needed for efficient orbit correction. In order to allow for the maximally needed kick angle of 0.4 mrad at top energy (50 GeV), the correctors have to provide an integrated magnetic field of 0.07 Tm. This corresponds to a magnetic field of 0.35 T over their length of 20 cm.

3.2.7. Multipole field errors

The sensitivity of the PS2 lattice to higher order multipole field components in the main magnets shall be studied in tracking simulations. It is reasonable to assume a set of multipole errors for the PS2 main magnets based on magnet measurements of already existing accelerators. The PS2 machine parameters are very similar to the J-PARC Main Ring [27], which has a circumference of about 1500 m, an injection energy of 3 GeV, an extraction energy of 50 GeV and similar physical apertures. Based on the measurements performed at J-PARC [48], a set of multipole components are assumed for the main PS2 magnets as summarized in Table 3.5. In particular, a good field region ($\Delta B/B_0 < 5 \times 10^{-4}$) up to the physical aperture is chosen in the dipole magnets. All multipole components represent the normal field component \tilde{b}_n relative to the corresponding main component in units of 10^{-4} , such that

$$B_y(x, y) + jB_x(x, y) = B_0 \sum_{n=0}^{\infty} (\tilde{b}_n + j\tilde{a}_n) \left(\frac{x + jy}{r_b} \right)^n, \quad (3.5)$$

where r_b is the reference radius and j is the imaginary unit, B_x and B_y define the magnetic field in x and y direction and B_0 is a normalization constant defined through the beam rigidity $B\rho$ (cf. Appendix A.1). Skew components \tilde{a}_n are not considered here. Note that the reference radius for the dipole magnets is larger than their gap height and is thus not of practical use. This reference radius was chosen for direct comparison of the multipole components in the different magnets. They can be rescaled to any smaller radius r_b in order to be used for the actual specification of the PS2 magnets and their measurement during production.

Table 3.5: Relative multipole components in units of 10^{-4} at the reference radius r_b .

Order n	Dipole, $r_b=5.95$ cm		Quadrupole, $r_b=5.95$ cm		Sextupole, $r_b=5.95$ cm	
	mean \tilde{b}_n/\tilde{b}_0	random \tilde{b}_n/\tilde{b}_0	mean \tilde{b}_n/\tilde{b}_1	random \tilde{b}_n/\tilde{b}_1	mean \tilde{b}_n/\tilde{b}_2	random \tilde{b}_n/\tilde{b}_2
0	10^4	5.0	–	–	–	–
1	0.3	0.2	10^4	5.0	–	–
2	4.0	2.0	–2	1.0	10^4	5.0
3	0.1	0.5	1.0	1	–0.5	1.5
4	–1.5	1.0	1.0	1.5	0.5	1.5
5	–0.1	0.1	3	1.0	–1.0	0.5
6	–1.5	0.3	0.5	1.0	1.0	0.5
7	0.1	0.1	0.5	0.5	0.5	0.5
8	–1.0	0.3	0.1	0.3	–4.0	0.3
9	–	–	0.5	0.3	0.1	0.5
10	–	–	0.1	0.3	0.1	0.5

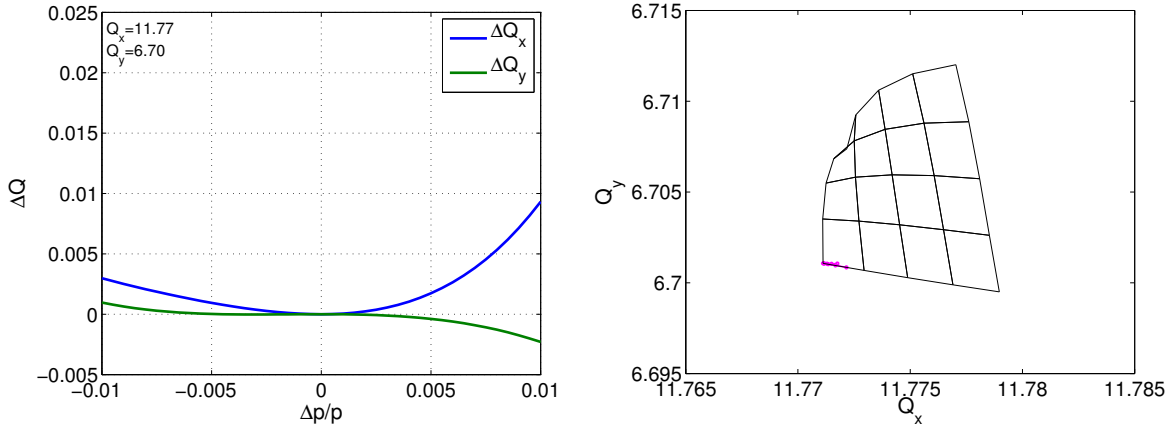


Figure 3.15: Nonlinear chromaticity (left) for the working point $Q_x = 11.77$, $Q_y = 6.70$ including all multipole errors and misalignments for the case of the 2 sextupole family scheme and the corresponding amplitude detuning (right) up to $4\sigma_{x,y}$ in units of the fixed target beam as indicated by black lines (which are separated by equidistant actions J_x and J_y). The magenta line in the tune diagram represents the chromatic detuning up to $\Delta p/p = \pm 0.004$ (exceeding already the RF bucket height).

The effect of these multipole errors on the nonlinear chromaticity is shown in Fig. 3.15 (left). Note the higher order terms in the chromatic tune-shift induced by the multipole errors distributed around the machine (cf. Appendix A.6). In particular third order components not present in the error-free lattice (cf. Section 3.2.5) can be identified. Figure 3.15 (right) shows the detuning with amplitude for on-momentum particles up to $4\sigma_{x,y}$ in units of the fixed target beam size (black lines) together with the nonlinear chromatic detuning up to $\Delta p/p = \pm 0.004$ (purple lines). Note that the tune footprint starts to fold in at the top left corner corresponding to horizontal amplitudes close to $4\sigma_x$, which is caused by higher order multipole errors. The overall detuning is one order of magnitude smaller than the anticipated space charge tune spread. The impact of the multipole errors on the stability of the particle motion will be studied in the following.

3.2.8. Dynamic aperture without synchrotron motion

Sextupole fields and higher order multipoles in combination with other machine imperfections like magnet misalignments and closed orbit errors impose limitations on the long term stability of the single particle motion. In order to study these limitations, typically a set of particles with different initial transverse positions (and usually zero transverse momenta) are numerically tracked for a large number of turns comparable to the storage time in the machine. The maximal transverse amplitudes up to which the particle motion remains stable is called the dynamic aperture. In all the studies presented here, the dynamic aperture is determined without the mechanical aperture.

Dynamic aperture for the error-free lattice

In the ideal lattice without magnetic field imperfections and multipole errors, the chromatic sextupoles and the magnetic fringe fields determine the nonlinearities of the machine. The four chromatic sextupole families can be tuned to minimize second order chromaticity and thus off-momentum beta-beat. However, at the same time they might introduce stronger amplitude detuning and reduce the dynamic aperture. The dynamic aperture is studied by tracking particles using MADX-PTC. For now, synchrotron motion is not taken into account but the dynamic aperture is determined for different momentum offsets (5D tracking). The tracking of the particles starts at the center of the straight section, where the dispersion function is zero and the beta functions have local minima (i.e. $\alpha_x = \alpha_y = 0$). The initial conditions are chosen along radial directions in the physical $x - y$ space with angular steps of 10° and zero transverse momenta. The dynamic aperture is then given by the area containing only initial conditions that result in stable particle motion. Figure 3.16 shows the dynamic aperture as obtained by tracking particles for 10000 turns powering only the two main sextupole families MS.2 and MS.3 (left) and powering all four families for minimizing Q'' in both planes (right) as discussed in Section 3.2.5 for the nominal working point $(Q_x, Q_y) = (11.76, 6.70)$. Note that the 100 ms long flat bottom of the PS2 corresponds to 22000 turns. Long

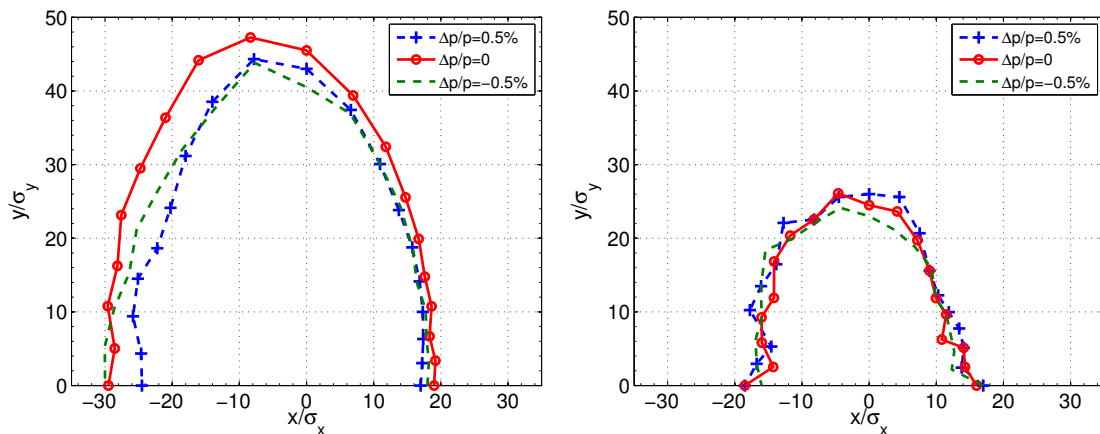


Figure 3.16: Dynamic aperture for the ideal PS2 lattice including fringe fields at the nominal working point $(Q_x, Q_y) = (11.76, 6.70)$, for the 2 family scheme (left) and the 4 family scheme with minimized Q'' (right) when tracking for 10000 turns.

term dynamic aperture studies are performed at a later stage. All dynamic aperture plots are normalized to units of beam sizes σ_x, σ_y of the high intensity fixed target beam at injection with the normalized emittances $(\varepsilon_{n,x}, \varepsilon_{n,y}) = (9, 6) \mu\text{m}$. Compared to the available physical aperture of $n_A(\sigma_{\text{FT}}) = 3.5$ (cf. Section 3.2.2), the area of stable particle motion is large for both sextupole schemes. However, by correcting second order chromaticity in the 4 family scheme, stronger amplitude detuning is introduced and the dynamic aperture is reduced significantly.

An intuitive picture of the global dynamics of the phase space and of destructive resonances limiting the dynamic aperture can be obtained from the Frequency Map Analysis (FMA) [49]. This technique, originally developed in 1988 for analyzing the stability of orbits in celestial mechanics, was introduced to particle accelerators a few years later. It was used to study the nonlinear properties of the ALS in Berkley both in simulations [50] and in measurements [51] and was applied to LHC simulations for understanding the impact of magnet errors [52]. Nowadays, FMA is a standard tool for the optimization of the nonlinear dynamics in light sources.

The basic idea of Frequency Map Analysis is to build a map from the physical configuration space (x - y) to the frequency (tune) space using numerical tools. The method relies on the NAFF algorithm [53] or one of its variants [54], which allow to determine the fundamental frequencies of the quasi-periodic particle motion (tunes) with high precision (for N_t turns of tracking data, the algorithm converges like $1/N_t^4$). A frequency map is created by applying one of these refined Fourier techniques to the turn-by-turn trajectories of individual particles as generated by numerical tracking of a large number of particles with different initial conditions. A quantitative measure for the stability of the particle motion can be inferred from the change of the tunes within two consecutive time intervals of equal length, as indicated by the tune diffusion rate d_ν . In particular, the tune diffusion rate d_ν can be defined as

$$d_\nu = \sqrt{(\nu_{x,1} - \nu_{x,2})^2 + (\nu_{y,1} - \nu_{y,2})^2}, \quad (3.6)$$

where $\nu_{x,1}$ and $\nu_{x,2}$ ($\nu_{y,1}$ and $\nu_{y,2}$) denote the horizontal (vertical) tunes for the first and the second half of N_t turns tracking data, respectively. Regular and thus stable trajectories exhibit small variations in the tunes and will thus have a small tune diffusion rate. On the other hand, unstable or chaotic motion is associated with a large tune diffusion rate. The FMA allows therefore to identify resonances in the tune diagram which lead to chaotic particle motion and eventually cause particle loss by diffusion to large amplitudes. In addition, these resonances can be traced back to the physical x - y space, which can help to explain dynamic aperture limitations.

The FMA is applied here to the PS2 lattice after tracking particles for $N_t = 1056$ turns. The frequency map for the case of two chromaticity correcting sextupole families at the nominal working point and on-momentum particles is shown in Fig. 3.17 (top). As already indicated in Table 3.3 (cf. Section 3.2.5), very small detuning with amplitude is obtained with the 2 family scheme, similar to the bare lattice consisting of dipoles and quadrupoles only. As the frequency map shows, a very linear detuning with amplitude is obtained even for particles with large action. Several resonances are crossed without limiting the dynamic aperture. This will change however once a realistic set of machine errors is used in the model. Minimizing Q'' by powering all four sextupole families as discussed in Section 3.2.5 significantly increases the amplitude detuning. This can be observed directly in the frequency map for on-momentum particles shown in Fig. 3.17 (bottom). The large cross term a_{xy} (cf. Table 3.3 in Section 3.2.5) leads

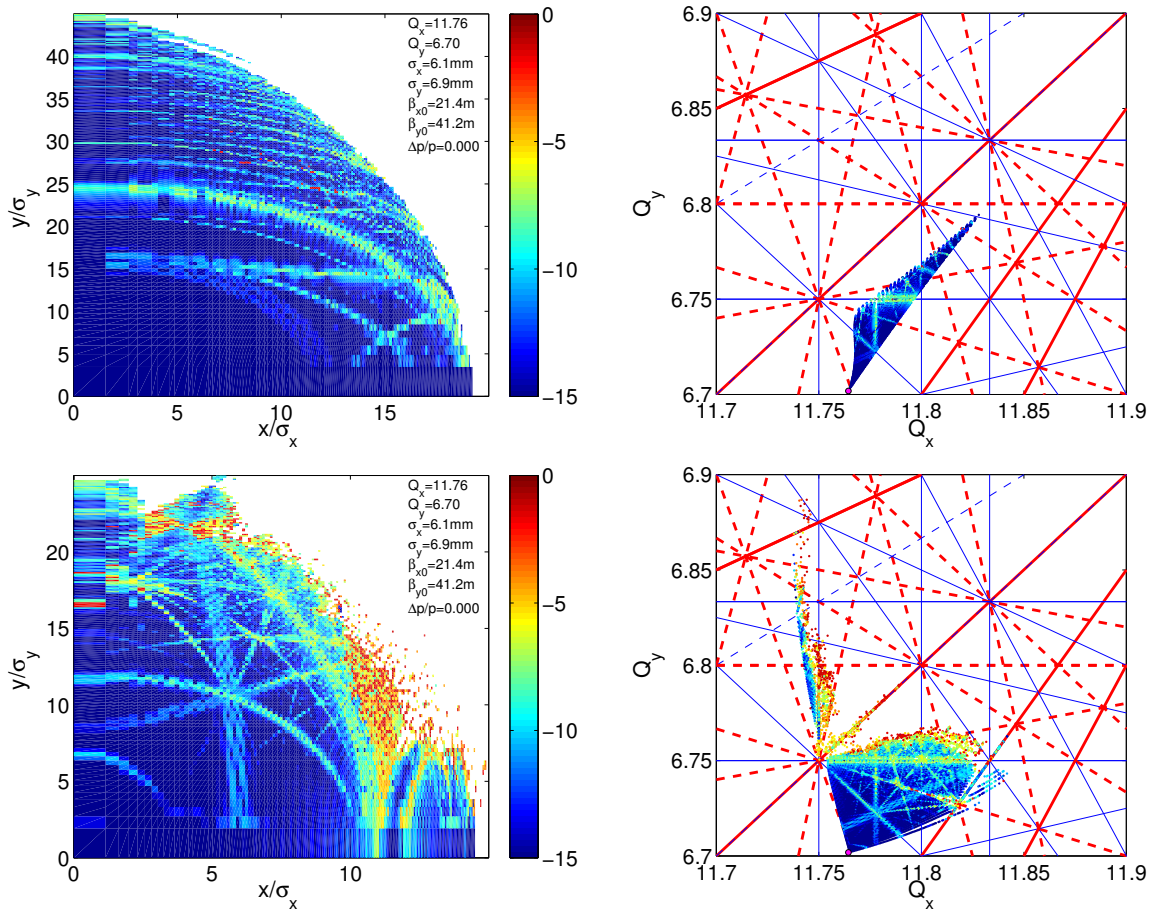


Figure 3.17: Diffusion map (left) and frequency map (right) for the scheme with two (top) and four (bottom) sextupole families at the nominal working point (magenta dot). The color code indicates the logarithm of the tune diffusion rate d_ν . The tune diagram shows resonances up to 6th order, where normal (skew) resonances are shown by solid (dashed) lines and red (blue) correspond to systematic (non-systematic) resonances.

to a strong detuning in the vertical plane for large horizontal amplitudes. Eventually, particles cross the nonlinear coupling resonance along the diagonal which is limiting the dynamic aperture in both planes (note the different scale in the graphs on the left). Thus, the additional sextupoles in the 4 family scheme reshape the tune-footprint and excite more resonances which reduce dynamic aperture for the working point studied here. In general however, the additional families provide more flexibility for controlling nonlinear effects which may allow to increase the dynamic aperture when taking into account the full range of machine imperfections.

Dynamic aperture in the presence of misalignments and orbit errors

The impact of misalignment and closed orbit errors on the dynamic aperture is studied for the 2 family sextupole scheme using the errors summarized in Table 3.4 (cf. Sec-

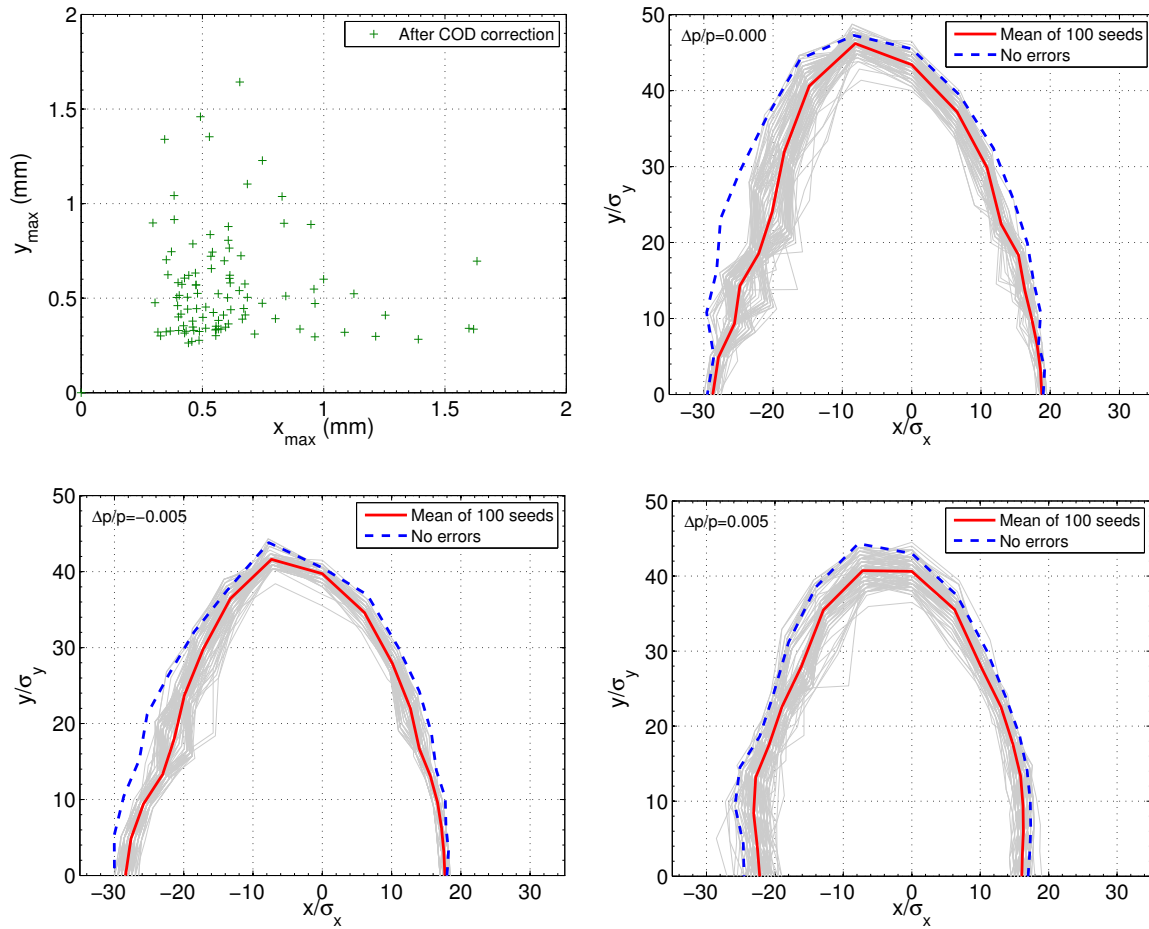


Figure 3.18: Closed orbit after correction and the resulting dynamic apertures for particles surviving 10000 turns with different values of momentum offset $\Delta p/p$ and the working point $(Q_x, Q_y) = (11.76, 6.70)$. The results for 100 errors seeds are plotted in grey, the mean of them is plotted in red. The blue dashed curve shows the dynamic aperture for the error-free lattice including the chromaticity correction sextupoles (2 families MS.2 and MS.3) and the fringe fields of the main magnets.

tion 3.2.6). The errors are assigned to all main magnets in the chromaticity corrected lattice. After correction of the closed orbit, the quadrupoles in the arcs are retuned to restore the initial betatron tunes of the error-free lattice. Finally, the two main sextupole families MS.2 and MS.3 are used to reset chromaticity back to zero. Random lattice configurations generated in this way are then used to study the sensitivity of the dynamic aperture on misalignments. Particles are tracked for 10000 turns with MADX-PTC without synchrotron motion (5D) but with fixed momentum offset. Figure 3.18 shows the maximal closed orbit excursion after the correction together with the resulting dynamic apertures for on-momentum particles and for particles with

$\Delta p/p = \pm 0.5\%$, in units of beam sizes σ_x and σ_y of the high intensity fixed target beam. The grey lines correspond to the dynamic aperture obtained for 100 error seeds. Their average is indicated by the red line. For comparison, the dynamic aperture for the error-free lattice (including the fringe field nonlinearities and the chromaticity correction sextupoles) is plotted as the blue dashed line. In all cases, the dynamic aperture is slightly reduced compared to the error-free lattice. The strongest reduction is observed for on-momentum particles. However, the dynamic aperture still remains large compared to the physical aperture of the machine. It is therefore concluded that misalignments and field errors causing closed orbit distortion do not impose a strong limitation to the single particle dynamics in the PS2 lattice.

Dynamic aperture in the presence of multipole errors and misalignments

The impact of multipole errors on the dynamic aperture of the PS2 lattice with the 2 family sextupole scheme is studied for a sample of 100 error seeds. The multipole components given in Table 3.5 (cf. Section 3.2.7) are assigned to the corresponding magnets in MADX-PTC, where the random errors are distributed following a Gaussian distribution cut at 2σ . It is assumed here that all four types of quadrupole magnets are described by the same error table. In each simulation, the closed orbit is corrected, the betatron tunes are rematched to the values of the error-free lattice and the chromaticities are reset to zero before tracking particles for 10000 turns. The distribution of the maximal closed orbit excursion after correction for the 100 error seeds and the resulting dynamic apertures for different momentum deviations are shown in Fig. 3.19. Compared to the error-free lattice, a significant reduction of the dynamic aperture is observed for both on and off-momentum particles. It is worth pointing out that this reduction is obtained even for the case of pure systematic multipole errors, i.e. without any distortion of the lattice symmetry. This can be explained by the fact that the magnets have a good field region roughly up to the reference radius $r_b = 5.95$ cm (cf. Section 3.2.7), which corresponds to about $6\sigma_x$ and $7\sigma_y$ pure betatron beam size of the fixed target beam for on-momentum particles at the location of maximal beta-functions ($\hat{\beta}_x = \hat{\beta}_y = 60$ m). By taking into account also the random errors in the simulation, the dynamic aperture seems to be restricted to the good field region of the main magnets.

A possible reason for the drastic reduction of the dynamic aperture as observed when taking into account the full range of multipole errors and machine imperfections could also be a strong resonance in the vicinity of the working point studied here. In order to obtain a global picture of the impact of these errors on the stability of single particle motion, a systematic study of the dynamic aperture as function of the working point is performed. As before, the initial conditions are chosen along radial directions in the physical $x-y$ space with angular steps of 10° and zero transverse momenta. The dynamic aperture can be characterized with a single parameter $n_{dyn.}(\sigma_{FT})$ (similar to the available physical aperture n_A , cf. Section 3.2.2), indicating the maximum beam size in units of fixed target beam size σ_{FT} that results in stable particle motion along all

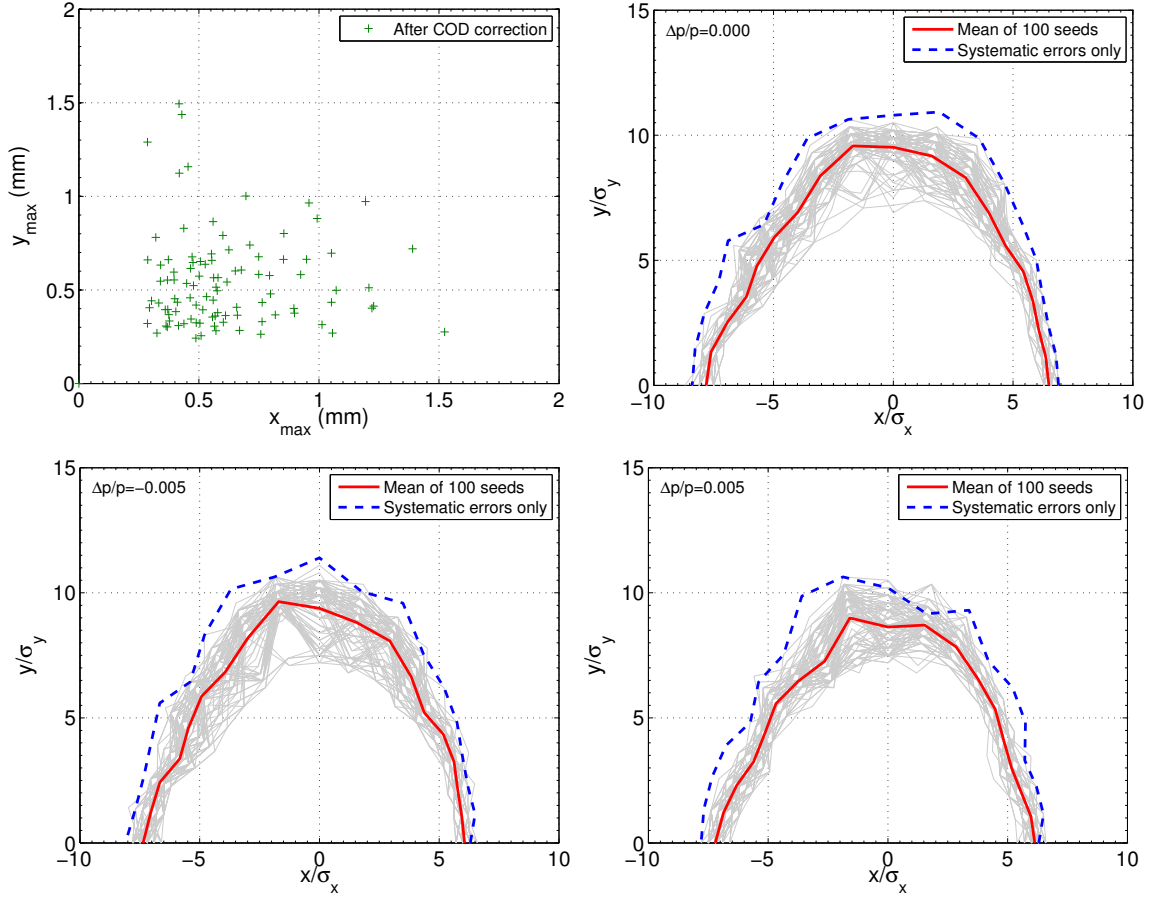


Figure 3.19: Closed orbit after correction and the resulting dynamic apertures for particles surviving 10000 turns with different momentum offsets for the working point $Q_x = 11.76, Q_y = 6.7$ with the 2 sextupole family scheme. All multipole errors and magnet misalignment errors are included in the simulations for the 100 error seeds, yielding the dynamic apertures as indicated by the grey lines. Their mean is plotted in red, while the blue curve shows the dynamic aperture for the case of systematic multipole errors only, i.e. preserving the lattice symmetry.

scanned directions in the $x - y$ configuration space. The dynamic aperture obtained by tracking on-momentum particles for 10000 turns is shown in Fig. 3.20 (left) for a wide range of working points of the PS2 lattice with chromaticity corrected to zero using the two main sextupole families. All simulations were performed with the same error seed, which will be referred to as the reference error seed in the following. For this error seed the dynamic aperture reaches up to $n_{dyn.}(\sigma_{FT}) = 8$ times the fixed target beam size in some areas of the tune diagram. A clear reduction of the dynamic aperture is observed close to systematic and non-systematic resonances of low order. Note the large stopband width of the structure resonance at $Q_x = 12$ resulting from the low

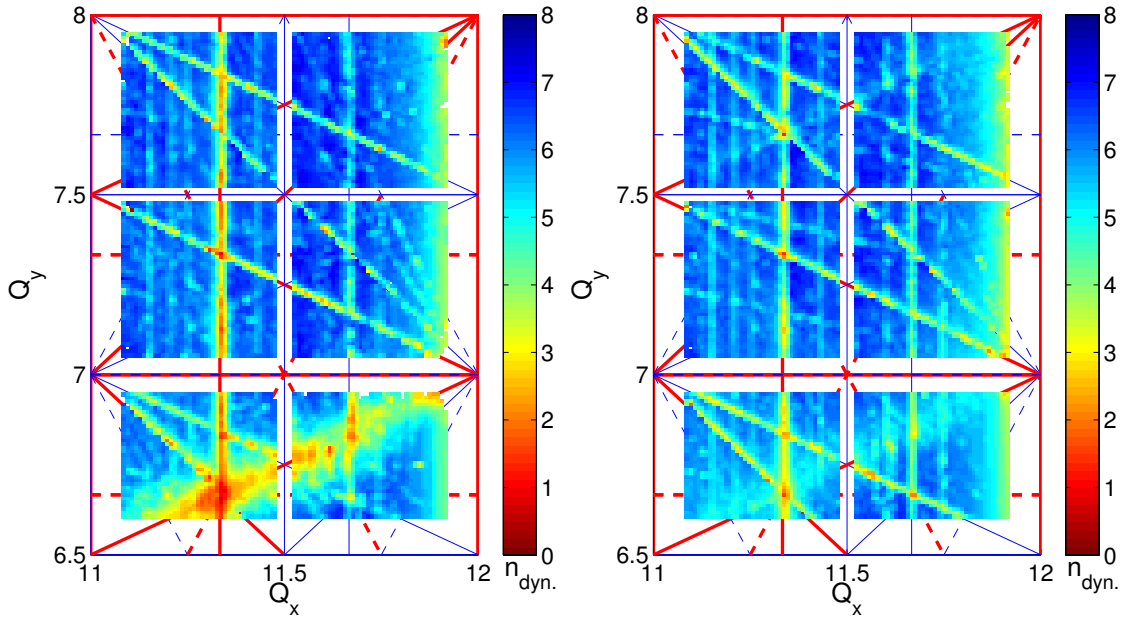


Figure 3.20: Tune scan for on-momentum particles including all multipole errors and misalignments for the reference error seed. The color code indicates the stable beam size $n_{dyn.}(\sigma_{FT})$ in units of the fixed target beam size. Systematic and non-systematic resonances up to 3^{rd} order are indicated by red and blue lines, respectively, where solid lines correspond to normal and dashed lines to skew components. The plot on the left is obtained using two sextupole families for chromaticity correction. Compensating the $Q_x - 2Q_y = -2$ resonance using all four chromatic sextupole families yields the plot on the right.

symmetry of the PS2 lattice and the orientation of the tune footprint. The systematic 3^{rd} order resonance at $3Q_x = 34$ is clearly excited, which was one of the reasons for placing the nominal working point above the half integer resonance at $2Q_x = 23$ (cf. Section 3.2.4). There, the 3^{rd} order resonance at $3Q_x = 35$ is much weaker as it is non-systematic.

In the area below $Q_y = 7$, the third order difference resonance $Q_x - 2Q_y = -2$ has a large stopband width and is clearly reducing the dynamic aperture for the nominal working point. As this resonance is systematic, the corresponding resonance driving term h_{10020} can be minimized by powering the four independent sextupole families accordingly. The resulting dynamic aperture as function of the working point is shown in Fig. 3.20 (right). Due to the compensation, the detrimental effects on dynamic aperture in the area around the $Q_x - 2Q_y = -2$ resonance is reduced to a minimum. On the other hand, the non-systematic resonance $Q_x + 2Q_y = 25$ seems to become more excited. It should be also mentioned that the correction of the h_{10020} is achieved on the expense of slightly enlarged second order chromaticity, i.e. an increase of $\Delta Q_x'' \approx 70$ and $\Delta Q_y'' \approx 80$ with respect to the 2 family scheme. Note that a correction of resonance

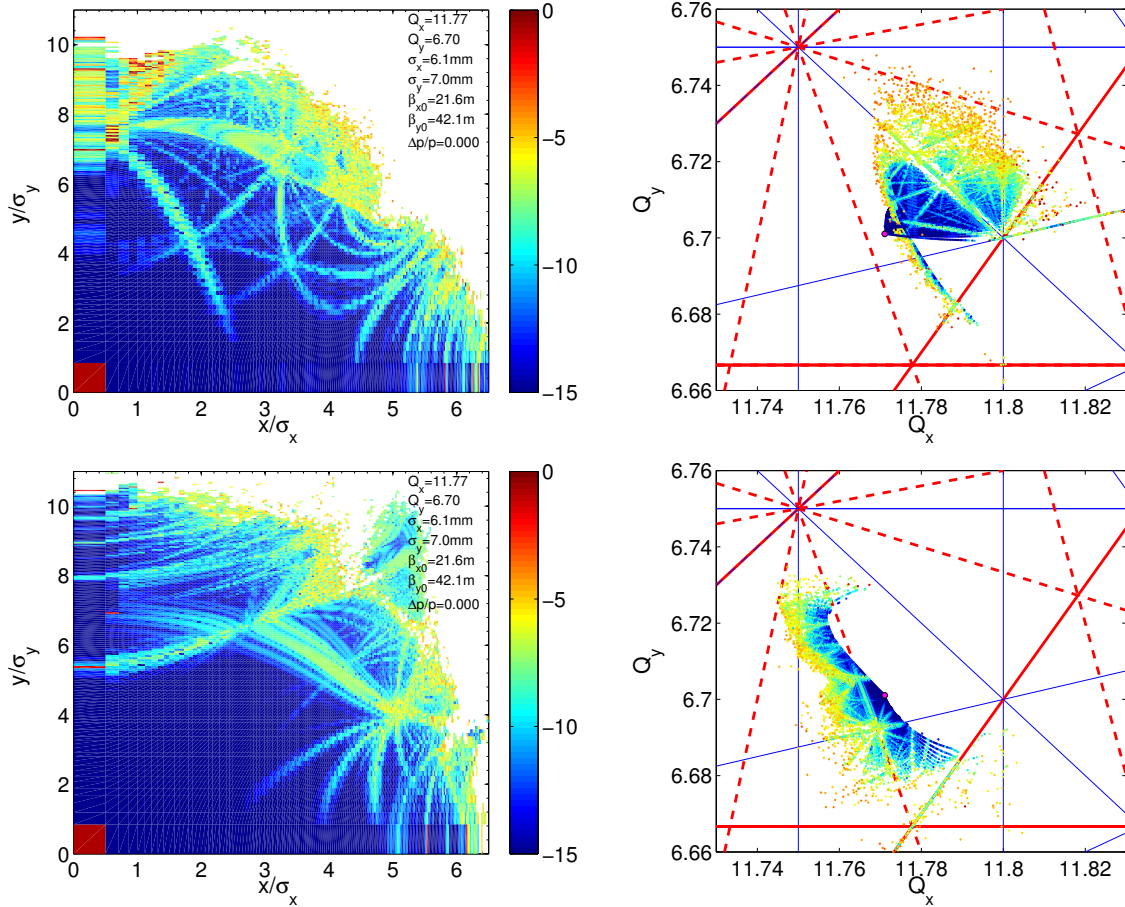


Figure 3.21: Frequency map analysis for the PS2 lattice including all machine errors for the 2 sextupole family scheme (left) and for the 4 family scheme tuned to minimize the h_{10020} resonance driving term (right). The color code indicates the logarithm of the tune diffusion rate d_ν . Resonances up to 6th order are shown in the tune diagram.

driving terms can be achieved without compromising the chromatic properties of the lattice by installing geometric sextupole families in non-dispersive regions of the ring. It was thus demonstrated that the dynamic aperture and thus the regularity of the single particle motion can be maximized by optimizing the strength of the four sextupole families. The final choice of the working point and the sextupole settings need to be studied in combination with space charge, which is beyond the scope of this thesis.

It is interesting to study the nonlinear detuning with amplitude induced by the higher order multipole errors. Figure 3.21 (top) shows the frequency map for the nominal working point $(Q_x, Q_y) = (11.77, 6.70)$ and the 2 family sextupole scheme in the case of on-momentum particles including all multipole errors and magnet misalignments for the reference error seed. Note that the frequency map is folded, i.e. different initial conditions in configuration space can yield identical tunes. In particular, for small vertical action J_y and increasing horizontal action J_x , particles will first exhibit

positive tune shift in Q_y . At a certain amplitude the derivative of the vertical tune shift is inverted. An indication for that was already observed in Fig. 3.15 (cf. Section 3.2.7) when plotting the detuning with amplitude up to $4\sigma_{x,y}$. Large horizontal actions finally yield negative vertical tune shift. Corresponding particles are found in the thin stripe pointing downwards in the tune diagram. The main source for this nonlinear tune shift with amplitude is coming from the high order systematic multipole components of the dipole magnets. Large amplitude particles exhibit chaotic motion as indicated by the large tune diffusion coefficient d_ν . As discussed before, this can be explained by the finite good field region of the magnets.

The frequency map for the PS2 lattice with all 4 sextupole families tuned to minimize the h_{10020} resonance driving term is shown in Fig. 3.21 (bottom). The tune footprint looks completely different compared to the 2 family scheme due to the amplitude dependent tune-shift induced by the chromatic sextupoles. The nonlinear detuning induced by the high order multipole errors can be clearly identified. As before, high tune diffusion coefficients due to chaotic motion are observed for large amplitude particles and high order resonances can be identified in the tune diagram. On the other hand, the particle motion remains regular with small amplitude dependent detuning for particles within the physical aperture.

3.2.9. Dynamic aperture including all errors and synchrotron motion

The dynamic aperture in the two cases discussed above is studied for the full particle motion including synchrotron oscillations. The 40-MHz RF cavity installed in the LSS of the PS2-lattice is adjusted to the nominal parameters of the stationary bucket, i.e. RF-voltage of $V_{\text{RF}} = 0.65$ MV, synchronous phase of $\varphi_s = 0$ and harmonic number $h = 180$. Particles with an initial momentum offset of $\Delta p/p = 0.003$ (close to the bucket height) and zero initial longitudinal phase offset are tracked for 25000 turns in 6D with MADX-PTC including all magnetic field errors and misalignments. For comparison, the cycle of the PS2 has a flat bottom of 100 ms, which corresponds to about 22000 turns. Figure 3.22 shows the resulting dynamic apertures. Note the big variation of the stable area in the case of the 2 family scheme for different error seeds. In contrast to that, the dynamic aperture is larger in the 4 family scheme (especially in the vertical plane) due to the minimization of the resonance driving term h_{10020} , as seen already in the tracking without synchrotron motion. Thus, it follows that indeed within a certain range the dynamic aperture of the PS2 lattice can be improved by tuning the chromatic sextupole families. Further optimization with additional correctors like harmonic sextupoles for resonance compensation and harmonic octupoles for correcting amplitude detuning could be subject of future studies. In addition, the nonlinear optimization has to be completed by space charge simulations, as periodic crossing of the third order resonance $Q_x + 2Q_y = 25$ below the working point may cause significant emittance blow-up if not compensated by additional correctors.

Finally, the dynamic aperture with synchrotron motion is studied for two alternative working points. A working point with similar transition energy as the nominal

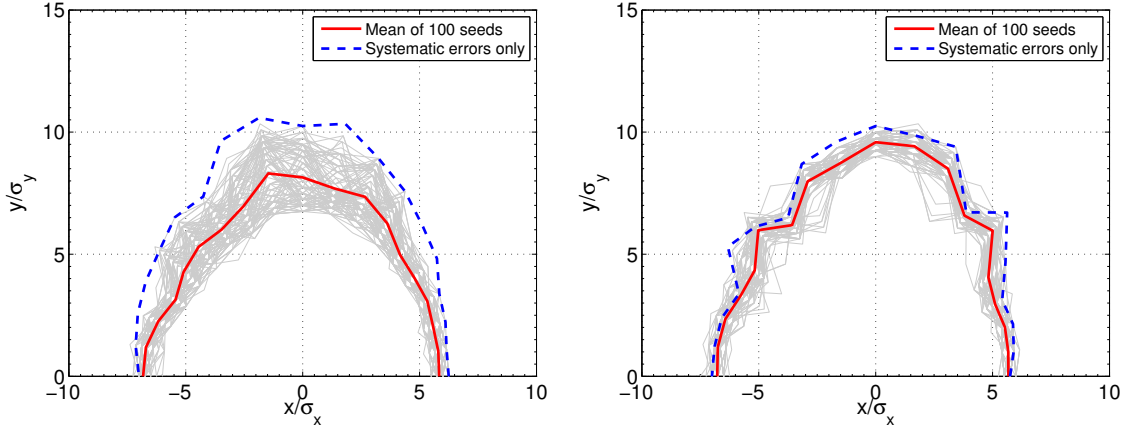


Figure 3.22: Dynamic apertures determined by tracking particles including synchrotron oscillations for 25000 turns in the case of 2 family sextupole scheme (left) and the 4 family scheme (right). The result of 100 error seeds (grey lines) are compared to the case of pure systematic multipole components preserving the lattice symmetry.

is found in the area around $(Q_x, Q_y) = (11.78, 7.7)$. However, similar to the nominal working point the 3^{rd} order resonance $Q_x + 2Q_y = 27$ may limit the achievable beam brightness for large space charge tune spread. In this respect, a better location of the working point seems to be around $(Q_x, Q_y) = (11.3, 7.26)$ as there were no excited low order resonances in this area of the tune diagram (cf. Fig. 3.20). This could be of particular interest for the LHC beams. The dynamic apertures for these two working points are shown in Fig. 3.23 for the 2 family scheme. Both provide sufficient dynamic aperture. Note that the RF-voltage is scaled according to the different values of γ_t in order to keep the bucket area constant (cf. Appendix B).

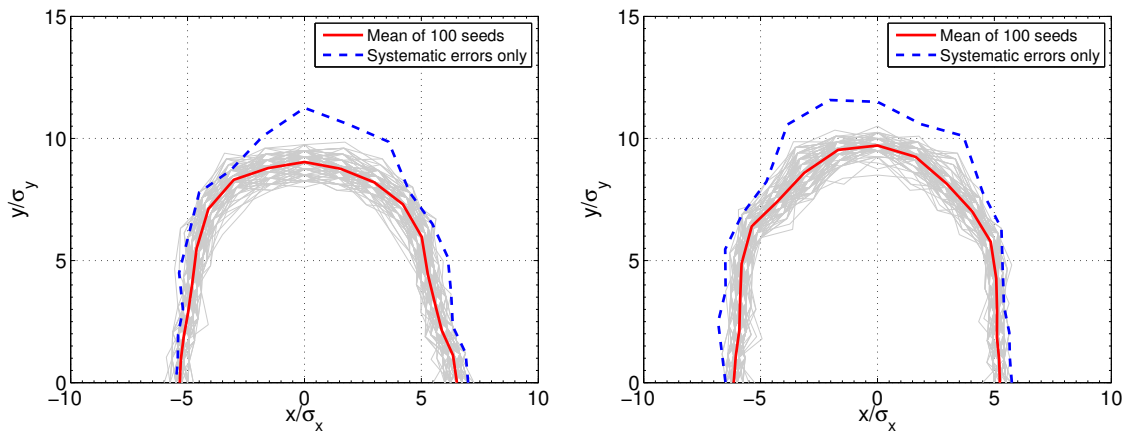


Figure 3.23: Dynamic aperture for the working points $(Q_x, Q_y) = (11.3, 7.25)$ on the left and $(Q_x, Q_y) = (11.78, 7.71)$ on the right for a set of 100 error seeds. Particles are tracked for 25000 turns including synchrotron oscillations.

3.3. Alternative PS2 lattice with threefold symmetry

Although a racetrack shape for the PS2 fits best to the requirements of integration into the existing CERN accelerator complex, an alternative lattice option with a threefold symmetry is studied. Due to the higher periodicity compared to the racetrack shape, a larger number of resonances is cancelled by the lattice symmetry. This is of particular interest for PS2, as it is a space charge dominated machine and thus particles exhibit large tune-spread at low energy.

3.3.1. Linear optics

The additional long straight section in the threefold symmetric lattice compared to the racetrack shape reduces the available length of bending magnets for a given circumference. The dipole filling factor in the arcs can be maximized by omitting dispersion suppressor modules. Zero dispersion in the straight sections can then be achieved by tuning the horizontal phase advance per arc to multiples of 2π . In this case, the 3×3 extended transport matrix is reduced to the unit matrix (cf. Eq. (A.37) in Appendix A.3) and the arc becomes achromatic. An extension of this approach to the “resonant lattice” was derived by Senichev [55]: resonances are cancelled in first order by proper phase advance of individual repetitive modules. The resonant condition requires an even number of arc cells $2M$ with an odd tune $2M - 1$ along the arc. Early lattice variants for the PS2 were developed exploiting this concept [56]. Note that the design of the negative momentum compaction lattice of the J-PARC Main Ring [27] is also based on this approach. However, due to space constraints for the PS2 design, the lattice solution with threefold symmetry presented below slightly deviates from this concept. In particular, each of the arcs consists of 5 NMC cells with a total phase advance in the horizontal plane of $\phi_{x,\text{ARC}} = 4 \cdot 2\pi$.

Three different types of quadrupoles with lengths of 1 m, 1.4 m and 2.4 m are needed for efficient operation of the 4 families in the arcs. A good filling factor of the NMC cell is achieved by reducing the number of dipoles per cell to nine compared to 13 in the racetrack lattice. Due to the required magnet-to-magnet drift spaces the length of the 135 dipoles is limited to 4.31 m, which translates to a kinetic energy of 46.3 GeV (for protons) for the maximum bending field of $B_0 = 1.7$ T. The ring consists of eight independent quadrupole families, four in the NMC cells and four in the LSSs. A summary of the machine parameters for this lattice option is listed in Table 3.6. For direct comparison between different lattice solutions, the layout of the doublet LSS is identical to the baseline racetrack lattice (cf. Section 3.2.1).

Figure 3.24 shows a plot of the optics functions for the NMC cell and for one super-period of the ring tuned to the working point $(Q_x, Q_y) = (14.21, 7.26)$, where $\gamma_t = 32.1i$. Note that the average beta functions are smaller compared to the racetrack lattice. On the other hand, the dispersion function reaches peak values of around $\hat{D}_x \approx 5$ m due to the resonant oscillation along the arc. The achromatic transport of the dispersion function through the arc can be demonstrated in normalized dispersion

Table 3.6: Machine parameters PS2 threefold symmetric lattice

Basic parameters	
Circumference, C (m)	1346.4
Superperiodicity	3
Maximum beam rigidity, $\hat{B}\rho$ (Tm)	157.63
Optics parameters	
Betatron tune, Q_x/Q_y	14.21/7.26
Maximum beta function, $\hat{\beta}_x/\hat{\beta}_y$ (m)	58/55
Minimum/maximum dispersion, \hat{D}_x (m)	-5.2/+5.0
Natural chromaticity, Q'_x/Q'_y	-18.6/-12.2
Specific natural chromaticity, ξ_x/ξ_y	-1.31/-1.68
Gamma at transition, γ_t	32.1 <i>i</i>
Dipole magnets	
Number of dipoles	135
Bending radius, ρ (m)	92.7
Bending angle, θ (mrad)	46.54
Length (m)	4.3
Minimum drift space between dipoles (m)	0.8
Gap height (mm)	84
Full aperture (cm)	12.6×6.5
Quadrupole magnets	
Number of quadrupoles	132
Number of independent families	8
Number of types (arc)	3
Lengths, arc (m)	1.0, 1.4, 2.4
Maximum normalized quadrupole gradient, arc (m^{-2})	0.11
Minimum drift space around quadrupoles (m)	1.3
Pole radius, arc (mm)	65
Full aperture, focusing quadrupoles (cm)	12.6×6.5
Full aperture, defocusing quadrupoles (cm)	11×7.5
Number of types, LSS	1
Pole radius, LSS (mm)	82
Length, LSS (m)	2.4
Chromatic sextupole magnets	
Number of sextupoles	60
Number of independent families	2
Number of types	1
Length (m)	0.4
Maximum normalized sextupole strength (m^{-3})	0.8

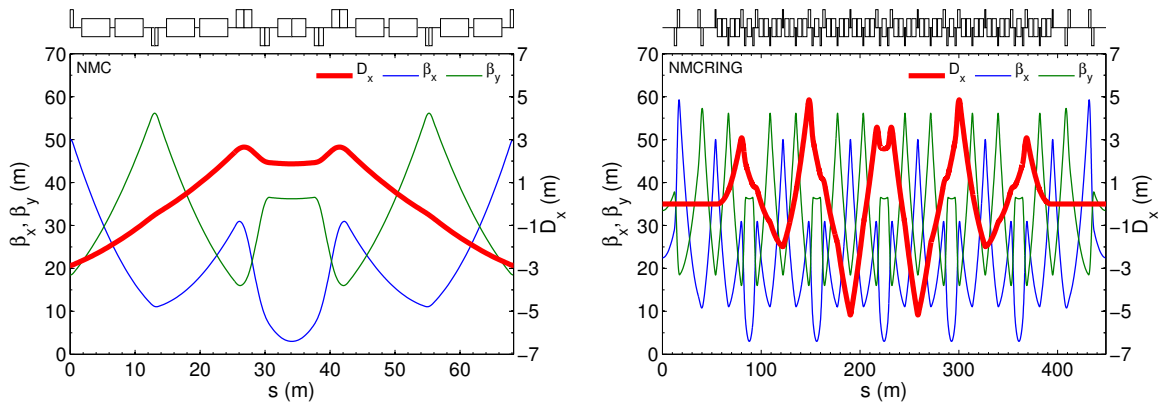


Figure 3.24: Optics functions in the NMC cell (left) and in one super-period of the threefold symmetric PS2 lattice (right), with $(Q_x, Q_y) = (14.21, 7.26)$ and $\gamma_t = 32.1i$. Note the resonant oscillation of the dispersion function D_x along the arc.

phase-space as shown in Fig. 3.25. The entire straight section up to the entrance of the arc corresponds to the origin of this phase-space diagram, as the dispersion action $J_{d,x}$ is zero. The dispersion action is increasing in the bending magnets (red lines) and is invariant through the quadrupoles and drift spaces (blue lines). The peak value of $J_{d,x}$ is reached in the center of the arcs (corresponding to the crossing of the $D'_{n,x}$ -axis with the largest value of $D_{n,x}$). The dispersion action is brought back to zero in the second half of the arc. As the dispersion function is on average negative in the bending magnets ($D_{n,x} < 0$), an imaginary γ_t is achieved.

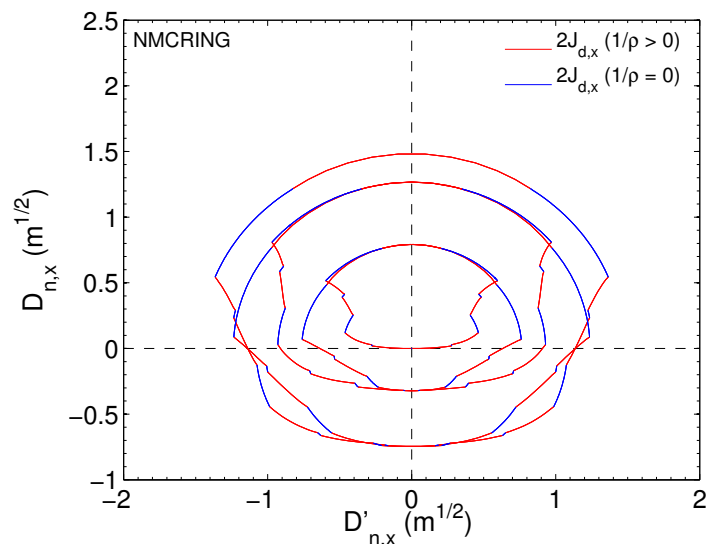


Figure 3.25: Dispersion action $J_{d,x}$ in the normalized dispersion phase-space coordinates $D_{n,x}$ and $D'_{n,x}$ for the PS2 ring with threefold symmetric lattice.

3.3.2. Physical aperture

The available aperture for the fixed target beam is calculated in the same way as for the nominal lattice (cf. Section 3.2.2). In particular, a maximal closed orbit uncertainty of $\Delta\hat{z}_{\text{co}} = 1$ mm, parasitic dispersion of $k_D = 0.1$ (i.e. 10%) and beta-beating of $k_\beta = 0.1$ (i.e. 20%) are assumed. Using the same geometry of the vacuum chambers as for the racetrack lattice yields an available aperture of $n_A(\sigma_{\text{FT}}) = 3.7$. This might be surprising at first, since the dispersion function reaches much larger peak values \hat{D}_x compared to the nominal lattice, where $\hat{D}_x \approx 3.3$ m and $n_A(\sigma_{\text{FT}}) = 3.5$. However, the horizontal β -functions are smaller at the location of maximal dispersion in the threefold symmetric lattice. Furthermore, the vertical beta functions are smaller at the locations of maximal beam size in the horizontal plane which makes better use of the physical aperture. The calculated beam sizes in all main magnets are shown in Fig. 3.26.

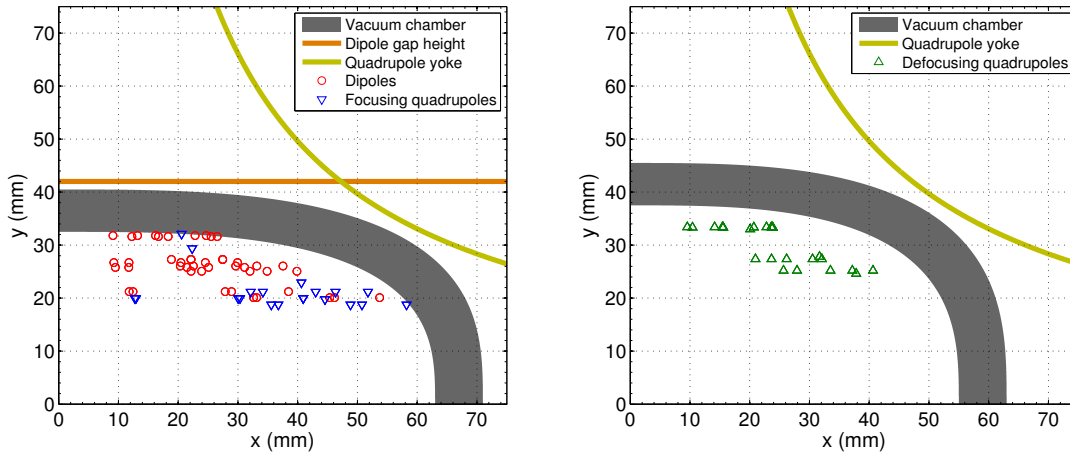


Figure 3.26: Physical aperture for the two types of vacuum chambers, for dipoles and focusing quadrupoles (left) and for defocusing quadrupoles (right) in the threefold symmetric PS2 lattice. The rms beam sizes multiplied by $n_A(\sigma_{\text{FT}}) = 3.7$ are calculated in all main magnets, assuming the errors discussed in the text.

3.3.3. Tuning flexibility

An interesting aspect to study in the threefold symmetric lattice is the tuning flexibility. The horizontal phase advance in the arcs is restricted to multiples of $\phi_{x,\text{arc}} = 4 \cdot 2\pi$ for dispersion suppression in the LSSs⁵. Therefore only the vertical phase advance can be adjusted using the quadrupole families in the arcs, while the horizontal tune of the machine has to be controlled by the long straight sections. However, they have to satisfy stringent constraints on the phase advances between beam transfer elements. In

⁵Other multiples of 2π for the total phase advance per arc $\psi_{x,\text{ARC}}$ are out of reach for the 5 NMC cells of this lattice.

addition, the optical functions at the beginning of the LSSs are fixed by the optics of the arc. The tuning range of the long straight section with these constraints is centered around $\psi_{x,\text{LSS}} = 0.75 \cdot 2\pi$ and the resulting horizontal tune of the machine is roughly $Q_x \approx 3 \cdot 4 + 3 \cdot 0.75 = 14.25$. The vertical tune Q_y on the other hand is more flexible.

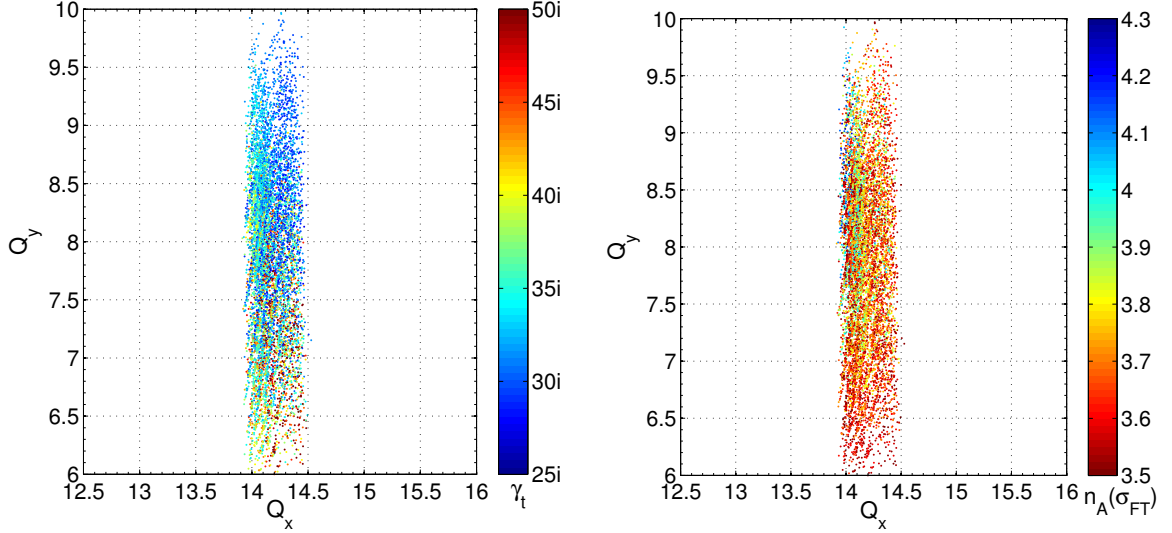


Figure 3.27: Tuning flexibility of the threefold symmetric NMC lattice. The color-code indicates values of γ_t (left) and the available aperture in units in units of beam sizes of the fixed target beam (right).

The tuning flexibility of the threefold symmetric lattice is addressed with the numerical method of a global scan of stable solutions (GLASS) [47], as presented already in Section 3.2.3. The normalized gradients of three quadrupole families of the NMC cell are varied systematically in steps of 0.001 m^{-2} , while the horizontal phase advance is tuned to $\mu_x = 4/5 \cdot 2\pi$ using the fourth family in the arc. In addition, two quadrupole families of the straight sections are scanned while the remaining two are used to match the optics to the arcs. For each stable solution, the available aperture for the high intensity fixed target beam is computed using the same assumptions as described above. All solutions with $n_A(\sigma_{\text{FT}}) > 3.5$ and maximum quadrupole gradients of 16 T/m are considered as valid. Note that the maximum *normalized* gradient in the threefold symmetric lattice is slightly larger compared to the racetrack lattice due to the smaller maximum beam rigidity $\hat{B}\rho$ (cf. Table 3.6). Figure 3.27 (left) shows the resulting values of γ_t as a function of the transverse tunes Q_x and Q_y in the tune diagram. As expected, the tuning flexibility is very limited in the horizontal plane with Q_x ranging between 13.95 and 14.5. This range may be reduced even further by imposing the beam transfer constraints on the phase advances in the LSSs. On the other hand, the vertical tune can be adjusted between $Q_y \approx 6$ with $\gamma_t \approx 50i$ and $Q_y \approx 10$ where $\gamma_t \approx 28i$. It is interesting to note that the transition energy γ_t in the threefold symmetric lattice depends on the *vertical* tune Q_y of the machine, while a clear

dependence on the horizontal tune was found for the racetrack lattice (cf. Section 3.2.3). This is caused by the resonant oscillations of the dispersion function along the arc and the fact that the horizontal phase advance per arc is fixed. Figure 3.27 (right) shows the available aperture for all valid solutions. Peak values of $n_A(\sigma_{\text{FT}}) = 4.3$ are reached in some cases. Note that the observed tuning range corresponds very well to three times the achievable phase advance range in the LSSs of the racetrack lattice. While the global tune scan is limited to some extent by the finite grid size of the quadrupole gradients, the lattice can be tuned a little further in the horizontal plane using refined matching routines. However, horizontal tunes above $Q_x = 14.6$ are hard to reach since the β -functions in the LSSs attain high peak values and some quadrupoles flip polarity. On the other hand, the tuning range can be enlarged by allowing for small dispersion in the LSSs and thus relaxing the horizontal phase advance constraint in the arcs.

3.3.4. Working point considerations

Figure 3.28 shows the relevant part of the tune diagram with resonances up to third order. Note that the third order resonance at $3Q_x = 43$ is non-systematic, which is beneficial for the resonant slow extraction of the fixed target beams. Furthermore, the region around the chosen working point $(Q_x, Q_y) = (14.21, 7.26)$ is free of systematic low order resonances. However, the systematic third order resonance $Q_x - 2Q_y = 0$ may become a limitation in connection with the negative detuning caused by space charge effects. In this case the working point could be moved up by one integer unit and set to $(Q_x, Q_y) = (14.19, 8.24)$. In this area all sextupole resonances are non-systematic.

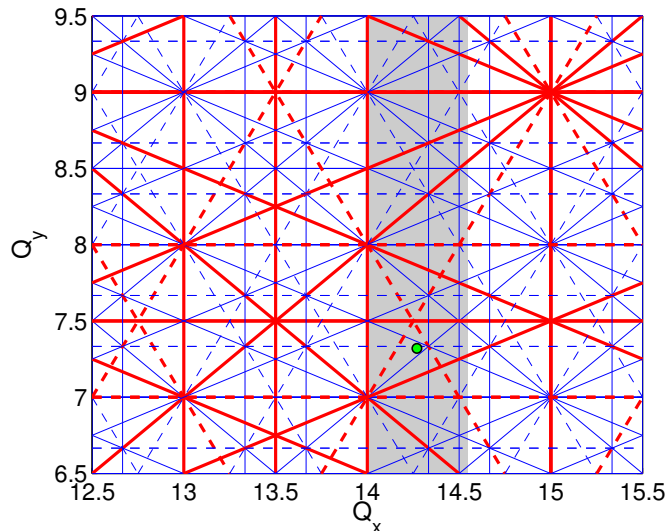


Figure 3.28: Tune diagram for a superperiodicity of three with resonances up to third order. Red lines correspond to systematic and blue lines to non-systematic resonances. Dashed lines indicate skew and solid lines normal resonances. The tuning range of the lattice is indicated by the grey area and the working point is marked by a green dot.

3.3.5. Chromaticity correction

Two families of chromatic sextupoles are installed around the quadrupole doublet insertion in the center of the NMC cells (similar to the 2 family scheme of the racetrack lattice and thus using the same naming convention), resulting in a total of 60 magnets. The positions of the sextupole magnets in the NMC cell are indicated in Fig. 3.29. Note

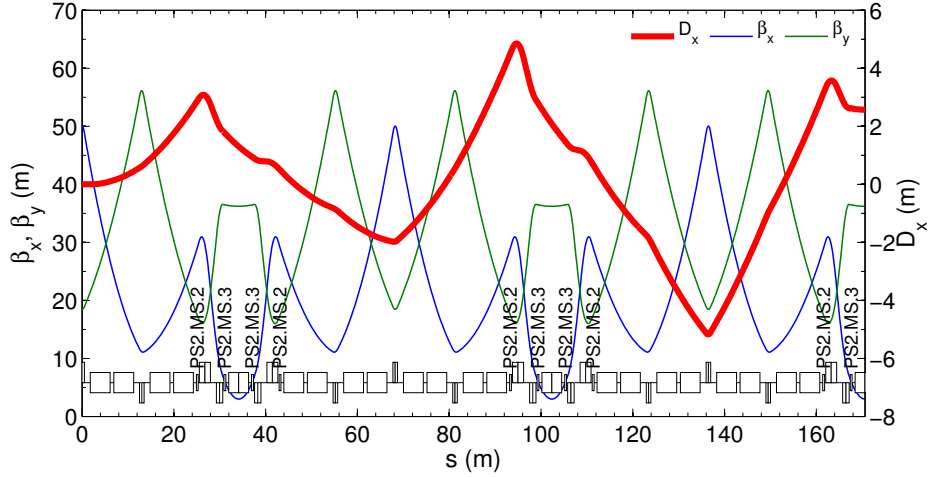


Figure 3.29: Chromaticity correction scheme of the threefold symmetric PS2 lattice together with the optics functions in one half arc.

that the dispersion function D_x is not regular at the location of the sextupole magnets around the arc due to the resonant phase advance in the horizontal plane. Therefore individual sextupoles exhibit different efficiencies for chromaticity correction. Further optimization of the chromaticity correction scheme as for example splitting the sextupole circuits into more families could be subject of future studies. This may become necessary in order to correct the chromatic beta-beat induced by the 2 family sextupole scheme, as shown in Fig. 3.30 for the two working points $(Q_x, Q_y) = (14.21, 7.26)$ and $(Q_x, Q_y) = (14.19, 8.24)$. Similar to the racetrack lattice, second order chromaticity and off-momentum beta-beat are stronger in the vertical plane and become particularly enhanced for higher vertical tunes. A summary of the chromatic and amplitude dependent tune shift terms for the threefold symmetric lattice is given in Table 3.7.

Table 3.7: Chromatic and amplitude terms for the threefold symmetric PS2 lattice

Sextupoles scheme	Q_x/Q_y	Q'_x/Q'_y	Q''_x/Q''_y	a_{xx}	a_{xy}	a_{yy}
bare lattice	14.21/7.26	-18.6/-12.2	103.2/58.7	23.5	33.5	27.1
2 sextupole families	14.21/7.26	0/0	42.3/180.2	-37.4	54.2	115.7
bare lattice	14.19/8.24	-20.2/-12.6	119.3/59.4	26.5	31.7	24.2
2 sextupole families	14.19/8.24	0/0	33.7/429.6	-68.6	45.6	90.4

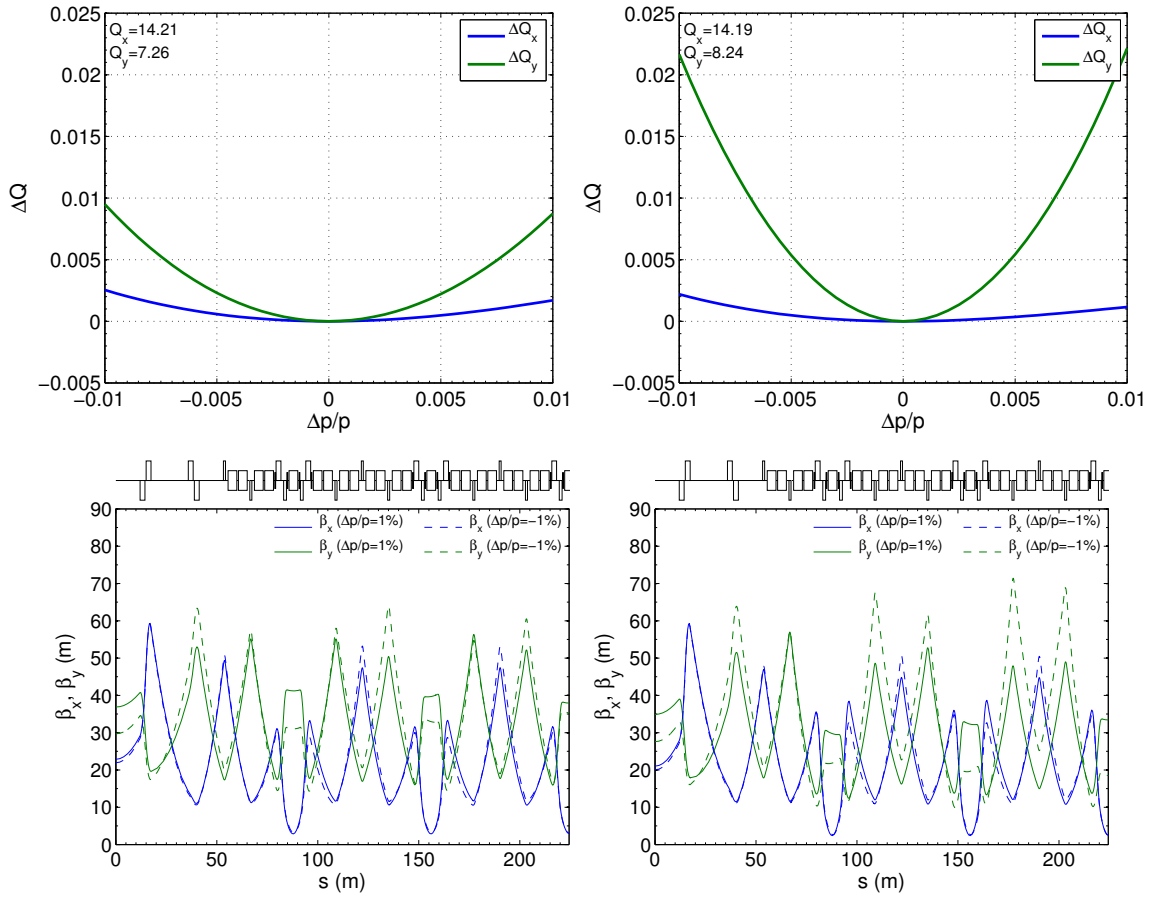


Figure 3.30: Off-momentum beta functions in half a super-period for $\Delta p/p \pm 1\%$ (bottom) and non-linear chromaticity (top), on the left for $(Q_x, Q_y) = (14.21, 7.26)$ and on the right for $(Q_x, Q_y) = (14.19, 8.24)$.

3.3.6. Correction of misalignment and closed orbit errors

In order to correct for closed orbit distortion, a total of 54 horizontal and 72 vertical dipole correctors together with 126 bi-planar beam position monitors are distributed around the ring. They are located around the focusing and defocusing quadrupole magnets, in order to profit from the local maxima of the beta functions. The performance of the orbit correction scheme is studied for a sample of 500 random error seeds using the same closed orbit errors as previously used for the racetrack PS2 lattice and summarized in Table 3.4 (cf. Section 3.2.6). Two iterations on orbit correction are performed using the MICADO algorithm in MADX. A random subset of 40 correctors in the horizontal and 52 correctors in the vertical plane are used for the correction, in order to account for the fact that not all correctors may be available in routine operation or during commissioning. Similarly, only a subset of 95% of the BPMs are considered to be functional. Figure 3.31 (top) shows the distribution of the maximum and rms closed orbit distortion before and after two iterations of the correction algorithm.

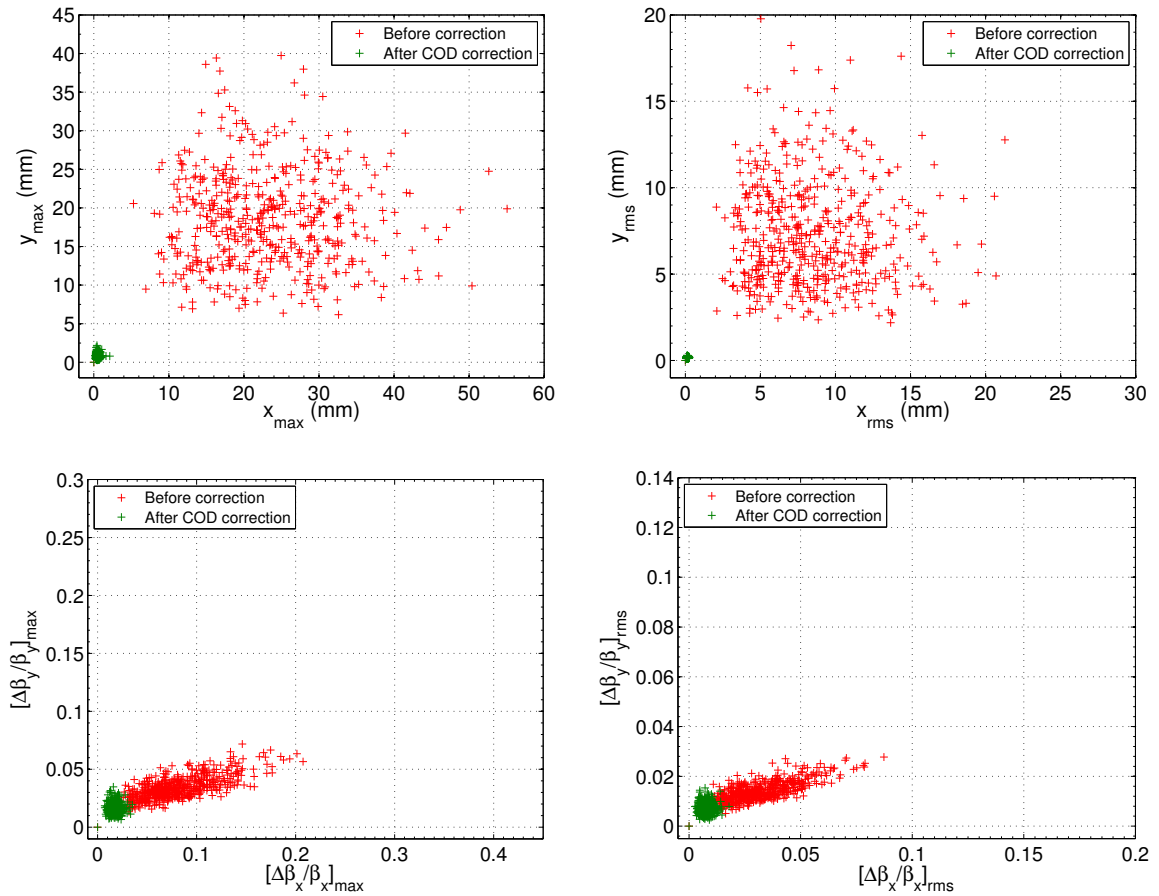


Figure 3.31: Distribution of the closed orbit distortion (top) and beta-beat (bottom) before and after two iterations of the correction algorithm in terms of maximal (left) and in terms of rms-values (right) for 500 error seeds.

The obtained results are comparable to the closed orbit correction in the racetrack lattice discussed in Section 3.2.6. In particular, none of the machine samples exceed 3 mm maximum orbit distortion after correction and average rms values are kept below 0.5 mm. The maximally required dipole kick is about 0.4 mrad, as for the racetrack lattice. Figure 3.31 (bottom) shows the maximum and rms beta-beat before and after the closed orbit correction. Similar to the observations with the racetrack lattice, the major part of the optics distortion is induced by feed-down effects due to large orbit excursion in the sextupole magnets. A significant reduction of the beta-beating to below 10% is achieved by the closed orbit correction.

3.3.7. Multipole field errors

The impact of higher order multipole errors is studied here assuming the same errors as used for the racetrack lattice. The corresponding multipole components are summarized in Table 3.5 (cf. Section 3.2.7). The effect of these multipole errors on

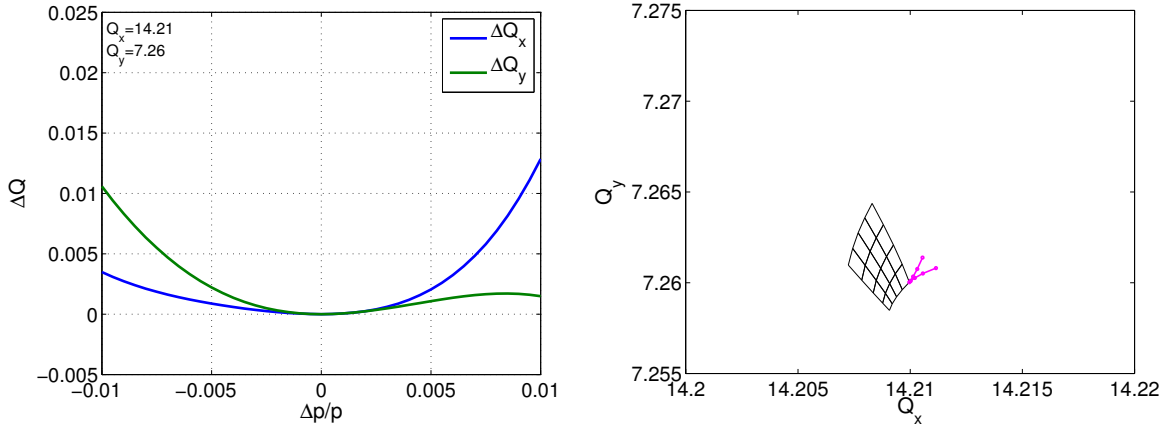


Figure 3.32: Nonlinear chromaticity (left) including all multipole errors and misalignments and the corresponding amplitude detuning (right) up to $4\sigma_{x,y}$ in units of the fixed target beam as indicated by black lines (which are separated by equidistant actions J_x and J_y) for the working point $(Q_x, Q_y) = (14.21, 7.26)$. The magenta line in the tune diagram represents the chromatic detuning up to $\Delta p/p = \pm 0.004$ (exceeding already the RF bucket height).

the nonlinear chromaticity is shown in Fig. 3.32 (left). The resulting nonlinear chromaticity is comparable with the racetrack lattice when including all machine errors. In particular, a significant third order chromaticity component is observed in the vertical plane in both cases. Figure 3.32 (right) shows the detuning with amplitude for on-momentum particles up to $4\sigma_{x,y}$ in units of the fixed target beam size (black lines) together with the nonlinear chromatic detuning up to $\Delta p/p = \pm 0.004$ (purple lines). The nonlinear dependence of the tune on the betatron amplitude caused by the multipole errors is clearly visible. However, the overall detuning is smaller compared to the racetrack lattice and in particular, it is one order of magnitude smaller than the anticipated space charge tune spread with LHC beams.

3.3.8. Dynamic aperture without synchrotron motion

The impact of the chromaticity sextupoles and all other machine errors such as misalignments and multipole errors on the stability of the single particle motion is studied in tracking simulations with MADX-PTC.

Dynamic aperture with and without orbit errors

For direct comparison with the racetrack lattice, the misalignment and orbit errors as summarized in Table 3.4 (cf. Section 3.2.6) will be used in the following. The errors are assigned to all main magnets in the chromaticity corrected lattice. After correction of the closed orbit, the quadrupoles in the arcs are retuned to restore the initial betatron

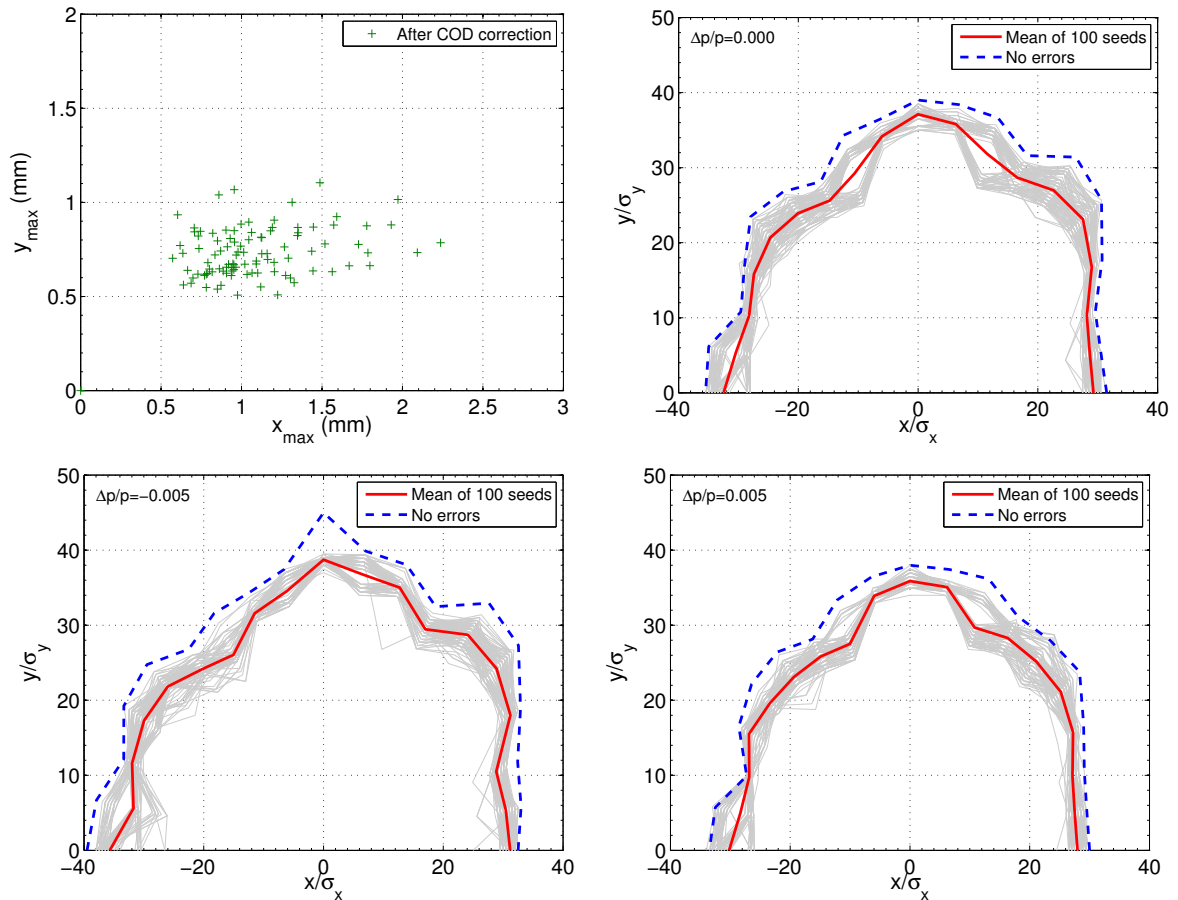


Figure 3.33: Closed orbit after correction and the resulting dynamic apertures for particles surviving 10000 turns with different values of momentum offset $\Delta p/p$ and the working point $(Q_x, Q_y) = (14.21, 7.26)$. The results for 100 errors seeds are plotted in grey, the mean of them is plotted in red. The blue dashed curve shows the dynamic aperture for the error-free lattice.

tunes of the error-free lattice and the linear chromaticity is corrected back to zero. Particles are tracked for 10000 turns in 5D (no synchrotron motion) with different momentum offsets. Figure 3.33 shows the maximal closed orbit excursion before and after the correction for a sample of 100 errors together with the resulting dynamic apertures in units of beam sizes σ_x and σ_y of the high intensity fixed target beam. The dynamic aperture of the error-free lattice is indicated by the dashed blue line. In all cases, the dynamic aperture is large compared to the available aperture of the machine $n_A(\sigma_{FT}) \approx 3.75$. Similar to the observations made for the racetrack lattice (cf. Section 3.2.8), closed orbit distortion and reduced lattice symmetry due to random errors of the magnet strengths play only a minor role for the stability of the single particle motion.

Dynamic aperture in the presence of multipole errors and misalignments

The impact of multipole field errors on the dynamic aperture is studied in the same way as for the racetrack lattice (cf. Section 3.2.7). For direct comparison between the two lattice options, the errors summarized in Table 3.5 were used in both cases. After assigning all errors, the closed orbit is corrected, the betatron tunes are rematched to the values of the error-free lattice and the chromaticities are reset to zero before tracking particles for 10000 turns. The distribution of the maximal closed orbit excursion after correction for the 100 error seeds and the resulting dynamic apertures for different momentum deviations are shown in Fig. 3.34. The dynamic aperture as obtained

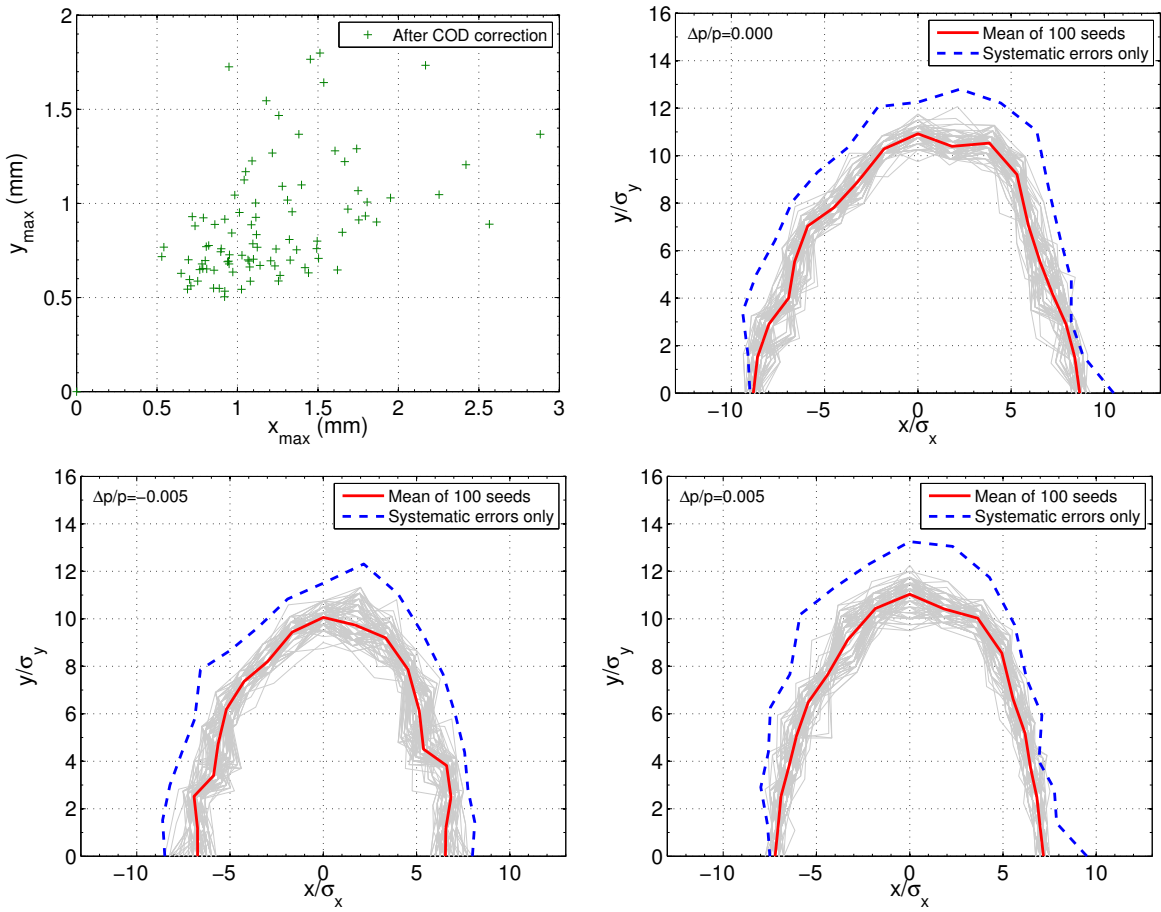


Figure 3.34: Closed orbit after correction and the resulting dynamic apertures for particles surviving 10000 turns with different momentum offsets for the working point $(Q_x, Q_y) = (14.21, 7.26)$. All multipole errors and magnet misalignment errors are included in the simulations for the 100 error seeds, yielding the dynamic apertures as indicated by the grey lines. Their mean is plotted in red, while the blue curve shows the dynamic aperture for the case of systematic multipole errors only, i.e. preserving the lattice symmetry.

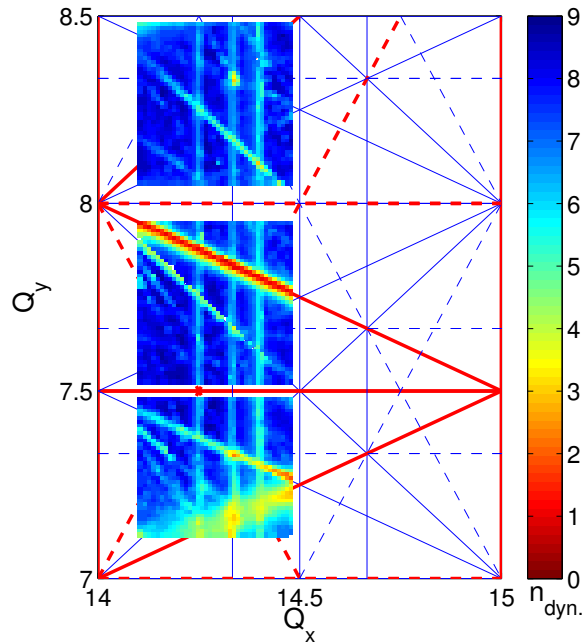


Figure 3.35: Tune scan for on-momentum particles including all multipole errors and misalignments for the reference error seed. The color code indicates the stable beam size $n_{dyn.}(\sigma_{FT})$ in units of the fixed target beam size. Systematic and non-systematic resonances up to 3rd order are indicated by red and blue lines, respectively, where solid lines correspond to normal and dashed lines to skew components.

without random errors and misalignments, i.e. including only systematic multipole errors and thus preserving the lattice symmetry, is indicated by the dashed blue line. As already observed for the racetrack lattice (cf. Section 3.2.8), the assumed multipole components result in a drastic reduction of the dynamic aperture, even if taking into account only systematic multipole errors.

A global picture of the impact of multipole errors on the dynamic aperture and excitation of resonances is obtained with a tune scan, i.e. a systematic study of the dependence of the dynamic aperture on the working point as described already in Section 3.2.8. Figure 3.35 shows the dynamic aperture $n_{dyn.}(\sigma_{FT})$ in units of the beam size of the fixed target beam as a function of the working point, as obtained by tracking on-momentum particles for 10000 turns in a series of MADX-PTC simulations for the reference error seed. Note that the matching to the different working points is achieved with the quadrupoles in the LSSs. In particular, in each of the three quadrants investigated here, the matching starts from a different optics solution as obtained with GLASS (cf. Section 3.3.3). In resonance-free areas of the tune diagram a maximum dynamic aperture of about $n_{dyn.}(\sigma_{FT}) \approx 9$ is obtained, which is larger compared to the racetrack lattice. This may be attributed to the fact that the beta functions are on average smaller in the threefold symmetric lattice and thus the dynamic aperture in

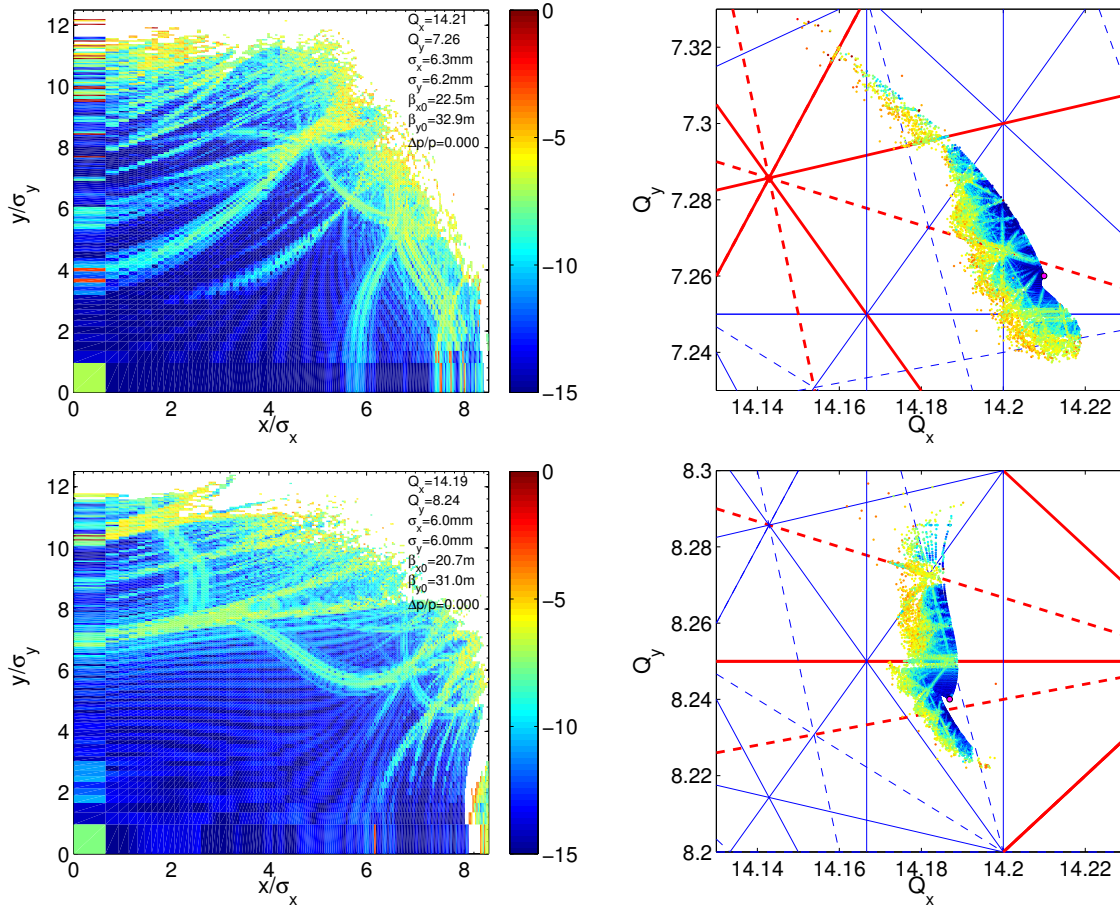


Figure 3.36: Frequency map analysis including all machine errors, on the right for the working point $(Q_x, Q_y) = (14.21, 7.26)$ and for $(Q_x, Q_y) = (14.19, 8.24)$ on the right. The color code indicates the logarithm of the tune diffusion rate d_ν . The magenta dot indicates the zero amplitude tune. Resonances up to 6th order are shown in the tune diagram.

units of rms beam size is slightly larger compared to the racetrack lattice. Furthermore, the increased lattice super-periodicity reduces the number of systematic resonances. Strong reduction of the dynamic aperture is observed close to low order resonances. In particular, the systematic third order resonance $Q_x + 2Q_y = 30$ is strongly excited limiting the stable particle motion to below the physical aperture. A comparably broad stopband is observed for the systematic third order resonance $Q_x - 2Q_y = 0$, similar as in the racetrack lattice. This resonance may become a limitation for the working point $(Q_x, Q_y) = (14.21, 7.24)$, when considering the incoherent space charge detuning. It is interesting to note that no strong resonances are observed in the area of the tune diagram between $Q_y = 8$ and $Q_y = 8.5$. Figure 3.36 shows a comparison of the Frequency maps for the working points $(Q_x, Q_y) = (14.21, 7.26)$ and $(Q_x, Q_y) = (14.19, 8.24)$ for the reference error seed. Strong nonlinear detuning with amplitude is observed in both

cases, in particular already for particles with small oscillation amplitude within the physical aperture. In other words, the linear detuning terms mainly due to sextupoles and octupole components are small compared to the higher order terms. This was already observed in Fig. 3.32 for the working point $(Q_x, Q_y) = (14.21, 7.26)$, when plotting the detuning with amplitude up to $4\sigma_{x,y}$. This is probably the reason why the tune diffusion coefficient for small actions is higher compared to the racetrack lattice (cf. Section 3.2.8), at least of the working points studied. High order resonances can be identified for large actions. However, the dynamic aperture is in general larger in the threefold symmetric lattice.

3.3.9. Dynamic aperture including all errors and synchrotron motion

A final check of the stability of the single particle motion is performed by tracking particles taking into account their synchrotron motion. The nominal PS2 bucket parameters are used, i.e. the RF-voltage of the 40 MHz cavity is adapted according to the value of γ_t (cf. Appendix B) in the threefold symmetric lattice. Particles with initial momentum offset of $\Delta p/p = 0.003$ (close to the bucket height) and zero initial longitudinal phase offset are tracked for 25000 turns in 6D with MADX-PTC including all magnetic field errors and misalignments as discussed above. Note that the cycle of the PS2 has a flat bottom of 100 ms, which corresponds to about 22000 turns. Figure 3.37 shows the resulting dynamic apertures for the working points $(Q_x, Q_y) = (14.21, 7.26)$ and $(Q_x, Q_y) = (14.19, 8.24)$ for a sample of 100 error seeds and for the case of including only systematic multipole components, i.e. preserving the lattice symmetry. Both working points exhibit a dynamic aperture larger than the physical aperture. Thus,

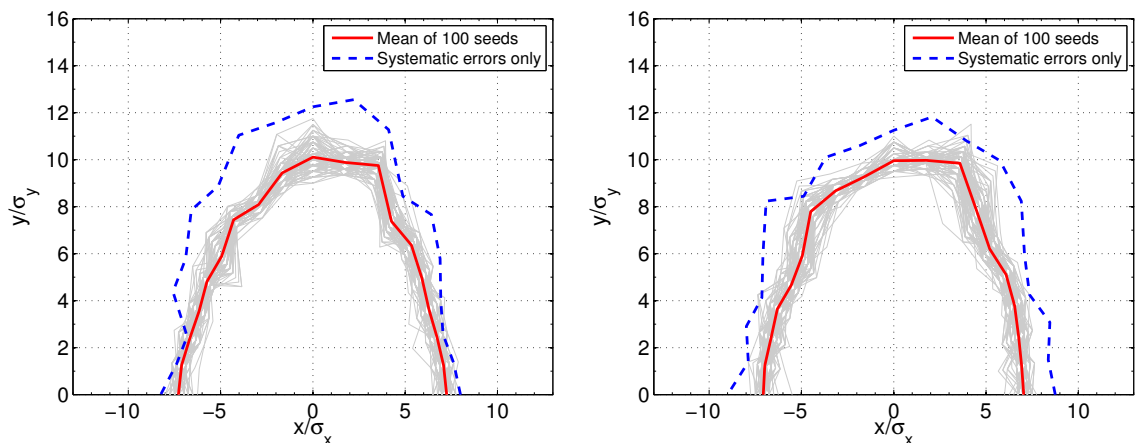


Figure 3.37: Dynamic aperture determined by tracking particles taking into account synchrotron motion for 25000 for the working points $(Q_x, Q_y) = (14.21, 7.26)$, on the left, and $(Q_x, Q_y) = (14.19, 8.24)$, on the right, with an initial momentum offset of $\Delta p/p = 0.003$. The result for 100 error seeds (grey lines) are compared to the case of considering only systematic multipole components, i.e. preserving the lattice symmetry.

it seems that the 2 family chromaticity correction scheme is adequate for the three-fold symmetric lattice, at least concerning the stability of single particle motion. In case chromatic effects like off-momentum beta-beat need to be controlled, additional sextupole families would have to be introduced.

3.4. Lattice comparison

The design of the PS2 lattice is constrained by the given circumference of 1346.4 m, which is determined by an optimized filling scheme of the SPS (cf. Section 3.1). The nominal PS2 lattice has a racetrack geometry with two zero dispersion long straight sections and top energy of 50 GeV (kinetic energy for protons). The working point of the machine can be adjusted in a wide range by changing the phase advance in the arc cells and re-matching the optics in the dispersion suppressor modules to the long straight sections. In comparison to that, the alternative lattice option based on a threefold symmetry has less available space for dipole magnets due to the additional long straight section⁶. Maximum dipole filling factor is thus achieved by omitting the dispersion suppressors. Zero dispersion in the long straight sections is achieved by setting the horizontal phase advance in the arcs to multiples of 2π . This imposes a strong limitation on the tuning flexibility in the horizontal plane, which may be a big disadvantage. In addition to that, the top energy is limited to 46.3 GeV. The available aperture is similar in both lattice options, i.e. slightly more than $n_A(\sigma_{FT}) = 3.5$ times the rms beam size of the fixed target beam, with slight advantages for the threefold lattice. On the other hand, smaller imaginary values of γ_t can be achieved in the racetrack option, which could be interesting for increasing the synchrotron tune and thus mitigating beam instabilities due to collective effects.

Chromaticity correction sextupoles are not imposing strong limitations on the dynamic aperture in the negative momentum compaction lattices for the PS2 studied here. In principle, two families of sextupoles are sufficient for correction of the linear chromaticity. As shown in the case of the racetrack lattice, a 4 sextupole family scheme provides additional flexibility for controlling off-momentum beta-beat or detuning with amplitude. In addition, the four sextupole families can be used for compensation of systematic resonances. This however can be achieved also with dedicated harmonic sextupoles, which could be installed in dispersion-free regions of the machine, such as the LSSs.

Closed orbit errors caused by misalignment and random errors in the main components of dipole and quadrupole magnets can be corrected efficiently in both lattice options with the proposed orbit correction scheme. The remaining closed orbit errors have only marginal impact on the dynamic aperture. In contrast to that, the assumed multipole errors of the dipoles, quadrupoles and sextupole magnets have a strong impact on the single particle dynamics. They clearly introduce higher order nonlinear

⁶The optics design and length of long straight section is the same for both lattice variants presented in this thesis.

chromaticity and nonlinear detuning with amplitude. Especially the nonlinear amplitude detuning can be dominant compared to the linear amplitude detuning induced by the chromaticity sextupoles and fringe fields of the quadrupole magnets. Furthermore, the multipole errors limit the dynamic aperture roughly to the good field region of the main magnets. This observation applies to both lattice options. However, the dynamic aperture in terms of rms beam size is in general slightly larger in the threefold symmetric lattice due to smaller average beta functions and the higher periodicity. The requirements on the field quality of the main magnets needs to be defined with the help of space charge simulations in future studies.

3.5. Consolidation and upgrade of the existing PS complex

The upgrade path of the LHC injector chain based on the construction of LP-SPL and PS2 aims at significantly increasing the intensity of LHC-type beams. Another important aspect of this project is to ensure high reliability of the LHC pre-accelerators. However, the new injector chain is expected to be ready for physics operation not before 2020 [33]. This in turn requires the existing injectors to operate at least until 2020. It was therefore concluded in the Chamonix LHC performance workshop in 2010 that a comprehensive consolidation of the existing machines is required [11]. This consolidation would then already improve the reliability of the injector complex. In addition, the electron cloud effect in the SPS was identified as the main performance limitation [57] of the entire injector chain. In fact, the higher beam transfer energy envisaged with PS2 would enhance the electron cloud effect at injection in the SPS [58], which would then become an even stronger limitation. At the same time, the SPS is the only machine of the injector complex that was not planned to be replaced by a new machine.

An alternative upgrade path is based on the consolidation and partial upgrade of the existing injector chain [59]. As already discussed in Section 3.1, the injection energy in the PSB will be raised from the present 50 MeV to 160 MeV with the connection of Linac4. The higher injection energy will allow for twice the beam brightness in the PSB for the same incoherent space charge tune spread. In view of reducing space charge effects at PS injection and thus preparing the PS for the higher beam brightness, an upgrade of the PSB extraction energy from 1.4 GeV to 2.0 GeV was proposed [59]. The feasibility of an upgrade for a higher PSB to PS transfer energy was then demonstrated in a comprehensive study [60]. In order to overcome performance limitations of the SPS, upgrade possibilities have been studied [57]. The upgrades for the higher beam transfer energy between the PSB and the PS as well as the power upgrade of the 200 MHz SPS RF system are part of the baseline of the LHC Injectors Upgrade (LIU) project [13]. Intensity and performance limitations in the SPS and their mitigation are addressed in more detail in the following chapter.

4. SPS optics with low transition energy

4.1. Intensity limitations for LHC beams in the SPS

The SPS is the last accelerator in the LHC injector chain. Proton beams for the LHC are injected at a momentum of 26 GeV/c from the PS and accelerated up to 450 GeV/c before injection into the LHC. The longitudinal bunch structure of LHC-type proton beams is produced already in the PS by multiple bunch splitting (and merging) using elaborate RF-manipulations [61]. The PS requires therefore a variety of RF-systems with different harmonics (cf. [62], Chapter 7). The nominal LHC bunch pattern has a 40 MHz structure, which corresponds to 25 ns bunch spacing. Omitting one of the bunch splittings before PS extraction results in bunch trains with 50 ns spacing and half the number of bunches, but with higher bunch intensity. This beam production mode was used in routine operation for LHC filling in 2011 and 2012. Longitudinal bunch rotation is performed just before extraction in the PS in order to fit the bunches into the 200 MHz RF bucket of the SPS. The usual LHC filling cycle in the SPS is designed for up to four injections from the PS. Since the length of the PS (double batch) cycle is 3 basic machine periods, i.e. 3.6 s, an injection plateau of 10.8 s is required in the SPS (the total cycle length is 21.6 s). Space charge effects on the SPS flat bottom might therefore limit the achievable brightness of LHC beams after upgrading the pre-injectors [63].

Even in absence of strong space charge effects, a series of intensity limitations for LHC beams in the SPS have been identified [32]. One of the most important limitations for beams with the nominal 25 ns bunch spacing is caused by electron cloud effects [64, 65]. In the presence of many bunches in the machine, residual gas ionization and beam induced multipacting on the vacuum chamber can generate a large number of electrons in the vacuum chamber which interact with the proton beam. This electron cloud drives a coupled bunch instability in the horizontal plane and a fast single bunch instability in the vertical plane, together with transverse emittance blow-up. The electron cloud build-up depends thereby on the beam structure and the properties of the vacuum chamber, i.e. the geometry and the secondary electron yield (SEY) of the inner surface. The SEY and thus the electron cloud build-up can be reduced by beam based electron bombardment, also known as *scrubbing*. However, this conditioning process can be very slow. Alternatively, the inner surface of the vacuum chambers can be coated with a thin layer of amorphous Carbon [66], which has lower SEY and thus prevents electron cloud build-up.

The main intensity limitation for single bunches in the SPS has been identified as transverse mode coupling instability (TMCI) at injection [67], which is mainly caused by the vertical beam coupling impedance of the kicker magnets [68]. The threshold

intensity with close to zero vertical chromaticity and typical longitudinal emittance for LHC-type beams ($\varepsilon_l \approx 0.35$ eVs) at injection into the SPS was found to be $N_{\text{thr}}^{\text{TMC}} \approx 1.6 \times 10^{11}$ p/b [69, 70] in 2010. The TMCI imposes therefore a serious limitation for the future high intensity LHC beams required for the HL-LHC upgrade⁷ [12], as chromaticity cannot be increased too much in order to avoid slow incoherent losses.

In the longitudinal plane, LHC-type beams in the SPS suffer from instabilities due to broadband and narrowband impedances. In particular, the reactive part of the SPS longitudinal impedance drives a single bunch instability due to the loss of Landau damping [71]. Narrowband impedances, possibly due to the fundamental and higher order modes (HOM) of the main 200 MHz and the fourth harmonic 800 MHz system, drive longitudinal coupled bunch instabilities which have a very low threshold in the SPS [32]. In routine operation with LHC beams, the 800 MHz RF system is used as Landau cavity in bunch shortening mode for increasing the synchrotron tune spread, which helps stabilizing the beam. Furthermore, controlled longitudinal emittance blow-up is performed during the ramp by injecting band-limited noise on the phase loop of the 200 MHz RF system [72] for stabilizing the beam at high energy.

Finally, beam loading will become an important limitation for high intensity LHC beams in the SPS. As mentioned above, longitudinal emittance blow-up is an effective measure for stabilizing the beam. Future LHC beams with higher intensity will require even more longitudinal emittance blow-up, which in turn requires larger voltage in the RF cavities for increasing the bucket size in order to avoid particle loss. However, less voltage will be seen by the beam for higher intensity due to the effect of beam loading and the limited available RF-power. This becomes critical in particular for extraction to the LHC. At flat top, the RF voltage is increased for reducing the bunch length before transferring the beam from the SPS 200 MHz bucket to the LHC 400 MHz bucket. Almost the maximum presently available RF voltage of $\hat{V}_{200} = 7.5$ MV is used for this manipulation for the nominal 25 ns beam in routine operation. Transferring beams with larger longitudinal emittance requires also more voltage at extraction. It is a peculiarity of the travelling wave cavities (TWC) installed in the SPS, that a rearrangement from the existing four cavities into six shorter cavities allows to reduce the effect of beam loading and at the same time reduce the beam coupling impedance [73]. However, in this case more total power is needed. An upgrade of the SPS RF-system including the rearrangement of the cavities and the construction of two additional power plants is in preparation [73], which will allow to have higher RF voltage available.

It should also be mentioned here, that in addition to the beam dynamics limitations discussed above, a series of other operational limitations are presently encountered in the SPS. They are caused by heating and outgassing of some of the kickers, sparking on the electrostatic septum ZS used for extraction to the North Area and outgassing of the internal dump TIDVG when disposing high intensity beams. Hardware modifications for eliminating or mitigating these limitations are part of the LIU project [74].

⁷Some upgrade scenarios of the LHC expect 50 ns bunch trains with single bunch intensities of more than 3.5×10^{11} p/b extracted from the SPS.

4.2. Motivation for lower transition energy in the SPS

One of the fundamental limitations for the achievable single bunch intensity in the SPS is imposed by the TMC instability in the vertical plane at injection. The main motivation for reducing the transition energy in the SPS comes from the fact that the intensity threshold $N_{\text{thr}}^{\text{TMC}}$ for the TMCI scales as (cf. [75] and Appendix C.1)

$$N_{\text{thr}}^{\text{TMC}} \propto \frac{|\eta|\varepsilon_l}{\beta_y}, \quad (4.1)$$

where ε_l is the longitudinal emittance, β_y is the vertical beta function at the location of the impedance source and η is the slip factor. In principle the threshold can be increased by injecting beams with larger longitudinal emittance. This option however is not so interesting, since the beam transmission between PS and SPS is degrading for larger longitudinal emittances unless additional cavities in the PS are used for optimizing the bunch rotation at extraction [76]. On the other hand, the threshold for the TMCI can be raised by increasing the slip factor η , which is defined as (cf. Section 2.1 and Appendix B.2)

$$\eta = \frac{1}{\gamma_t^2} - \frac{1}{\gamma_0^2}. \quad (4.2)$$

The slip factor is a function of the beam energy and the transition energy. In the nominal SPS optics for LHC-type proton beams the gamma at transition is $\gamma_t = 22.8$ and at injection (26 GeV/c) the relativistic gamma is $\gamma_0 = 27.7$, i.e. the beam is injected above transition. It follows directly that η increases with energy and the TMCI is most critical at injection energy. Furthermore, the slip factor can be increased throughout the acceleration cycle by reducing γ_t . Figure 4.1 shows η normalized to the value in the nominal SPS optics as function of γ_t , i.e. $\eta/\eta_{\gamma_t=22.8}$, for the case of injection (26 GeV/c) and for the case of extraction (450 GeV/c). By definition, the ratio $\eta/\eta_{\gamma_t=22.8}$ becomes equal to 1 at $\gamma_t = 22.8$, the value of the nominal optics. It should be emphasized that the largest relative gain is achieved at injection, which is the most critical part of the cycle with respect to the TMCI, as mentioned before. As the injection energy is only slightly larger than the transition energy in the nominal optics, a moderate reduction of γ_t by a few units translates into a large increase of the slip factor and thus a significant increase of the instability threshold can be expected. A possible way of overcoming the TMCI at injection is therefore to lower γ_t .

It should be mentioned here that the single bunch electron cloud instability can be described as TMC-like instability in simplified analytical models [77, 78]. In this case, a similar scaling law for the instability threshold can be derived for the electron cloud instability. Reducing the transition energy of the SPS will thus increase the instability thresholds for the transverse mode coupling instability and for the single bunch electron cloud instability. Furthermore, the threshold for longitudinal coupled bunch instabilities and the threshold for the loss of Landau damping scale with the slip

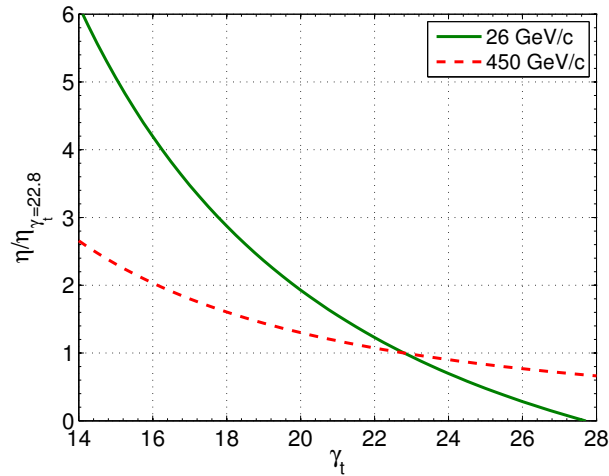


Figure 4.1: Slip factor η relative to the slip factor of the nominal optics ($\gamma_t = 22.8$) as a function of γ_t . At injection $\gamma_0 = 27.7$ (26 GeV/c), at extraction $\gamma_0 = 480$ (450 GeV/c).

factor η and will also be raised proportionally.

The possibility of changing the transition energy of the SPS as possible cure for single bunch instabilities was studied experimentally in 1998 already [79]. At that time the most critical intensity limitation for single bunches in the SPS was imposed by a microwave instability caused by the impedance of the pumping ports, which were shielded later in the course of the impedance reduction campaign during the shutdown 2000/2001 [80].

4.3. Nominal and low transition energy optics of the SPS

4.3.1. Reducing transition energy in the SPS

The SPS has a super-symmetry of six with a regular FODO lattice built of 108 cells, 16 per arc and 2 per long straight section (LSS). In the nominal SPS optics, the phase advance per cell is close to $\pi/2$ in both planes, resulting in betatron tunes Q_x , Q_y , between 26 and 27. Recalling that the transition energy is defined through the integral of the dispersion function D_x in regions with finite bending radius ρ , i.e. in the bending magnets,

$$\frac{1}{\gamma_t^2} = \frac{1}{C} \oint \frac{D_x(s)}{\rho(s)} ds, \quad (4.3)$$

a reduction of γ_t is achieved by increasing D_x in the dipoles. Past proposals for reducing the transition energy in the SPS considered the installation of additional quadrupoles in the arcs for inducing dispersion waves [82]. Separating these quadrupoles by a phase advance of odd multiples of π allows to change the transition energy with minimum

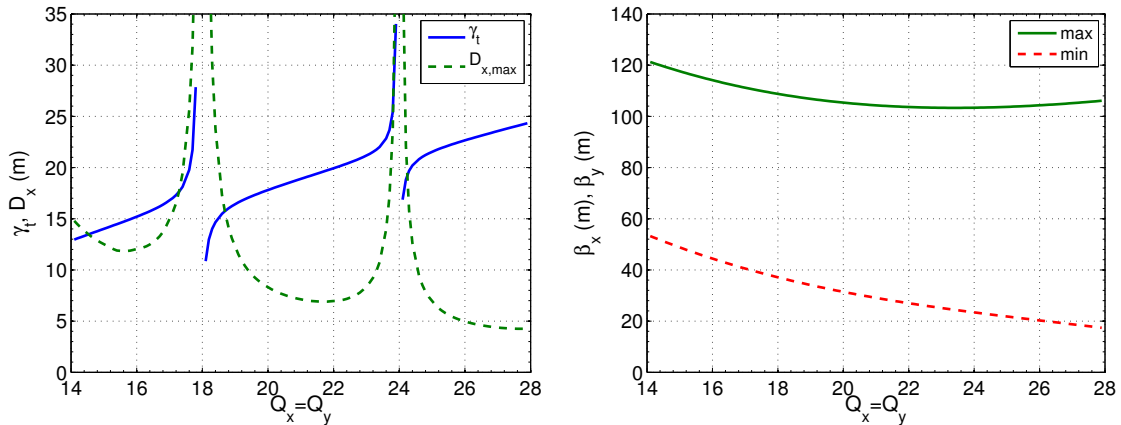


Figure 4.2: Transition energy and maximum dispersion around the ring (left) and the maximum and minimum values of the beta functions (right) as function of the tunes, where Q_y is set equal to Q_x . Similar plots can be found in [81].

optics distortion. Note that this concept is also used for the γ_t -jump scheme in the PS [23].

In 2010, a series of alternative solutions for modifying γ_t of the SPS were investigated [83]. One of them is based on inverting the polarity of selected quadrupoles in the arcs such that two consecutive FODO cells are changed into a FODODOFO structure. In another solution, the central quadrupole of two consecutive FODO cells is powered individually in order to excite dispersion waves. However, both schemes require new or additional power supplies and thus hardware modification for lowering γ_t , since the present SPS lattice has only two quadrupole families controlling the focusing and the defocusing quadrupoles, respectively. The most elegant and promising approach is based on the fact that in a regular FODO lattice, the transition energy scales with the horizontal tune such that $\gamma_t \propto Q_x$. This relation was already derived in Section 2.2, assuming that the lattice is built entirely of FODO cells containing bending magnets (i.e. no straight sections). In the case of the SPS the transition energy can be approximated as $\gamma_t \approx \frac{96}{108} Q_x$, since the long straight sections do not contribute and the number of FODO cells in the arc is 96 compared to the 108 FODO cells in total. In other words, the arcs represent 8/9 of the SPS circumference. Figure 4.2 shows the transition energy and the maximum dispersion around the ring together with the maximum and minimum values of the beta functions as calculated by MADX. For Q_x close to multiples of the machine super period, resonant dispersion waves with large amplitude are excited around the ring resulting in the asymptotic behavior of γ_t . This asymptotic behaviour was exploited during the machine study session for lowering γ_t in the SPS [84], which aimed at increasing the threshold of the microwave instability in 1998 [79]. The SPS was operated in this experiment with tunes close to 24 and $\gamma_t = 19.59$. However, it is difficult to obtain stable machine conditions close to the

Table 4.1: Optics parameters in the SPS

SPS optics	Nominal (Q26)	Low γ_t (Q20)
Horizontal tune, Q_x	26.13	20.13
Vertical tune, Q_y	26.18	20.18
Natural chromaticity, Q'_x/Q'_y	-32.6/-32.63	-22.7/-22.7
Specific natural chromaticity, ξ_x/ξ_y	-1.25/-1.25	-1.13/-1.13
Maximum beta functions, $\hat{\beta}_x \approx \hat{\beta}_y$ (m)	105	105
Minimum beta functions, $\check{\beta}_x \approx \check{\beta}_y$ (m)	20	30
Maximum dispersion, \hat{D}_x (m)	4.5	8
Transition energy, γ_t	22.8	18
Slip factor η at 26 GeV/c	0.62e-3	1.8e-3
Slip factor η at 450 GeV/c	1.9e-3	3.1e-3
Phase advance per cell, $\mu_x \approx \mu_y$	$4 \cdot 2\pi/16$	$3 \cdot 2\pi/16$

“resonant” tunes and this is not acceptable for regular machine operation. Sufficiently far away from multiples of the superperiod, γ_t scales indeed linearly with Q_x and can thus be lowered by simply reducing the horizontal phase advance around the machine. It should be noted that dispersion suppression in the long straight sections can be achieved only for certain phase advances along the arcs. In particular, the arcs become achromatic if the phase advance along the 16 FODO cells is close to multiples of 2π and thus the transfer matrix of the arc becomes the unit matrix (I-transformer). Then, resonant dispersion waves are excited in the arcs and dispersion is suppressed in the long straight sections. This condition is roughly satisfied for the nominal working point of the SPS, where the phase advance per arc is $\mu_x \approx 4 \cdot 2\pi$.

The first possible achromatic solution with lower γ_t is obtained by reducing the phase advance per arc to $\mu_x \approx 3 \cdot 2\pi$, corresponding to a phase advance per cell of about $3/8\pi$. Keeping similar phase advances in both planes⁸, the resulting machine tunes are about $Q_x, Q_y \approx 20$. This optics will therefore be referred to as the “Q20” optics in the following. The nominal SPS optics for LHC filling on the other hand will be called “Q26”, since $Q_x, Q_y \approx 26$. A summary of the corresponding optics parameters is given in Table 4.1. A comparison of the optics functions for the two cases⁹ is shown in Fig. 4.3. It is interesting to note that the maximum beta function values are about the same in both optics, while the minimum beta function values are increased from about 20 m to around 30 m in the Q20 optics due to the weaker focusing. It should be emphasized that the fractional tunes of the Q20 optics have been chosen to be identical with the nominal optics in order to allow for direct comparison in experimental studies. The

⁸It is not a necessary condition to have similar phase advances in both planes. Optics variants with different integer tunes in the horizontal and vertical plane will be discussed in Section 4.8.2

⁹According to the SPS design report [85], a few dipoles were removed from the regular FODO lattice in the arcs close to the straight sections in order to reserve space for extraction kickers. The dispersion suppression in the straight sections is not following a “missing dipole” scheme.

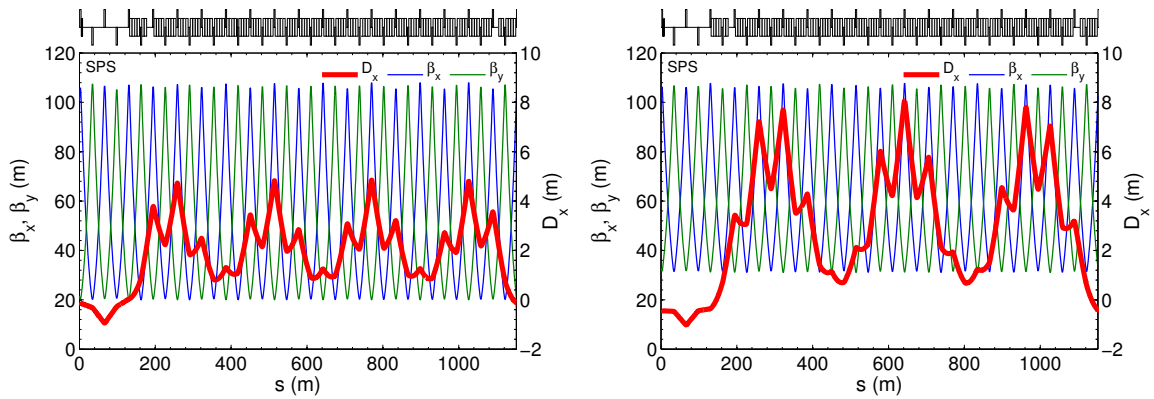


Figure 4.3: Nominal optics (Q26) of the SPS for 1/6 of the circumference (left). The phase advance per FODO cell is close to $\pi/2$, resulting in a total phase advance of $\mu_x \approx 4 \cdot 2\pi$ per arc and thus 4 big oscillations of the dispersion function. New optics (Q20) with low γ_t (right). The phase advance per cell is reduced to $3/8\pi$, resulting in a phase advance of $3 \cdot 2\pi$ per arc with 3 big dispersion oscillations in the arcs and dispersion suppression in the straight sections (corresponding to $s < 120$ m in the plot).

resulting residual dispersion in the long straight sections is then comparable between the two optics. However, due to the reduced phase advance, the dispersion function follows 3 instead of 4 big oscillations along the arc and peak values are increased from around 4.5 m to about 8 m in the Q20 optics. The larger dispersion function in the bending magnets results in the desired decrease of the transition energy from $\gamma_t = 22.8$ of the nominal optics to $\gamma_t = 18$ (cf. Fig. 4.2). This corresponds to a 2.85 times larger slip factor at injection energy and 1.6 times larger slip factor at extraction energy compared to the nominal optics (cf. Fig. 4.1).

In principle, the next possible solution for achromatic arcs and lower γ_t is found for horizontal tunes around 14, for which the phase advance per arc is close to $\mu_x \approx 2 \cdot 2\pi$. In this case, an even larger increase of the slip factor is obtained since the transition energy is reduced to $\gamma_t < 15$. A similar optics configuration was already used during machine studies in 1978 [81], before the transfer line TT10 was upgraded for the higher injection energy of 26 GeV and the SPS was turned into the Sp \bar{p} S proton antiproton collider. In order to avoid transition crossing with high intensity single bunches as required for the Sp \bar{p} S, the optics of the SPS was tuned to the working point $(Q_x, Q_y) = (15.38, 15.42)$ for dropping the transition energy below the former injection energy of 15.8 GeV. While in the nominal optics the intensity of single bunch proton beams was limited to 3.5×10^{10} p/b due to losses and instabilities during transition crossing, the design intensity of the Sp \bar{p} S project of 1×10^{11} p/b was achieved in the experiments using the lower γ_t . However, the bucket area reduction caused by the larger slip factor was unfavorable for testing the expected high energy beam conditions during proton antiproton collisions. The implications of reducing the transition energy of the SPS are discussed in the following.

4.3.2. Implications of using lower transition energy in the SPS

RF voltage

As discussed above, the transition energy of the SPS can be reduced by changing the working point of the machine. However, the available RF voltage V may impose some limitation on the achievable increase of the slip factor. In particular, the longitudinal bucket area \mathcal{B} scales as (cf. Appendix B.5)

$$\mathcal{B} \propto \sqrt{\frac{E_0 e V}{\omega_0^2 |\eta|}} \tilde{\alpha}_{\mathcal{B}}(\varphi_s), \quad (4.4)$$

where E_0 and ω_0 are the energy and the angular revolution frequency of the synchronous particle, respectively, and $\tilde{\alpha}_{\mathcal{B}}(\varphi_s)$ is a factor accounting for the bucket area reduction when the beam is accelerated and depends therefore on the synchronous phase φ_s . In case of a stationary bucket, i.e. $\tilde{\alpha}_{\mathcal{B}} = 1$, an increase of the slip factor requires a proportional increase of the voltage in the RF cavities $V \propto \eta$ for keeping the bucket area constant. The scaling is more complicated during acceleration, since a given acceleration rate \dot{E}_0 requires (cf. Appendix B.1)

$$V = \frac{2\pi}{\omega_0} \frac{\dot{E}_0}{\sin \varphi_s}. \quad (4.5)$$

Inserting this expression for the RF voltage V into Eq. (4.4) shows that the synchronous phase angle φ_s yielding a certain bucket area is a function of the slip factor η . The corresponding values for φ_s and V can be calculated numerically. Figure 4.4 shows the calculated voltage for the SPS 200 MHz cavities V_{200} along the ramp of the LHC filling cycle for a constant bucket area of $\mathcal{B} = 0.6$ eVs, which is the typical operational setting for the early part of the ramp. The two voltage curves correspond to the nominal optics with $\gamma_t = 22.8$ and the Q20 optics, where $\gamma_t = 18$. Furthermore, the ratio between the slip factor in the Q20 optics $\eta_{\gamma_t=18}$ to the slip factor in the nominal optics $\eta_{\gamma_t=22.8}$ is shown as a function of the beam energy. At flat bottom, the slip factor ratio has its maximum $\eta_{\gamma_t=18}/\eta_{\gamma_t=22.8} \approx 2.85$ and the RF voltage scales proportionally. During the ramp the ratio between the RF voltages required for $\gamma_t = 18$ and for $\gamma_t = 22.8$ is decreasing because of two effects. Firstly, the ratio between the slip factors is quickly dropping towards the minimum value of $\eta_{\gamma_t=18}/\eta_{\gamma_t=22.8} \approx 1.6$ for increasing energy. Secondly, a given bucket area at a given acceleration rate requires a smaller synchronous phase φ_s for a larger slip factor. Thus, the scaling of the voltage for keeping the bucket area constant is smaller than the mere ratio of the slip factors. This effect becomes dominant for higher acceleration rates like in the second part of the ramp.

Considering that the presently available¹⁰ voltage in the 200 MHz RF system is limited to $V_{200} \leq 7.5$ MV, a transition energy below $\gamma_t = 16$ is out of reach when

¹⁰Higher RF voltage will be available after the upgrade of the RF system [73].

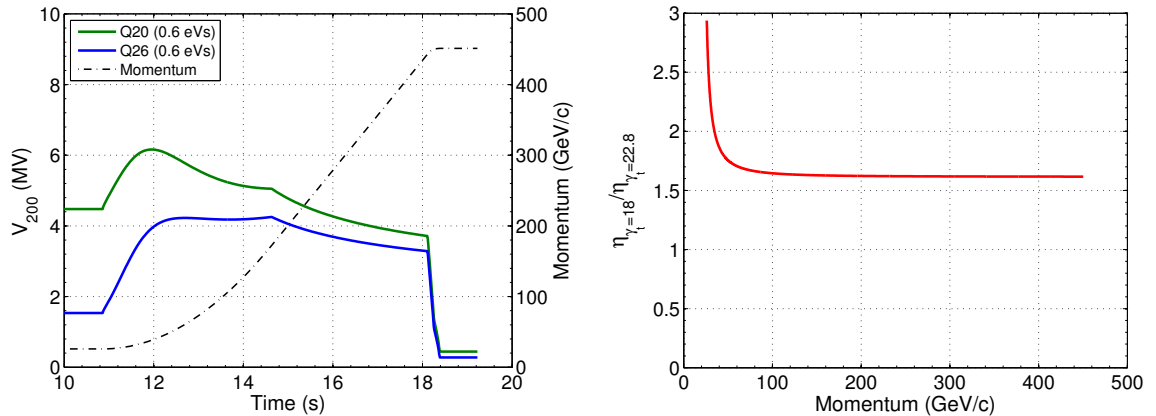


Figure 4.4: Voltage programs for the 200 MHz SPS RF system along the LHC filling cycle for a constant bucket area of $\mathcal{B} = 0.6$ eVs, calculated for the nominal optics ($\gamma_t = 22.8$) and for the Q20 optics ($\gamma_t = 18$), together with the beam momentum (left). The ratio of the corresponding slip factors is shown as function of momentum (right).

keeping the same magnetic cycle. Furthermore, if a considerably larger bucket area is needed along the ramp in order to allow for controlled longitudinal emittance blow-up or larger injected emittance, the available RF voltage could eventually become a limitation. This limitation can be overcome by reducing the acceleration rate at the expense of longer cycles and thus increased LHC filling time. However, there is another important aspect related to the available RF voltage and the beam transfer from SPS to the LHC, as discussed below.

Basically the maximum available voltage is used in the nominal LHC filling cycle at flat top in order to shorten the bunches adiabatically for beam transfer to the LHC 400 MHz RF system. Thus, for a given longitudinal emittance ε_l the bunches will be longer at extraction in the low γ_t optics due to the limited RF voltage, since the bunch length τ scales like (cf. Appendix B.4)

$$\tau \propto (\varepsilon_l^2 \eta / V)^{1/4}. \quad (4.6)$$

However, it might not be necessary to have the same longitudinal emittance at extraction: as mentioned already, controlled longitudinal emittance blow-up is performed during the second half of the ramp in order to cure the longitudinal instability observed during the ramp of the LHC filling cycle. The intensity threshold for loss of Landau damping $N_{\text{thr}}^{\text{LLD}}$ (for a stationary bucket) due to the reactive part of a broadband impedance scales like [86]

$$N_{\text{thr}}^{\text{LLD}} \propto \varepsilon_l^2 |\eta| \tau. \quad (4.7)$$

Assuming for the moment a given bunch length τ , the instability threshold is deter-

mined by the product $\varepsilon_l^2 |\eta|$. A larger slip factor will thus provide the same stability for smaller longitudinal emittance as long as the product $\varepsilon_l^2 |\eta|$ is constant. According to Eq. (4.6) the bunch length depends exactly on the product $\varepsilon_l^2 |\eta|$ and will thus not depend on the transition energy. In particular, the smaller longitudinal emittance required for the same stability in the low γ_t optics should give the same bunch length as the larger emittance in the nominal optics [86]. In this sense a lower γ_t optics is not expected to impose additional constraints on the RF voltage for achieving certain bunch length at extraction from the SPS. However, the transient beam loading for high intensity LHC beams still requires an upgrade of the SPS RF system [73].

Injection dogleg

LHC proton beams are extracted from the PS at a momentum of 26 GeV/c and transferred through the TT2-TT10 line to the SPS injection channel in LSS1 [87]. In addition to the injection elements like septa, kickers and the injection beam dump, LSS1 accommodates the SPS internal beam dump system. Closed orbit bumps of about 7 mm are created in both transverse planes in order to increase the physical aperture during the beam disposal. This static chicane in the SPS injection region, also known as injection dogleg, is achieved by a voluntary displacement of the three quadrupole magnets QDA.11710, QFA.11810 and QDA.11910 by several millimeters, as summarized in Table 4.2. Figure 4.5 shows the injection dogleg and the resulting closed orbit around

Table 4.2: Quadrupole displacement in LSS1.

	QDA.11710	QFA.11810	QDA.10119	
Δx	-4.80	-2.97	-4.80	mm
Δy	-5.00	-16.49	-5.00	mm

the machine for the Q26 optics. The small leakage of the orbit bump in the horizontal plane for the nominal working point of the Q26 optics $(Q_x, Q_y) = (26.13, 26.18)$ is due to the fact that the quadrupole displacements were originally calculated for tunes around 26.6, as used in the SPS for fixed target beams. The closed orbit $u_{co}(s)$ resulting from the three displaced quadrupoles can be calculated as (cf. Appendix A.5)

$$u_{co}(s) = \frac{\sqrt{\beta_u(s)}}{2 \sin \pi Q_u} \sum_{i=1}^3 \sqrt{\beta_u(s_i)} \cos [\pi Q_u + \psi_u(s) - \psi_u(s_i)] (K_u L)_i \Delta u_i, \quad (4.8)$$

where u stands for either x or y , $\psi_u(s)$ is the phase advance from the beginning of the lattice to position s , and $(K_u L)_i$ is the integrated normalized gradient of the quadrupole with index i which is displaced by Δu_i . Associating the quadrupoles QDA.11710, QFA.11810 and QDA.11910 with the indices $i = 1, 2, 3$, respectively, the conditions for

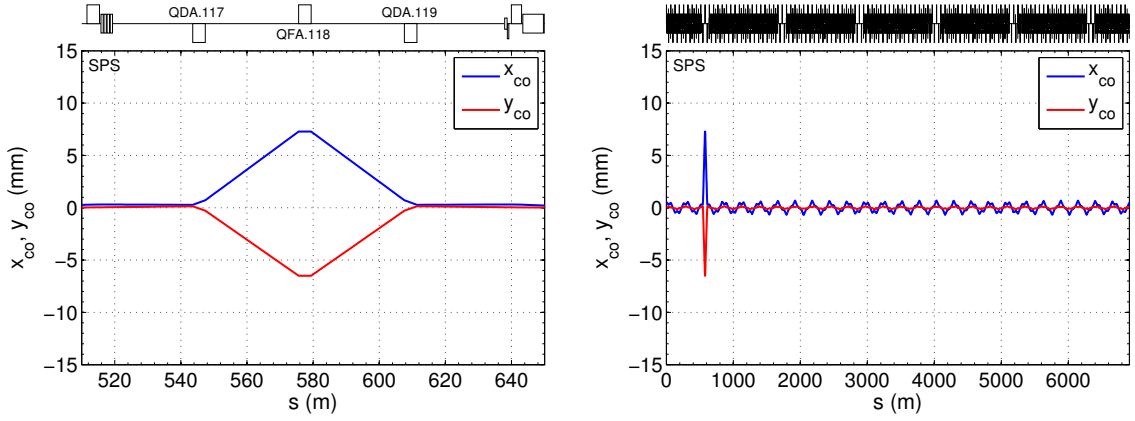


Figure 4.5: Injection dogleg created by the voluntary quadrupole displacement in LSS1 (left) and the resulting closed orbit (right) for the Q26 optics.

a zero closed orbit outside the chicane, $u_{co}(s_3) = 0$ and $u'_{co}(s_3) = 0$, can be written as

$$\begin{aligned} \sqrt{\beta_{u,1}} \cos(\pi Q_u - \psi_{u,13}) \Delta\theta_{u,1} + \sqrt{\beta_{u,2}} \cos(\pi Q_u - \psi_{u,23}) \Delta\theta_{u,2} + \sqrt{\beta_{u,3}} \cos(\pi Q_u) \Delta\theta_{u,3} &= 0, \\ \sqrt{\beta_{u,1}} \sin(\pi Q_u - \psi_{u,13}) \Delta\theta_{u,1} + \sqrt{\beta_{u,2}} \sin(\pi Q_u - \psi_{u,23}) \Delta\theta_{u,2} + \sqrt{\beta_{u,3}} \sin(\pi Q_u) \Delta\theta_{u,3} &= 0, \end{aligned} \quad (4.9)$$

where $\Delta\theta_{u,i} = (K_u L)_i \Delta u_i$ is the deflection angle generated by the displaced quadrupole with index i and $\psi_{u,jk} = \psi_u(s_k) - \psi_u(s_j)$ is the phase advance between locations s_j and s_k . These conditions are not satisfied in the Q20 optics, since the phase advance between the quadrupoles is significantly reduced, the beta functions are larger and the effective dipole kick is smaller due to the smaller quadrupole gradients. This non-closure of the injection dogleg results in a large closed orbit distortion around the ring in the Q20 optics, as shown in Fig. 4.6 (left).

The cleanest solution for restoring the closed orbit for both optics is obviously the realignment of the quadrupole magnets back on axis. However, this might reduce the available aperture for the high intensity fixed target beams during the beam dump and needs to be studied carefully [87]. Alternatively, the closed orbit can be restored using existing orbit correctors close to the displaced quadrupoles, adjusted to the required dipole kicks for satisfying Eq. (4.9). Sufficient closure of the orbit bump in the Q20 optics can be achieved at low energy, where the SPS orbit correctors MDV.11705, MDHD.11832 and MDVA.11904 adjacent to the displaced quadrupoles can provide sufficient dipole field strength. At top energy, the orbit in the SPS is usually not corrected when extracting beam to the LHC in order to preserve the orbit in the transfer lines and thus ensure reproducibility of the collimator settings. In order to allow for a clean extraction from the Q20 optics and a proper matching of the LHC transfer lines, a correction of the injection dogleg might be required at top energy using predefined settings in only a few correctors. These correctors would then need

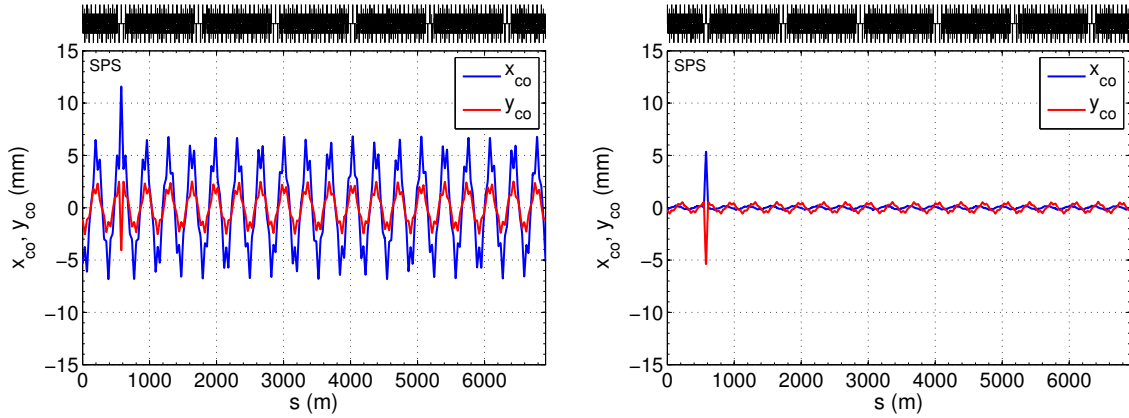


Figure 4.6: Closed orbit in the Q20 optics including the voluntary quadrupole displacements in LSS1 for the bare lattice (left) and after correction using existing SPS orbit correctors MDV.11705, MDHD.11832 and MDVA.11904 (right).

to be equipped with interlock switches to protect the LHC injection elements in case of failure.

Closing the injection chicane in the horizontal plane for the Q20 optics requires a deflection angle of about $\theta_x = -53 \mu\text{rad}$ close to QFA.11810. The adjacent wide aperture dipole corrector MDHD.11832 can provide the required field strength at extraction energy after minor hardware modification. The dipole corrector MDHD.11832 is an MDHC type magnet with 4 coils and total maximum integrated field of $B_y L = 0.11 \text{ Tm}$ at $4 \times 25 \text{ A}$ [88], which corresponds to $\hat{\theta}_x = 73 \mu\text{rad}$ at 450 GeV. The coils are presently connected in parallel and the corresponding power converter is limited to 20 A so that the maximum integrated field is restricted to $B_y L = 0.023 \text{ Tm}$ (or $\hat{\theta}_x = 261 \mu\text{rad}$ at 26 GeV and $\hat{\theta}_x = 15 \mu\text{rad}$ at 450 GeV). The required field strength can be achieved by recabling the 4 coils into series. In the vertical plane sufficient correction is already achieved by setting the two correctors MDV.11705 and MDVA.11904 to their maximum field strength, which corresponds to a deflection angle of $\hat{\theta}_y = -12.4 \mu\text{rad}$ at top energy. Figure 4.6 (right) shows the closed orbit in the Q20 optics with the three correctors MDV.11705, MDHD.11832 and MDVA.11904 set to the discussed values. The required field strength in these three correctors is readily available at injection energy. Until the coils of the horizontal corrector MDHD.11832 are reconfigured to form a series circuit, a similar correction can be achieved at high energy by using two additional horizontal correctors around the injection dogleg.

Available aperture

As discussed in the above sections, lowering the transition energy requires larger horizontal dispersion in the location of the bending magnets. The Q20 optics has a significantly increased dispersion function in the arcs, which reduces the available aperture.

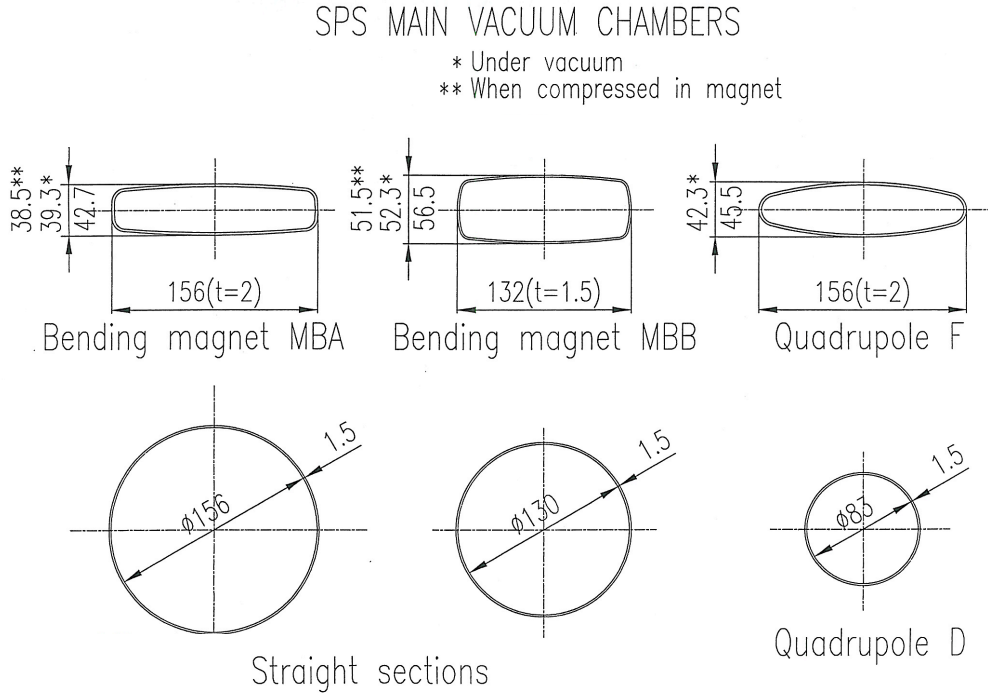


Figure 4.7: Basic types of SPS vacuum chambers. ©CERN.

Since the SPS was originally designed for injection below transition, the vacuum chambers provide large horizontal aperture in order to accommodate the increased horizontal beam size due to the larger momentum spread during transition crossing. Figure 4.7 shows the six basic types of vacuum chambers of the SPS.

The available aperture can be calculated using the formalism that was already introduced in section 3.2.2. Note that a similar formalism, but extended with the estimation of the beam halo and collimator settings, is used in aperture calculations for the LHC (cf. [1], Chapter 4.3). Here, the available aperture normalized to the rms beam size $\sigma_u = \sqrt{\beta_u(s)\varepsilon_u}$ is defined as

$$a_u(s) = \frac{A_u(s) - \left[u_{co}(s) + \Delta\hat{u}_{co}\sqrt{\beta_u(s)/\hat{\beta}_u} + (1+k_\beta) \left(|D_u(s)| + k_{D_u}\hat{D}_u\sqrt{\beta_u(s)/\hat{\beta}_u} \right) \hat{\delta} \right]}{(1+k_\beta)\sqrt{\beta_u(s)\varepsilon_u}}, \quad (4.10)$$

where $A_u(s)$ is the physical aperture defined by the vacuum chamber, $u_{co}(s)$ is the actual closed orbit, $\Delta\hat{u}_{co}$ is an assumed maximum closed orbit error and u stands for either x or y . The maximum beta function, maximum dispersion and maximum momentum spread are denoted as $\hat{\beta}_u$, \hat{D}_u and $\hat{\delta}$, respectively. The factor k_{D_u} accounts for parasitic dispersion and k_β is the beta-beat factor. Since the SPS has a regular lattice, the beta-beat is typically not bigger than 10% and the parasitic dispersion can

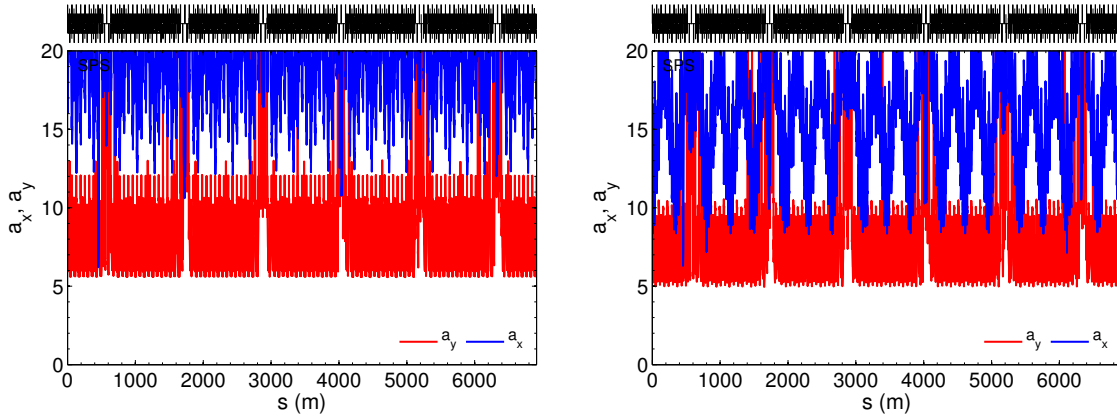


Figure 4.8: Available aperture for the LHC beam at injection into the SPS ($\hat{\delta} = 0.004$, $\varepsilon_{n,x} = \varepsilon_{n,y} = 3.5 \mu\text{m}$) for the Q26 nominal optics (left) and the Q20 low γ_t optics (right), assuming $k_\beta = 0.05$, $k_{D_u} = 0.1$ and $\Delta\hat{u}_{co} = 3 \text{ mm}$.

be estimated with a maximum of 10%. Thus, $k_\beta = 0.05$ and $k_{D_u} = 0.1$ will be used in the following. Operational experience shows that the maximum closed orbit error in the SPS can easily reach $\Delta\hat{u}_{co} = 3 \text{ mm}$ in both planes, even after correction. The nominal LHC beam has normalized transverse emittances of $\varepsilon_{n,x} = \varepsilon_{n,y} = 3.5 \mu\text{m}$ and a maximum momentum spread of $\hat{\delta} = 0.004$ at injection¹¹ into the SPS at 26 GeV/c. The available aperture in the Q20 optics compared to the Q26 optics for the above parameters is shown in Fig. 4.8, taking into account the injection dogleg and the apertures of machine elements as defined in the SPS model of the CERN optics repository [89]. The correction of the injection dogleg as shown in Fig. 4.6 (right) is used for the Q20 optics. Still, the large dispersion in the Q20 optics results in a clear reduction of the available aperture in the arcs compared to the nominal optics. However, the horizontal aperture restriction in both optics is due to the momentum scraper TIDP (at $s = 458 \text{ m}$) which is assumed to be set to 32 mm in the model (which corresponds to a half aperture of 41 mm). For this setting, the available aperture in the horizontal plane normalized to the rms beam size of the nominal LHC beam is about $a_x \approx 6$ in both optics. In the vertical plane, the available aperture in the arcs is restricted by the vacuum chambers of the MBA type main dipole magnets in the center of each FODO cell, so that $a_y \approx 5.5$ for the nominal LHC beam parameters in the Q26 optics and $a_y \approx 5$ in the Q20 optics. The small reduction of the available aperture in the Q20 optics compared to the Q26 optics is acceptable for regular operation with high intensity. For comparison, the available aperture for the operational high intensity fixed target beam is $a_y < 3$ in the nominal SPS optics, since it is injected at 14 GeV/c with $\varepsilon_{n,y} \approx 7.5 \mu\text{m}$.

¹¹The momentum spread or more precisely the bucket height $\hat{\delta}_B$ in the nominal optics might be higher than $\hat{\delta} = 0.004$ on the flat bottom, if the voltage of the main RF system is increased beyond $V_{200} = 2 \text{ MV}$. However, in the Q20 optics this is just about the limit that might be reached with the presently available maximum voltage and represents thus a conservative estimation.

Injection and extraction

Preservation of the transverse emittance through the injector chain is crucial for maximizing the LHC luminosity reach. Since the optical functions at the injection point of the SPS in LSS1 are slightly modified in the Q20 optics compared to their nominal values, the injection transfer line TT2-TT10 needs to be rematched. Otherwise, the injected beam will filament in the transverse phase space after injection, which results in undesired emittance growth. This emittance blow-up will be estimated in the following.

A betatron mismatch results in a growth of the emittance by a factor \mathcal{F}_u , which can be estimated as [90]

$$\mathcal{F}_u = \frac{1}{2} \left[\frac{\beta_{u,0}}{\beta_{u,m}} + \left(\alpha_{u,0} \sqrt{\frac{\beta_{u,m}}{\beta_{u,0}}} - \alpha_{u,m} \sqrt{\frac{\beta_{u,0}}{\beta_{u,m}}} \right)^2 + \frac{\beta_{u,m}}{\beta_{u,0}} \right], \quad (4.11)$$

where $\alpha_{u,0}$ and $\beta_{u,0}$ are the reference or target Twiss parameters, $\alpha_{u,m}$ and $\beta_{u,m}$ are the mismatched Twiss parameters and u stands for either x or y . A mismatch of the dispersion function results in an emittance blow-up by a factor \mathcal{J}_u , which is obtained as [91]

$$\mathcal{J}_u = 1 + \frac{(\Delta D_{n,u})^2 + (\Delta D'_{n,u})^2}{2\varepsilon_u} \delta_{\text{rms}}^2, \quad (4.12)$$

where $\Delta D_{n,u}$ is the deviation of the mismatched normalized dispersion from the target normalized dispersion, $\Delta D'_{n,u}$ is similarly the deviation of the normalized dispersion derivative and u stands for x or y . The definition of the normalized dispersion phase-space coordinates $D_{n,u}$ and $D'_{n,u}$ can be found in Appendix A.4. Note that the emittance blow-up resulting from dispersion mismatch depends on the rms physical emittance ε_u and the rms momentum spread δ_{rms} , such that it becomes large for small beams with large momentum spread. This is typically the case for LHC beams.

The transverse physical emittance after filamentation denoted as ε'_u is then given by the product of the injected emittance and the blow-up factors, i.e.

$$\varepsilon'_u = \mathcal{F}_u \mathcal{J}_u \varepsilon_u. \quad (4.13)$$

For the following analysis, it is assumed that the SPS is operated with the Q20 optics, while the injection transfer line TT2-TT10 remains with the standard settings “perfectly” matched to the Q26 optics. Thus, the reference Twiss parameters at the first SPS quadrupole seen by the injected beam (QDA.11910) are identified with the corresponding values of the Q20 optics. The mismatched Twiss parameters are given by the corresponding values in the Q26 optics. Table 4.3 shows the relevant optics parameters as calculated by MADX. The blow-up factors for the betatron mismatch \mathcal{F}_u can be calculated without any assumption about the phase space distribution and

Table 4.3: Twiss parameters at SPS injection

	Q26 optics	Q20 optics
α_x/α_y	0.569/-2.296	0.646/-1.855
β_x/β_y (m)	21.4/101.9	32.8/103.1
D'_x/D'_y	0.023/ 0.000	0.020/ -0.002
D_x/D_y (m)	-0.34/ 0.01	-0.51/-0.12

are found as $\mathcal{F}_x \approx \mathcal{F}_y \approx 1.11$. In comparison to that, the emittance blow-up due to the mismatch of the dispersion functions can be estimated as $\mathcal{J}_x \approx \mathcal{J}_y < 1.01$, when considering an rms momentum spread of $\delta_{\text{rms}} = 0.002$ and a transverse normalized emittance of $\varepsilon_n = 1.5 \mu\text{m}$ in both planes. Thus, the total emittance blow-up can be estimated roughly as 12% in both planes for the typical LHC beam parameters during the 2012 run as considered here. Given the tight budget for emittance growth along the LHC injector chain, rematching of the TT2-TT10 transfer line is recommended before using the Q20 optics in routine operation for LHC filling.

Another source of emittance blow-up is caused by injection errors, i.e. steering errors of the injected beam. However, these injection errors are usually corrected in operation using steering magnets in the last part of the TT10 transfer line.

It is important to note that the beam is injected off-center through the defocusing quadrupole QDA.11910 in the SPS before the injection kickers steer it onto the closed orbit. This allows minimizing the required strength of the injection kicker as the feed-down effect (cf. Appendix A.5) in the quadrupole provides an additional deflection for the injected beam. The feed-down effect is further enhanced by the voluntary displacement of this quadrupole for realizing the injection dogleg as discussed above. The deflection angle will be smaller in the Q20 optics, since the gradient in all main quadrupole magnets is reduced by about 30% to achieve the lower betatron tunes. Thus, the beam needs to be injected with a smaller horizontal angle with respect to the closed orbit in the SPS in order to recover the missing deflection from the quadrupole. However, this brings the beam closer to the edge of the injection septum, which is in general not favorable. A cleaner solution would be to increase the strength of the MKP injection kickers. The two options are discussed in the following.

The SPS injection channel was upgraded during the years 2000-2001 in preparation for the LHC era [87]. The bunch spacing of the LHC ion beams requires a rise time of the SPS injection kickers of less than 115 ns. This was achieved by reducing the length of the kickers and increasing their characteristic impedance [92]. The present layout of the SPS injection channel therefore consists of twelve short ‘S-type’ kickers, which are arranged in two tanks (MKPA.11931 and MKPA.11936) of five and one tank (MKPC.11952) of two magnets. They are used for the injection of LHC ion beams at 17.1 GeV/c/q. In addition to that, four unmodified ‘L-type’ kickers in a fourth tank (MKP.11955) are needed for the injection of LHC proton beams at 26 GeV/c. In

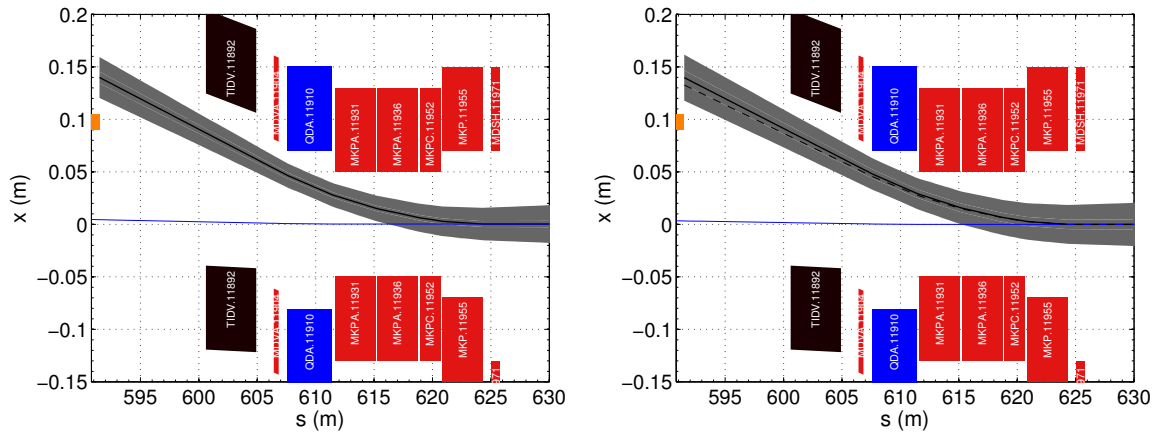


Figure 4.9: The SPS injection channel for the Q26 optics (left), where the colored boxes represent the various machine elements according to their respective physical aperture. The black line indicates the beam trajectory at injection and the grey area corresponds to the 5σ envelope of the LHC beam ($\varepsilon_n = 3.5\ \mu\text{m}$) including the dispersive part and orbit errors for the nominal MKP charging voltage of 48.4 kV. The blue line indicates the closed orbit of the circulating beam. The septum magnet is represented by the small orange box. For the Q20 optics (right), the dashed line represents the injection trajectory for the MKP charging voltage of 48.4 kV, while the solid black line and the grey area indicate the trajectory and the 5σ beam envelope for 51.0 kV.

this case, the nominal charging voltage of 48.4 kV in each of the (four) pulse forming networks (PFNs) will generate an integrated dipole field strength of 0.0329 Tm/magnet in the L-type kickers with a rise time smaller than 220 ns and 0.0174 Tm/magnet in the S-type kickers (cf. [62], Chapter 13).

Figure 4.9 shows the horizontal injection trajectory together with the 5σ envelope of the nominal LHC beam ($\varepsilon_n = 3.5\ \mu\text{m}$) starting from the exit of the septum magnet, taking into account the voluntary displacement of the quadrupoles in the injection region. In the Q26 optics the distance between the beam center and the edge of the septum magnet is about 35 mm with the nominal charging voltage setting of 48.4 kV for the MKP injection kickers. Using the same voltage setting with the Q20 optics requires injecting the beam with a smaller angle with respect to the closed orbit, since the defocusing quadrupole QDA.11910 provides less deflection angle due its reduced quadrupole strength. This brings the beam about 7 mm closer to the edge of the septum magnet, which might still be tolerable considering the small emittance of LHC beams. In this case the available aperture at the exit of the septum magnet is about $a_x \approx 6.5$ normalized to the LHC beam size with $\varepsilon_n = 3.5\ \mu\text{m}$, assuming a matched transfer line. On the other hand, restoring the nominal distance of the beam center from the edge of the septum magnet requires a field strength of the injection kickers equivalent to a charging voltage of 51.0 kV. The corresponding 5% increase of the voltage falls

within the capabilities of the present hardware and should be possible to achieve after kicker conditioning [93]. It should be mentioned that the above calculations for the Q20 optics are based on the closed orbit including the correction for the non-closure of the injection dogleg as shown in Fig. 4.6 (right).

The conventional fast extraction from the SPS Q20 optics to the LHC requires rematching of the two transfer lines TI2 and TI8 according to the corresponding change of the optical functions at the extraction points. In addition to that, the extraction bumps which bring the beam close to the extraction septa need to be readjusted to the reduced phase advance in the Q20 optics. Further details on the setup of the extraction with the Q20 optics can be found in Refs. [94, 95].

Beam dump

The SPS internal beam dump system (cf. [62], Chapter 20) is located in LSS1 close to the injection region. In case of emergency conditions or if deliberately activated, the kicker magnets MKDV and MKDH deflect the circulating beam on one of the two internal dump targets TIDH and TIDV, depending on the beam energy [96]. The two vertical kickers MKDV extract the beam onto the corresponding absorber block with a rise time of about $1\ \mu\text{s}$. The three horizontal kickers MKDH have a rise time of about one full SPS turn ($23\ \mu\text{s}$) and sweep the beam across the dump block. This allows increasing the beam dilution and therefore reducing the local energy deposition density and heat load. Figure 4.10 shows the corresponding measured kicker waveforms and the charging voltage for the two kicker systems as set by the SPS tracking system.

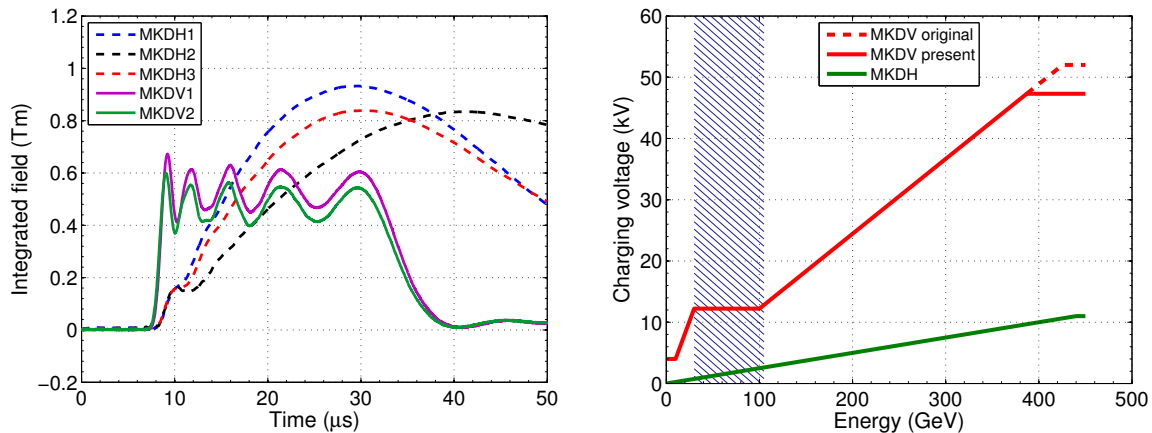


Figure 4.10: SPS beam dump kicker waveforms measured with a charging voltage of 52 kV on the MKDV and 11 kV on the MKDH magnets (left). The corresponding charging voltages as function of momentum as set by the SPS tracking system (right). The maximum charging voltage for the MKDV kickers is presently clipped at 47.3 kV in order to minimize the risk of sparking and voltage breakdown. The blue hatched area indicates the forbidden zone in which the beam cannot be dumped properly.

Since the dynamic operating range of the high power kicker switches is lower than the typical energy span between injection and extraction in the SPS, the beam dump system is separated into two energy regimes. Below 30 GeV the charging voltage for the MKDV kickers is increased linearly with the beam energy so that the beam is dumped onto the low energy absorber block TIDH. The “forbidden zone” between about 30–105 GeV does not allow for a clean extraction as the field strength of the MKDV kickers is kept constant and the deflection angle is decreasing progressively. Above 105 GeV the beam is dumped on the TIDV dump block further downstream. The TIDV itself was originally designed for the fixed target beams with beam energies up to 300 GeV. The higher peak intensity and higher density of LHC beams required a redesign of the dump block replacing the original Al_6Cu core by a graphite block (cf. [62], Chapter 20). The new beam dump is therefore named TIDVG. Further modifications of the dump core in view of the future LHC beam intensities are presently under study [97].

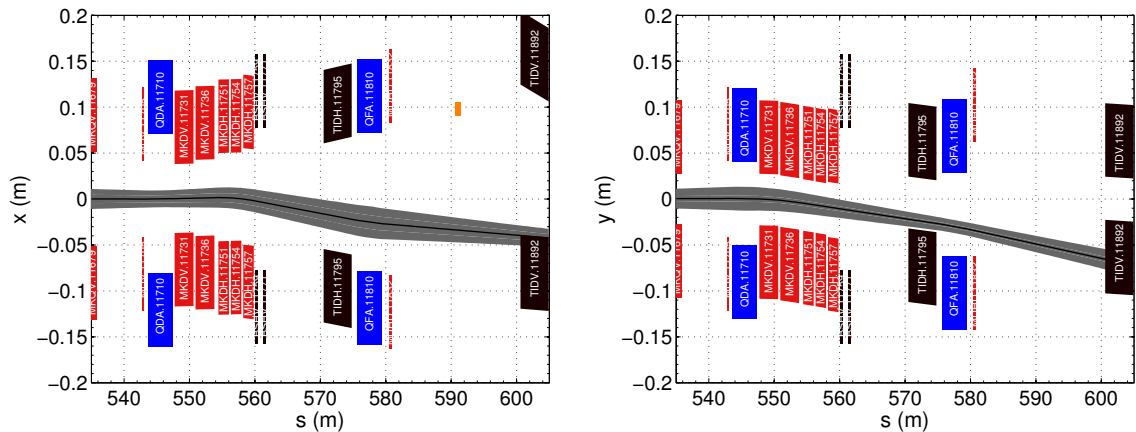


Figure 4.11: The 5σ envelope of the LHC beam with $\varepsilon_n = 3.5\ \mu\text{m}$ when it is dumped at 105 GeV in the Q20 optics. The calculated envelope includes the dispersive part and optics distortions as described in the text, together with the misalignment of the quadrupoles in LSS1 and the corresponding closed orbit correction.

Since the beta functions are in general larger in the Q20 optics, the available aperture in case of a beam dump on the TIDV is studied for the lowest possible beam energy. Figure 4.11 shows the 5σ envelope of the LHC beam with $\varepsilon_n = 3.5\ \mu\text{m}$ when it is dumped on the TIDV at 105 GeV in the Q20 optics. The beam envelope includes the dispersive part ($\hat{\delta} = 0.004$) with an additional 10% parasitic dispersion, 10% beta-beat, 3 mm maximum closed orbit uncertainty and the closed orbit including the injection dogleg and its correction as discussed above. The trajectories shown in the plots correspond to the maximum field strengths of the respective kicker waveforms. The colored boxes represent the relevant machine elements according to their respective physical aperture for the circulating beam. The beam is deflected vertically downwards onto the front face of the TIDV absorber block, which has a larger horizontal dimension

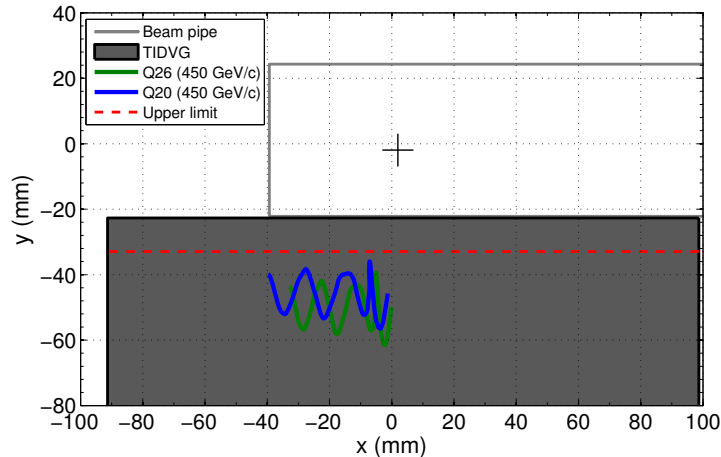


Figure 4.12: Simulated sweep along the front face of the TIDV in the Q26 and the Q20 optics, when the beam is dumped at 450 GeV with a charging voltage of 47.3 kV for the MKDV. The red dashed line indicates the upper limit for the beam position.

than the vacuum chamber for the circulating beam shown in the plot. Thus the available aperture is not critical in the horizontal plane. On the other hand the aperture is tighter in the vertical plane, in particular where the deflected beam has to pass through the vacuum chamber above the low energy beam dump TIDH. The vertical beam size around the focusing quadrupole QFA.11810 is increased in the Q20 optics as the vertical beta function is 50% larger compared to the nominal optics. Nevertheless, the available aperture is larger than the 5σ envelope of the nominal LHC beam at 105 GeV shown in the graph.

In the course of the SPS upgrade for operation beyond the original top energy of 300 GeV, a third PFN shared between the two MKDs was added to the individual PFNs for each magnet of the original layout. Thus, failure in one of the MKDVs directly affects the kick strength of the other MKDV magnet. Various failure scenarios have been studied in tracking simulations [98]. In order to reduce the risk of voltage breakdowns, the maximum operating voltage for the MKDVs has been limited to about 47 kV (cf. Fig. 4.10). Above 400 GeV the beam will thus receive less vertical deflection than originally designed and will be dumped closer to the top edge of the absorber block TIDVG. The situation is even more critical in the Q20 optics: since part of the total vertical deflection is obtained from the feed-down effect in the focusing quadrupole QFA.11810, the beam will be dumped even closer to the edge of the TIDVG due to the reduced quadrupole gradient. Figure 4.12 shows the position of the beam when it is dumped on the TIDV at 450 GeV with a charging voltage of 47.3 kV for the Q26 and the Q20 optics as obtained from MADX simulations using the kicker waveforms presented in Fig. 4.10. In both optics the beam center remains below the upper limit of 10 mm from the edge of the graphite block during the entire dump sweep, as required in order

to properly deposit the beam energy. It should be emphasized that the simulation for the Q20 optics includes the previously discussed correction of the closed orbit distortion caused by the injection dogleg. Without this correction, the closed orbit at the location of the TIDVG has a positive offset and thus the beam will be dumped about 3 mm higher up. Even in this case, the beam would be dumped properly on the absorber block. The horizontal plane is much less critical. Compared to the nominal optics, the beam receives less deflection back on axis from the focusing quadrupole QFA.11810 in the Q20 optics which results in a larger excursion of the beam along the front face of the TIDVG. In conclusion, the present design of the SPS internal beam dump can be used also for the Q20 optics without modification, when using the same maximum charging voltage of 47.3 kV for the MKDV kickers.

4.4. SPS nonlinear model

Since there are no hardware modifications required for implementing the Q20 optics in the SPS, the new optics could be tested directly in machine studies. One of the first subjects of a series of measurements was the chromatic behavior of the SPS in the new optics. Another important aspect concerns the resonance excitation in comparison with the Q26 optics.

4.4.1. Nonlinear chromaticity

The nonlinear chromaticity of the SPS was already studied in a series of measurements between 2000 and 2002 [99, 100]. In particular, the aim of these measurements was to establish a nonlinear optics model that would allow to reproduce the chromatic properties of the SPS. As discussed in more detail in Appendix A.6, the dependence of the betatron tunes on the momentum deviation $\delta \equiv \frac{\Delta p}{p_0}$ is given by

$$Q_{x,y}(\delta) = Q_{x,y} + Q'_{x,y} \delta + \frac{1}{2} Q''_{x,y} \delta^2 + \frac{1}{6} Q'''_{x,y} \delta^3 + \frac{1}{24} Q''''_{x,y} \delta^4 + \dots, \quad (4.14)$$

where $Q'_{x,y}$ is equal to the linear chromaticity, which is dominated by the quadrupoles (natural chromaticity) and sextupole components in dispersive regions, $Q''_{x,y}$ is dominated by octupole components in dispersive regions, and so on. Thus, assigning systematic multipole components to the main lattice magnets allows to establish an effective optics model of the SPS, which can reproduce the measured nonlinear chromaticity. Comparing the fit results obtained from measurements performed between 2000 and 2006 [101], it became clear that the beam conditions, the supercycle composition and optics errors have an important impact on the chromatic behavior of the machine.

A series of measurements were performed in 2012, directly comparing the Q26 with the Q20 optics in the same machine conditions, i.e. using the same supercycle composition (apart from the different optics in the cycle used for the measurements) and the same low intensity beam ($N \approx 4 \times 10^{10}$ p/b) at 26 GeV/c. Figure 4.13 shows

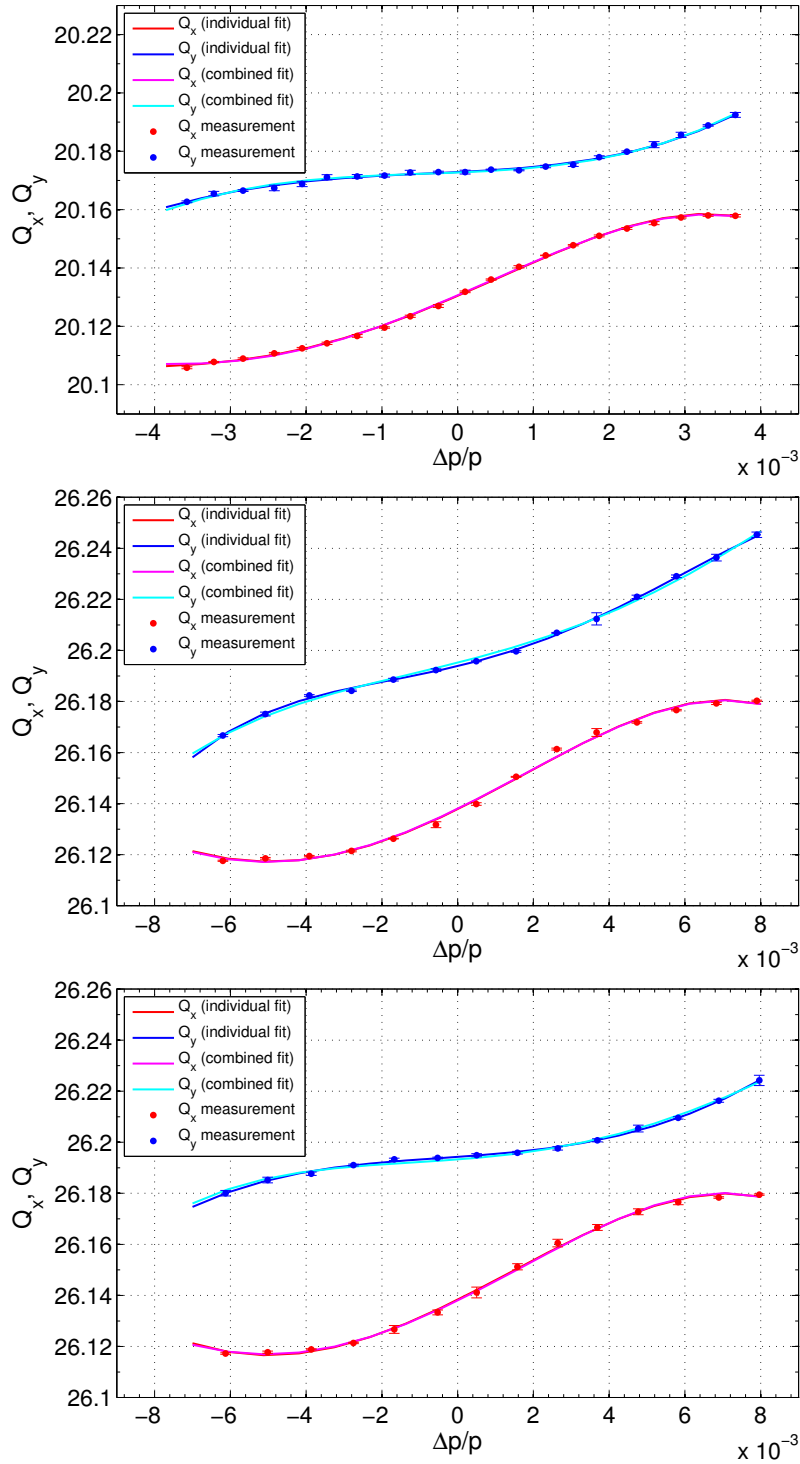


Figure 4.13: Measurement of the nonlinear chromaticity in the Q20 optics (top) and in the Q26 optics with high vertical chromaticity (middle) and with low vertical chromaticity (bottom). Note the different scale on the horizontal axis. The solid lines represent the MADX-PTC model, where multipole components were determined by individual fits of the corresponding measurement (red and blue) or by a combined fit of all three Q_x measurements (magenta and cyan).

Table 4.4: Multipole components for the SPS main magnets obtained by individual fits of the corresponding chromaticity measurements.

Order	Variable	Element	Q20	Q26 (high Q'_y)	Q26 (low Q'_y)	
$Q'_{x,y}$	{	ksfa (m^{-3})	LSFA	$+0.4883 \cdot 10^{-1}$	$+0.7123 \cdot 10^{-1}$	$+0.7026 \cdot 10^{-1}$
		ksfb (m^{-3})	LSFB	$+0.2892 \cdot 10^{-1}$	$+1.3682 \cdot 10^{-1}$	$+1.3513 \cdot 10^{-1}$
		ksda (m^{-3})	LSDA	$-0.2917 \cdot 10^{-1}$	$-1.4395 \cdot 10^{-1}$	$-1.3252 \cdot 10^{-1}$
		ksdb (m^{-3})	LSDB	$-0.4517 \cdot 10^{-1}$	$-1.5110 \cdot 10^{-1}$	$-1.4249 \cdot 10^{-1}$
$Q'_{x,y}$	{	$K_2^a L$ (m^{-2})	MBA	$+2.13 \cdot 10^{-3}$	$+1.12 \cdot 10^{-3}$	$+1.15 \cdot 10^{-3}$
		$K_2^b L$ (m^{-2})	MBB	$-3.23 \cdot 10^{-3}$	$-1.82 \cdot 10^{-3}$	$-1.86 \cdot 10^{-3}$
$Q''_{x,y}$	{	$K_3^f L$ (m^{-3})	QF	$+0.84 \cdot 10^{-1}$	$+0.87 \cdot 10^{-1}$	$+0.59 \cdot 10^{-1}$
		$K_3^d L$ (m^{-3})	QD	$-1.84 \cdot 10^{-1}$	$-3.88 \cdot 10^{-1}$	$-0.86 \cdot 10^{-1}$
$Q'''_{x,y}$	{	$K_4^a L$ (m^{-4})	MBA	$-5.94 \cdot 10^0$	$-5.26 \cdot 10^0$	$-5.93 \cdot 10^0$
		$K_4^b L$ (m^{-4})	MBB	$-3.54 \cdot 10^0$	$-7.92 \cdot 10^0$	$-5.88 \cdot 10^0$
$Q''''_{x,y}$	{	$K_5^f L$ (m^{-5})	QF	$-1.04 \cdot 10^3$	$-0.61 \cdot 10^3$	$-0.27 \cdot 10^3$
		$K_5^d L$ (m^{-5})	QD	$+0.89 \cdot 10^3$	$+18.4 \cdot 10^3$	$+2.74 \cdot 10^3$

the measurement results of the nonlinear chromaticity for the Q20 optics (top) and measurements for the Q26 optics with high vertical chromaticity setting (middle) and with low vertical chromaticity setting (bottom). The accessible range of $\Delta p/p$ without particle loss at aperture limitations is much smaller in the Q20 optics due to the larger dispersion in the arcs, i.e. the higher momentum compaction factor. Each data point is obtained as the average of at least 4 measurements and the error bars indicate their standard deviation. Table 4.4 shows the strength of the four chromatic sextupole families (ksfa, ksfb, ksda and ksdb) as set for the three measurements. The lattice octupoles were set to zero strength during all the measurements. The same table also describes the multipole components in the SPS MADX model that were used to reproduce the measured nonlinear chromaticity: sextupole components ($K_2^a L$, $K_2^b L$) and decapole components ($K_4^a L$, $K_4^b L$) are assigned to the two types of main dipoles (MBA, MBB), respectively. Note that these multipole components are the first two “allowed” errors of dipole magnets with respect to their symmetry. Furthermore, octupolar components ($K_3^f L$, $K_3^d L$) as well as dodecapole errors ($K_5^f L$, $K_5^d L$) are attributed to the main focusing and defocusing quadrupoles (QF, QD), respectively, even though the first allowed error of quadrupoles are dodecapole components. Similar to the method described in [101], a response matrix of the nonlinear chromaticity as function of the individual multipole components was generated using MADX-PTC. A least squares minimization based on the Singular Value Decomposition (SVD) algorithm (cf. [102], Chapter 2.6) is used for fitting the multipole components of the model in order to reproduce the measurements.

In a first step, the three data sets were treated individually. The resulting nonlinear chromaticities as reproduced with MADX-PTC are shown by the red (horizontal) and

blue (vertical) lines in Fig. 4.13 and the corresponding multipole errors are summarized in Table 4.4. Good agreement is found for the sextupole components $K_2^a L$ and $K_2^b L$ obtained for the two measurements with the Q26 optics. They are consistent with the values found from previous measurements of the SPS nonlinear chromaticity [100] and studies of dynamic effects on the chromaticity during the cycle [103]. Already in the design phase of the SPS [85] it was clear that saturation effects of the main dipoles and eddy currents induced in the vacuum chamber create a significant sextupole component in the machine and thus have a large impact on the linear chromaticity. Since these effects are purely caused by the dipole magnets, they should be the same in the two optics. However, it appears that even larger values for $K_2^a L$ and $K_2^b L$ are needed to reproduce the measured linear component of the chromaticity in the Q20 optics. Thus, in order to explain the difference between the two optics, there have to be additional sextupole components in the machine not taken into account yet. Possible sources could be sextupolar fields in the main quadrupoles (although not allowed with respect to their symmetry) or residual fields in the chromaticity sextupoles, as they are operated at a comparably low strength in the Q20 optics. Note that the natural chromaticity in the Q20 optics is smaller compared to the Q26 optics due to the reduced quadrupole gradients. In addition, the dispersion in the arcs is larger, which makes the sextupoles more effective for chromaticity correction (cf. Appendix A.6).

Regarding the fitted octupole components $K_3^f L$ and $K_3^d L$, reasonable agreement between the three measurement cases is obtained considering the fact that the second order chromaticities $\frac{1}{2}Q''_{x,y}$ are quite small in the SPS, which increases the fit uncertainty. The values obtained for the decapole components $K_4^a L$ and $K_4^b L$ are also in reasonable agreement between the three measurements, which is consistent with the fact that the main source could be errors in the dipole magnets that should be the same in both optics. In contrast to that, a quite large spread is observed for the dodecapole components $K_5^f L$ and $K_5^d L$. A possible explanation for this could be that the fits were not well constrained for these high order components. In fact, it was already ascertained in the past [100] that the fitted higher order multipole components are sensitive to the considered range of $\Delta p/p$. The difference between the measurement with the Q20 optics and the measurements with the Q26 optics could also be explained by a real difference of the dodecapole errors of the quadrupoles, as the quadrupole gradients are different in the two optics.

In order to establish a set of multipole components that can describe the measured nonlinear chromaticities in the two optics consistently, a combined SVD on all three measurement cases was performed. This allows to impose additional constraints on the fit parameters and thus to determine the higher order multipole components more accurately. It appears that values for the octupole components $K_3^f L$ and $K_3^d L$ and the decapole components $K_4^a L$ and $K_4^b L$ can be found that describe all three measurements sufficiently well. As the discrepancy in the sextupole components $K_2^a L$ and $K_2^b L$ between the two optics is too large, independent fit values are used for the Q20 optics, while a combined fit is performed only for the measurements with the Q26

Table 4.5: Multipole components obtained by a combined fit of three independent measurements in comparison with fit results of measurements performed between 2000 and 2002 [100].

Order	Variable	Element	Q20	Q26	Q26 [100]
$Q'_{x,y}$	$K_2^a L$ (m ⁻²)	MBA	$+2.12 \cdot 10^{-3}$	$+1.14 \cdot 10^{-3}$	$(+1.05 \pm 0.31) \cdot 10^{-3}$
	$K_2^b L$ (m ⁻²)	MBB	$-3.19 \cdot 10^{-3}$	$-1.88 \cdot 10^{-3}$	$(-2.11 \pm 0.93) \cdot 10^{-3}$
$Q''_{x,y}$	$K_3^f L$ (m ⁻³)	QF	$+0.75 \cdot 10^{-1}$		$(+0.55 \pm 0.55) \cdot 10^{-1}$
	$K_3^d L$ (m ⁻³)	QD	$-2.03 \cdot 10^{-1}$		$(-1.60 \pm 0.74) \cdot 10^{-1}$
$Q'''_{x,y}$	$K_4^a L$ (m ⁻⁴)	MBA	-5.74		-12.49 ± 5.75
	$K_4^b L$ (m ⁻⁴)	MBB	-5.10		-12.49 ± 5.75
$Q''''_{x,y}$	$K_5^f L$ (m ⁻⁵)	QF	$-0.87 \cdot 10^3$	$-0.48 \cdot 10^3$	-
	$K_5^d L$ (m ⁻⁵)	QD	$+2.04 \cdot 10^3$	$+7.75 \cdot 10^3$	-

optics¹². Similarly, individual fit parameters for the two optics cases are also used for the dodecapole errors $K_5^f L$ and $K_5^d L$, which is plausible as the quadrupoles have different strength in the two optics and they are suspected to represent the main error source. The results of a combined SVD on all three measurements are summarized in Table 4.5 and the corresponding nonlinear chromaticities as computed with MADX-PTC are shown in Fig. 4.13 (magenta and cyan lines for the horizontal and vertical plane, respectively). Note that the difference between the model established from individual fits and the model obtained with the combined SVD is very small (the curves basically overlap in most part of the $\Delta p/p$ range accessible by measurements). This confirms that the discrepancy in the higher order multipole components found by the individual SVDs is mostly related to insufficient constraints on the fit parameters. The results for the Q26 optics obtained with the combined SVD fit are within the error bars of the average of all measurements performed between 2000 and 2002 [100], as summarized in the right column of Table 4.5, apart from a slightly larger difference for the decapole components. Note that no dodecapole fit parameters were used in the past. It is thus concluded that the new fitting technique based on a combined SVD of different measurement sets presented here allows to impose additional constraints on the fit parameters and reduce their uncertainty. Future studies on the nonlinear optics model of the SPS should include detuning with amplitude, as described in [104].

4.4.2. Tune scans

Already during the first experimental studies with the Q20 optics it was observed that due to the smaller natural chromaticity and the considerably increased dispersion in the arcs, significantly smaller sextupole gradients are needed for chromaticity correction. However, the location of the sextupole magnets in the lattice is not optimal for the Q20

¹²Note that this approach represents one possibility of accounting for any difference in sextupole fields between the two optics, even though this difference should not come from the dipoles themselves.

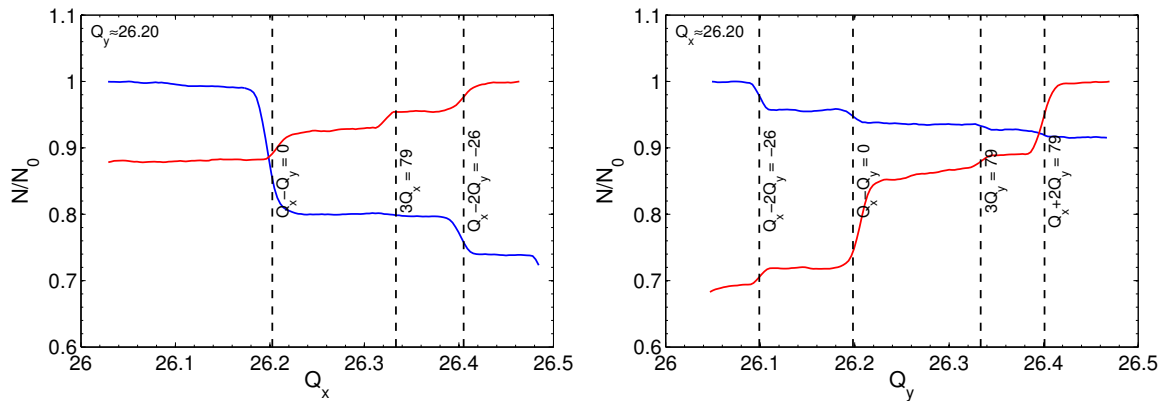


Figure 4.14: Intensity evolution during a dynamic scan of the working point in the SPS Q26 optics, for constant vertical tune at $Q_y = 26.20$ (left) and constant horizontal tune $Q_x = 26.20$ (right). The blue (red) curve corresponds to increasing (descending) tunes in the plane of the scans. The intensity is normalized to the value at the beginning of the corresponding measurement (each curve is recorded on a different supercycle). Important resonances are indicated by dashed lines.

optics due to the reduced phase advance along the arcs. In order to study a possible detrimental effect on the dynamic aperture, *dynamic* tune-scans were performed in both optics for a direct comparison of their resonance behavior.

Dynamic variation of the betatron tunes for measuring particle losses due to resonance crossing in the SPS was done already in 1976 [105]. Systematic studies on the dependence of beam size and beam lifetime on the working point were performed in LEP [106] in order to optimize the machine performance. Similar measurements were performed in the SPS [107] for optimizing the working point for LHC beams, and in SIS18 at GSI [108, 109] for identifying resonances. More recently, dynamic tune scans for different chromaticity settings were carried out in the PS [110] in order to study lattice resonances at the future injection energy of 2 GeV.

The measurement principle of the dynamic tune scan used here for comparing resonance behavior of the two optics in the SPS can be described as follows: the beam intensity is recorded during a slow variation of the betatron tunes over a period of about 3 s. Large particle oscillations will be induced when the working point is close to a resonance, which results in particle loss. The strength of the resonances can be inferred from the slope of the recorded losses as function of time. In order to enhance the observed losses and thus increase the sensitivity to resonances, the beam is injected deliberately with a large injection error in both planes for provoking transverse emittance blow-up due to filamentation. The measurements presented here were performed with a low intensity single bunch beam ($N \approx 4 \times 10^{10}$ p/b) on the injection plateau at 26 GeV/c. Figure 4.14 shows an example of the normalized intensity recorded during a dynamic scan of the working point in the Q26 optics, varying the horizontal tune and

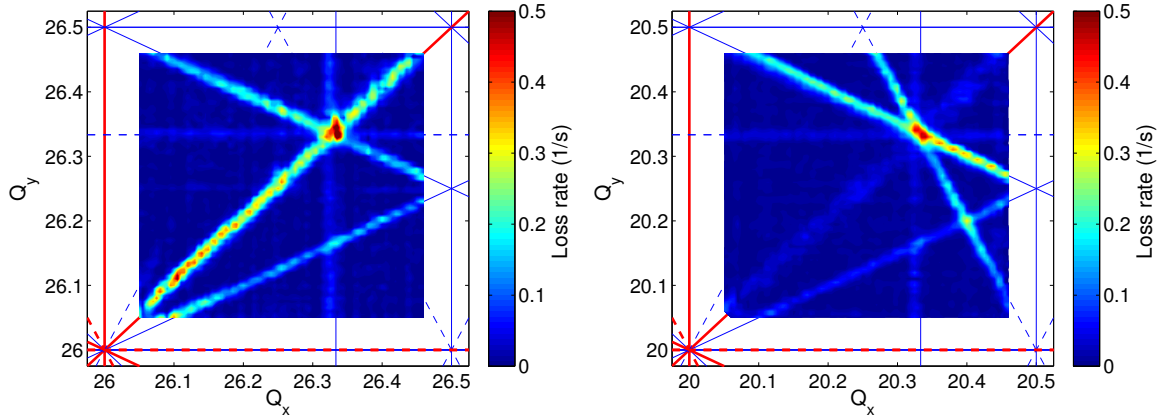


Figure 4.15: Experimental tune scans in the SPS with the nominal Q26 optics (left) and the low γ_t Q20 optics (right). The color-code indicates the loss rate $\frac{\Delta N(t)}{N(t)}/\Delta t$ during a dynamic scan of the fractional tunes, as obtained by averaging over 4 scan directions. The underlying tune diagram shows resonances up to third order, with systematic resonances in red and non-systematic in blue. Solid lines correspond to normal and dashed lines to skew resonances.

keeping the vertical tune at $Q_y \approx 26.20$ (left) and likewise for a variation of the vertical tune with a constant horizontal tune of $Q_x \approx 26.20$ (right). The blue curves indicate the scans with increasing tunes and the red curves correspond to descending tunes. Clear losses are observed around the coupling resonance ($Q_x \approx Q_y$) and the sextupole resonances as marked by the dashed lines. It is important to note that the amount of losses at the resonances depend on the direction in which they are crossed. This can be explained by the fact that the particle distribution is changed after crossing a resonance and thus the behavior close to another resonance can be different. It is therefore important to accumulate data in different scan directions (always starting with fresh beam) in order to obtain a representative picture of the global resonance structure.

A series of dynamic tune scans were performed for comparing the resonance behavior in the two optics. The typical machine settings for LHC beams in the SPS were chosen for the measurements, i.e. low (positive) chromaticity in both planes, zero current in the octupoles and the typical closed orbit of a few mm (rms) at the fractional tunes ($\nu_x, \nu_y = 0.13, 0.18$). In each measurement, either the horizontal or the vertical tune was systematically varied, while the tune in the other plane was kept constant and changed only in small steps in between supercycles. This procedure was repeated for all 4 scan directions. The resulting resonance diagrams for the two optics are shown in Fig. 4.15, where the color code indicates the loss rate, i.e. $\frac{\Delta N(t)}{N(t)}/\Delta t$, averaged over the four scan directions. Resonances up to third order can be clearly identified in both optics. In the case of Q26, it appears that the difference coupling resonance $Q_x - Q_y$ was creating higher particle losses compared to the Q20 optics. Note that the

linear coupling in the SPS can be corrected with the skew quadrupoles. The normal sextupole resonances $3Q_x$, $Q_x - 2Q_y$ and $Q_x + 2Q_y$ and the skew resonance at $3Q_y$ seem to be excited in both optics. A surprisingly strong third order skew resonance at $2Q_x + Q_y$ is observed in the Q20 optics. The source for this resonance is unknown. However, the area close to the fractional tunes usually used for the LHC beams in the SPS ($\nu_x, \nu_y = 0.13, 0.18$) is free of strong resonances in both optics. Thus, similarly as for the Q26 optics, no dynamic aperture limitations are expected for LHC beams in the Q20 optics. For completeness, it should be emphasized that the measured loss rates depend on the exact beam conditions and are therefore not directly comparable between the two optics.

4.5. High intensity single bunch beams

4.5.1. Transverse mode coupling instability

One of the main intensity limitations in the SPS comes from a fast single bunch instability at injection. As already mentioned before, this instability has been identified as vertical transverse mode coupling instability (TMCI) in the past [111, 67]. Early studies trying to characterize the instability concentrated on low longitudinal emittance beams [69]. In measurements performed in 2011 [70], the instability threshold for bunches with the nominal longitudinal emittance of $\varepsilon_l \approx 0.35$ eVs injected into the Q26 optics has been found to be at around $N_{\text{thr}}^{\text{TMC}} \approx 1.6 \times 10^{11}$ p/b.

As explained in Section 4.2, one of the main motivations for lowering the transition energy comes from the fact that the intensity threshold for the TMCI $N_{\text{thr}}^{\text{TMC}}$ scales with the slip factor $|\eta|$. In particular, for a broadband resonator impedance Z_y^{BB} with resonance frequency ω_r , the instability threshold is proportional to¹³ (cf. [75] and Appendix C.1)

$$N_{\text{thr}}^{\text{TMC}} \propto \frac{\varepsilon_l |\eta|}{\beta_y} \frac{\omega_r}{|Z_y^{\text{BB}}|} \left(1 + \frac{Q'_y \omega_0}{\eta \omega_r} \right), \quad (4.15)$$

where ω_0 is the angular revolution frequency, Q'_y is the vertical chromaticity and β_y corresponds to the beta function at the location of the impedance. In case the machine impedance is not created by a single source, the individual impedance contributions have to be weighted by the beta functions at their respective locations. Even if the beta functions are slightly higher in the Q20 optics compared to the Q26 optics, a significant increase of the TMCI threshold at injection energy is expected, since the phase slip factor η is 2.85 times higher. Note that in the SPS, the TMCI is most critical at injection, as proton beams are injected above transition and thus η is increasing with energy. Furthermore, the longitudinal beam distribution enters the SPS mismatched

¹³This scaling is valid for long bunches, i.e. $\tau > \pi/\omega_r$. This applies to the case of the SPS at injection, assuming that the impedance can be described by a broadband resonator with resonance frequency $\omega_r/2\pi = 1.3$ GHz corresponding to the beam pipe cutoff frequency and $\tau \approx 3$ ns after filamentation.

and thus the longitudinal emittance is smallest right at injection, i.e. before the blow-up due to filamentation which is typically of the order of 10-20%.

A measurement campaign in the beginning of 2013 has been devoted to studies of the TMC instability at SPS injection in both the Q26 and the Q20 optics. Both cycles were tuned to low but positive vertical chromaticity, i.e. $\xi_y \equiv Q'_y/Q_y \approx 0.05$, and zero current in the machine octupoles. In the Q20 optics the RF voltage for the 200 MHz system was chosen as $V_{200} = 4$ MV and the 800 MHz system was used in bunch shortening mode with a voltage of $V_{800} = 0.4$ MV. For direct comparison between the two optics, the RF voltages for the Q26 cycle were scaled proportionally to the slip factors in the two optics, i.e. $V_{200} = 1.4$ MV and $V_{800} = 0.14$ MV. In other words, the same bucket area was used in both optics. Note that in routine operation with LHC beams, the RF voltages in the Q26 optics at injection are usually set to $V_{200} = 2$ MV and $V_{800} = 0.2$ MV.

The stability at injection of single bunch proton beams with longitudinal emittances in the range between $\varepsilon_l \approx 0.2$ eVs and $\varepsilon_l \approx 0.45$ eVs (measured before bunch rotation in the PS) and intensities up to $N \approx 4.5 \times 10^{11}$ p/b was studied in the two optics. Depending on intensity, the transverse emittance of the injected beam was between $\varepsilon_n \approx 1 \mu\text{m}$ and $\varepsilon_n \approx 3.5 \mu\text{m}$. For each injection, the longitudinal beam profile in the PS before the bunch rotation was recorded in order to infer the longitudinal emittance of the extracted beam. In the SPS, the intensity along the cycle is obtained from the Beam Current Transformer (BCT). However, due to the 9 ms integration time, fast losses at injection cannot be assessed with the BCT measurement. Therefore, the longitudinal beam profile along the first 1000 turns in the SPS (≈ 23 ms) was acquired with the wall current monitor. The intensity evolution in the first part of the cycle can be obtained by integration of the longitudinal beam profile, after calibration to the BCT signal with low intensity beams. In addition to monitoring the coherent transverse beam motion using the SPS Qmeter and BBQ [112] systems, the vertical intra bunch motion was recorded with the SPS Head-Tail monitor [113].

Figure 4.16 shows examples of the beam intensity evolution along the flat bottom for the two SPS optics. Bunches with a longitudinal emittance of about $\varepsilon_l \approx 0.35$ eVs, i.e. the nominal longitudinal emittance for LHC beams at SPS injection, are stable in the Q20 optics for intensities up to about $N \approx 4.3 \times 10^{11}$ p/b. It should be noted that capture losses were increasing with intensity, reaching slightly more than 5% in some cases. These capture losses cannot be observed on the BCT, but can only be inferred from the longitudinal beam profile evolution. With the same longitudinal emittance of $\varepsilon_l \approx 0.35$ eVs, a fast instability in the vertical plane is observed for intensities of about $N \approx 4.5 \times 10^{11}$ p/b and above, which results in fast losses within the first 1000 turns after injection. In comparison to that, for the same longitudinal emittance the beam becomes unstable already for intensities above $N \approx 1.6 \times 10^{11}$ p/b in the Q26 optics. As expected, for a 20% smaller longitudinal emittance of about $\varepsilon_l \approx 0.28$ eVs the instability threshold is decreased by about 20% in both optics. It is interesting to note that for this longitudinal emittance a weak vertical instability is observed in the

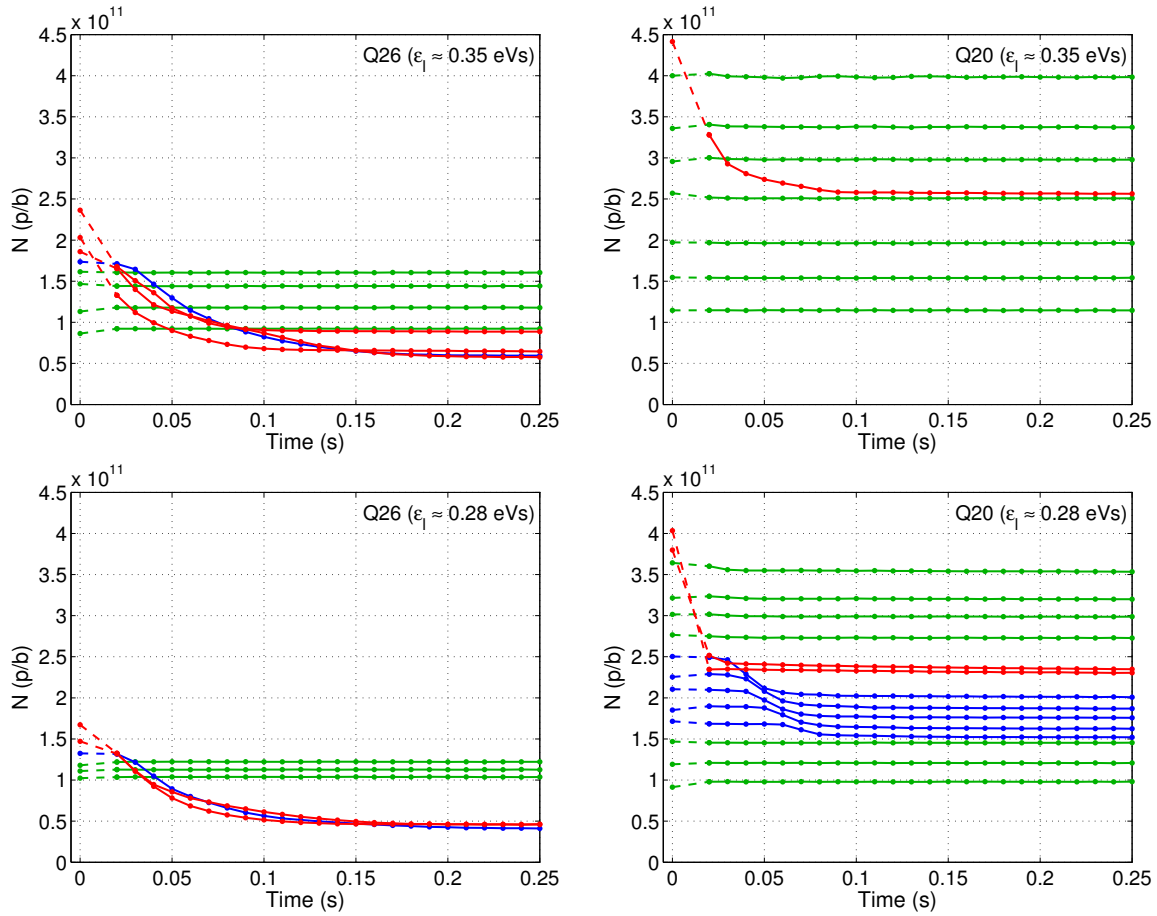


Figure 4.16: Intensity along the flat bottom for the Q26 optics (left) and for the Q20 optics (right), for longitudinal emittances of $\varepsilon_l \approx 0.35$ eVs (top) and $\varepsilon_l \approx 0.28$ eVs (bottom) measured before the bunch rotation in the PS. Solid lines were obtained from the SPS BCT. The intensity at injection is obtained from the calibrated integral of the longitudinal beam profile measured during the first turn in the SPS. The dashed lines connect the intensity at injection with the corresponding BCT measurement. Green curves correspond to cases where the beam is stable. Unstable cases with losses within the first 23 ms after injection (i.e. 1000 turns) are indicated by red curves (“fast losses”) and unstable cases with losses occurring later in the cycle are indicated by blue curves (“slow losses”).

Q20 optics for an intermediate range of intensities (1.6×10^{11} p/b $< N < 2.7 \times 10^{11}$ p/b) in addition to the fast instability at high intensity. It should be mentioned that a very similar observation was made during measurements with the Q26 optics with very small longitudinal emittance ($\varepsilon_l \approx 0.16$ eVs) in 2007 [68]: a weak instability was observed for a small intensity region around $N \approx 0.6 \times 10^{11}$ p/b and a strong instability for $N > 0.8 \times 10^{11}$ p/b. This was explained by transverse mode coupling (and decoupling for the case of the instability at intermediate intensities).

A summary of the vertical beam instability observations during the 2013 measurement campaign for the Q26 and the Q20 optics is presented in Fig. 4.17. In particular, the longitudinal emittance measured in the PS before the bunch rotation is shown as a function of the beam intensity at PS extraction, and the beam stability in the SPS is indicated by the color code. In the case of the Q26 optics, a linear dependence of the intensity threshold as a function of the longitudinal emittance is observed, as expected from Eq. (C.207). Close to the instability threshold, the growth rate of the vertical coherent motion is small, which results in “slow losses”. On the other hand, “fast losses” within the first 1000 turns after injection are observed for intensities much higher than the threshold for a given longitudinal emittance. The picture is different for the Q20 optics. In particular, a large area of weak instability is observed for longitudinal emittances below $\varepsilon_l \approx 0.32$ eVs and intensities in the range 1.1×10^{11} p/b $< N < 2.3 \times 10^{11}$ p/b. Besides that, the threshold intensity for the strong instability scales with the expected linear dependence on the longitudinal emittance. It is interesting to note that there are no cases with “slow losses” close to the threshold for the strong instability and intensities higher than $N \approx 3.3 \times 10^{11}$ p/b. These measurements will be compared to numerical simulations as described in the following.

The transverse impedance of the SPS is currently believed to be dominated by the ferrite loaded kicker magnets and the resistive wall impedance of the vacuum chambers. It is important to mention that seven out of the eight MKE extraction kickers have been coated (*serigraphed*) within the last years in order to reduce their longitudinal impedance and thus mitigate operational limitations due to heating [114]. The serigraphy reduced also the broadband impedance of the MKE kickers, but introduced a narrowband impedance at low frequency. The first impedance model for the SPS [68] was based on analytical calculations of the resistive wall and kicker impedances, and 3D simulations for the beam position monitors. This model was extended later to account also for the impedance of the RF cavities as obtained from 3D simulations. A realistic model of all SPS kickers based on 3D simulations has been developed more recently [115], taking into account the serigraphy and the segmentation for the C-shaped MKE kickers and the segmentation of the four MKP injection kickers. These refined calculations of the kicker impedances are included in the present SPS impedance model, which can be used for beam dynamics simulations. For this purpose, the global wake functions are obtained by summing the wake functions of the individual impedance sources weighted by the beta functions at their corresponding locations. It should be emphasized that the wake functions for the Q20 and the Q26 optics are slightly different due to their different beta functions at the location of impedance sources.

The global wake functions obtained from the present SPS impedance model are used as input for the macroparticle simulation code HEADTAIL [116]. Figure 4.18 shows the vertical growth rate in the two SPS optics for different longitudinal emittances and bunch intensities as obtained from a series of HEADTAIL simulations. Note that the simulations are initialized with a quasi matched longitudinal distribution as opposed to the measurements, where the bunch rotation is performed before the ex-

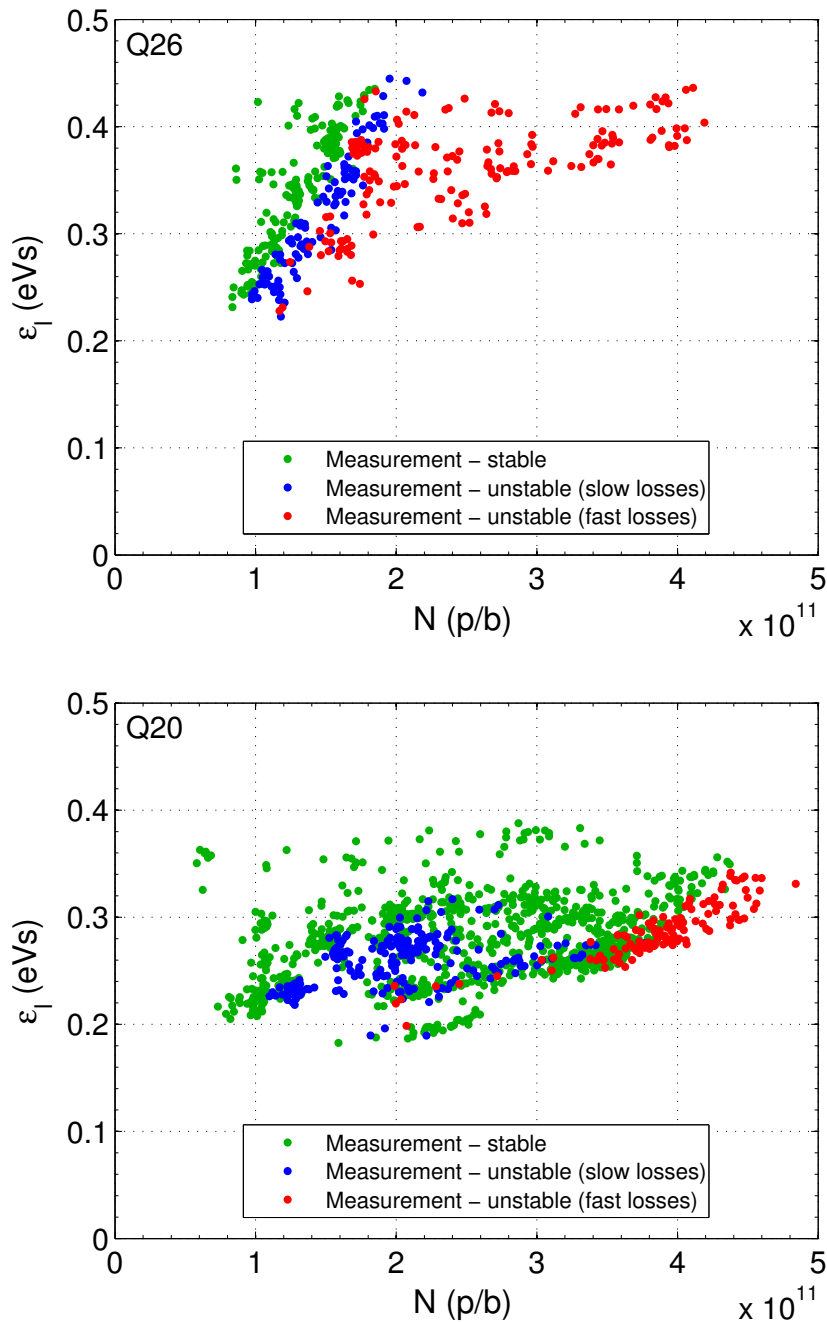


Figure 4.17: Experimental study of beam stability at injection with the Q26 optics (top) and Q20 optics (bottom). Each data point shows the longitudinal emittance measured in the PS before bunch rotation as a function of the beam intensity at the PS extraction, where the color code indicates if the beam was stable in the SPS. Green points correspond to stable cases. Unstable cases are marked by red dots if losses occurred within the first 1000 turns after injection (“fast losses”) and blue dots if losses occurred later in the cycle.

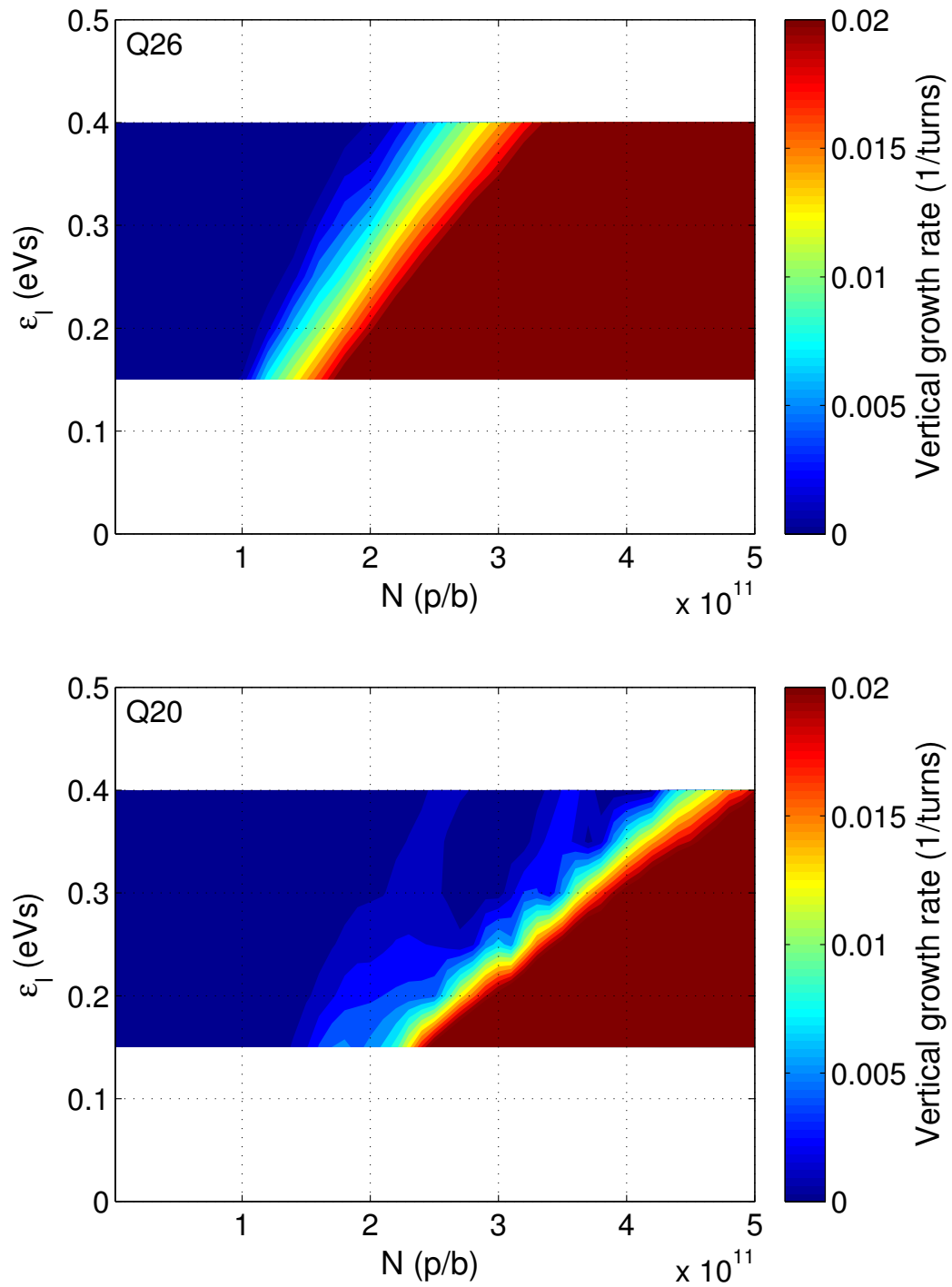


Figure 4.18: Vertical growth rate as a function of the intensity per bunch and the longitudinal emittance as obtained from a series of HEADTAIL simulations for the Q26 optics (top) and the Q20 optics (bottom). The color scale is clipped, i.e. areas in red correspond to growth rates of 0.02/turns or higher.

Table 4.6: HEADTAIL simulation parameters for TMCI simulations.

SPS optics	Q20	Q26
Betatron tunes Q_x/Q_y	20.13/20.18	26.13/26.18
$\bar{\beta}_{x,y}$ (m)	54.6	42
\bar{D}_x (m)	3.75	2.3
Gamma at transition γ_t	18	22.8
γ_0	27.7	27.7
RF-voltage at 200 MHz, V_{200} (MV)	4	1.4
RF-voltage at 800 MHz, V_{800} (MV)	0.4	0.14
Chromaticity Q'_x, Q'_y	1, 5	1, 5
2 nd order chromaticity Q''_x/Q''_y (10^2)	2.7/6.6	5/1.3
3 rd order chromaticity Q'''_x/Q'''_y (10^5)	-18.7/14.5	-4/2
Normalized transverse emittance ε_n (μm)	2	2
Number of bunch slices	500	500

traction from the PS and the beam is injected longitudinally mismatched into the SPS. Thus, the effect of longitudinal emittance blow-up due to filamentation is not taken into account in the simulations. Nevertheless, it is remarkable that the main features of the experimental observations can be reproduced: the simulations predict a linear dependence of the intensity threshold on the longitudinal emittance, as observed with somewhat similar slopes in the measurements (cf. Fig. 4.17). In fact, the ratio of the threshold increase with the Q20 optics compared to the Q26 optics found in the simulations is in agreement with the experiment. Furthermore, the island of slow instability that was observed experimentally in the Q20 optics is obtained similarly with HEADTAIL, although not as pronounced. It should be emphasized that the effect of the 800 MHz cavity as used during the experiments is included in the simulations. In addition, nonlinear chromaticity components up to third order corresponding to the measurements described in Section 4.4.1 are taken into account. A summary of the simulation parameters for the two optics is given in Table 4.6. Amplitude detuning is not included, even though it was not corrected during the measurements.

Figure 4.19 shows the coherent mode spectrum¹⁴ as a function of bunch intensity for the two SPS optics simulated with HEADTAIL for a longitudinal emittance of $\varepsilon_l \approx 0.3$ eVs. The corresponding vertical growth rates are compared with measured growth rates in Fig. 4.20. In order to account for the longitudinal emittance blow-up due to filamentation after injection in the SPS, measurement cases with a longitudinal emittance of $\varepsilon_l \approx 0.28$ eVs before the bunch rotation in the PS are chosen for the comparison. In the simulation for the Q26 optics, the beam is stable up to an intensity of $N = 1.50 \times 10^{11}$ p/b. At $N = 1.60 \times 10^{11}$ p/b the beam becomes unstable due to the coupling of the (azimuthal) mode -1 with mode -2 and probably also mode -3.

¹⁴Further details on the representation of the coherent mode spectrum can be found in Ref. [68].

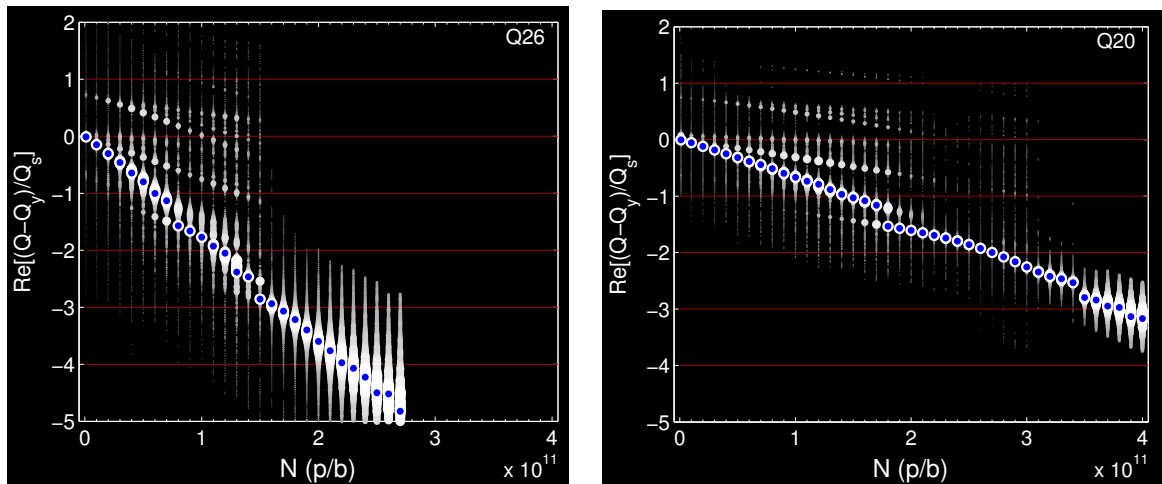


Figure 4.19: Mode spectrum of the coherent vertical motion as simulated with HEAD-TAIL for $\varepsilon_l \approx 0.3$ eVs using the present SPS impedance model for the Q26 optics (left) and the Q20 optics (right). The simulation parameters are summarized in Table 4.6. The coherent modes are represented as white dots. The size of the dots indicate the corresponding spectral amplitude. The dominant mode for each intensity is marked by a blue dot.

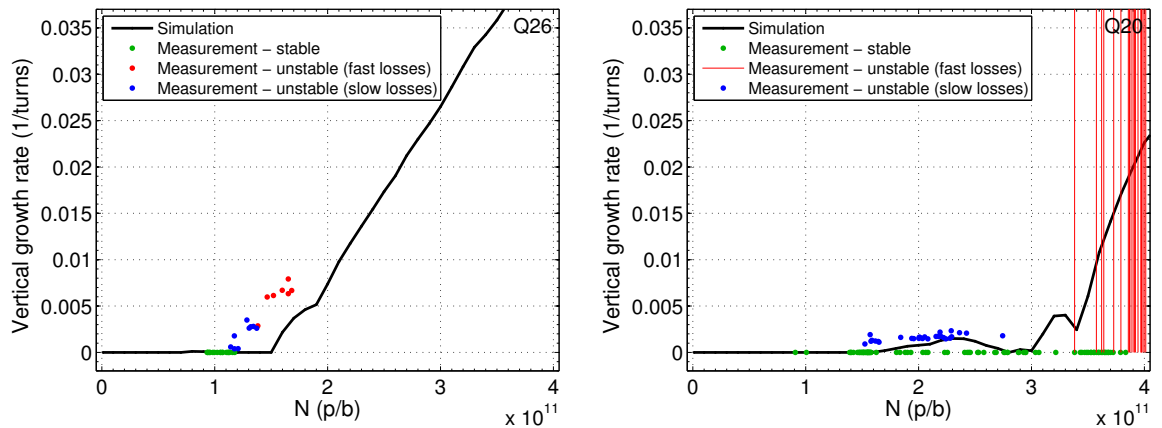


Figure 4.20: Vertical growth rate as function of intensity as simulated with HEAD-TAIL for $\varepsilon_l \approx 0.3$ eVs in comparison with the measured growth rate for cases with $\varepsilon_l \approx 0.28$ eVs before bunch rotation in the PS for the Q26 (left) and the Q20 optics (right). Cases for which the growth rate could not be fitted are shown as vertical lines.

The vertical growth rate is increasing quickly for higher intensities. In comparison to the simulation, the instability onset was observed in the measurements with the Q26 optics already at about $N \approx 1.20 \times 10^{11}$ p/b. This could be explained by the fact that

the present impedance model accounts only for about 70% of the measured coherent tune shift with intensity [115], i.e. there are still some significant impedance sources in the machine not included in the model. However, it is worth pointing out that the same slope of the growth rate as function of intensity is observed in simulations and in the measurements beyond the respective instability threshold. As already pointed out before, the situation is more complex in the case of the Q20 optics. In the HEADTAIL simulations for the longitudinal emittance of $\varepsilon_l \approx 0.3$ eVs, a weak vertical instability with growth rates below 0.002/turns is observed in the intermediate intensity range (1.4×10^{11} p/b $< N < 2.8 \times 10^{11}$ p/b). This corresponds to the intensity region in the coherent mode spectrum, where mode -1 approaches mode 0 and thus could be a weak coupling. Note that the weak instability observed in the measurements has similar growth rates, however the intensity range for which it is observed is slightly shifted towards a smaller bunch current. This could be explained again by the missing impedance contributions in the model. The strong transverse mode coupling instability as simulated with HEADTAIL with $\varepsilon_l \approx 0.3$ eVs appears for intensities larger than $N = 3.0 \times 10^{11}$ p/b. It seems that first mode -1 couples with mode -2 and later also with mode -3. The onset of the strong instability is observed in the measurements with a longitudinal emittance of $\varepsilon_l \approx 0.28$ eVs before the bunch rotation in the PS at around $N \approx 3.4 \times 10^{11}$ p/b. Unfortunately it was not possible to fit a growth rate for these measurements due to problems with the beam instrumentation related to the high bunch intensity. Nevertheless, the unstable cases are indicated by vertical lines in Fig. 4.20. The instability onset is observed for slightly higher intensity compared to the simulation. This might be explained by Landau damping created by amplitude detuning, as due to brightness limitations in the PSB the transverse emittance had to be increased to more than $\varepsilon_n = 3 \mu\text{m}$ in order to reach the required small longitudinal emittance and high intensity.

Finally, the intra bunch motion as measured with the SPS Head-Tail monitor is compared for a few example cases with the results of HEADTAIL simulations in Fig. 4.21. A clear pattern of travelling waves without nodes is observed in the measurement for high intensity in the Q26 optics, which is the typical signature of a TMCI [68]. A very similar intra bunch motion is also observed in the HEADTAIL simulation for comparable beam parameters. Two example cases are shown for the Q20 optics: for high beam intensity, where the strong instability is observed, a travelling wave pattern is observed both in the measurement and in the simulation. It should be emphasized that the characteristics of the intra bunch motion is well reproduced in the simulation. For an intermediate intensity at which the weak instability occurs, it seems that in the simulation the intra bunch motion has one node in the center of the bunch. This could be related to the fact that mode -1 is dominating the instability. Very similar observations are also made in the measurement, however not as clear.

Despite the fact that only about 70% of the measured coherent tune shift is reproduced in the present SPS impedance model, the qualitative agreement between the measurements and the HEADTAIL simulation is remarkable. Similar simulations will

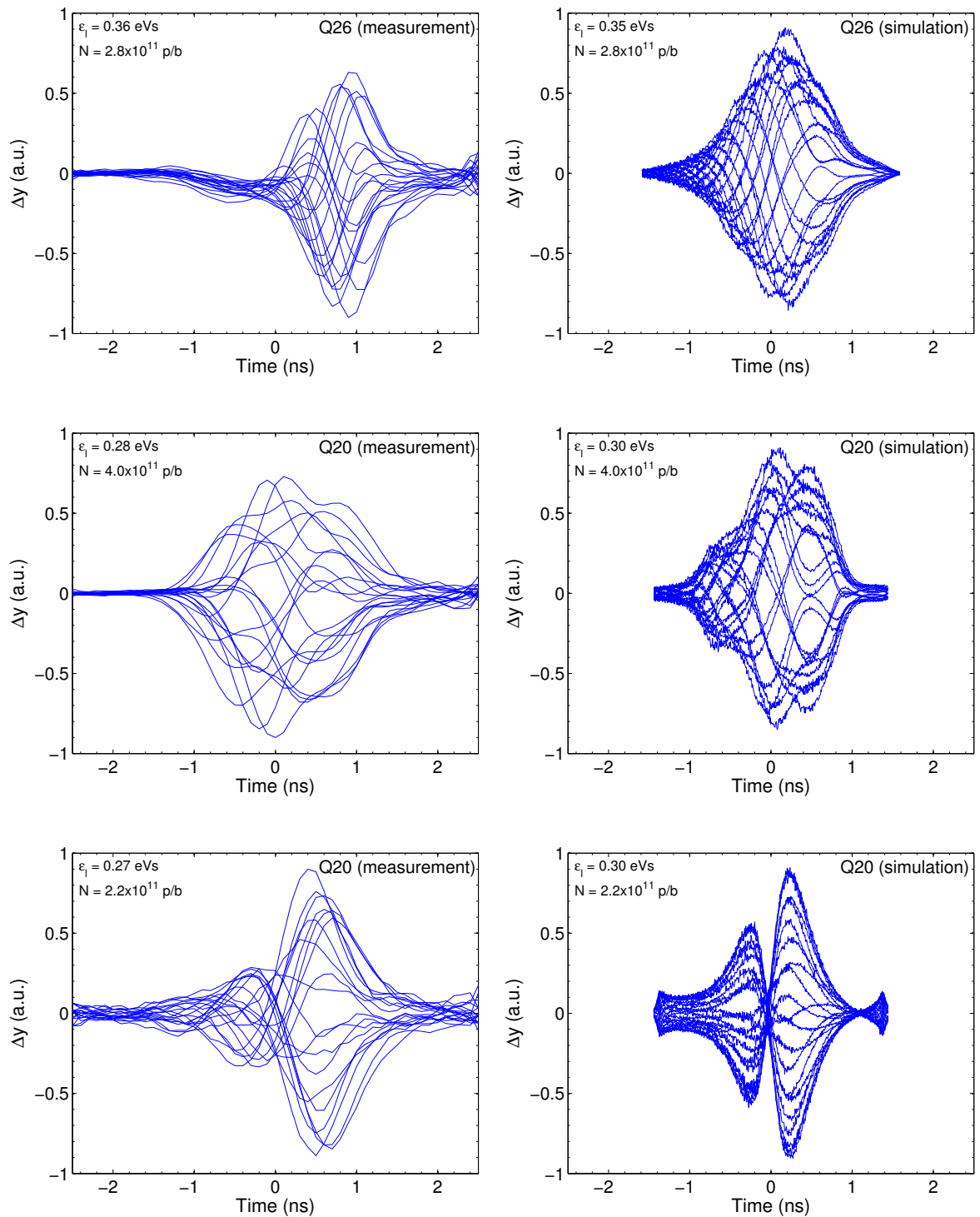


Figure 4.21: Comparison of the vertical intra bunch motion between the SPS Head-Tail monitor measurement (left) and the corresponding HEADTAIL simulations (right). One case is shown for the Q26 optics and two cases for the Q20 optics, as indicated together with the beam parameters in the graphs.

thus allow assessing the impact of changes of the vertical impedance on the beam stability in the future.

The presented experimental study of the TMCI threshold in the SPS shows that the range of bunch intensities envisaged by the HL-LHC project is within reach with the Q20 optics for the nominal longitudinal emittance of $\varepsilon_l \approx 0.35$ eVs. Thus the TMCI in the SPS is not considered a performance limitation for future LHC beams any longer.

4.6. LHC-type beams in the SPS

In the standard LHC beam production scheme (cf. [62], Chapter 12), between two and four PS batches are transferred to the SPS at a momentum of 26 GeV/c. As already mentioned briefly in Section 4.1, the longitudinal bunch spacing of the LHC beams is defined through the RF manipulations in the PS [61]. In the case of the nominal 25 ns bunch spacing, each PS batch consists of 72 bunches. However, in order to minimize electron cloud effects in the LHC, the alternative 50 ns bunch spacing was used for physics during the 2011 and 2012 runs. The 50 ns beam is produced in the same way as the nominal beam with 25 ns bunch spacing but without the last longitudinal bunch splitting. Therefore, the 50 ns beam usually has about twice higher beam brightness, but only 36 bunches per PS batch. Figure 4.22 shows a typical example of the intensity along the SPS cycle for the 50 ns beam in the Q20 optics recorded in 2012. Note that the flat bottom has a length of $3 \times 3.6 \text{ s} = 10.8 \text{ s}$ in order to accommodate the four injections from the PS. This type of magnetic cycle was used in all measurements presented in this section. Soon after the beginning of the ramp, losses of typically 2-3% are observed, which are mainly due to particles that are not captured in the RF buckets at injection. Just before reaching the extraction momentum of 450 GeV/c, the cleaning of the transverse tails of the beam distribution by means of fast scrapers results in a further intensity reduction by about 3-5%. Note that, as usual for multi-bunch beams with a total intensity above 5×10^{12} p in the SPS, the transverse feedback is needed for LHC beams in order to damp coupled bunch instabilities. The setup of the feedback thus had to be adapted to the decreased phase advance in the Q20 optics.

The first experimental studies with bunch trains in the Q20 optics were performed in the beginning of 2011. Several machine development sessions were devoted to the optimization of the RF settings and to experiments addressing longitudinal instabilities. In fact, a direct comparison of the longitudinal instability thresholds in the two optics was performed. Of particular interest was also the answer to the question, if the presently available voltage of the SPS 200 MHz RF system is sufficient for providing bunches that are short enough at flat top to be transferred to the 400 MHz bucket of the LHC. In addition to that, limitations specific to the different types of LHC beams in the SPS were studied. The 50 ns beam usually has higher intensity per bunch and, as mentioned above, higher beam brightness. Therefore space charge effects on the long flat bottom could become an important performance limitation for high brightness beams in the future. The main challenges for the 25 ns beams are longitudinal

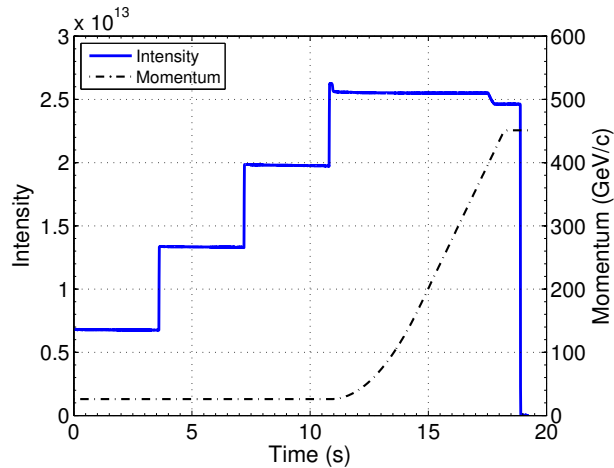


Figure 4.22: Typical example of the total intensity along the SPS cycle for the 50 ns beam with the Q20 optics in 2012.

instabilities, beam loading, and the electron cloud effect, which affects transverse beam stability, transverse emittances and beam lifetime. All these performance limitations were addressed in experimental studies and in simulations, as discussed in the following.

4.6.1. Longitudinal instabilities in the SPS

An overview of the longitudinal instabilities observed in the SPS can be found in Ref. [117]. The main observations can be summarized as follows: the longitudinal multi-bunch instability with LHC beams in the SPS has a very low intensity threshold. In the Q26 optics for example, a single batch of the 50 ns beam with nominal longitudinal emittance $\varepsilon_l = 0.35$ eVs and 2×10^{10} p/b becomes unstable during the ramp, even with the RF feedback, feedforward and the longitudinal damper on. The instability threshold seems to be independent of the number of batches in the machine, i.e. the same instability is observed for a given intensity per bunch with one or four batches of the 50 ns beam in the machine (with gaps of 250 ns between batches). The fundamental and higher order modes (HOMs) of the main 200 MHz and the fourth harmonic 800 MHz system are possible impedance sources driving this instability [57]. The search for other impedance sources is ongoing. For a non-accelerating bucket, the threshold intensity for the longitudinal coupled bunch instability $N_{\text{thr}}^{\text{LCB}}$ due to narrow-band impedances in a single RF system scales as [71]

$$N_{\text{thr}}^{\text{LCB}} \propto \frac{\varepsilon_l^2 |\eta|}{E_0 \tau}, \quad (4.16)$$

where E_0 is the energy of the synchronous particle and τ is the bunch length. After an initial increase of the threshold with energy in the first part of the cycle, which is related to the increasing slip factor $|\eta|$ close to γ_t , the instability becomes more critical

at higher energies.

In routine operation, the fourth harmonic 800 MHz RF system is used in bunch shortening mode [118] in order to increase the synchrotron frequency spread and thus enhance Landau damping. The voltage of the 800 MHz RF system is usually programmed to one-tenth of the voltage of the 200 MHz RF system throughout the cycle. Nevertheless, individual bunches injected with smaller longitudinal emittance can become unstable during the ramp, as observed for example with the 50 ns beam for an intensity of about $N \approx 1.2 \times 10^{11}$ p/b in the Q26 optics [86]. This observation could be an indication of loss of Landau damping. Based on the Sacherer criterion [119], the threshold intensity for loss of Landau damping in a single harmonic RF system due to the reactive part of a broadband impedance scales as [71]

$$N_{\text{thr}}^{\text{LLD}} \propto \frac{\varepsilon_l^2 |\eta| \tau}{E_0}. \quad (4.17)$$

Note that the intensity threshold for the loss of Landau damping has a similar dependence on beam energy as the longitudinal coupled bunch instability. The evolution of the threshold values for narrowband resonant impedances and for the imaginary part of a broadband impedance as function of time along the cycle are shown in Ref. [71] for different values of γ_t . Detailed studies on the loss of Landau damping in a double RF system and its application to the observations in the SPS can be found in Ref. [120].

In order to stabilize the beam at high energy in routine operation, controlled longitudinal emittance blow-up is performed during the second part of the ramp by introducing band-limited noise on the phase loop of the 200 MHz RF system [72]. However, the longitudinal emittance blow-up in a double RF system has its own limitations due to the presence of beam loading [121].

As the longitudinal instability thresholds scale with the slip factor η , a clear gain of beam stability is expected when using the Q20 optics. This applies especially to the low energy part of the cycle, where the slip factor ratio between the two optics is largest and the RF voltage can be increased proportionally (cf. Fig. 4.4). In particular, on the flat bottom the expected intensity thresholds for longitudinal instabilities in the Q20 optics are almost three times higher compared to the Q26 optics. This provides significant margin for future high intensity beams with the Q20 optics, while in the nominal optics the 50 ns LHC beam with an intensity of $N \approx 1.8 \times 10^{11}$ p/b at injection (as typically used for LHC filling in 2012) is at the limit of stability on the injection plateau. Note that raising the instability threshold in the nominal optics would require to inject the beam with larger longitudinal emittance, which usually results in higher losses at the PS-to-SPS transfer unless additional RF voltage can be used for the bunch rotation at PS extraction [122].

At higher energies, the instability thresholds are still higher in the Q20 optics when assuming the same longitudinal emittance. However, in order to achieve the same bunch length for extraction to the LHC a smaller longitudinal emittance is required in Q20 compared to the Q26 optics due to the limited RF voltage. In fact, it is expected

that for the same bunch length at extraction the longitudinal stability will be the same in the two optics, as discussed already in more detail in Section 4.3.2.

Experimental studies with 50 ns beams

A direct experimental comparison of the beam stability in the Q20 and the Q26 optics for the same beam conditions was performed. The operational voltage program V_{200} for the 200 MHz RF system used for the Q26 optics in 2012 is shown in Fig. 4.23 (solid blue line). The first batch is injected at $V_{200}=2$ MV and after about 50 ms, the RF voltage is set to 3 MV for the rest of the flat bottom as this improves transmission. Note that in the Q26 optics the matched voltage at injection would be around $V_{200} = 0.75$ MV. However, higher RF voltage is used at injection in routine operation with multi-bunch LHC beams in order to reduce the effect of beam loading and thus minimize capture losses, as already anticipated in the LHC design report (cf. [62], Chapter 16). The first part of the ramp is programmed such as to provide a constant bucket area of $\mathcal{B} = 0.6$ eVs. In the second part of the ramp, the RF voltage is kept constant at around $V_{200} = 4.2$ MV in order to increase the bucket area and thus avoid particle loss in case controlled longitudinal emittance blow-up is performed (which usually takes place between 185 GeV/c and 420 GeV/c). The 200 MHz RF system is set to $V_{200} = 7$ MV at flat top in order to shorten the bunches for the beam transfer to the LHC 400 MHz bucket. A similar voltage program but scaled to the higher slip factor was developed for the Q20 optics, as also shown in Fig. 4.23 (solid green line). Note that the chosen setting of $V_{200}=5.6$ MV on the injection plateau yields the same mismatch with respect to the injected longitudinal bunch distribution as in the Q26 optics (the additional voltage step after the first injection was omitted here).

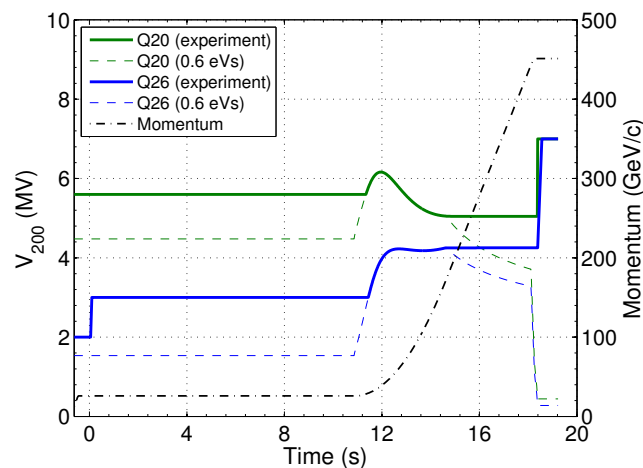


Figure 4.23: The 200 MHz RF voltage programs for both optics as used during the measurements with the 50 ns beam (solid lines) together with the magnetic cycle (black curve). For comparison, the RF voltage providing a constant bucket area of $\mathcal{B} = 0.6$ eVs is also shown (dashed lines).

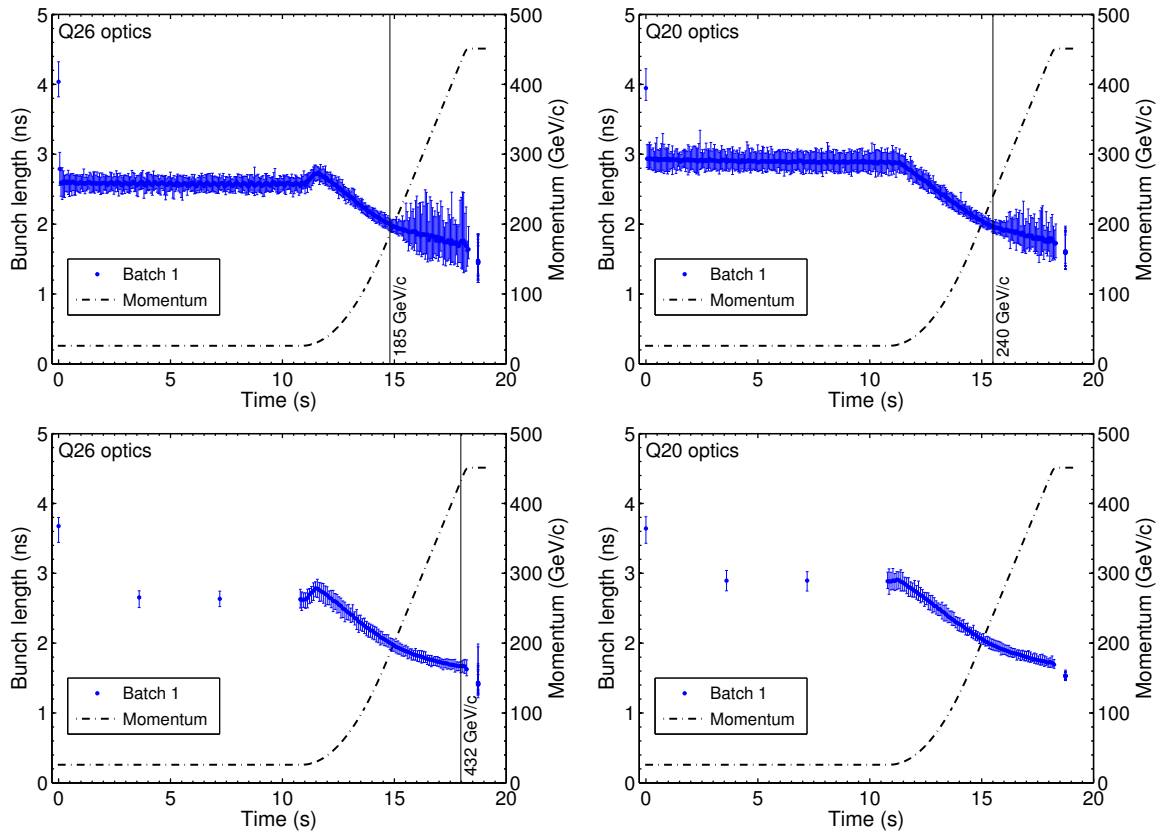


Figure 4.24: Typical examples of the averaged bunch length variation along the cycle for the Q26 optics (left) and the Q20 optics (right) for single batches of the 50 ns LHC beam in the following conditions: intensity of $N \approx 1.2 \times 10^{11}$ p/b at flat top in a single RF system (top) and with higher intensity $N \approx 1.6 \times 10^{11}$ p/b at flat top with the 800 MHz RF system switched on (bottom). The peak-to-peak bunch length spread within the batch is shown by the error bars. The vertical lines indicate the instability onset. *Courtesy of T. Argyropoulos.*

A set of measurements was performed with single batches of the 50 ns beam with an intensity of around $N = 1.3 \times 10^{11}$ p/b at injection and about nominal longitudinal emittance. Without controlled emittance blow-up and using only the 200 MHz RF system with its feedback, feedforward and longitudinal damper, the beam became unstable during the ramp in both optics. Figure 4.24 (top) shows typical examples of the average bunch length of all 36 bunches along the cycle for the two optics. When bunches become unstable and thus exhibit large dipole and quadrupole oscillations, the bunch length spread within the batch (as indicated by the error bars in the plots) starts to increase. Note that at the moment of the instability onset the beam parameters such as longitudinal emittance, bunch length and intensity are similar in the two measurements. As expected from the discussion of the intensity thresholds above, the instability appears at higher energy in the low γ_t (Q20) cycle.

Better beam stability was achieved by switching on the 800 MHz RF system in

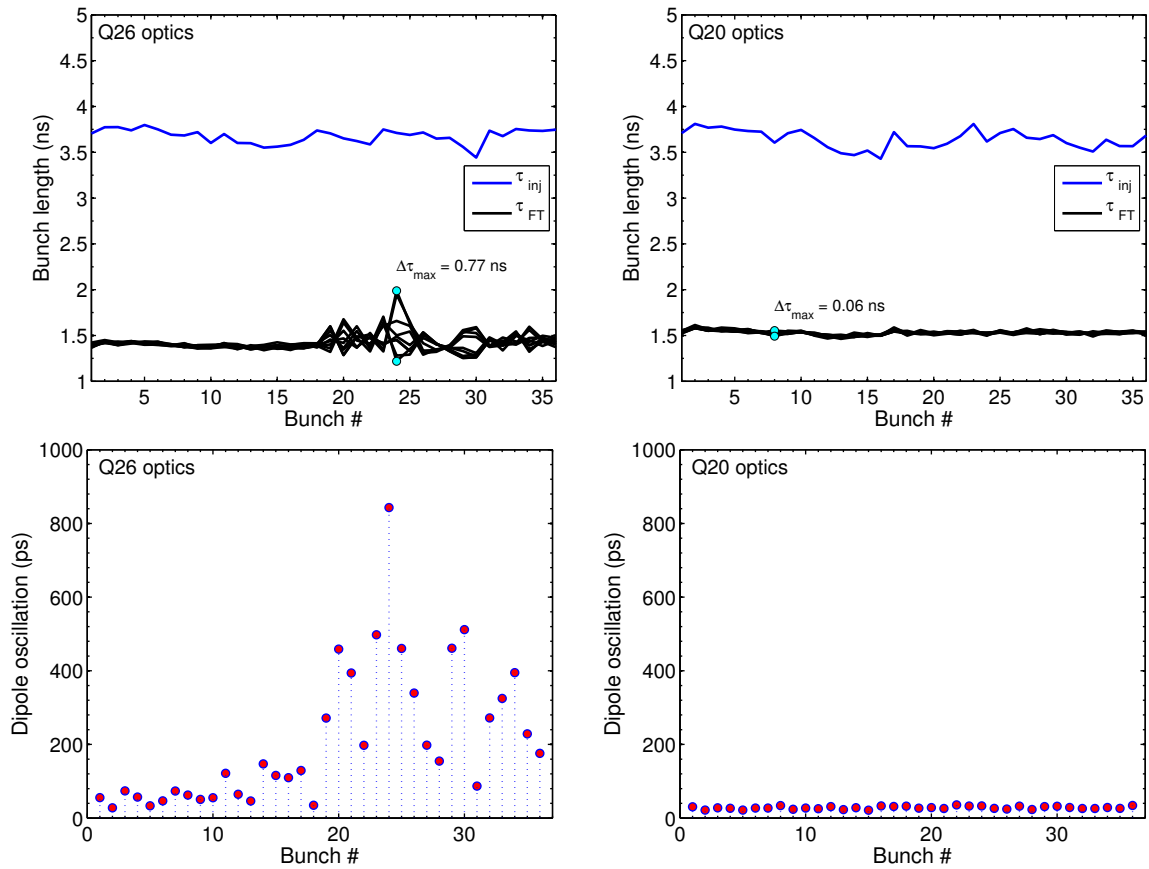


Figure 4.25: Bunch length (top) and bunch position (bottom) oscillations at flat top for the 36 bunches of a single batch of the 50 ns beam with $N \approx 1.6 \times 10^{11}$ p/b at flat top with the 800 MHz RF system in bunch shortening mode. The measurements for Q26 (left) and for Q20 (right) correspond to the same cycles as in Fig. 4.24 (bottom). The bunch length is shown at injection and for eight measurements on flat top. *Courtesy of T. Argyropoulos.*

bunch shortening mode and programming the corresponding RF voltage V_{800} to the usual 1/10 level of the 200 MHz voltage, i.e. $V_{800} = V_{200}/10$. This was sufficient to stabilize the beam in the Q20 cycle up to intensities of about $N \approx 1.6 \times 10^{11}$ p/b at flat top, with $\tau \approx 1.53$ ns and $\varepsilon_l \approx 0.42$ eVs as shown in Fig. 4.24 (bottom). However, in the Q26 cycle some bunches were still unstable at flat top ($\tau \approx 1.41$ ns, $\varepsilon_l \approx 0.46$ eVs). This becomes evident when analyzing the bunch length variation and longitudinal bunch position oscillations at flat top as obtained from eight longitudinal beam profiles acquired during one synchrotron period, see Fig. 4.25. In the Q26 optics, large dipole (bunch position) and quadrupole (bunch length) oscillations were observed. Stable beam conditions were obtained in the Q20 optics with average bunch lengths slightly larger than 1.5 ns at flat top, which is comparable to the operational bunch length of $\tau \approx 1.5$ ns at extraction in the Q26 optics after controlled longitudinal emittance blow-up. The beam intensity used here is close to the maximum that the PS was able to

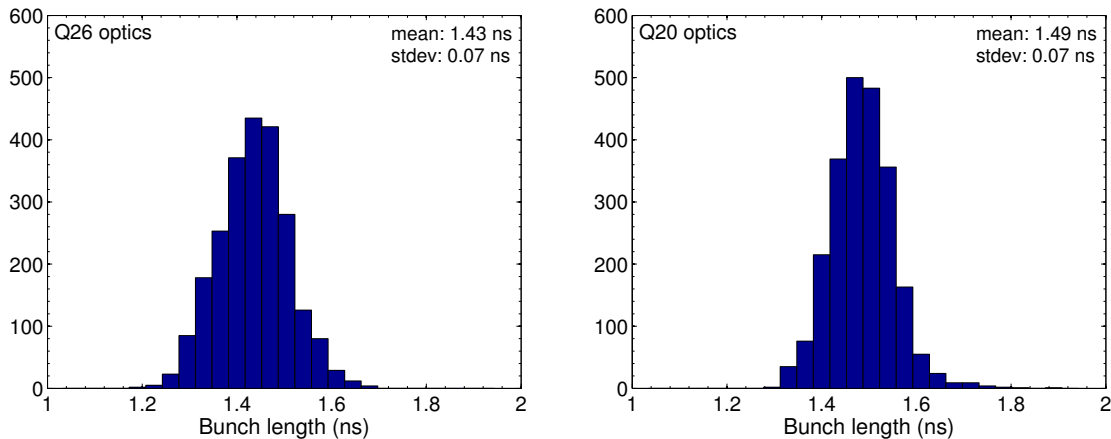


Figure 4.26: Bunch length distribution at flat top (before extraction) for the Q26 optics (left) and the Q20 optics (right) for the 50 ns LHC beam with $N \approx 1.6 \times 10^{11}$ p/b. Only cases with 4×36 bunches per extraction are considered.

deliver in 2011 and 2012 in stable conditions with the nominal longitudinal emittance at extraction ($\varepsilon_l = 0.35$ eVs).

After successful transfer of single bunches from the SPS Q20 optics to the LHC in June 2012 [95], a machine development session in August 2012 was dedicated to test the transfer of the 50 ns beam with $N \approx 1.6 \times 10^{11}$ p/b at SPS flat top with two and four PS batches. One LHC filling with the Q20 optics was performed without controlled emittance blow-up in the SPS so that the beam had $\varepsilon_l \approx 0.37$ eVs and $\tau \approx 1.5$ ns at extraction. The corresponding bunch length distribution at SPS flat top for all extractions with four PS batches is shown in Fig. 4.26 (right). For comparison, the bunch length distribution measured on the same day in the Q26 optics for the same beam intensity (but with controlled longitudinal emittance blow-up) is shown in Fig. 4.26 (left). The mean bunch length is only slightly larger in the Q20 optics. A second filling of the LHC with the Q20 optics was performed with controlled longitudinal emittance blow-up in the SPS, leading to $\varepsilon_l \approx 0.5$ eVs and $\tau \approx 1.7$ ns at SPS flat top. No increase of the capture losses at LHC injection compared to the first fill was observed [123]. Thus, it seems that longitudinal emittances of about $\varepsilon_l \approx 0.5$ eVs, as typically used for LHC filling with the Q26 optics in 2012 routine operation [124], can also be used with the Q20 optics, despite the increased bunch length.

Experimental studies with 25 ns beams

A comparison of the longitudinal instability thresholds in a single RF system in the SPS was also performed with the nominal LHC beam with 25 ns bunch spacing. Similar to the studies with the 50 ns beam, comparable voltage programs were used for the two optics. In particular, a constant RF voltage of $V_{200} = 1.8$ MV for the entire flat bottom was chosen in the case of Q26, and the same value scaled to the larger η was used for Q20, i.e. $V_{200} = 5.25$ MV. In both optics the ramp was performed with a constant bucket

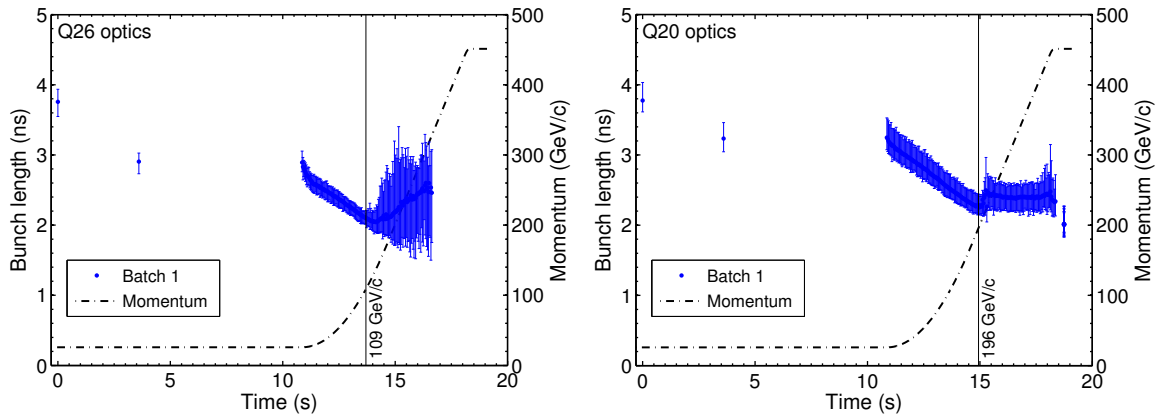


Figure 4.27: Example of the longitudinal instability threshold with a single batch of the 25 ns beam with $N \approx 1.2 \times 10^{11}$ p/b at injection in the Q26 optics (left) and the Q20 optics (right) using only the 200 MHz RF system. *Courtesy of T. Argyropoulos.*

area of $\mathcal{B} = 0.65$ eVs in the first part of the ramp, constant voltages in the second part of the ramp and at flat top, where the RF voltage was raised to $V_{200} = 7$ MV. The 800 MHz RF system remained switched off and no controlled longitudinal emittance blow-up was performed. Figure 4.27 shows typical examples of the bunch length evolution along the Q26 (left) and the Q20 (right) cycles for beam intensities of about $N \approx 1.2 \times 10^{11}$ p/b at injection. The beam was dumped by the machine protection system in the case of the Q26 optics due to losses caused by the instability. As expected, the instability occurs at higher energy in the Q20 optics, roughly according to the slip factor ratio between the two optics (above 100 GeV/c the η ratio is about 1.6, cf. Fig. 4.4). However, a clearly lower threshold intensity per bunch is observed in both optics in comparison to the measurements with the 50 ns beam (cf. Fig. 4.24, top). In fact, it seems that the energy at the onset of the longitudinal instability E_{thr} scales as $1/E_{\text{thr}} \propto N/T_b$ [117], where T_b denotes the bunch spacing.

A few machine development sessions towards the end of 2012 were dedicated to studies of the 25 ns beam with higher than nominal intensity in the Q20 optics. As shown in Fig. 4.28, with optimized voltage programs for the 200 MHz and the 800 MHz RF systems and controlled longitudinal emittance blow-up during the ramp a maximum intensity of $N = 1.3 \times 10^{11}$ p/b could be achieved in stable conditions: in particular, the total voltage of the 200 MHz cavities was set to $V_{200} = 4.5$ MV at flat bottom and for the first injection, while it was lowered to $V_{200} = 2.5$ MV for the injection of the other PS batches. During acceleration, the bucket area was increased to $\mathcal{B} \geq 0.65$ eVs in order to minimize losses for the high beam intensity, which required almost the maximum RF voltage at the beginning of the ramp (cf. Fig. 4.28, top left). The voltage for the 800 MHz RF system was set as usual to $V_{800} = V_{200}/10$. A larger bunch length spread is observed after the controlled longitudinal emittance blow-up in the second part of the ramp (cf. Fig. 4.28, top right). In particular, bunches at the beginning and the end of each PS batch have a larger bunch length, as can be seen from the measurements on

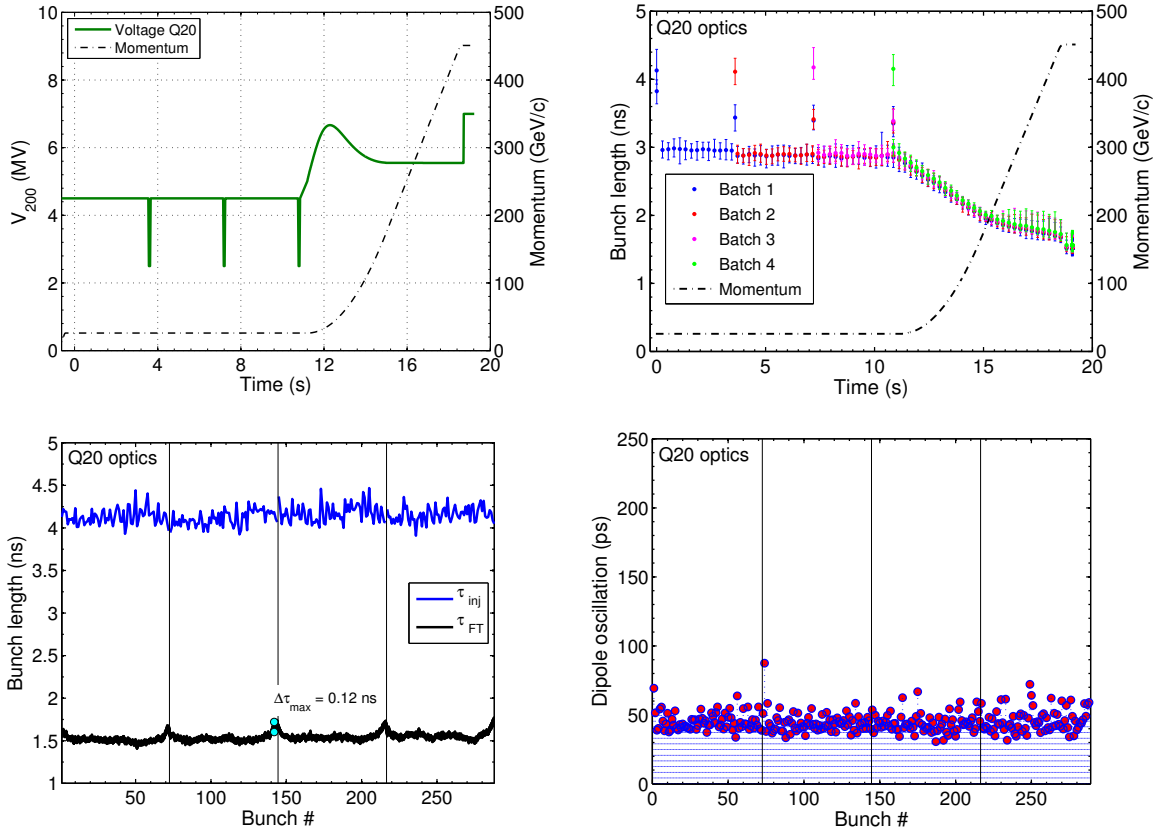


Figure 4.28: Measurements with four PS batches of 72 bunches spaced at 25 ns with $N \approx 1.30 \times 10^{11}$ p/b at SPS flat top, using an optimized voltage program (top left). The average bunch length evolution along the cycle (top right), the bunch length distribution along the bunch train at injection and at flat top (bottom left) and the dipole oscillations at flat top (bottom right) show stable beam conditions. *Courtesy of T. Argyropoulos.*

the flat top (cf. Fig. 4.28, bottom left). This is most probably due to the change of the synchrotron frequency distribution along the batch caused by beam loading, for which the efficiency of the controlled longitudinal emittance blow-up depends on the position along the bunch train [121]. Nevertheless, the obtained bunch length spread and the average bunch length of $\tau \approx 1.55$ ns would be acceptable for injection into the LHC. Furthermore, only very small dipole oscillations were measured at flat top (cf. Fig. 4.28, bottom right), demonstrating the beam stability. It should be emphasized that, due to losses related to the beam capture and losses on the flat bottom, an intensity of more than $N \approx 1.4 \times 10^{11}$ p/b had to be injected in order to reach $N \approx 1.3 \times 10^{11}$ p/b at flat top (without scraping). When injecting beams with even higher intensity, the transmission was significantly decreasing (e.g. about 85% for $N \approx 1.55 \times 10^{11}$ p/b at injection). A possible explanation for this could be increased losses on the flat bottom related to electron cloud effects, as the machine was never scrubbed for this high intensity. In

addition to that, it was observed that the bunch length at flat top was increasing strongly with beam intensity, which could be due to beam loading in the travelling wave cavities, which reduces the effective RF voltage seen by the beam. It should be mentioned that the performance of the SPS RF system will be significantly improved after the rearrangement of the 200 MHz RF cavities and the RF power upgrade [73]. Another possible reason for the bunch lengthening could be longitudinal emittance blow-up due to instabilities. Further studies with high intensity 25 ns beams need to be performed in the future. However, it should be emphasized that the stable beam conditions achieved for the 25 ns beam with $N \approx 1.3 \times 10^{11}$ p/b at flat top with the Q20 represent a new record performance for the SPS, which could not be reached with the Q26 optics in the past.

4.6.2. Space charge studies with 50 ns beam

As mentioned before, space charge effects on the 10.8 s long injection plateau of the SPS cycle might become a limitation for the achievable brightness of future LHC beams. In 2012, the operational 50 ns beam routinely delivered to the LHC for physics had a bunch intensity of typically around $N \approx 1.65 \times 10^{11}$ p/b at SPS extraction (up to $N \approx 1.85 \times 10^{11}$ p/b at injection) and transverse emittances slightly below $\varepsilon_n = 1.65 \mu\text{m}$ [125] in both planes. Assuming Gaussian distributions for all planes and zero vertical dispersion, the corresponding incoherent tune shift due to direct space charge can be calculated as (cf. [16] and Appendix C.1)

$$\Delta Q_x^{\text{SC}} = -\frac{r_p}{2\pi\beta_0^2\gamma_0^3} \frac{N}{\sqrt{2\pi}\sigma_l} \oint \frac{\beta_x}{\sqrt{\varepsilon_x\beta_x + D_x^2\delta_{\text{rms}}^2} (\sqrt{\varepsilon_x\beta_x + D_x^2\delta_{\text{rms}}^2} + \sqrt{\varepsilon_y\beta_y})} ds, \quad (4.18a)$$

$$\Delta Q_y^{\text{SC}} = -\frac{r_p}{2\pi\beta_0^2\gamma_0^3} \frac{N}{\sqrt{2\pi}\sigma_l} \oint \frac{\beta_y}{\sqrt{\varepsilon_y\beta_y} (\sqrt{\varepsilon_x\beta_x + D_x^2\delta_{\text{rms}}^2} + \sqrt{\varepsilon_y\beta_y})} ds, \quad (4.18b)$$

where $r_p = 1.54 \times 10^{-18}$ m is the classical proton radius, $\varepsilon_x = \varepsilon_{n,x}/\beta_0\gamma_0$ and $\varepsilon_y = \varepsilon_{n,y}/\beta_0\gamma_0$ are the physical emittances, δ_{rms} is the rms relative momentum spread and σ_l is the rms bunch length in meters. Thus, using the typical longitudinal beam parameters at SPS flat bottom, i.e. 4σ bunch length of $\tau \approx 3$ ns (corresponding to $\sigma_l = 22$ cm) and $\delta_{\text{rms}} \approx 0.0015$, the maximum space charge tune shift is obtained as $\Delta Q_x^{\text{SC}} = -0.09$ and $\Delta Q_y^{\text{SC}} = -0.16$ in the Q26 optics. The tune shift is smaller in the horizontal plane, since the momentum spread within the bunch decreases the horizontal beam density through the dispersion function, while there is usually no dispersion in the vertical plane. It should be emphasized that the horizontal dispersion function also enters in the calculation of the vertical tune shift. Thus, a lattice with larger dispersion generally exhibits smaller space charge tune spread. For example, using the same beam parameters as above, the space charge tune shift in the Q20 optics is obtained as $\Delta Q_x^{\text{SC}} = -0.08$ and $\Delta Q_y^{\text{SC}} = -0.13$, which is about 15% smaller compared to the Q26 optics. This can be seen also in Fig. 4.29, which shows the space charge tune shift divided by the bunch intensity as a function of the normalized transverse emittance for

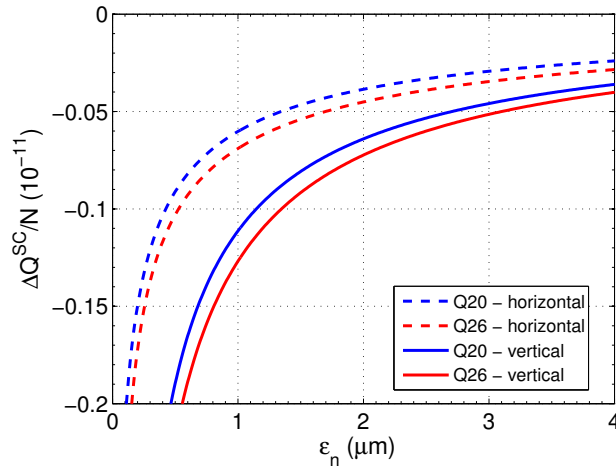


Figure 4.29: Direct space charge incoherent tune shift ΔQ^{SC} divided by the bunch intensity N as function of the normalized transverse rms emittance ε_n assuming equal emittances and the typical longitudinal beam parameters on the SPS injection plateau, $\tau = 3$ ns ($\sigma_l = 22$ cm) and $\delta_{\text{rms}} = 0.0015$, comparing the Q20 and the Q26 optics.

the Q20 and the Q26 optics, assuming round beams and the longitudinal parameters discussed above. Depending on the plane and the transverse emittance, the direct space charge tune shift is between 10% and 20% smaller in the Q20 optics. The difference is even bigger for emittances below $1 \mu\text{m}$ as the dispersive part of the beam size becomes dominant.

Regarding the requirements for the HL-LHC project [12], the future 25 ns LHC beam will exhibit a space charge tune-shift of about $\Delta Q_y^{\text{SC}} = -0.20$ in the Q20 optics (or equivalently $\Delta Q_y^{\text{SC}} = -0.23$ in the Q26 optics). For maintaining equal beam parameters along the bunch train, beam loss and emittance blow-up on the 10.8 s long SPS flat bottom have to be kept as small as possible. In general, the maximum space charge tune spread that can be achieved without beam degradation is determined by resonances intersecting the tune footprint. For example, with the usual working point of the Q20 optics ($Q_x, Q_y = 20.13, 20.18$) and the HL-LHC beam parameters, the space charge necktie extends over the vertical resonance $Q_y = 20$, i.e. particles in the beam core are pushed into the integer resonance. This situation leads to an emittance blow-up of the beam core without losses (provided that the physical aperture of the machine is sufficiently large) until the beam brightness is reduced such that the space charge tune footprint does not overlap with the resonance any more. Thus, in order to avoid emittance blow-up, the working point has to be moved sufficiently far away from the integer resonance. A different behavior is observed when resonances are encountered by particles in the beam tails, i.e. particles with large betatron amplitudes and thus small space charge tune shift. In this case, resonances can lead to diffusion of particles into a beam halo and eventually cause losses due to the reduced dynamic aperture in

the vicinity of the resonance. An additional complication comes from the synchrotron motion: since particles with large synchrotron amplitude oscillate between the head and the tail of the bunch, their space charge tune shift is modulated with twice the synchrotron tune due to the variation of the line density along the bunch¹⁵. This tune modulation can induce periodic crossing of resonances [126], which can lead to emittance growth, beam halo formation and bunch shortening (related to the loss of particles with large synchrotron amplitude). Such detrimental effects might be mitigated by faster synchrotron motion [127], as individual particles might not be trapped so easily by a resonance. Nevertheless, for long storage times as in the case of the SPS, it is crucial to place the space charge necktie in a region of the tune diagram clear of strong resonances.

As presented in Section 4.4.2, a *dynamic* tune scan using a low intensity non-space charge dominated beam did not reveal strong resonances (cf. Fig. 4.15) around the working point $(Q_x, Q_y = 20.13, 20.18)$, especially above the diagonal $(Q_x = Q_y)$. However, even comparably weak resonances in combination with the above discussed space charge effects can become important in case of long storage times. As discussed in the following, different working points were therefore tested with a high brightness beam in order to identify possible limitations due to space charge effects.

In general, incoherent space charge effects are single bunch phenomena and thus do not require bunch trains to be studied. Furthermore, the highest beam brightness presently available from the PS complex is achieved for single bunch beams. However, these high brightness single bunches are used for machine studies only and usually suffer from large cycle-to-cycle intensity variation due to fluctuations at injection into the PSB. In addition, the wire scanners used for the beam size measurement in the SPS have a better signal-to-noise ratio for higher total intensity, i.e. for bunch trains. Thanks to the successful implementation of the “Batch Compression, Bunch Merging and Splitting” (BCMS) scheme [128] in 2012, the PS was able to provide a beam with 50 ns bunch spacing and similar brightness as envisaged by the HL-LHC/LIU projects. In particular, the delivered intensity of $N \approx 1.95 \times 10^{11}$ p/b and normalized transverse emittances of $\varepsilon_n \approx 1.1 \mu\text{m}$ in both planes yield an incoherent space charge tune shift of $\Delta Q_x^{\text{SC}} \approx -0.11$ and $\Delta Q_y^{\text{SC}} \approx -0.20$ at injection energy in the Q20 optics. This BCMS beam was studied in the SPS with different working points in order to see how much space in the tune diagram is needed for accommodating the incoherent tune spread and minimizing emittance blow-up and losses. Figure 4.30 shows the tested working points together with the corresponding emittance measurements and the observed losses.

First, the horizontal tune was varied between $Q_x = 20.07$ and $Q_x = 20.23$, while the vertical tune was kept at approximately $Q_y \approx 20.19$ (cf. Fig. 4.30, left). For each working point setting, a *single batch* of 24 bunches of the 50 ns BCMS beam was injected in five consecutive supercycles with the transverse damper on. The same damper settings were used for all working points. The typical voltage program and RF settings for 50 ns

¹⁵A similar tune modulation can also be caused by large chromaticity. This is however of less importance in the case of the SPS, since the machine is usually operated with small chromaticity.

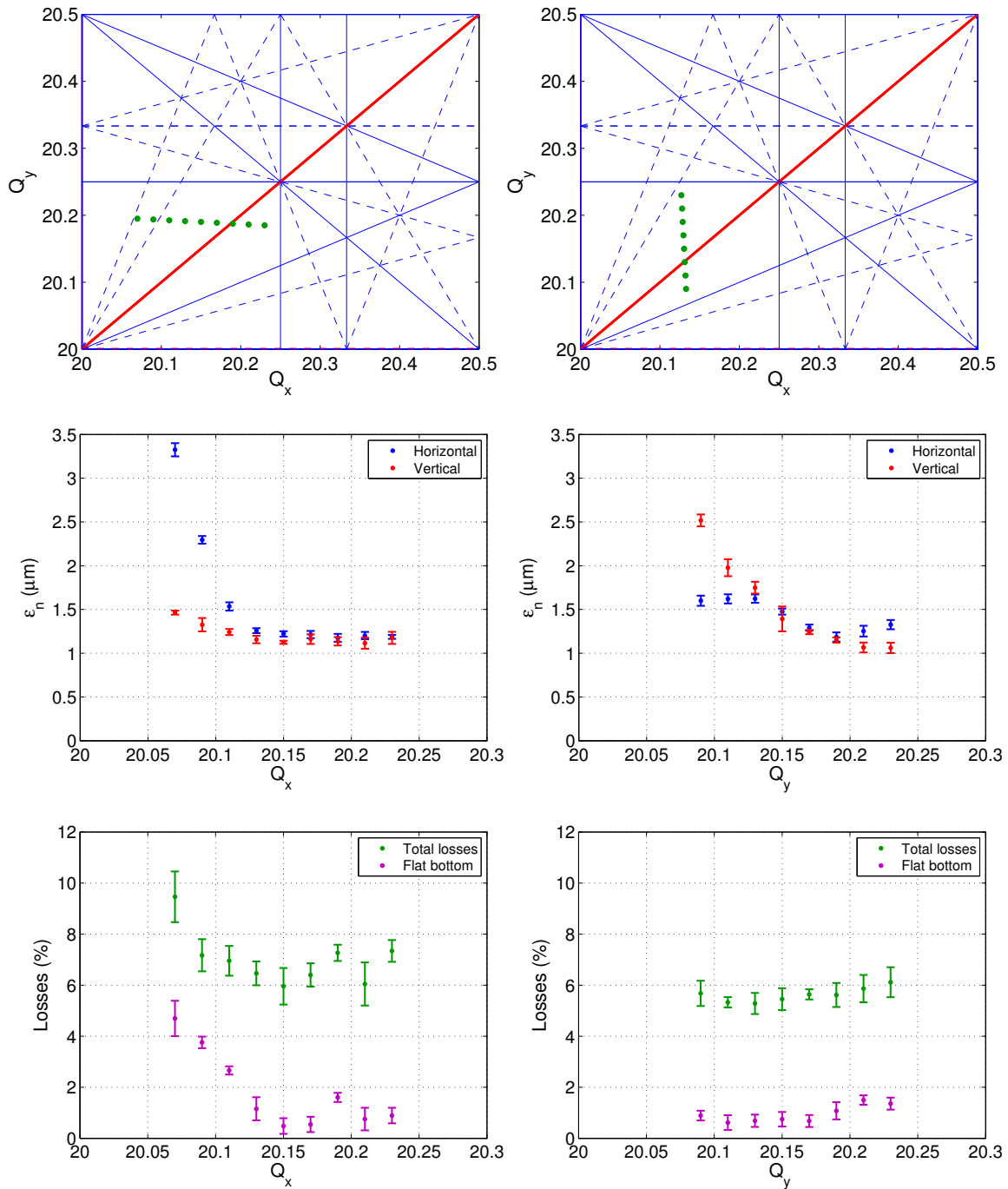


Figure 4.30: Working point scan in the SPS Q20 cycle for LHC beams injecting a single batch of the BCMS high brightness 50 ns beam, varying the horizontal tune (left) and the vertical tune (right). The tested working points are illustrated in the tune diagrams (top). The transverse emittances at the end of the long flat bottom as determined by averaging over five cycles (middle) as well as the corresponding losses on the flat bottom and total losses in the cycle (bottom) are shown.

beams in the Q20 optics (c.f. Section 4.6.1) were used. The transverse beam profiles were measured with the wire scanners in turn acquisition mode (average profile along the bunch train) at the end of the 10.8 s long injection plateau. For each plane and each working point, the emittance is determined as the average of the five individual emittance measurements using the wire scanners BWS.416H and BWS.519V and the error bars are given by their standard deviation. Constant emittances in both planes are obtained for horizontal tunes equal to or above $Q_x = 20.13$. Mainly horizontal emittance blow-up is observed for lower horizontal tunes. At the same time the integrated losses on the flat bottom are enhanced. These losses might be related to particles with large synchrotron amplitude close to the separatrix of the RF bucket, since the total losses from injection up to flat top (without scraping) were around 7% independent of the horizontal tune (apart from the setting $Q_x = 20.07$). The observations therefore resemble the expected blow-up of the beam core “without losses”.

A corresponding working point scan was performed in the vertical plane keeping the horizontal tune at about $Q_x \approx 20.13$ (cf. Fig. 4.30, right). In this case, emittance blow-up due to the integer resonance is measured for vertical tunes below $Q_y \leq 20.19$. Note that similar emittance blow-up in both planes is observed for vertical tunes between $Q_y = 20.13$ and $Q_y = 20.19$. This can be explained by the fact that the incoherent space charge tune footprint is overlapping with the coupling resonance, which is transferring part of the blow-up from the vertical to the horizontal plane and thus equalizing the emittances. Note that practically constant horizontal emittances were measured for working points below $Q_y = 20.13$, i.e. for working points below the diagonal. For high vertical tunes, i.e. $Q_y > 20.19$ no blow-up is observed in the vertical plane. However, it seems that there is a slight emittance growth in the horizontal plane. The origin for this blow-up is not fully understood. A possible explanation could be the fact that when adjusting the vertical tune, also the horizontal tune was slightly changing as depicted in the top graph (right) of Fig. 4.30. In particular, when increasing the vertical tune the working point was moving towards the horizontal integer resonance. In fact for $Q_y = 20.23$ the horizontal tune reached almost $Q_x = 20.12$, which is just the limit at which the blow-up was observed during the horizontal tune scan. Thus, the reason for the blow-up here could be the vicinity to the horizontal integer resonance. Concerning losses, no particular dependence on the vertical tune is observed. The total losses up to flat top were around 6% in all cases, occurring mainly at the beginning of the ramp. Losses on the flat bottom were around 1%.

The measurements discussed above suggest that for the 50 ns BCMS beam used here, the working point should be placed above $Q_x = 20.13$ and $Q_y = 20.20$ in order to avoid emittance blow-up due to the stopband of the integer resonances. This is compatible with the calculated space charge tune shifts of $\Delta Q_x^{\text{SC}} = -0.11$ and $\Delta Q_y^{\text{SC}} = -0.20$. A further cross check was obtained with bunch-by-bunch emittance measurements using the same beam from the PS but with *three injections*¹⁶ in the SPS. Figure 4.31

¹⁶The production of the BCMS beam requires more time in the PS so that the injection timings in the SPS had to be delayed by 365 ms. Thus only three instead of the usual four injections could

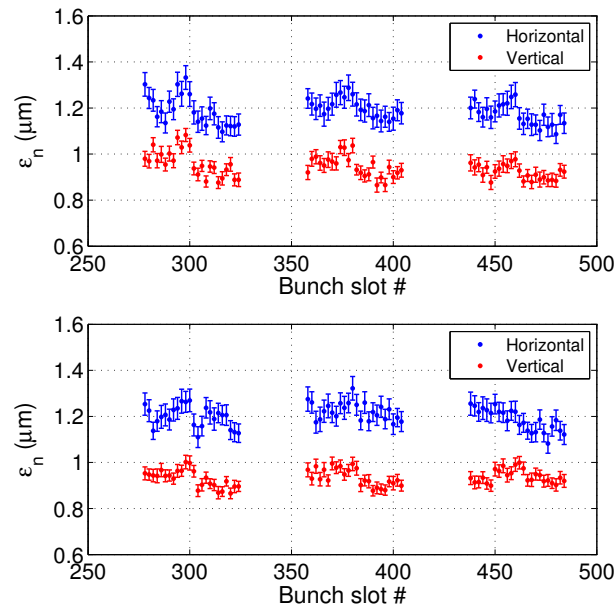


Figure 4.31: Bunch-by-bunch emittance measurement at the end of the flat bottom for three batches of the 50 ns BCMS beam and the working points $Q_x, Q_y = 20.13, 20.19$ (top) and $Q_x, Q_y = 20.17, 20.23$ (bottom). The data shown here corresponds to single wirescanner measurements using BWS.416H and BWS.416V in bunch-by-bunch mode and the error bars are determined by the uncertainty of the Gaussian fits. Note that the absolute emittance values can vary from shot to shot due to systematics in the profile measurements.

shows examples of the transverse emittances along the bunch train for two different working points measured at the the end of the flat bottom. For the working point ($Q_x, Q_y = 20.13, 20.19$), which was at the limit with respect to emittance blow-up in the tune scan, a tendency of slightly increased beam sizes at the beginning of the bunch train can be observed (especially in the vertical plane). Since this trend is correlated with the storage time at injection energy, the higher emittances could indicate some blow-up due to space charge. In order to exclude blow-up due to other incoherent effects, another set of measurements was performed with a working point that is further away from the integer resonances, i.e. ($Q_x, Q_y = 20.17, 20.23$). In this case, practically equal emittance behavior is observed for the three batches. Note that the bunch-to-bunch variation within the batch originates from the pre-injectors, in particular from variations between different PSB rings and the bunch merging and splitting processes in the PS. The resulting brightness variation along the bunch train might be the reason for the blow-up of individual bunches observed with the lower working point.

be accommodated on the flat bottom of the existing SPS cycle. In the future, the timing of the cycle in the PS has to be optimized or an additional basic period of 1.2s has to be added to the SPS flat bottom for injecting four batches.

Considering that the losses on the flat bottom are very small (cf. Fig. 4.30) and comparable to typical operational values, it can be concluded that for working points sufficiently far away from the integer resonances in both planes, a space charge tune shift of up to $\Delta Q_y^{\text{SC}} = -0.20$ can be accommodated on the SPS long injection plateau without relevant beam degradation between PS batches.

4.6.3. Electron cloud effects with 25 ns bunch spacing

As mentioned already, an electron cloud (EC) can build up in the vacuum chamber during the passage of a bunch train of positively charged particles with small bunch spacing [129]. Primary electrons can be generated by residual gas ionization or photoemission induced by the synchrotron radiation of the beam hitting the inner surface of the beam pipe. These primary electrons are accelerated by the electric field of successively passing bunches in the direction perpendicular to the beam motion. When they impact on the vacuum chamber with their broad energy spectrum, secondary electrons are generated due to secondary electron emission. The secondary electron yield (SEY) defines thereby the number of secondary electrons emitted per incident electron. The SEY is a function of the energy of the incident electron and is a wall surface property. For untreated materials usually used for the production of beam pipes such as stainless steel and copper, the SEY is typically larger than unity for electron energies above a few tens or hundred eV. As a consequence, if the traversal time of the electrons across the vacuum chamber cross section is close to the bunch spacing, an exponentially increasing number of secondary electrons, an “electron cloud”, is accumulated during consecutive bunch passages [130]. This phenomenon is also referred to as beam induced multipacting. The threshold SEY, also called multipacting threshold, above which this EC build-up is occurring depends on the vacuum chamber geometry, the beam parameters such as bunch spacing, bunch intensity and bunch length, and the presence of magnetic fields like in dipole and quadrupole magnets. The EC build-up saturates when an equilibrium between electron production and losses at the chamber wall is reached thanks to the electron cloud’s own space charge. In sections of the machine which exhibit large SEY, this saturation level is usually reached within a single passage of the bunch train. If the SEY is close to the build-up threshold, the EC may build up only after more than one beam passage, i.e. over many turns. On the other hand, the number of electrons in the vacuum chamber might decay significantly in gaps between bunches much larger than the bunch spacing or after the beam passage if the bunch train covers only part of the machine circumference, as electrons with low energy have a high probability to be absorbed into the chamber wall. For example, the length of the four batches of the LHC beam corresponds roughly to one quarter of the SPS circumference and the EC usually disappears before the arrival of the first bunch of the train.

In addition to secondary electron emission, electrons hitting the vacuum chamber cause power deposition on the chamber wall and neutral molecular desorption resulting in dynamic pressure rise (defined as the difference between the maximum and the

minimum pressure recorded during the cycle). Moreover, the interaction of the beam particles with the electrons accumulated in the vacuum chamber can result in coherent transverse single and coupled bunch instabilities [131, 132]. The threshold electron density above which such instabilities are observed depends, among many other parameters, on the synchrotron tune Q_s , the bunch intensity and the transverse beam size. Even below this threshold density, the EC can be detrimental for the beam quality as it can cause incoherent emittance blow-up and slow losses.

The EC effect has been identified as a possible performance limitation for the SPS since LHC type beams were injected into the machine for the first time in the early years of 2000. At that time a severe pressure rise was measured all around the machine (in the order of 10^{-5} mbar) [64, 65]. Furthermore, fast transverse beam instabilities at injection of single batches of the 25 ns beam together with important losses and strong emittance blow-up of the trailing bunches of the train were observed [133, 134]. Running with high chromaticity in both planes ($\xi_x, \xi_y \approx 0.5 - 1$) was the only way to achieve decent beam lifetime and control the emittance blow-up [135]. The instabilities driven by the electron cloud in the SPS have been characterized as follows [136]: in the horizontal plane, a coupled bunch instability was observed with fast growth rates of typically around 50 turns, practically independent of intensity. It is believed that the corresponding horizontal wake field is caused by the fact that the spatial structure of the electron cloud slowly follows the horizontal position of the bunches along the train and thus couples their motion. In the vertical plane, the electron cloud was driving a single bunch instability with growth rates from about 500 turns for an intensity just above the build-up threshold up to 100 turns for twice this intensity. Since 2002, dedicated machine development runs with 25 ns beams were carried out almost every year of operation in order to study the EC effect [137] and to condition the inner surfaces of the beam pipes, i.e. reduce the SEY by beam induced electron bombardment (*scrubbing*) and therefore mitigate the EC effect. Thanks to the conditioning achieved with these scrubbing runs, the 50 ns LHC beam does not suffer from EC effects in the SPS in the parameter range presently accessible. On the other hand, the EC effect with 25 ns bunch spacing can be much more severe compared with 50 ns beams. In 2012, several machine studies have been devoted to gaining a deeper understanding on the present status of the EC in the SPS and on scrubbing mechanisms [138]¹⁷. Some important results from these machine studies, in particular concerning the achievable beam quality with the 25 ns beam and measurements with the Q26 and the Q20 optics will be discussed in the following.

Measurements on the long flat bottom - Q26

Thanks to the conditioning accumulated during the scrubbing runs in the years from 2002 onwards, the EC effect gradually became less severe and the beam quality of the

¹⁷This reference contains also an exhaustive list of references about electron cloud related studies in the SPS and electron cloud mitigation techniques.

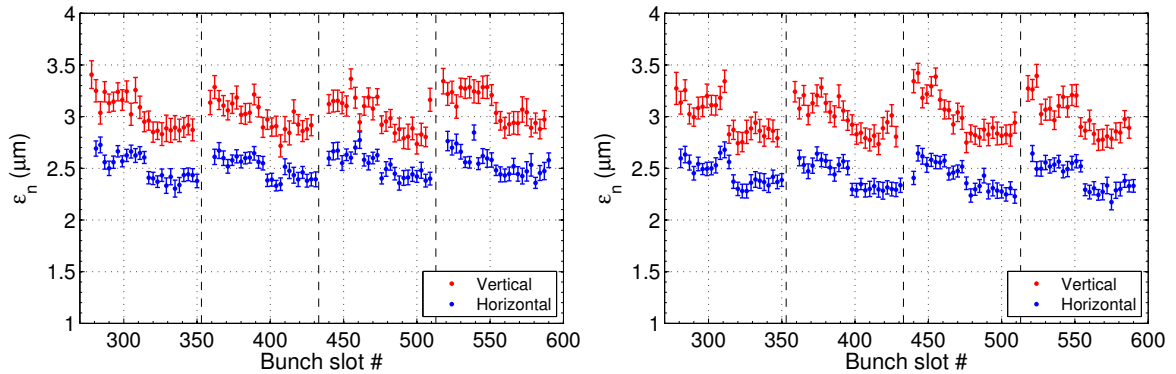


Figure 4.32: Example for the bunch-by-bunch emittances of the 25 ns beam (sample of every third bunch) measured right after injection of the fourth batch (left) and measured at about 20 s in the cycle (right) using the wire-scanners BWS.416H and BWS.519V for the horizontal and vertical planes, respectively. The error bars are deduced from the fit parameter uncertainty of the Gaussian fit of the beam profiles.

25 ns LHC beam in the SPS steadily improved. In addition to that, the dynamic pressure rise typically observed together with EC build-up was also reduced in the course of these scrubbing runs and is nowadays, although still present with 25 ns beams, orders of magnitude smaller compared to the first injection tests in 2000 (typically on the order of 10^{-8} mbar). During machine studies in 2012, the PS delivered batches of 72 bunches of the *nominal* LHC beam with around 1.25×10^{11} p/b with normalized transverse emittances of around $2.5 \mu\text{m}$. In order to study possible detrimental effects due to EC, four batches were injected on a flat bottom cycle with an injection plateau of more than 20 s. For these studies the Q26 optics was used in order to allow for direct comparison with previous results and observations. Figure 4.32 shows the result of bunch-by-bunch emittance measurements for two different acquisition times in the cycle, namely right after the injection of the fourth batch (left) and at the end of the flat bottom at around 20 s (right). Since the total number of acquisitions per measurement is limited by the memory of the wire-scanner front-end, a sample of every third bunch was recorded in each shot. Here the error bars correspond to the uncertainty of the fit parameter for the individual Gaussian fits without any systematic errors. All four batches in the SPS exhibit very similar emittance behaviour along the bunch train. It is worth pointing out that the measured emittances in the first half of each batch in the SPS are slightly larger compared to the second half. This structure can only be explained by differences of the beam characteristics already at or due to their injection in the PS¹⁸. The measurements thus confirm that until 2012 the SPS has

¹⁸The 72 bunches of each SPS batch are produced by multiple longitudinal splitting of six bunches in the PS [61]. These six bunches are extracted from two consecutive PSB cycles, which deliver single bunches from four and two booster rings respectively. Thus, the first $4 \times 12 = 48$ bunches of each SPS batch are treated equally on the PS flat bottom and any difference in their emittance

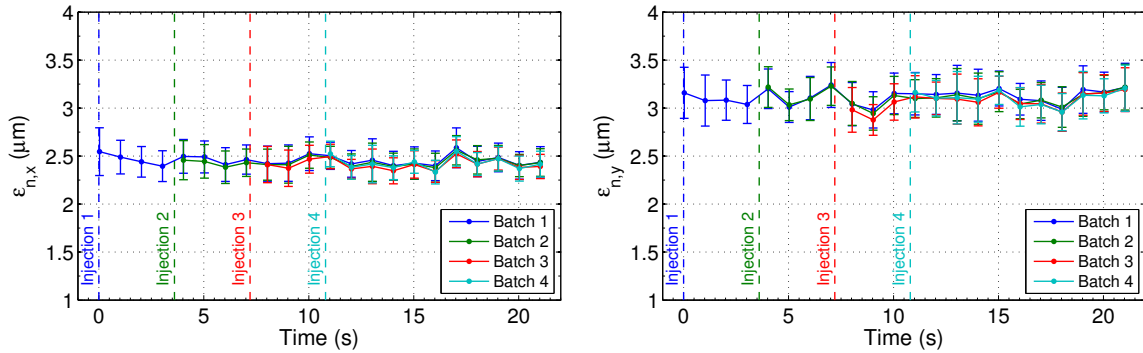


Figure 4.33: Bunch-by-bunch emittance in the horizontal (left) and the vertical plane (right) plotted as average per batch versus time along the SPS long flat bottom cycle. The error bars indicate the rms spread within the batch over three measurements.

been well scrubbed and the 25 ns LHC beam presently does not suffer from degradation due to EC effects at nominal intensity (1.25×10^{11} p/b at injection). In particular, no significant emittance growth is observed on the 20s long flat bottom (i.e. around 10s storage time with four batches): Figure 4.33 shows the evolution of the average transverse emittances per batch as a function of time along the cycle using a series of measurements as described above. In particular, each data point corresponds to the average emittance per batch (as obtained from three bunch-by-bunch measurements) and the error bars indicate the corresponding spread of measured emittances. Within these error bars, the transverse beam size is conserved all along the long flat bottom. It is interesting to note that the obtained average emittances of the four batches seem strongly correlated. This can be explained by systematic noise effects, which affect the bunch-by-bunch emittance measurement of all four batches in the same way.

In addition to the transverse feedback controlling coupled bunch instabilities, large positive vertical chromaticity ($\xi_y > 0.5$) was needed in the past [139] for mitigating the electron cloud driven fast instability in the vertical plane when one or more batches of 25 ns beams were injected into the SPS. In 2012, this instability was not observed when running with the typical operational chromaticity settings ($\xi_y \approx 0.2$). The chromaticity setting has a direct impact on coherent instabilities but also on the beam lifetime. Figure 4.34 (left) shows the total intensity along the second part of the cycle for different settings of vertical chromaticity for 288 bunches of around 1.2×10^{11} p/b. Incoherent effects for large chromaticity significantly reduce the lifetime. In fact the best lifetime is obtained for ξ_y between 0.1 and 0.3, as shown in Fig. 4.34 (right). For these settings no coherent instabilities were observed. However, it should be mentioned that instabilities of bunches in the third and fourth batch were observed for lower chromaticity settings ($\xi_y \approx 0.05$), which could be related to either EC effects or simply to the machine impedance.

(and intensity) could be attributed to intensity differences between the PSB rings.

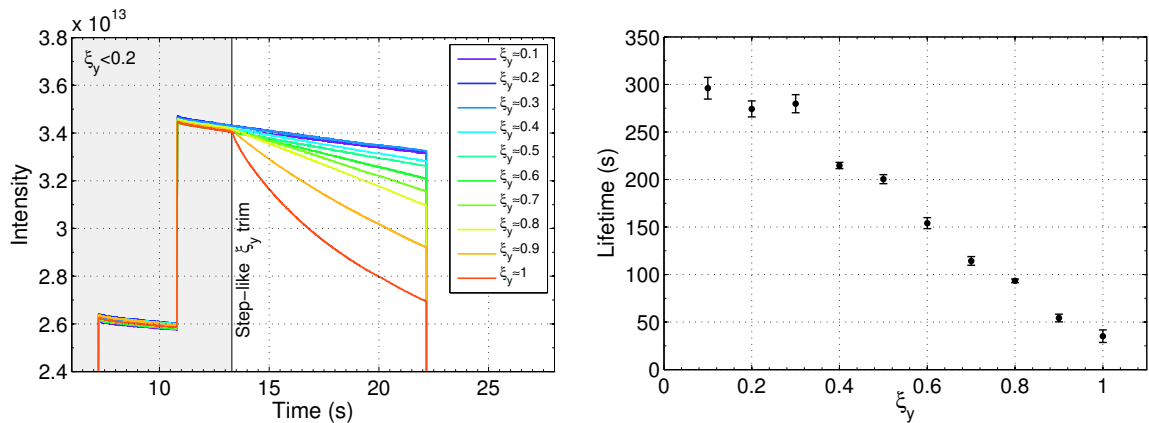


Figure 4.34: Total intensity along the cycle when changing the vertical chromaticity at around 13 s in the cycle from $\xi_y < 0.2$ to the values indicated by the color code (left) and the corresponding average beam lifetime as function of the chromaticity (right).

Finally, the 25 ns beam with ultimate intensity (around 1.8×10^{11} p/b) was injected on the long at bottom cycle only for a few hours during the 2012 scrubbing run [138] due to limitations coming from the heating of the non-serigraphed MKE kicker and strong dynamic pressure rise (vacuum spikes). These limitations were also the reason why only a maximum of three batches could be injected. Unfortunately, the bunch-by-bunch mode of the wire scanners was not fully operational at that moment. Emittance measurements using the turn acquisition mode were only performed with two batches. Therefore, no conclusions on the beam quality and detrimental effects from the EC for high intensity beams could be drawn from these experiments. However, a clear reduction of the beam lifetime along the 20 s flat bottom compared to the beam with the nominal intensity was observed.

Measurements at flat top - Q20

In the second half of 2012, a series of machine studies were devoted to 25 ns beams with the Q20 optics. Rather than performing a direct comparison with the previously discussed measurements in the Q26 optics, the focus was put on increasing the beam intensity and on acceleration to 450 GeV/c. The aim was to identify performance limitations and the achievable beam parameters at extraction to the LHC in the present conditioning state of the SPS. Therefore the studies concerned two main aspects. Firstly, optimization of the RF settings for achieving longitudinal beam stability up to flat top (as discussed already in Section 4.6.1). Secondly, careful monitoring of the transverse emittances using the wire scanners in bunch-by-bunch mode in order to identify possible beam degradation due to coherent and incoherent EC or any other intensity effects. As expected from the measurements with the Q26 optics, no indication for emittance blow-up or beam instabilities was observed for four batches of the 25 ns beam with nominal intensity ($N \approx 1.20 \times 10^{11}$ p/b at injection) in the Q20

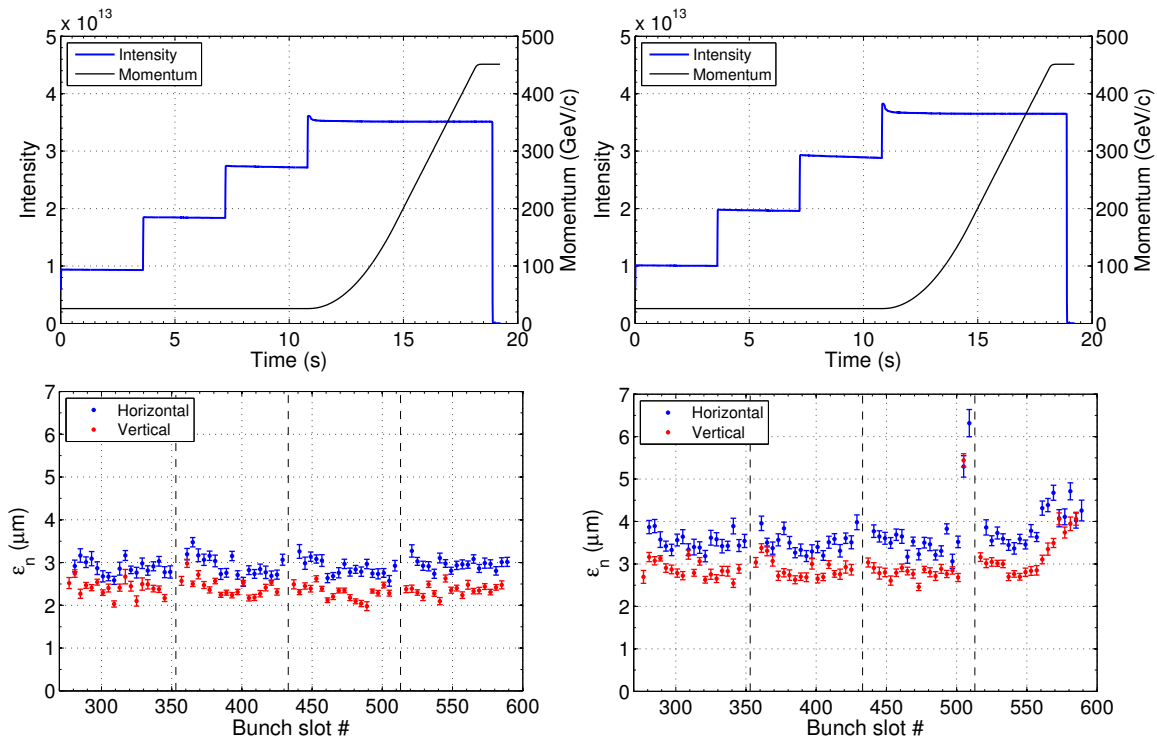


Figure 4.35: Typical example for the total beam intensity along the cycle for the 25 ns beam with four batches of 72 bunches (top) and the corresponding bunch-by-bunch transverse emittances measured at flat top (bottom) in the Q20 optics using the wire scanners BWS.416H and BWS.519V. The error bars are deduced from the fit parameter uncertainty. The plots show measurements for two different intensities corresponding to $N \approx 1.30 \times 10^{11}$ p/b (left) and $N \approx 1.40 \times 10^{11}$ p/b (right) at injection.

optics and typical chromaticity settings, despite the dynamic pressure rise usually observed in the presence of LHC beams with 25 ns bunch spacing (on the order of a few 10^{-8} mbar). Even for slightly higher intensity, i.e. $N \approx 1.30 \times 10^{11}$ p/b at injection, no beam degradation due to EC effects could be observed when measuring the bunch-by-bunch emittance of the four batches of 72 bunches after ramping to top energy as shown in Fig. 4.35 (left). However, when increasing the intensity of the injected beam to about $N \approx 1.40 \times 10^{11}$ p/b, emittance blow-up of the trailing bunches of the fourth and sometimes also of the third batch could be observed at flat top, as shown in Fig. 4.35 (right). Emittance measurements at the end of the flat bottom showed that this blow-up happens already at injection energy¹⁹. This blow-up is probably caused by a fast instability right after injection, since in some cases losses for the corresponding bunches could be observed on the Fast Beam Current Transformer (FBCT). It was tried to stabilize the beam by increasing the chromaticity and increasing the gain of the

¹⁹These measurements were performed on a modified magnetic cycle with a 300 ms longer flat bottom during another machine development session.

transverse feedback. However during the available machine study sessions in 2012, stable beam conditions for an intensity of $N \approx 1.40 \times 10^{11}$ p/b or higher were not achieved. Further studies and optimization would be needed to see if the observed instability can be cured by optimizing the chromaticity and the transverse damper settings. Although it cannot be concluded from any direct measurement, the observations of the losses and emittance blow-up of trailing bunches of the train in combination with the dynamic pressure rise always observed with the 25 ns beam are strong indications for EC effects.

The spatial EC distribution was measured in the presence of a dipole field using dedicated Electron cloud strip detectors [140] with vacuum chambers reproducing those of the two types of SPS dipole chambers.²⁰ Consistent with numerical simulations [141], it was observed that the electrons are concentrated in the center for low bunch intensities, while for increasing intensity the region covered by the EC gets wider with most of the electrons located in two outer stripes [142]. It should be emphasized that the SPS vacuum chambers were never conditioned with 25 ns beams with high bunch intensities in the past, and thus these outer regions exhibit probably a higher SEY. Therefore, an improvement of the beam quality and reduction of the pressure rise might be obtained gradually after operating the machine extensively with these beam conditions, as for example during a scrubbing run.

In conclusion, EC effects do not to play a role for the beam quality on the time scale of the SPS cycle for intensities up to $N \approx 1.30 \times 10^{11}$ p/b at injection in the present conditioning state of the SPS. For higher intensities, it seems that EC effects are the cause of transverse emittance blow-up and losses of the trailing bunches of the third and fourth batch. In further machine development sessions and scrubbing runs, it will be studied whether these issues can be mitigated by machine conditioning. If not, the LIU project aims at coating the SPS vacuum chambers with a thin film of amorphous Carbon, which provides an SEY close to unity.

Electron cloud instability - simulation studies

The experimental studies performed in 2012 did not aim at a direct comparison between the nominal Q26 and the Q20 optics with respect to EC instabilities or emittance blow-up. Therefore it is interesting to study the impact of the lower transition energy on the threshold of the single bunch EC instability in numerical simulations and eventually compare the results with existing analytical models. The electron cloud build-up around the ring is expected to be similar in the two optics, as the average beam size around the ring is not changed significantly (less than about 20%) and besides, the EC build-up is not very sensitive to the transverse beam sizes. It is thus assumed in the

²⁰The electron cloud strip detectors, also called EC monitors, are used to study the EC formation in controlled conditions, as for example the spatial electron distribution and relative electron densities for different beam conditions and different sample materials inserted. As the stainless steel samples used in the discussed measurements were installed in 2012, they do not exhibit the same conditioning as the vacuum chambers in the regular SPS dipoles and are thus not representative for the conditioning state of the rest of the machine.

Table 4.7: HEADTAIL simulation parameters for EC simulations.

SPS optics	Q20	Q26
Betatron tunes Q_x/Q_y	20.13/20.18	26.13/26.18
$\bar{\beta}_{x,y}$ in straight sections (m)	54.6	42
$\bar{\beta}_x$ in MBB-type dipoles (m)	45.5	34.4
$\bar{\beta}_y$ in MBB-type dipoles (m)	78.4	72.3
\bar{D}_x in MBB dipoles (m)	3.0	1.8
Gamma at transition γ_t	18	22.8
γ_0	27.7	27.7
Synchrotron tune Q_s	0.017	0.0059
RF-voltage at 200 MHz, V_{200} (MV)	5.75	2
Chromaticity Q'_x/Q'_y	0/0	0/0
Normalized transverse emittances ε_n (μm)	2.5	2.5
Bunch length σ_l (m)	0.23	0.23
Momentum spread δ_{rms}	0.002	0.002
Number of kick sections	57	57
Number of bunch slices	50	50
size of the electron grid	$20 \times \sigma_x, 20 \times \sigma_y$	$20 \times \sigma_x, 20 \times \sigma_y$

following that the electron density around the machine *is the same for the two optics*. It is not attempted to provide an exact prediction for the EC instability thresholds in the two optics, in particular since the studies presented here are based on simplified assumptions. It is rather intended to obtain a relative scaling of the EC instability threshold between the Q26 and the Q20 optics in particular at injection energy, at which EC effects in the SPS are usually most critical.

Macroparticle simulations were performed with the HEADTAIL tracking code [116]. The simulation parameters used in the following studies are summarized in Table 4.7. Note that for the simulations in the bending magnets the parameters of the MBB type dipoles are chosen, as their vertical aperture results in a lower SEY threshold for the EC build-up and thus a higher electron density compared to the MBA dipoles. In HEADTAIL, the EC is represented by thin slices of macroparticles distributed at discrete positions around the machine circumference. For simplicity, the EC is initialized with a uniform spatial distribution of electrons with zero velocity. The interaction of the bunch macroparticles with the electrons is computed by a Particle-In-Cell (PIC) solver, such that the bunch slices interact consecutively with the EC. An instability can be triggered, since the motion of subsequent slices is coupled through the distortion of the EC distribution induced by the passing bunch, i.e. the EC acts as a wake field. In order to limit incoherent emittance growth due to numerical artifacts, the EC is distributed over 57 evenly spaced interaction points. After a complete bunch passage the EC is reset to the initial distribution for the next interaction

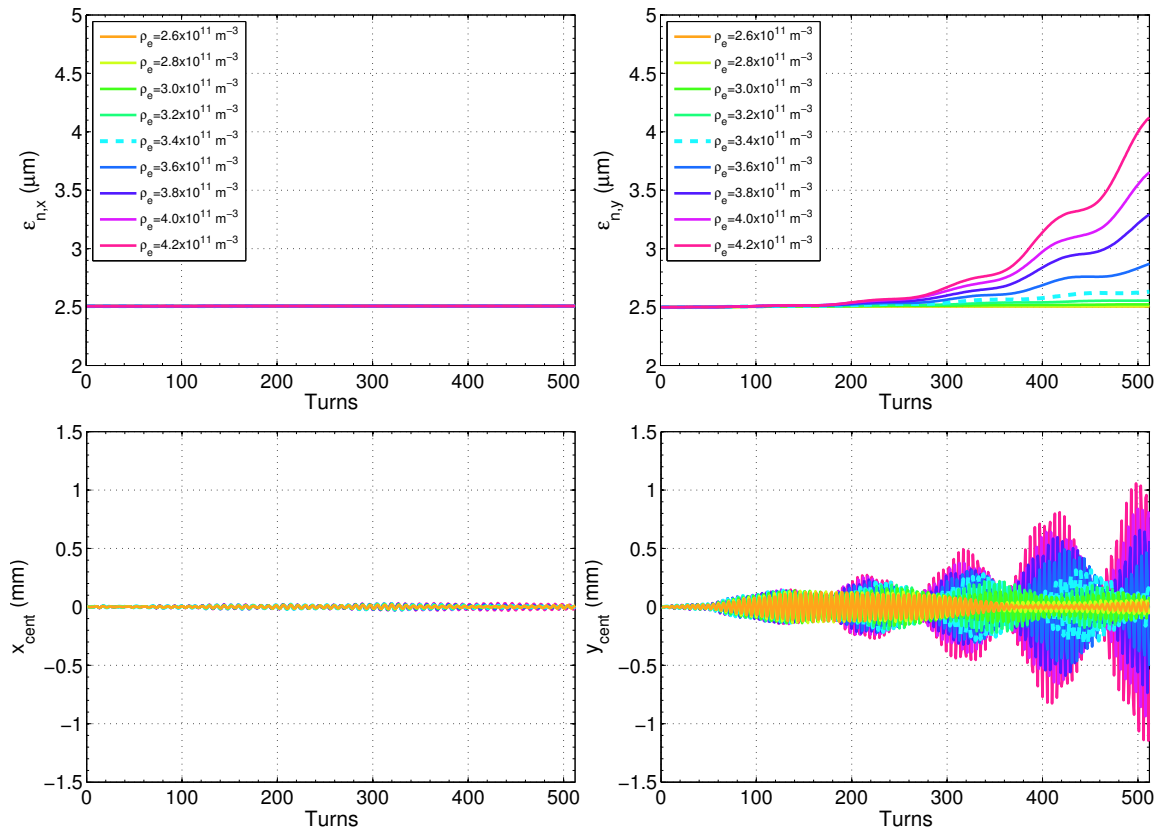


Figure 4.36: HEADTAIL simulations with $N = 1.3 \times 10^{11}$ p/b for the Q26 optics in bending magnets, showing the evolution of the horizontal (left) and vertical (right) normalized emittances (top) for different electron cloud densities as indicated by the color-code and the corresponding vertical centroid motion (bottom). The dashed line marks the threshold electron density $\rho_{e,\text{thr}} = 3.4 \times 10^{11} \text{ m}^{-3}$.

section. Unless stated otherwise, it is assumed in the following that the electrons are located in the magnetic field of the main bending magnets of the machine, since they represent the major part of the machine circumference. Due to the external magnetic field in the vertical direction, the electrons can move freely only in the vertical plane but are bound close to the field lines in the horizontal plane (cyclotron motion). This is modeled by freezing the electron motion in the horizontal plane (strong magnetic field approximation). The EC instability affects then only the vertical plane and can be observed as an exponential growth of the vertical emittance due to the increasing amplitude of the coherent headtail motion.

Figure 4.36 shows the evolution of the horizontal (left) and vertical (right) emittance (top) and the corresponding centroid motion (bottom) for the Q26 optics at injection energy simulated with HEADTAIL for different electron densities ρ_e . Since the simulation was performed for dipole magnets (cf. Table 4.7) and thus the electron motion is bound to the vertical direction, no instability is observed in the horizontal

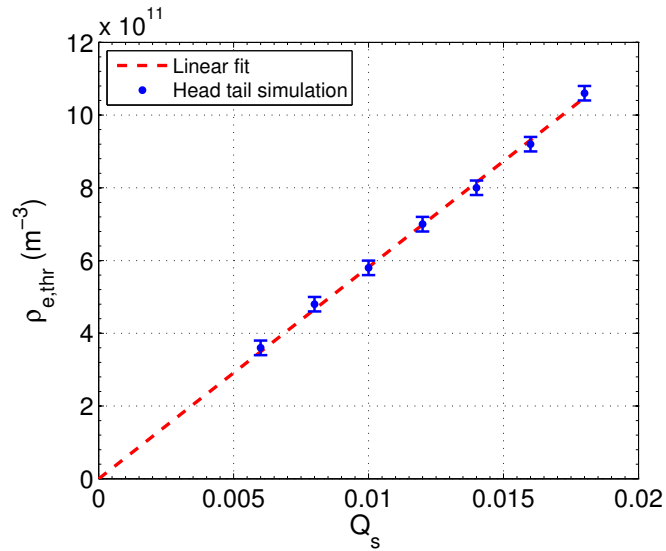


Figure 4.37: HEADTAIL simulations yielding the instability threshold density $\rho_{e,\text{thr}}$ as function of the synchrotron tune Q_s for constant bunch parameters. Simulated points are compared with the predicted linear dependence. The “error bars” of the threshold densities indicate the step size between consecutive ρ_e values in the corresponding simulation series.

plane. On the other hand, coherent oscillations with exponentially growing amplitude are excited in the vertical plane for electron densities above the threshold value $\rho_{e,\text{thr}}$ (marked by a dashed line), which is also observed in the form of coherent emittance growth. The threshold density is defined here as the lowest electron density for which an emittance growth of more than 5% is observed within the simulated 512 turns. Note that this interval corresponds to three synchrotron periods in the Q26 optics at injection energy.

As the synchrotron motion is significantly faster in the Q20 optics due the higher slip factor compared to the Q26 optics, it is interesting to study the dependence of the instability threshold on the synchrotron tune Q_s . Therefore a series of simulations were performed for different values of Q_s . The variation of Q_s is achieved by changing the transition energy (momentum compaction factor) and adapting the RF-voltage proportional to the slip factor η for keeping the bucket area constant. In this way the longitudinal bunch parameters like momentum spread and bunch length remain constant. Figure 4.37 shows the scaling of the instability threshold density $\rho_{e,\text{thr}}$ for the case of the MBB dipoles as obtained by a series of HEADTAIL simulations. For each setting of Q_s , a scan of the electron density was performed. The threshold density $\rho_{e,\text{thr}}$ is obtained here as the lowest electron density for which the vertical emittance growth exceeds 5% within *three synchrotron periods*. The resulting dependence of $\rho_{e,\text{thr}}$ can be fitted in good agreement with a linear dependence on the synchrotron tune Q_s . This is consistent with analytical descriptions of the single bunch EC instability as a

fast head-tail (or TMC) instability: a simple model is based on the two particle model, which yields [132] for the EC driven instability a threshold electron density of

$$\rho_{e,\text{thr}} = \frac{2\gamma_0 Q_s}{\pi r_p C \beta_y}, \quad (4.19)$$

where $r_p = e^2/(4\pi\epsilon_0 mc^2) = 1.54 \times 10^{-18}$ m is the classical particle radius of a proton and C is the machine circumference. It should be emphasized that in this simplified picture, the threshold electron density for the fast head-tail instability does not depend on the intensity of the proton bunch as it was assumed that the integrated wake field per revolution can be estimated as $W_0 \approx 8\pi\rho_e C/N$ and thus the dependence on the bunch intensity N cancels out. Therefore this formula gives only a rough estimate of the threshold density with the correct order of magnitude (for the parameters of the Q26 optics $\rho_{e,\text{thr}} \approx 1.4 \times 10^{11} \text{ m}^{-3}$). However, the dependence on the synchrotron tune Q_s is in excellent agreement with the numerical simulations. The same functional dependence on Q_s for given longitudinal bunch parameters was also found by treating the EC instability in the framework of TMC instabilities and approximating the wake field of the electron cloud as broadband resonator [77, 78].

As discussed already in great detail in Section 4.3, changing the optics of the SPS from the Q26 to the Q20 optics leads to slightly larger beta functions. This will on one hand make the kick of the EC on the beam particles more effective and thus reduce the threshold electron density as accounted for in the two particle model in Eq. (4.19). On the other hand, the larger beam size reduces the proton charge density and therefore results in a weaker pinching of the electrons, i.e. smaller electron oscillation frequency and smaller amplitude, which will raise the instability threshold density. This dependence on the beam size was already realized in simulation studies concerning the energy dependence of the single bunch electron cloud instability threshold in the course of the PS2 project [58], however the beam size variation was due to the different beam energies considered. In order to study the dependence on the optics functions, a set of simulations as described above is repeated for different values of the beta functions. Note that here the dispersion function was set to zero in order to restrict the variation of the beam size to the beta function dependence. It should be emphasized that the machine optics is modelled by HEADTAIL as a uniform focusing channel, i.e. using the smooth approximation. Therefore, only the average beta function is changed in the code. This is of course not reflecting local differences in the beam sizes for different optics. Nevertheless, a first idea of the impact of different optical functions can be obtained. Figure 4.38 shows the dependence of $\rho_{e,\text{thr}}$ on changes of β_x and β_y assuming that the electron cloud is located in the magnetic field of the bending magnets. The machine parameters of the Q26 optics are used (apart from the dispersion which is set to zero). Similar as before, the threshold density is defined as lowest electron density for which the emittance growth over three synchrotron periods (512 turns) exceeds 5%. Note that the threshold density $\rho_{e,\text{thr}}$ decreases for larger values of the beta functions. In fact, fitting the obtained results with a power function yields a dependence like

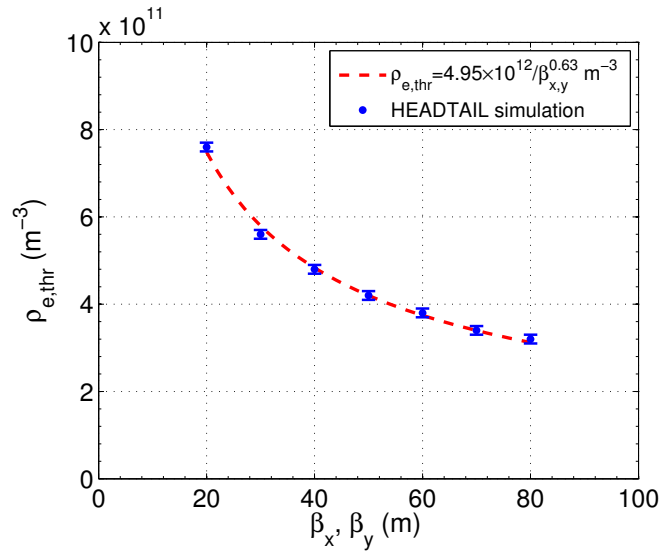


Figure 4.38: HEADTAIL simulations yielding the instability threshold density $\rho_{e,thr}$ as function of β_y in the bending magnets. The “error bars” of the threshold densities indicate the step size between consecutive ρ_e values in the corresponding simulation series.

$\rho_{e,thr} \propto 1/\beta_{x,y}^{0.63}$. Clearly, the simplified analytical models do not incorporate all subtle details of the electron proton interaction causing the ECI. Therefore a semi-analytical approach was developed in the past [77], where the wake field of the electron cloud was obtained from numerical simulations and then fitted by a broadband resonator impedance. However, this approach does not allow to express a functional dependence of the threshold density on the beta functions in a closed form.

Based on the above results, it can be inferred that the threshold electron density for the EC instability will be higher in the Q20 optics compared to the nominal optics. This is demonstrated in a series of simulations for the two optics using the parameters summarized in Table 4.7. Simulations were performed for different beam intensities in order to cover the target parameter range of the HL-LHC project [12]. Note that in this study the longitudinal and transverse emittances are assumed to be constant independent of the beam intensity (the HL-LHC project requires transverse emittances of about $\varepsilon_n \approx 2\mu m$ in both planes). While high chromaticity in the vertical plane is one of the measures for mitigating the electron cloud instability in the SPS, the simulations are carried out with zero chromaticity in order to simplify the comparison. Figure 4.39 shows the obtained threshold electron density $\rho_{e,thr}$ at injection energy as function of the bunch intensity N , for simulations of the EC located in field free regions (left) or in the MBB dipoles (right). In both cases, the threshold electron density $\rho_{e,thr}$ is around twice higher in the Q20 optics compared to the nominal optics. The difference between the two optics seems to be more significant at lower bunch intensities. In field free regions, the electrons can move freely in both transverse directions and thus

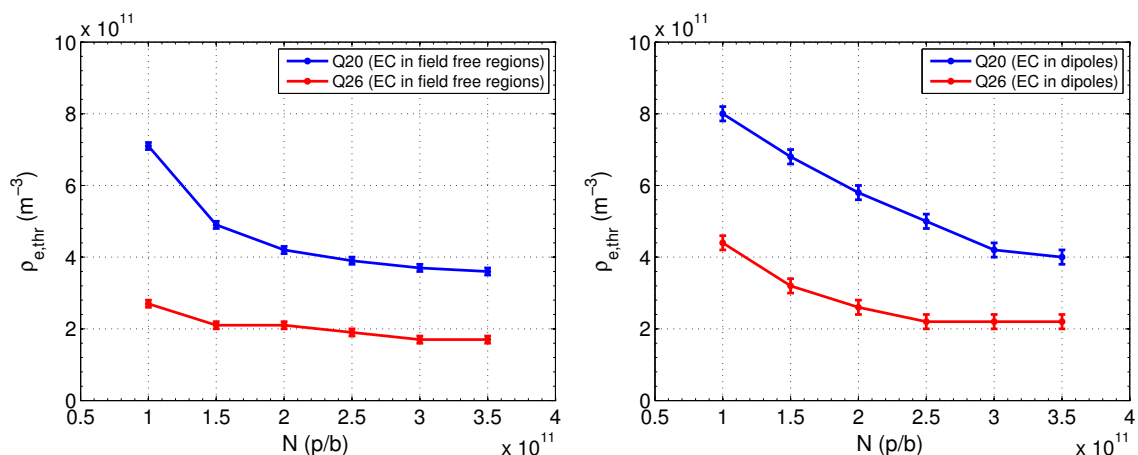


Figure 4.39: HEADTAIL simulations yielding the instability threshold density $\rho_{e,thr}$ as function of intensity per bunch comparing the Q26 with the Q20 optics, for field free regions (left) and for the EC located in MBB dipoles (right). The “error bars” of the threshold densities indicate the step size between consecutive ρ_e values in the corresponding simulation series.

the proton bunch can become unstable in both planes. However, the beam stability is observed to be more critical in the vertical plane. Since the beam has to stay the same number of turns in the machine irrespective of the optics and the synchrotron tune, the instability threshold is defined here as the lowest electron density for which the emittance grows by more than 5% within the full simulation interval of 512 turns²¹. Note that the instability thresholds are slightly lower in the field free regions. However the areas with bending magnets are nevertheless more critical, since they represent the majority of the machine circumference.

In conclusion, the numerical simulations presented above predict about twice higher thresholds for the EC driven single bunch instability in the Q20 optics due to the faster synchrotron motion. It should be emphasized however, that these simulations are based on the simplified assumption of a uniform initial electron distribution. Therefore it would be interesting to study the behavior of the instability thresholds in the two optics using a more realistic initial electron distribution (consisting of two vertical stripes for the case of the bending magnets) instead, as done in studies for the LHC [143]. In order to obtain a full picture about the implications of the higher intensity and increased beam brightness as foreseen in the upgrade programs, further simulations with different transverse emittances need to be performed. As already shown in [58], smaller emittances reduce the instability threshold and are thus more critical for beam stability similar to higher bunch intensity. Finally, the case of the flat top in the SPS could be studied, since the ratio of η in the two optics rapidly

²¹This definition is favorable for the Q26 optics, as the 512 turns correspond to three synchrotron periods only compared to almost nine synchrotron periods in the Q20 optics.

drops from 2.85 at injection to 1.6 at top energy and in addition the total RF voltage is limited to $V_{200} \leq 7.5 \text{ MV}$ and thus the beneficial effect of the lower γ_t is less pronounced. Considering furthermore the higher beta functions in the Q20 optics, the threshold electron density could be quite similar in the two optics. However, it should be emphasized that, from the experience in the SPS with the nominal optics, the low energy part of the cycle is more critical with respect to EC effects. This is probably due to the controlled longitudinal emittance blow-up during the high energy part of the ramp (cf. Section 4.6.1), which seems to be beneficial also for the mitigation of EC effects.

4.7. Low gamma transition optics - operational deployment

4.7.1. Overview

As indicated already before, changing the optics of the SPS to Q20 does not require hardware modifications. Therefore it was possible to perform a series of machine studies in parallel to normal physics operation, as discussed above. After an extensive period of experiments and successful validation tests in 2012, it was decided to deploy the Q20 optics in routine operation for LHC filling. A short timeline of the main milestones of the deployment of the Q20 optics for LHC proton beams is listed below. Further details can be found in reference [144].

- *July 2010*, in the SPSU beam dynamics working group it was proposed to test the Q20 optics experimentally [83];
- *November 2010*, first beam set-up in short flat bottom cycle and a fast ramping cycle, achieving more than 3×10^{11} p/b in single bunches with emittances below $3 \mu\text{m}$ with very low chromaticity and low losses;
- *May-June 2011*, optimized settings for LHC single bunches along the ramp (including capture voltage) and evaluated emittance vs intensity;
- *July 2011*, proved stability of longitudinal beam parameters for 50 ns beam up to intensities of $N \approx 1.6 \times 10^{11}$ p/b;
- *November 2011*, set-up of the Q20 LHC-type cycle for 25 ns beams (two batches) with $N \approx 1.1 \times 10^{11}$ p/b and 50 ns beams with $N \approx 1.7 \times 10^{11}$ p/b at flat top
- *February 2012*, during the Chamonix 2012 LHC performance workshop, it was proposed to switch SPS operation for LHC 50 ns beams to Q20 optics by fall 2012;
- *April 2012*, implemented new TT10 transfer line optics matched to the Q20 optics;

- *May 2012*, preparation of the extraction from the Q20 optics, including rematching of LHC transfer lines [94] and setup of the extraction bumps and extraction elements;
- *June 2012*, set-up of the beam transfer from the Q20 optics to the LHC during a machine development session [95]; Injected high brightness single bunches of $N \approx 3 \times 10^{11}$ p/b with $\varepsilon_n \approx 2 \mu\text{m}$ to the LHC for the first time;
- *July 2012*, decided in LHC Machine Committee (LMC) 141 to perform necessary commissioning steps to deploy Q20 operationally in September 2012;
- *August 2012*, tested injection into the LHC with 50 ns beams. First ramp and squeeze for both beams delivered by the SPS Q20 optics.
- *September 2012*, final set-up of the extraction and beam transfer [123]. SPS starts delivering 50 ns beam to the LHC with Q20 on 29/09/2012 - Q20 is the operational optics for LHC beams in the SPS;
- *October 2012*, first injection of 25 ns beam into the LHC from the SPS Q20 optics;
- *November 2012*, preparation of the 25 ns beam with higher than nominal intensity for the LHC scrubbing run;
- *December 2012*, delivered high brightness BCMS beams [128] to the LHC: 50 ns version for testing emittance preservation up to LHC collision and 25 ns version for the LHC pilot physics run;
- *January-February 2013*, ion beams were delivered to the LHC with the Q20 optics for the p-Pb run;

Thanks to the excellent performance and the successful injection tests in summer 2012, the Q20 became operational for LHC filling after the Technical stop 3 and delivered 50 ns beams for physics since the end of September 2012. With the typical intensity of $N \approx 1.7 \times 10^{11}$ p/b at flat top, minor controlled longitudinal emittance blow-up on the ramp was sufficient for ensuring longitudinal beam stability in the SPS. At extraction, the longitudinal emittance was thus slightly smaller compared to the operation with the Q26 optics and the bunch length was slightly larger, i.e. $\varepsilon_l \approx 0.45$ eVs and $\tau \approx 1.6$ ns in Q20 compared to $\varepsilon_l \approx 0.5$ eVs and $\tau \approx 1.5$ ns in Q26 [124]. In order to minimize horizontal emittance blow-up due to Intrabeam Scattering (IBS) on the LHC flat bottom, batch-by-batch longitudinal emittance blow-up was performed in the LHC right after each injection [145] in routine operation after switching to the Q20 optics. Its mitigating effect on the horizontal emittance growth was demonstrated in MD studies [146].

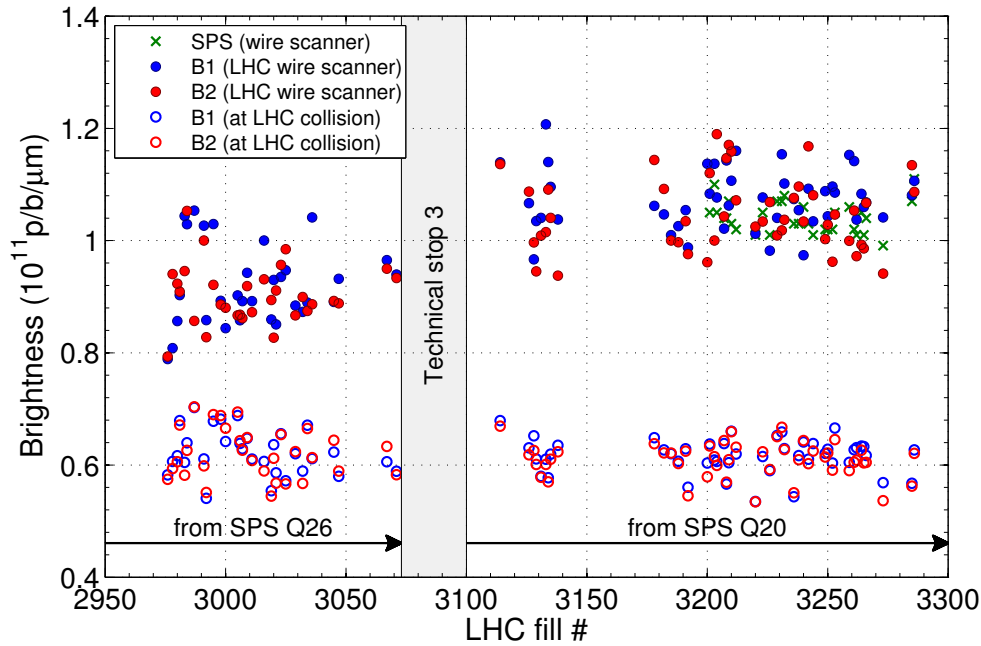


Figure 4.40: Mean intensity divided by mean normalized emittance (brightness) along the second half of the 2012 LHC physics run with 50 ns bunch spacing, during the SPS operation with the Q26 optics (before Technical stop 3) and the Q20 optics (after Technical stop 3). Measurements for beam 1 and beam 2 were performed with the LHC wire scanners right after injection of the first batch (full markers). For comparison the brightness obtained from the emittance measurement at the end of the SPS flat bottom (crosses) and the brightness obtained from the convoluted emittance determined from the specific luminosity at the beginning of collision in the LHC (circles) are also shown. The error bars (not shown) are typically on the order of 10-20%.

4.7.2. Operational performance

Due to intermittent problems with the SPS wire scanners related to the high intensity of the LHC beams, it was not possible to reliably monitor the beam brightness at extraction for each LHC fill. Thus a performance comparison between the two optics is difficult. However, the transverse emittance is measured in the LHC after the injection of the first batch for practically each physics fill. The beam brightness provided by the different SPS optics can be deduced therefore from the measurements on the LHC flat bottom. Figure 4.40 shows the evolution of the mean intensity per bunch divided by the mean transverse emittance of the first batch of 144 bunches for physics fills in the second half of 2012 [147]. Measurements obtained with the LHC wire scanners right after injection show a clear trend of about 15% higher brightness for the period after switching to the Q20 optics. These measurements are in good agreement with the brightness determined from wire scanner measurements at the end of the SPS flat

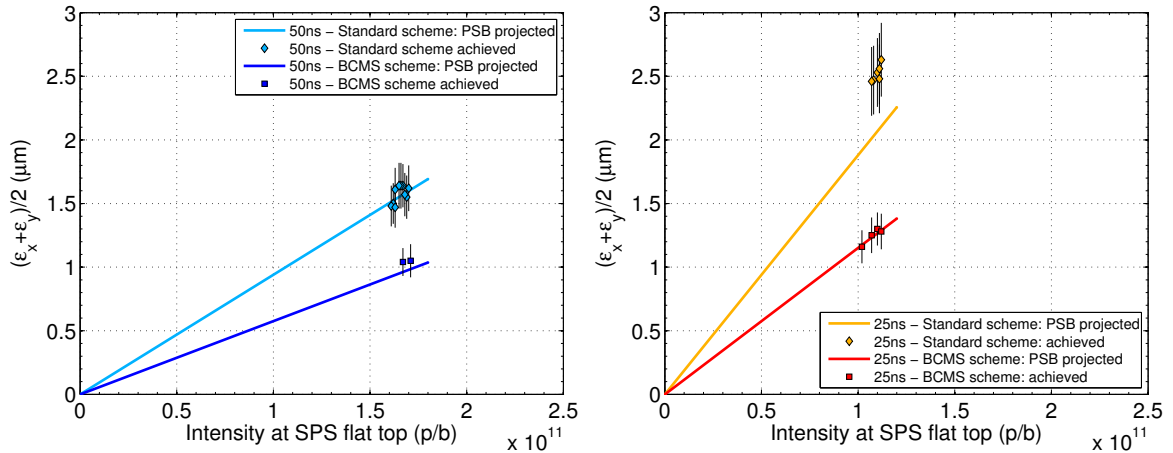


Figure 4.41: Beam parameters achieved in the SPS in 2012 with the Q20 optics for 50 ns beams (left) and 25 ns beams (right) extracted to the LHC. For more details, see description in the text.

bottom (using BWS.416H and BWS.519V) and the intensity at extraction. This is a clear indication for the excellent brightness preservation between the two machines. However, despite the higher beam brightness at LHC injection after switching to Q20, the brightness at the LHC flat top (beginning of colliding beams) as obtained from the measured luminosity was observed to remain constant (circles) and so no gain in terms of peak luminosity was achieved yet. In fact, although the specific luminosity of certain bunches was indeed much higher than before switching to Q20, other bunches seemed to have reduced luminosity due to an increased emittance blow-up along the LHC cycle [146]. In general, the reasons for the large emittance blow-up in the LHC (up to 40%) are not yet understood and will have to be addressed in the future for fully exploiting the performance potential of the LHC complex.

During the few months of operation with the Q20 optics, the trajectories in the LHC transfer lines had to be corrected more frequently compared to the operation with the Q26 optics. These trajectory corrections are usually performed in order to minimize losses at injection. For both optics and both transfer lines, the SPS extraction septa (MSE) and the orbit at the SPS extraction points were identified as the main sources for trajectory fluctuations [148]. It was found that increased longitudinal losses at injection due to the deliberately enhanced population of satellite bunches in the bunch train were misinterpreted as losses caused by trajectory drifts. In fact, the analysis presented in [148] showed that the orbit reproducibility is rather similar for both optics. The corresponding diagnostic tools in the control room will be improved in the future in order to better guide the steering in the transfer lines.

In addition to the standard 50 ns LHC physics beam, a variety of other beam types were delivered by the SPS Q20 optics to the LHC. Figure 4.41 shows an overview of the

best performance achieved for different beam types with 50 ns (left) and 25 ns bunch spacing (right) delivered in the end of 2012, in terms of average transverse emittance as function of average intensity per bunch. All emittance values are determined from wire scans (using BWS.416H and BWS.519V) at the end of the SPS flat bottom in order to profit from the higher resolution at low energy. It should be emphasized that these measurements are in good agreement with the emittance values obtained on the LHC flat bottom right after injection. The error bars include the statistical uncertainty (several measurements) and a systematic uncertainty (assumed as 10%). The intensity is measured at extraction, i.e. after the usual cleaning of beam tails with scrapers (cf. Section 4.6). The obtained brightness is compared with a projection of the beam parameters measured in the PSB in 2012 as reported in [149]²² to the SPS, taking into account the LIU budgets for emittance growth and losses of 5% in each case for the PS and 10% for the SPS, respectively. In the case of the 50 ns beam produced with the traditional bunch splitting scheme in the PS, the obtained brightness in the SPS agrees well with the projection of the PSB measurements. This is plausible as this was the LHC physics beam in 2012 and it was thus continuously and carefully optimized across the whole injector chain. The 50 ns BCMS beam was used only for a few times in order to study the emittance preservation from the injectors up to LHC flat top and the increase in luminosity due to lower emittances. Nevertheless, the achieved performance is close to the projected line. The nominal 25 ns beam (standard scheme) used for the LHC scrubbing run in December 2012 is below the expectation from the PSB measurements. The reason for that is not clear yet. Possible explanations could be incoherent emittance blow-up due to space charge effects in the PS or EC effects in the SPS, or slow losses on the SPS flat bottom due to the larger transverse beam size compared to the other beam types. It might also be that this beam was simply not as thoroughly optimized compared to the 50 ns physics beam. Finally, the performance of the BCMS variant of the 25 ns beam agrees again well with the projection from the PSB data. It should be emphasized that this beam was not suffering from EC instabilities or incoherent emittance growth in the SPS. Note that it was not possible to inject more than three batches of the BCMS beams into the SPS due to technical reasons (cf. Section 4.6.3) and each of these batches had only 48 bunches instead of the usual 72. Therefore the EC build-up was much less critical compared to the standard 25 ns beam.

In the middle of February 2013, the LHC and the CERN accelerator chain entered the first long shutdown period of the LHC era (LS1). They are presently undergoing consolidation and maintenance works. They will be gradually start operation again in the second half of 2014 in order to be ready for the LHC Run II in 2015.

²²The average transverse emittance at extraction from the PSB was measured for Ring 3 as function of intensity, showing a dependence like $\varepsilon_n = (1.16 \times 10^{-12} \times N + 0.04) \mu\text{m}$ for the beam with a longitudinal emittance of $\varepsilon_l \approx 1.19 \text{ eVs}$ used for the traditional bunch splitting schemes in the PS and similarly $\varepsilon_n = (1.42 \times 10^{-12} \times N + 0.03) \mu\text{m}$ for the beam with $\varepsilon_l \approx 0.86 \text{ eVs}$ as required for the BCMS production scheme in the PS.

4.8. Outlook

4.8.1. Future studies

The Q20 optics was successfully deployed as operational optics for LHC beams in the SPS in the last part of the 2012 run. As the SPS was able to deliver 50 ns beams with higher brightness compared to the Q20 optics and there were no fundamental problems or issues found during operation, the Q20 optics will be used as default machine configuration for LHC beams in the future. Remaining questions in view of the high intensity and high brightness beams envisaged for the HL-LHC era [12] mainly concern longitudinal instabilities and electron cloud effects for beams with 25 ns bunch spacing.

After the implementation of the Q20 optics and the mitigation of the TMCI instability, longitudinal instabilities and beam loading remain the biggest challenges for high intensity LHC-type beams in the SPS. Future experimental studies will aim at maximizing the intensity with 25 ns beams and a better understanding of the longitudinal instabilities encountered in the SPS.

Concerning electron cloud effects, it is not clear yet if the SPS vacuum chambers can be sufficiently conditioned by beam induced electron bombardment (scrubbing) so that beam degradation due to electron cloud effects is suppressed sufficiently. Future studies after the long shutdown should therefore aim at a better understanding of the scrubbing process and other possible electron cloud mitigation measures in order to decide if the SPS vacuum chambers need to be coated for reducing their SEY.

Another subject for future studies is the optimization of the SPS working point for high beam brightness, in particular in case the LHC has to be operated with 50 ns beams due to limitations coming from electron effects in the LHC itself.

Using the Q20 optics for LHC ion beams is also being studied [150], as the larger beam sizes compared to the nominal optics are expected to mitigate not only the space charge tune shift but also Intrabeam Scattering (IBS) effects. In 2013, the SPS Q20 optics was used to deliver both proton and Pb^{82+} ion beams to the LHC for the p-Pb run [151]. A clear benefit from the Q20 optics is shown in simulation studies for space charge and IBS effects for ion beams. Although the improvement is less obvious in measurements, slightly better beam lifetime was observed with the Q20 optics. Further data analysis and simulation studies are ongoing, in order to decide if the Q20 optics should be used in operation also for LHC ion beams in the future.

4.8.2. Split tunes

Although the transition energy in a regular FODO lattice like the SPS is almost entirely determined by the horizontal betatron tune, both transverse tunes were reduced by six integer units in the Q20 optics. However, the associated increase of the minimum beta function values is particularly unfavourable in the vertical plane: a larger beta function at the location of important impedance sources results in a lower intensity threshold

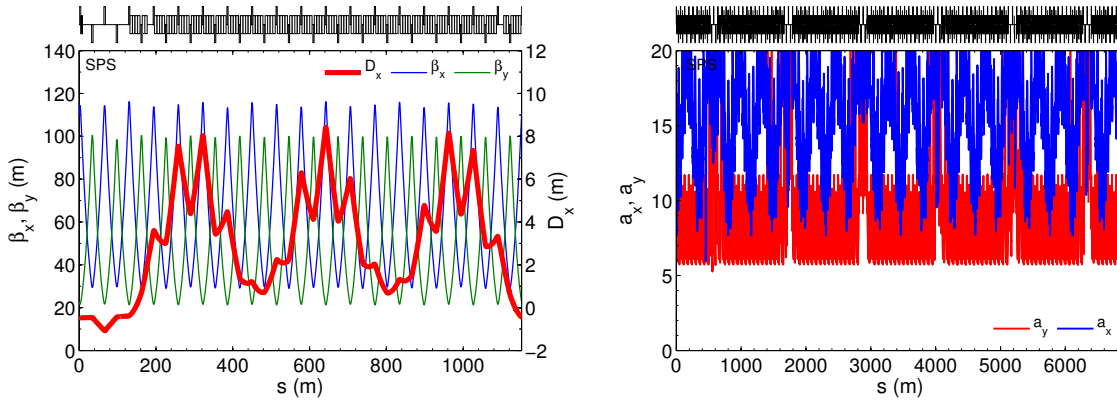


Figure 4.42: Optics functions in one super-period of the SPS (left) for the split tunes ($Q_x, Q_y = 20.13, 26.18$) and the corresponding calculation of the available aperture for the LHC beam at injection into the SPS ($\hat{\delta} = 0.004$, $\varepsilon_{n,x} = \varepsilon_{n,y} = 3.5 \mu\text{m}$), assuming $k_\beta = 0.05$, $k_{D_u} = 0.1$, $\Delta\hat{u}_{co} = 3 \text{ mm}$ (right).

for the TMCI, as shown by Eq. (4.1). In addition, the aperture of the SPS vacuum chambers is generally smaller in the vertical dimension and thus more critical for the round LHC beams. The horizontal aperture on the other hand is largely sufficient, even for large excursions of the dispersion function. An interesting alternative option for achieving the low transition energy of the Q20 optics is therefore to reduce solely the horizontal tune of the machine. Figure 4.42 shows the optics functions in one super period of the SPS (left) when it is tuned to ($Q_x, Q_y = 20.13, 26.18$) and the corresponding calculation of the available aperture around the machine (right). With this split tunes optics the vertical beta functions remain close to their nominal values, while they are only slightly increased in the horizontal plane. The large dispersion in the arcs results then in the desired low transition energy of $\gamma_t = 17.8$. Note that the available aperture (calculated in the same way as in Section 4.3.2 but without taking into account the effect of the injection dogleg) is about the same as in the nominal Q26 optics in the vertical plane (cf. Fig. 4.8, left), while in the horizontal plane it is reduced only marginally compared to the Q20 optics (cf. Fig. 4.8, right). Thus, in addition to the increased available aperture, all instabilities in the vertical plane such as TMCI at injection and EC instabilities will have yet higher intensity thresholds in the split tunes optics compared to the normal Q20 optics.

Running the SPS with these split tunes was not tested in machine studies yet, but could be an interesting option for machine operation after the long shutdown. In particular, it is interesting to point out that the smaller vertical beta function in combination with the slightly larger dispersion results in an additional reduction of the incoherent space charge tune shift in the vertical plane ΔQ_y^{SC} : Figure 4.43 shows a comparison of the direct space charge tune shift as function of the normalized transverse emittance (assuming round beams) normalized to the bunch intensity for

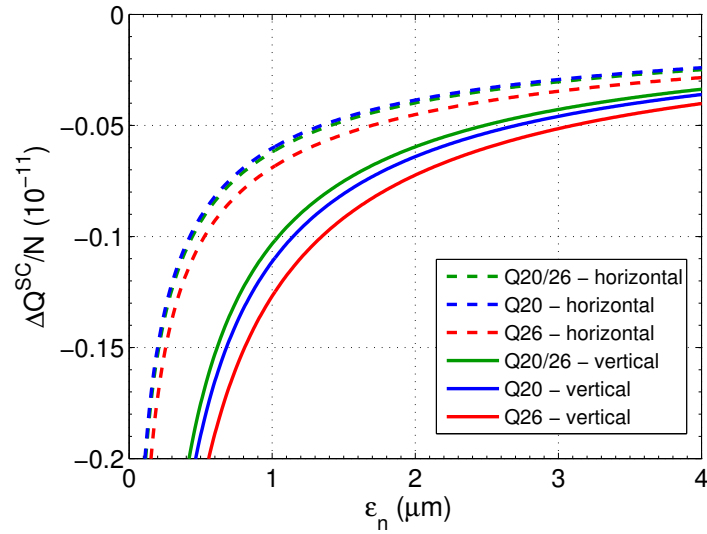


Figure 4.43: Direct space charge incoherent tune shift ΔQ^{SC} divided by the bunch intensity N as function of the normalized transverse rms emittance ε_n assuming equal emittances and the typical longitudinal beam parameters on the SPS injection plateau, $\tau = 3 \text{ ns}$ ($\sigma_l = 22 \text{ cm}$) and $\delta_{\text{rms}} = 0.0015$, comparing the Q26 optics with the Q20 and the split tunes optics.

different optics, similarly as done in Section 4.6.2. Compared to the Q26 optics, the split tunes ($Q_x, Q_y = 20.13, 26.18$) result in about 20% smaller space charge detuning in the vertical plane and thus increase the performance reach for high brightness beams. Finally, it should be emphasized also that, similar to the Q20 optics, no hardware modification would be necessary for deploying the split tunes optics.

5. Summary and conclusions

The transition energy, which is determined by the transverse beam optics, plays a central role for the performance of synchrotrons. Firstly, transition crossing can be avoided by designing a machine with negative momentum compaction (i.e. imaginary transition energy). This is exploited for the PS2 design study, as it allows to eliminate performance limitations usually encountered close to transition. Secondly, even if transition crossing is not encountered during the acceleration cycle of a machine, the value of transition energy can have a large impact on beam instabilities. This is demonstrated for the case of the SPS, where a significant increase of instability thresholds and thus performance reach for LHC beams is achieved by lowering the transition energy.

The extension of the analytical description of the negative momentum compaction (NMC) module of S.Y. Lee *et al.* developed in this thesis accounts for the betatron stability criterion. Only a subset of the possible combinations of the horizontal phase advance in the NMC module and the prescribed dispersion function at its entrance results in stable betatron motion in both transverse planes. Optics solutions yielding a desired value for the transition energy can be identified and used as starting point for the lattice optimization of a machine based on NMC cells.

Two lattice options for the PS2 design study based on NMC cells were thereby developed. The baseline option has a racetrack shape with dispersion suppressor modules at the arc extremities. The alternative option is based on a threefold symmetry, where the zero dispersion in the straight sections is achieved by resonant phase advance in the arcs. Due to the limited flexibility of the horizontal phase advance in the arcs of the threefold symmetric lattice, the baseline option provides a clear advantage for tuning the machine. In addition, lower imaginary transition energy can be reached. The physical aperture around the machine is effectively used in both lattice options. The chromaticity correction with 2 sextupole families installed around the quadrupoles in the central part of each NMC cell is very efficient, without introducing strong nonlinear chromaticity, amplitude detuning or dynamic aperture limitations. Nevertheless, the 4 sextupole family scheme proposed for the racetrack option provides additional flexibility for resonance compensation, optimization of amplitude detuning or minimization of second order chromaticity. The study of the sensitivity of the PS2 NMC lattice options with respect to machine imperfections shows that the feed-down effects of quadrupole misalignments represent the largest contributions to the closed orbit distortion. The large beta-beating induced by quadrupole misalignments is explained by the feed-down effect in sextupole magnets due to the induced closed orbit distortion. In particular, the beta-beating is significantly reduced by closed orbit correction. Finally, the main limitation for single particle dynamics for both NMC lattice options for the PS2 is imposed by multipole errors of the main magnets. In general, the dynamic aperture

in terms of rms beam size is slightly larger in the threefold symmetric lattice due to smaller average beta functions and the higher periodicity. In the case of the racetrack lattice, the dynamic aperture can be improved slightly for the nominal working point by compensating a third order resonance by optimizing the settings of the 4 family chromaticity correction scheme.

The direct impact of the slip factor on the performance of an operating synchrotron is described in the second part of the thesis. Present intensity limitations for LHC proton beams in the SPS scale linearly with the phase slip factor. Since these beams are injected above transition in the SPS, a reduction of the transition energy allows to increase the slip factor and thus proportionally raise the instability thresholds. The transition energy in a FODO lattice like the SPS scales with the horizontal phase advance in the arcs. Compared to the Q26 optics ($Q_x, Q_y = 26.13, 26.18$) usually used for LHC beams in the SPS where $\gamma_t = 22.8$, the transition energy in the Q20 optics ($Q_x, Q_y = 20.13, 20.18$) is reduced to $\gamma_t = 18$. Thus, the slip factor is increased almost 3 times at injection energy ($\gamma = 27.7$) and 1.6 times at extraction ($\gamma = 480$).

The larger dispersion function in the arcs with the Q20 optics and the increased beta functions are acceptable with respect to the available aperture in the SPS, thanks to the small emittances of LHC beams and the large dimensions of the vacuum chambers. The smaller gradient in the lattice quadrupoles in Q20 results in a slightly reduced vertical deflection when the beam is disposed on the high energy beam dump. Nevertheless, the beam position on the front face of the beam dump block remains within the required limits. The orbit bump in the SPS injection region as created by the voluntary quadrupole displacement is not closed in the Q20 optics, which results in an orbit oscillation of about 7 mm amplitude in the horizontal and 3 mm in the vertical plane. While this non-closure can be corrected at low energy with the existing orbit correctors, a correction at high energy and during extraction would require small hardware modification of existing correctors and interlocking. However, up to now the orbit remained uncorrected at high energy, even during extraction to the LHC.

The measured nonlinear chromaticity of the SPS is dominated by third order components, for both the Q26 and the Q20 optics. These third order components are reproduced consistently for both optics by decapole components in the two types of main dipole magnets. On the other hand, the measured linear part of the chromaticity cannot be explained by sextupole components in the dipole magnets common to both optics. As observed from the losses recorded during dynamic tune scans, the normal sextupole resonances are excited similarly in both optics. However, a comparably strong skew sextupole resonances ($2Q_x + Q_y$) is observed only in the Q20 optics. Nevertheless, the area close to the fractional tunes usually used for the LHC beams in the SPS ($\nu_x, \nu_y = 0.13, 0.18$) is free of strong resonances in both optics.

The intensity threshold for the single bunch transverse mode coupling instability in the vertical plane at injection is increased by more than a factor 2 with the Q20 optics compared to the Q26 optics, as demonstrated both in measurements and simulations. Macroparticle simulations using the wake fields of the present SPS impedance model

reproduce the experimental observations, including the weak instability in the Q20 optics for an intermediate intensity range. In the longitudinal plane, the multibunch instability during acceleration is observed at higher beam energy in the Q20 optics compared to the Q26 optics, i.e. has a higher instability threshold, for both 25 ns and 50 ns beams. For achieving the same bucket area in the two optics, a higher RF voltage is needed in Q20 due to the higher slip factor. As the maximum voltage is used at flat top in both optics for reducing the bunch length before the transfer from the SPS 200 MHz RF system to the LHC 400 MHz bucket, the bunches are longer in the Q20 optics for a given longitudinal emittance. However, similar bunch length at flat top can be achieved in both optics, as the same beam stability is obtained with smaller longitudinal emittance in the Q20 optics. Nevertheless, longitudinal instabilities remain one of the main limitations for future LHC beams. The record intensity of around $N \approx 1.30 \times 10^{11}$ p/b with 4 PS batches of the 25 ns beam in stable conditions was achieved with the Q20 optics. Reaching higher intensities was difficult not only because of longitudinal instabilities, but also due to transverse emittance blow-up on the flat bottom for bunches at the end of the third and fourth batch. This could be related to electron cloud effects, as the machine was never scrubbed for such high intensities. In contrast to that, several scrubbing runs were performed with the 25 ns beam with the nominal intensity ($N \approx 1.15 \times 10^{11}$ p/b). For this intensity the beam quality is presently not affected by electron cloud effects, as the beam is stable for low vertical chromaticity settings and there is no measurable emittance growth on a 20 s flat bottom with the Q26 optics. Furthermore, no emittance blow-up was observed in the Q20 optics for intensities up to $N \approx 1.30 \times 10^{11}$ p/b. The question if electron cloud effects can be suppressed for higher beam intensities by scrubbing runs remains subject of future studies. In any case, the situation should be less critical in the Q20 optics, since numerical simulations predict that the onset of the electron cloud driven single bunch instability at injection energy occurs at about twice higher electron density. Concerning space charge effects, the incoherent tune spread is reduced by about 15% in the Q20 optics compared to the Q26 optics, due to the increased dispersion function. Measurements show, that a vertical space charge tune shift of up to $\Delta Q_y^{SC} = -0.20$ can be accommodated on the SPS injection plateau in the Q20 optics without relevant beam degradation between PS batches.

The Q20 optics became operational for delivering LHC beams in the second half of 2012. Since then, the beam brightness as measured after injection in the LHC was improved on average by about 15%. The Q20 optics is now the nominal optics for LHC beams in the SPS. Even further performance improvement might be achieved in the future with the proposed split tunes optics ($Q_x, Q_y = 20.13, 26.18$), as it provides the low transition energy of the Q20 optics and similar vertical beta functions as the Q26 optics. This results in a further increase of transverse instability thresholds, and in addition a further reduction of the vertical space charge tune spread by another 5% compared to the Q20 optics.

Appendix

The following introduction to the main concepts of accelerator physics is based on Refs. [14] and [152], unless indicated differently. Note that the coordinate system of MADX [28] is used here.

A. Transverse particle motion

The motion of charged particles in an accelerator is usually described in the comoving Frenet-Serret coordinate system $(\hat{x}, \hat{y}, \hat{s})$, where \hat{x} and \hat{y} are the unit vectors in horizontal and vertical directions respectively and \hat{s} the unit vector following the design trajectory. The s -dependent Hamiltonian is then written as

$$H(x, p_x, y, p_y, t, -E; s) = -\left(1 + \frac{x}{\rho}\right) \left[\sqrt{\frac{E^2}{c^2} - m^2 c^2 - (p_x - qA_x)^2 - (p_y - qA_y)^2} + qA_s \right], \quad (\text{A.1})$$

where $\rho(s)$ defines the radius of curvature, m is the particle rest mass, c the speed of light, q is the particle charge and the components of the vector potential are denoted as $A_x(s)$, $A_y(s)$ and $A_s(s)$. The conjugate phase space variables are the horizontal position x with the corresponding momentum p_x , the vertical position y with the momentum p_y and the time t with the total energy E . Since the transverse momenta are usually much smaller than the total momentum $p = \sqrt{E^2/c^2 - m^2 c^2}$, the Hamiltonian can be expanded to second order in p_x and p_y , which yields

$$H(x, p_x, y, p_y, t, -E; s) = -\left(1 + \frac{x}{\rho}\right) \left[p - \frac{(p_x - qA_x)^2 + (p_y - qA_y)^2}{2p} + qA_s \right]. \quad (\text{A.2})$$

In the case of pure transverse magnetic fields (neglecting fringe fields), $A_x = A_y = 0$ and A_s is usually expanded in a power series such that

$$A_s = -B_0 \operatorname{Re} \left[\sum_{n=0}^{\infty} \frac{b_n + ja_n}{n+1} (x + jy)^{n+1} \right], \quad (\text{A.3})$$

where j is the imaginary number and B_0 is a normalization constant. The magnetic field $\mathbf{B} = B_x(x, y) \hat{x} + B_y(x, y) \hat{y}$ is defined as $\mathbf{B} = \nabla \times \mathbf{A}$, i.e.

$$B_x = \frac{\partial A_s}{\partial y}, \quad B_y = -\frac{\partial A_s}{\partial x}, \quad (\text{A.4})$$

which can be conveniently written in the complex 2D representation also known as the Beth representation, i.e.

$$B_y(x, y) + jB_x(x, y) = B_0 \sum_{n=0}^{\infty} (b_n + ja_n)(x + jy)^n. \quad (\text{A.5})$$

In this representation, b_n define the normal components of the field and a_n define the skew components, where

$$a_n = \frac{1}{B_0 n!} \left. \frac{\partial^n B_x}{\partial x^n} \right|_{x=y=0} \quad \text{and} \quad b_n = \frac{1}{B_0 n!} \left. \frac{\partial^n B_y}{\partial x^n} \right|_{x=y=0}. \quad (\text{A.6})$$

Note that the normalization constant B_0 is usually chosen equal to the main dipole field strength such that $b_0 = 1$. Using the magnetic rigidity $B\rho = p_0/q$, the constant B_0 can be expressed as $B_0 b_0 = B\rho/\rho$. Note that $p_0 = m\gamma_0\beta_0 c$ denotes the momentum of the reference particle, where β_0 and γ_0 are the corresponding relativistic factors.

A.1. Equations of motion

Since the synchrotron motion is usually much slower than the betatron motion, the Hamiltonian can be treated in the *adiabatic approximation*. The equations of motion describing betatron oscillations in the transverse plane are then given by

$$x' \equiv \frac{dx}{ds} = \frac{\partial H}{\partial p_x}, \quad p'_x \equiv \frac{dp_x}{ds} = -\frac{\partial H}{\partial x}, \quad y' \equiv \frac{dy}{ds} = \frac{\partial H}{\partial p_y}, \quad p'_y \equiv \frac{dp_y}{ds} = -\frac{\partial H}{\partial y}. \quad (\text{A.7})$$

Using the Hamiltonian of Eq. (A.2), the magnetic field as defined in Eq. (A.4) and $B\rho = p_0/q$ the equations of motion can be written as

$$x'' - \frac{\rho + x}{\rho^2} = -\frac{B_y p_0}{B\rho p} \left(1 + \frac{x}{\rho}\right)^2, \quad (\text{A.8a})$$

$$y'' = +\frac{B_x p_0}{B\rho p} \left(1 + \frac{x}{\rho}\right)^2, \quad (\text{A.8b})$$

where higher order terms were neglected. Expanding Eqs. (A.8a) and (A.8b) up to first order in x and y yields the linearized equations of motion

$$x'' + \left(\frac{1 - \delta}{\rho^2(1 + \delta)} + \frac{K_1(s)}{1 + \delta} \right) x = \frac{\delta}{\rho(1 + \delta)}, \quad (\text{A.9a})$$

$$y'' - \left(\frac{K_1(s)}{1 + \delta} \right) y = 0, \quad (\text{A.9b})$$

where $\delta \equiv \Delta p/p_0 = (p - p_0)/p_0$ is the fractional momentum offset, $K_1(s) = B_1/(B\rho)$ is the quadrupole gradient function and $B_1 = \partial B_y/\partial x$ evaluated at the reference orbit.

Solutions for the particle motion in the horizontal plane as described by Eq. (A.9a) have the form

$$x = x_{co}(s) + x_\beta(s) + D_x(s)\delta, \quad (\text{A.10})$$

where $x_{co}(s)$ describes the closed orbit distortion as caused by dipole-like field errors. The term $x_\beta(s)$ describes the betatron motion representing the homogenous solution of Eq. (A.9a) and $D_x(s)\delta$ defines the off-momentum closed orbit, where

$$x_\beta'' + [K_x(s) + \Delta K_x(s)]x_\beta = 0, \quad (\text{A.11})$$

$$D_x(s)'' + [K_x(s) + \Delta K_x(s)]D_x(s) = \frac{1}{\rho} + \mathcal{O}(\delta), \quad (\text{A.12})$$

with $K_x(s) = 1/\rho^2 + K_1(s)$ and $\Delta K_x(s) = [-\frac{2}{\rho^2} - K_1(s)]\delta + \mathcal{O}(\delta^2)$. Accordingly, the solution for the particle motion in the vertical plane can be written as

$$y = y_{co}(s) + y_\beta(s). \quad (\text{A.13})$$

Note that the dispersive part of the solution is omitted here, as it was tacitly assumed that there are no vertical bending magnets. As in the horizontal plane, $y_\beta(s)$ satisfies

$$y_\beta'' + [K_y(s) + \Delta K_y(s)]y_\beta = 0, \quad (\text{A.14})$$

where $K_y(s) = -K_1(s)$ and $\Delta K_y(s) = K_1(s)\delta + \mathcal{O}(\delta^2)$. For the following calculation, the closed orbit terms x_{co} and y_{co} will not be considered and the chromatic perturbation terms $\Delta K_x(s)$ and $\Delta K_y(s)$ will be neglected. Equations (A.11) and (A.14) can then be written as the well known Hill's equation

$$u'' + K_u(s)u = 0, \quad (\text{A.15})$$

where u stands for either x or y and the subscript β was dropped.

A.2. Solution of Hill's equation

The solution for Hill's equation for constant K_u are found as

$$u = \begin{cases} v \cos \sqrt{K_u}s + w \sin \sqrt{K_u}s, & K_u > 0, \\ v + w s, & K_u = 0, \\ v \cosh \sqrt{-K_u}s + w \sinh \sqrt{-K_u}s, & K_u < 0, \end{cases} \quad (\text{A.16})$$

where v and w are integration constants to be determined by the initial conditions. Note that the second case with $K_u = 0$ corresponds to a magnet free drift space. Let's represent the phase-space coordinates u and u' of a particle at location s by the

state-vector $\mathbf{u}(s)$,

$$\mathbf{u}(s) = \begin{pmatrix} u(s) \\ u'(s) \end{pmatrix}. \quad (\text{A.17})$$

The solution to Hill's equation for piece-wise constant K_u can then be conveniently described in a matrix formalism such that

$$\mathbf{u}(s) = M_u(s|s_0) \mathbf{u}(s_0), \quad (\text{A.18})$$

where M_u represents the betatron transport matrix from location s_0 to s . Imposing initial conditions $u(s_0)$ and $u'(s_0)$, the transfer matrix for constant K_u is found as

$$M_u(s|s_0) = \begin{cases} \begin{pmatrix} \cos \sqrt{K_u} l & \frac{1}{\sqrt{K_u}} \sin \sqrt{K_u} l \\ -\sqrt{K_u} \sin \sqrt{K_u} l & \cos \sqrt{K_u} l \end{pmatrix}, & K_u > 0 \text{ (focusing)}, \\ \begin{pmatrix} 1 & l \\ 0 & 1 \end{pmatrix}, & K_u = 0 \text{ (drift)}, \\ \begin{pmatrix} \cosh \sqrt{|K_u|} l & \frac{1}{\sqrt{|K_u|}} \sinh \sqrt{|K_u|} l \\ -\sqrt{|K_u|} \sinh \sqrt{|K_u|} l & \cos \sqrt{|K_u|} l \end{pmatrix}, & K_u < 0 \text{ (defocusing)}, \end{cases} \quad (\text{A.19})$$

where $l = s - s_0$ is the length of the element. For a quadrupole magnet, $K_u = \pm K_1$ where the sign depends on the plane and will be positive (negative) for focusing quadrupoles and negative (positive) for defocusing quadrupoles in the horizontal (vertical) plane²³. In *thin lens approximation*,

$$M_{focusing} = \begin{pmatrix} 1 & 0 \\ -\frac{1}{f} & 1 \end{pmatrix}, \quad M_{defocusing} = \begin{pmatrix} 1 & 0 \\ \frac{1}{f} & 1 \end{pmatrix}, \quad (\text{A.20})$$

it is assumed that the quadrupole length $l \rightarrow 0$ such that the focal length f is given by

$$f = \lim_{l \rightarrow 0} \frac{1}{|K_1|l}. \quad (\text{A.21})$$

For the case of a sector bending magnet, $K_x = 1/\rho^2$ and $K_y = 0$. Thus, the transfer matrix reduces to a drift space in the vertical plane and becomes in the horizontal (deflecting) plane

$$M_{x,sectorbend} = \begin{pmatrix} \cos \theta & \rho \sin \theta \\ -\frac{1}{\rho} \sin \theta & \cos \theta \end{pmatrix} \xrightarrow[\text{approximation}]{\text{small angle}} \begin{pmatrix} 1 & l \\ 0 & 1 \end{pmatrix}, \quad (\text{A.22})$$

²³The convention is such that a quadrupole which has a focusing effect in the horizontal plane is called focusing quadrupole, while it is actually defocusing in the vertical plane

where $\theta = l/\rho$ is the bending angle and ρ is the bending radius. In small angle approximation the transfer matrix is reduced to a drift space, where l corresponds to the length of the bending magnet.

Using the transfer matrices for individual elements as described above, the total transfer matrix for an accelerator structure is obtained by matrix multiplication. Assuming a transfer line composed of elements a, b and c represented by the matrices $M_{u,a}$, $M_{u,b}$ and $M_{u,c}$, respectively, the total transfer matrix is calculated by

$$M_{u,a \rightarrow c} = M_{u,c} \cdot M_{u,b} \cdot M_{u,a}, \quad (\text{A.23})$$

and so on. For the case of a periodic structure with length L , the transfer matrix is a periodic function of s . In this case let $\mathbf{M}_u(s)$ denote the periodic transfer matrix from a location s to $s + L$ such that

$$\mathbf{M}_u(s) = M_u(s + L|s) = M_{u_n} \dots M_{u,2} M_{u,1}, \quad (\text{A.24})$$

where the structure is composed of n individual elements. Applying Floquet's theorem for periodic beam transport sections (like circular accelerators), the solution $u(s)$ for Hill's equation can be represented as a pseudo-harmonic oscillation with varying amplitude $\sqrt{\beta_u(s)}$,

$$u(s) = \sqrt{2J_u\beta_u(s)} \cos(\psi_u(s) + \psi_{u,0}), \quad (\text{A.25a})$$

$$u'(s) = -\sqrt{\frac{2J_u}{\beta_u(s)}} \left[\sin(\psi_u(s) + \psi_{u,0}) + \alpha_u(s) \cos(\psi_u(s) + \psi_{u,0}) \right], \quad (\text{A.25b})$$

$$\psi_u(s) = \int_0^s \frac{ds}{\beta_u(s)}, \quad (\text{A.25c})$$

where the Courant-Snyder parameters $\alpha_u(s) = -\beta'_u(s)/2$, $\beta_u(s)$ and $\gamma_u(s) = \frac{1+\alpha_u^2(s)}{\beta_u(s)}$ were introduced and $\psi_u(s)$ is called the betatron phase advance. The phase offset $\psi_{u,0}$ and the invariant action J_u are to be determined by the initial conditions. The betatron motion in the phase-space (u, u') at location s is then described by an invariant ellipse enclosing an area of $2\pi J_u$. The geometrical shape of this ellipse is thereby defined by the Courant-Snyder parameters (see Fig. A.1 showing the case of the horizontal plane). In particular, the Courant-Snyder invariant $\zeta(u, u')$ defined as

$$\zeta(u, u') = \frac{1}{\beta_u} [u^2 + (\alpha_u u + \beta_u u')^2] = \gamma_u u^2 + 2\alpha_u u u' + \beta_u u'^2, \quad (\text{A.26})$$

is equal to twice the action J_u . A distribution of particles in the phase-space is then usually described by an rms beam emittance as described below. Let $G(u, u')$ be the normalized particle distribution function such that $\int G(u, u') du du' = 1$. The moments

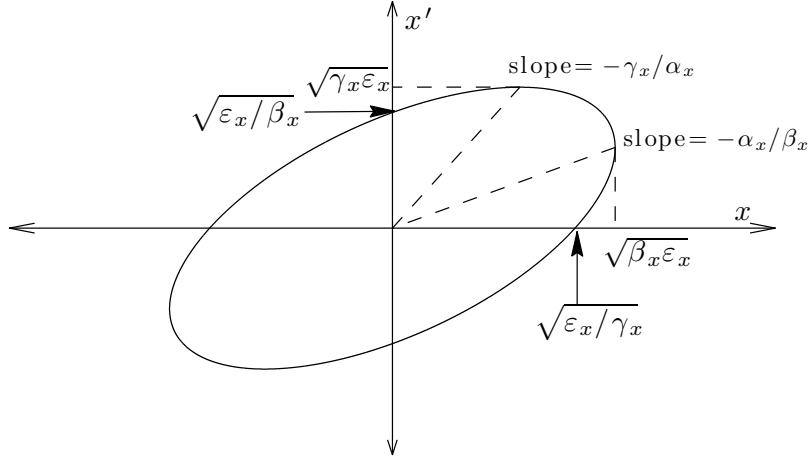


Figure A.1: Properties of the Courant-Snyder invariant ellipse for the case of the horizontal phase-space $x-x'$.

of the particle distribution are

$$\langle u \rangle = \int u G(u, u') du du', \quad (\text{A.27a})$$

$$\langle u' \rangle = \int u' G(u, u') du du', \quad (\text{A.27b})$$

$$\sigma_u^2 = \int (u - \langle u \rangle)^2 G(u, u') du du', \quad (\text{A.27c})$$

$$\sigma_{u'}^2 = \int (u' - \langle u' \rangle)^2 G(u, u') du du', \quad (\text{A.27d})$$

$$\sigma_{uu'} = \int (u - \langle u \rangle) (u' - \langle u' \rangle) G(u, u') du du', \quad (\text{A.27e})$$

where σ_u and $\sigma_{u'}$ are the rms beam widths in the $u - u'$ phase space and $\sigma_{uu'}$ is the correlation. The rms beam emittance ε_u , also called physical emittance, is then

$$\varepsilon_u = \sqrt{\sigma_u^2 \sigma_{u'}^2 - \sigma_{uu'}^2}. \quad (\text{A.28})$$

The betatron amplitude function $\beta_u(s)$ is defined through the envelope equation

$$\frac{1}{2}\beta_u + K_u \beta_u - \frac{1}{\beta_u} \left[1 + \left(\frac{\beta_u'}{2} \right)^2 \right] = 0, \quad (\text{A.29})$$

as obtained by inserting the solution given in Eq. (A.25a) into Hill's equation. The number of betatron oscillations per revolution is given by the betatron tune, which is

defined as

$$Q_u = \nu_u = \frac{1}{2\pi} \oint \frac{ds}{\beta_u(s)}. \quad (\text{A.30})$$

Using the Courant-Snyder parameterization, the periodic transfer matrix $\mathbf{M}_u(s)$ can be represented as

$$\mathbf{M}_u(s) = \begin{pmatrix} \cos \phi_u + \alpha_u(s) \sin \phi_u & \beta_u(s) \sin \phi_u \\ -\gamma_u(s) \sin \phi_u & \cos \phi_u - \alpha_u(s) \sin \phi_u \end{pmatrix}, \quad (\text{A.31})$$

where $\phi_u = \psi_u(s + L) - \psi_u(s)$ denotes the phase advance along the structure with period length L . Stability of a repetitive cell or periodic structure requires thereby $|\cos \phi_u| \leq 1$ in both transverse planes.

The transfer matrix $M(s_2|s_1)$ describing the transport in any beam line from location s_1 to s_2 is found as

$$M_u(s_2|s_1) = \begin{pmatrix} \sqrt{\frac{\beta_2}{\beta_1}}(\cos \psi_u + \alpha_1 \sin \psi_u) & \sqrt{\beta_1 \beta_2} \sin \psi_u \\ -\frac{1+\alpha_1 \alpha_2}{\sqrt{\beta_1 \beta_2}} \sin \psi_u + \frac{\alpha_1 - \alpha_2}{\sqrt{\beta_1 \beta_2}} \cos \psi_u & \sqrt{\frac{\beta_1}{\beta_2}}(\cos \psi_u - \alpha_2 \sin \psi_u) \end{pmatrix}, \quad (\text{A.32})$$

where α_1, β_1 and α_2, β_2 denote the Courant-Snyder (twiss) parameters at location s_1 and s_2 , respectively, and $\psi_u = \psi_u(s_2) - \psi_u(s_1)$.

A.3. Solution for off-momentum particles

As for the solution of Hill's equation, the chromatic perturbation term $\Delta K_x(s)$ will be neglected in the following for finding a solution for the dispersion function as defined through Eq. (A.12). Then, to lowest order in δ , the (horizontal) dispersion function $D_x(s)$ satisfies the inhomogeneous equation

$$D_x(s)'' + K_x(s)D_x(s) = 1/\rho. \quad (\text{A.33})$$

The solution $D_x(s)$ for this equation is a sum of the homogenous solution and a particular solution, which can be represented using the matrix formalism

$$\begin{pmatrix} D_x(s_2) \\ D'_x(s_2) \end{pmatrix} = M_x(s_2|s_1) \begin{pmatrix} D_x(s_1) \\ D'_x(s_1) \end{pmatrix} + \begin{pmatrix} d_x \\ d'_x \end{pmatrix}, \quad (\text{A.34})$$

where $M_x(s_2|s_1)$ is the 2×2 transfer matrix for the homogenous equation as discussed above and d_x, d'_x are the components of the dispersion vector \bar{d}_x representing the particular solution. It turns out convenient to represent the transfer matrix in Eq. (A.34)

by a 3×3 matrix \mathcal{M}_x , such that

$$\begin{pmatrix} D_x(s_2) \\ D'_x(s_2) \\ 1 \end{pmatrix} = \begin{pmatrix} M_x(s_2|s_1) & \bar{d}_x \\ 0 & 1 \end{pmatrix} \begin{pmatrix} D_x(s_1) \\ D'_x(s_1) \\ 1 \end{pmatrix} = \mathcal{M}_x \begin{pmatrix} D_x(s_1) \\ D'_x(s_1) \\ 1 \end{pmatrix}. \quad (\text{A.35})$$

In this formalism, the 3×3 transfer matrix for a pure sector bending magnet becomes

$$\mathcal{M}_{x,\text{sectorbend}} = \begin{pmatrix} \cos \theta & \rho \sin \theta & \rho(1 - \cos \theta) \\ -\frac{1}{\rho} \sin \theta & \cos \theta & \sin \theta \\ 0 & 0 & 1 \end{pmatrix} \xrightarrow[\text{approximation}]{\text{small angle}} \begin{pmatrix} 1 & l & \frac{1}{2}l\theta \\ 0 & 1 & \theta \\ 0 & 0 & 1 \end{pmatrix}. \quad (\text{A.36})$$

Assuming that the accelerator structure under consideration has no vertical bending magnets, all other transfer matrices discussed above are simply extended to 3×3 dimensions according to Eq. (A.35), where the dispersion vector \bar{d} is zero. For a *periodic structure*, the transfer matrix $\mathbf{M}_x(s)$ extended to 3×3 dimensions in the horizontal plane is found by imposing the closed orbit condition, i.e. $D_x(s + L) = D_x(s)$ and $D'_x(s + L) = D'_x(s)$ yielding

$$\mathcal{M}_x = \begin{pmatrix} \cos \phi_x + \alpha_x \sin \phi_x & \beta_x \sin \phi_x & (1 - \cos \phi_x - \alpha_x \sin \phi_x)D_x - \beta_x \sin \phi_x D'_x \\ -\gamma_x \sin \phi_x & \cos \phi_x - \alpha_x \sin \phi_x & \gamma_x \sin \phi_x D_x + (1 - \cos \phi_x + \alpha_x \sin \phi_x)D'_x \\ 0 & 0 & 1 \end{pmatrix}, \quad (\text{A.37})$$

where D_x and D'_x are the values of dispersion and its derivative at location s . Although not shown here, a corresponding derivation can be done in the vertical plane for obtaining the vertical dispersion D_y . However, at least without errors (i.e. in the ideal lattice), the vertical dispersion in circular accelerators is usually zero.

A.4. Normalized dispersion and dispersion action

For practical reasons in accelerator lattice design, it is often useful to use *normalized* dispersion phase-space coordinates. First, the dispersion \mathcal{H} function is defined as

$$\mathcal{H}(D_x, D'_x) = \gamma_x D_x^2 + 2\alpha_x D_x D'_x + \beta_x D_x'^2 = \frac{1}{\beta_x} [D_x^2 + (\beta_x D'_x + \alpha_x D_x)^2]. \quad (\text{A.38})$$

In regions without dipoles, the dispersion function is described by the homogenous betatron equation of motion (cf. Appendix A.3) and therefore the \mathcal{H} function is invariant. In regions with dipoles on the other hand, it is not invariant. The *normalized dispersion* phase-space coordinates are defined as

$$\begin{cases} D_{n,x} = \frac{1}{\sqrt{\beta_x}} D_x = \sqrt{2J_{d,x}} \cos \psi_{d,x}, \\ D'_{n,x} = \sqrt{\beta_x} D'_x + \frac{\alpha_x}{\sqrt{\beta_x}} D_x = -\sqrt{2J_{d,x}} \sin \psi_{d,x}, \end{cases} \quad (\text{A.39})$$

where $J_{d,x}$ is the dispersion action defined as

$$J_{d,x} = \frac{1}{2} \mathcal{H}(D_x, D'_x), \quad (\text{A.40})$$

and $\psi_{d,x}$ is the dispersion phase advance, which in a straight section is identical to the betatron phase advance ψ_x . The normalized dispersion coordinates can be useful for matching the dispersion function to zero at the exit of a dispersion suppressor module. Normalized dispersion coordinates for the vertical plane are defined correspondingly.

A.5. Linear magnet imperfections

In this section, the effect of linear magnet imperfections will be discussed. The Hill's equations in the presence of magnetic field errors become

$$\begin{cases} x'' + K_x(s)x = -\frac{\Delta B_y}{B\rho}, \\ y'' + K_y(s)y = \frac{\Delta B_x}{B\rho}, \end{cases} \quad (\text{A.41})$$

where ΔB_x and ΔB_y denote the magnetic field errors which can be described in a multipole expansion similar to Eq. (A.5).

Dipole field errors

Consider a single dipole field error $\Delta\theta = \Delta Bdl/B\rho$ at position s_0 , where ΔBdl is the integrated field error. The phase-space coordinates before and after the error can be written as

$$u_- = \begin{pmatrix} u_0 \\ u'_0 - \Delta\theta \end{pmatrix}, \quad u_+ = \begin{pmatrix} u_0 \\ u'_0 \end{pmatrix} \quad (\text{A.42})$$

and the closed orbit condition becomes

$$\mathbf{M}_u \begin{pmatrix} u_0 \\ u'_0 \end{pmatrix} = \begin{pmatrix} u_0 \\ u'_0 - \Delta\theta \end{pmatrix}. \quad (\text{A.43})$$

The resulting closed orbit at position s_0 is then

$$\begin{cases} u_0 = \frac{\beta_{u,0}\Delta\theta}{2 \sin \pi\nu_u} \cos \pi\nu_u, \\ u'_0 = \frac{\Delta\theta}{2 \sin \pi\nu_u} (\sin \pi\nu_u - \alpha_{u,0} \cos \pi\nu_u). \end{cases} \quad (\text{A.44})$$

Note that the closed orbit becomes infinite if the tune ν_u of the machine reaches integer values, as the orbit kicks due to dipole field errors add up systematically every turn. Therefore integer tunes have to be avoided in machine operation. On the other hand,

the effect of dipole-like errors is minimized for half-integer tunes.

In general, the closed orbit at any location s around the ring is calculated using the transport matrix $M_u(s|s_0)$

$$\begin{pmatrix} u(s) \\ u'(s) \end{pmatrix}_{co} = M_u(s|s_0) \begin{pmatrix} u_0 \\ u'_0 \end{pmatrix}. \quad (\text{A.45})$$

For many distributed dipole errors around the ring, the closed orbit u_{co} at any location s can be obtained by integrating around the circumference C , such that

$$u_{co}(s) = \frac{\sqrt{\beta_u(s)}}{2 \sin \pi \nu_u} \int_s^{s+C} \sqrt{\beta_u(\tilde{s})} \frac{\Delta B(\tilde{s})}{B\rho} \cos(\pi \nu_u + \psi_u(s) - \psi_u(\tilde{s})) d\tilde{s}. \quad (\text{A.46})$$

An estimation of the closed orbit distortion caused by a distribution of N random dipole errors around the machine with an rms kick angle $\Delta\theta_{rms}$ can be given by

$$u_{co} \approx \frac{\bar{\beta}_u}{2\sqrt{2} |\sin \pi \nu_u|} \sqrt{N} \Delta\theta_{rms}, \quad (\text{A.47})$$

where $\bar{\beta}_u$ is the average beta function. Note that a dipole kick is also obtained from magnet misalignments through the so called feed-down effects. For example, a displaced quadrupole generates a dipole kick

$$\Delta\theta = K_u L \Delta u = \frac{\Delta u}{f}, \quad (\text{A.48})$$

where Δu is the displacement of the quadrupole and $K_u L = \frac{1}{f}$ is the integrated normalized gradient of the quadrupole with length L , recalling that $K_x = K_1$ and $K_y = -K_1$ are the normalized quadrupole gradients with $K_1 = \frac{1}{B\rho} \frac{\partial B_y}{\partial x}$.

Gradient errors

In the presence of gradient errors, the Hill's equation describing the perturbed betatron motion becomes

$$u'' + [K_u(s) + \Delta K_u(s)] u = 0, \quad (\text{A.49})$$

where $\Delta K_u(s)$ denotes the quadrupole errors around the machine. Note that this equation was already encountered in a similar form in the derivation of Hill's equations in the context of chromatic gradient errors, cf. Eq. (A.11). Let \mathbf{M}_u be the unperturbed one turn transfer matrix. The transfer matrix of an infinitesimal gradient error of length ds_1 localized at position s_1 is given by

$$m_u(s_0) = \begin{pmatrix} 1 & 0 \\ -\Delta K_u(s_1) ds_1 & 1 \end{pmatrix}. \quad (\text{A.50})$$

The one turn transfer matrix including this localized perturbation is then calculated as $\tilde{\mathbf{M}}_u(s_1) = \mathbf{M}_u(s_1) m_u(s_1)$, which yields

$$\tilde{\mathbf{M}}_u(s_1) = \begin{pmatrix} \cos \phi_u + \alpha_u(s_1) \sin \phi_u - \beta_u(s_1) \Delta K_u(s_1) ds_1 \sin \phi_u & \beta_u(s_1) \sin \phi_u \\ -\gamma_u(s_1) \sin \phi_u - [\cos \phi_u + \alpha_u(s_1) \sin \phi_u] \Delta K_u(s_1) ds_1 & \cos \phi_u - \alpha_u(s_1) \sin \phi_u \end{pmatrix}, \quad (\text{A.51})$$

where ϕ_u is the phase advance around the unperturbed lattice. The phase advance in the perturbed machine $\tilde{\phi}_u$ is obtained from $\text{Tr}[\tilde{\mathbf{M}}_u(s_1)] = \cos \tilde{\phi}_u$. It follows therefore that

$$\cos \tilde{\phi}_u - \cos \phi_u = -\frac{1}{2} \beta_{u,1} \Delta K_u(s_1) ds_1 \sin \phi_u. \quad (\text{A.52})$$

The phase advance difference $\Delta \phi_u = \tilde{\phi}_u - \phi_u$ and the tune shift $\Delta \nu_u$ can be approximated as

$$\Delta \phi_u = \frac{1}{2} \beta_u(s_1) \Delta K_u(s_1) ds_1, \quad \Delta \nu_u = \frac{1}{4\pi} \beta_u(s_1) \Delta K_u(s_1) ds_1. \quad (\text{A.53})$$

In the case of distributed gradient errors, the tune shift becomes

$$\Delta \nu_u = \frac{1}{4\pi} \oint \beta_u(s_1) \Delta K_u(s_1) ds_1. \quad (\text{A.54})$$

It follows that the tunes are particularly sensitive to gradient errors in locations with high beta functions. Similarly, the gradient errors introduce a variation of the beta functions around the ring which is called beta-beat. For estimating the beta-beat, the transfer-matrix at location s_2 is written as

$$\tilde{\mathbf{M}}_u(s_2) = M_u(s_2 + C|s_1) m_u(s_1) M_u(s_1|s_2), \quad (\text{A.55})$$

where $m_u(s_1)$ is again the transfer matrix of the infinitesimal gradient error at location s_1 and $M_u(s_1|s_2)$ is the transport matrix from s_1 to s_2 . Using the general transport matrix as given in Eq. (A.32), the difference of the off-diagonal elements between the unperturbed and the perturbed lattice $\Delta[\mathbf{M}_u(s_2)]_{12} = [\tilde{\mathbf{M}}_u(s_2)]_{12} - [\mathbf{M}_u(s_2)]_{12}$ can be calculated as

$$\Delta[\mathbf{M}_u(s_2)]_{12} = -\Delta K_u(s_1) ds_1 \beta_u(s_1) \beta_u(s_2) \sin[\psi_u(s_1) - \psi_u(s_2)] \sin[\phi_u - \psi_u(s_1) + \psi_u(s_2)]. \quad (\text{A.56})$$

The matrix element $[\tilde{\mathbf{M}}_u(s_2)]_{12}$ can be expanded

$$\begin{aligned} [\tilde{\mathbf{M}}_u(s_2)]_{12} &= \tilde{\beta}_u(s_2) \sin \tilde{\phi}_u \approx [\beta_u(s_2) + \Delta \beta_u(s_2)] [\sin \phi_u + \Delta \phi_u \cos \phi_u] \\ &\approx \beta_u(s_2) \sin \phi_u + \beta_u(s_2) \Delta \phi_u \cos \phi_u + \Delta \beta_u(s_2) \sin \phi_u, \end{aligned} \quad (\text{A.57})$$

where the first term is $\beta_u(s_2) \sin \phi_u = [\mathbf{M}_u(s_2)]_{12}$. Therefore

$$\begin{aligned} \Delta[\mathbf{M}_u(s_2)]_{12} &= \beta_u(s_2) \Delta \phi_u \cos \phi_u + \Delta \beta_u(s_2) \sin \phi_u \\ &= \frac{1}{2} \beta_u(s_1) \beta_u(s_2) \Delta K_u(s_1) ds_1 \cos \phi_u + \Delta \beta_u(s_2) \sin \phi_u, \end{aligned} \quad (\text{A.58})$$

where the phase advance shift found in Eq. (A.53) was used. Inserting Eq. (A.58) into Eq. (A.56) finally yields

$$\Delta \beta_u(s_2) = - \frac{\Delta K_u(s_1) ds_1 \beta_u(s_1) \beta_u(s_2)}{2 \sin \phi_u} \cos [\phi_u - \psi_u(s_1) + \psi_u(s_2)] \quad (\text{A.59})$$

using $2 \sin [\psi_u(s_1) - \psi_u(s_2)] \sin [\phi_u - \psi_u(s_1) + \psi_u(s_2)] + \cos \phi_u = \cos [\phi_u - \psi_u(s_1) + \psi_u(s_2)]$. For distributed gradient errors around the ring, the beta-beat can be calculated as

$$\frac{\Delta \beta_u(s)}{\beta_u(s)} = - \frac{1}{2 \sin \phi_u} \int_s^{s+C} \Delta K_u(s_1) \beta_u(s_1) \cos [\phi_u - \psi_u(s_1) + \psi_u(s)] ds_1. \quad (\text{A.60})$$

Feed-down effects

As mentioned already in the discussion of dipole field errors, magnet misalignments introduce field errors due to feed-down effects. This is demonstrated below for an example of a horizontally displaced sextupole magnet. Replacing x by $x + \Delta x$ in the field expansion of Eq. (A.5) with only b_2 being nonzero yields

$$\begin{cases} \tilde{B}_x = \frac{1}{2} B_2 [2xy + 2y\Delta x], \\ \tilde{B}_y = \frac{1}{2} B_2 [x^2 - y^2 + 2x\Delta x + (\Delta x)^2], \end{cases} \quad (\text{A.61})$$

where $B_2 = \partial^2 B_y / \partial x^2$. The effective field $\Delta B_x = \tilde{B}_x - B_x$ and $\Delta B_y = \tilde{B}_y - B_y$ caused by the misalignment error is then

$$\begin{cases} \Delta B_x = B_2 y \Delta x, \\ \Delta B_y = B_2 [x\Delta x + \frac{1}{2}(\Delta x)^2]. \end{cases} \quad (\text{A.62})$$

Thus, an upright sextupole magnet displaced in the horizontal plane yields a normal quadrupole and a normal dipole field. It can be shown that the same sextupole magnet displaced in the vertical plane yields a skew quadrupole and a normal dipole field. The feed-down effects in any other higher order magnet can be derived similarly.

A.6. Non-linear beam dynamics

Chromaticity

As already discussed in section A.3, off-momentum particles oscillate around the closed orbit defined by $D_x \delta$. The momentum offset will also create an error in the focusing

strength of quadrupole magnets ΔK_u ,

$$\begin{cases} \Delta K_x(s) = [-\frac{2}{\rho^2} - K_1(s)]\delta + \mathcal{O}(\delta^2) \approx -K_1(s)\delta, \\ \Delta K_y(s) = K_1(s)\delta + \mathcal{O}(\delta^2) \approx K_1(s)\delta. \end{cases} \quad (\text{A.63})$$

Note that these chromatic gradient errors were already encountered in Eqs. (A.11) and (A.14) when deriving the Hill's equations. With Eq. (A.54) the resulting tune shift can be calculated as

$$\Delta\nu_x = \frac{1}{4\pi} \oint \beta_x(s) \Delta K_x(s) ds \approx \left(-\frac{1}{4\pi} \oint \beta_x(s) K_1(s) ds \right) \delta, \quad (\text{A.64a})$$

$$\Delta\nu_y = \frac{1}{4\pi} \oint \beta_y(s) \Delta K_y(s) ds \approx \left(\frac{1}{4\pi} \oint \beta_y(s) K_1(s) ds \right) \delta. \quad (\text{A.64b})$$

The chromaticity is then defined as the derivative of the betatron tunes with respect to the momentum deviation, i.e.

$$C_u = Q'_u = \frac{d(\Delta\nu_u)}{d\delta}. \quad (\text{A.65})$$

It follows from Eqs. (A.64a) and (A.64b) that the natural chromaticity arising from quadrupoles is negative. This is due to the fact that particles with larger momentum are focussed less which means a smaller tune. The *specific chromaticity* $\xi_u \equiv C_u/\nu_u$ (i.e. $\xi_u \equiv Q'_u/Q_u$) is around 1 for a FODO lattice and can be a few units in case of strong focusing insertions. An off-center orbit through a sextupole magnet creates a quadrupole field due to feed down effects. This can be exploited for correcting chromaticity, where the orbit of off-momentum particles is proportional to the momentum offset. The magnetic flux in sextupoles is

$$\frac{\Delta B_x}{B\rho} = \frac{B_2}{B\rho} xy = K_2 xy, \quad (\text{A.66a})$$

$$\frac{\Delta B_y}{B\rho} = \frac{B_2}{2B\rho} (x^2 - y^2) = \frac{K_2}{2} (x^2 - y^2), \quad (\text{A.66b})$$

where $K_2 = B_2/B\rho$ is the effective sextupole strength. Inserting the horizontal position of an off-momentum particle $x = x_\beta(s) + D_x(s)\delta$ yields

$$\frac{\Delta B_x}{B\rho} = [K_2(s)D_x(s)\delta] y_\beta + K_2(s)x_\beta y_\beta, \quad (\text{A.67a})$$

$$\frac{\Delta B_y}{B\rho} = [K_2(s)D_x(s)\delta] x_\beta + \frac{K_2(s)}{2} (x_\beta^2 - y_\beta^2) + \frac{K_2(s)}{2} D_x^2(s)\delta^2. \quad (\text{A.67b})$$

The first term is linearly dependent on the momentum offset and the particle displacements x_β or y_β respectively. The effective quadrupole focusing is thus

$$\Delta K_x = K_2(s)D_x(s)\delta, \quad \Delta K_y = -K_2(s)D_x(s)\delta. \quad (\text{A.68})$$

The chromaticity including the effect of sextupoles in the lattice is then

$$\mathcal{C}_x = -\frac{1}{4\pi} \oint \beta_x(s)[K_1(s) - K_2(s)D_x(s)]ds, \quad (\text{A.69a})$$

$$\mathcal{C}_y = +\frac{1}{4\pi} \oint \beta_y(s)[K_1(s) - K_2(s)D_x(s)]ds. \quad (\text{A.69b})$$

Therefore sextupoles placed in dispersive regions can be used for correcting chromaticity. Note that sextupoles are the lowest order non-linear elements. For minimizing their strength, they should be located in high dispersion areas where the beta function ratio β_x/β_y (β_y/β_x) takes large values for correcting horizontal (vertical) chromaticity. The same result can be derived in the general frame work of resonance driving terms.

Resonance driving terms

A very powerful technique for describing non-linear effects in particle accelerator physics is perturbation theory, which allows to calculate the so-called Hamiltonian resonance driving terms. The s dependent Hamiltonian for a magnetic lattice including up to sextupole magnets can be written in a dimensionless form as

$$H(x, p_x, y, p_y; s) = \frac{1}{(1+\delta)} \left(\frac{p_x^2 + p_y^2}{2} + \frac{x^2}{2\rho^2} + \frac{K_1}{2} (x^2 - y^2) \right) + \frac{K_2}{6(1+\delta)} (x^3 - 3xy^2), \quad (\text{A.70})$$

assuming that each magnetic element can be represented by a piece-wise constant Hamiltonian. The non-linear one-turn map $\mathcal{M}_{0 \rightarrow n}$ for a ring consisting of n elements can be written in normal form [152]

$$\mathcal{M}_{0 \rightarrow n} \equiv \mathcal{A}_0^{-1} e^{i h} \mathcal{R}_{0 \rightarrow n} \mathcal{A}_0 = \mathcal{A}_0^{-1} \exp \left(: \sum_{i=1}^n \hat{V}_i + \frac{1}{2} \sum_{i < j} [\hat{V}_i \hat{V}_j] + \dots : \right) \mathcal{R}_{0 \rightarrow n} \mathcal{A}_0, \quad (\text{A.71})$$

where $\mathcal{R}_{0 \rightarrow n}$ represents a rotation, \mathcal{A}_i is the normalizing map where the subscripts 0 and n denote elements of the ring. The exponential Lie operator defined as

$$e^{i f} g = g + [f, g] + \frac{1}{2!} [f, [f, g]] + \dots \quad (\text{A.72})$$

was used and $[f, g] = \sum_{i=1}^n \left(\frac{\partial f}{\partial x_i} \frac{\partial g}{\partial p_i} - \frac{\partial f}{\partial p_i} \frac{\partial g}{\partial x_i} \right)$ is the Poisson bracket (with x_i and p_i being canonical variables). It is assumed that the non-linear Lie map $e^{i h}$ can be expanded

into orders of the multipole strength in the vector potential, which is represented by $\hat{V}_i = \mathcal{R}_{0 \rightarrow i} \mathcal{A}_i V_i$ and $V_i = \frac{q}{p} A_s$. Note that in the one-turn map given by Eq. (A.71), all non-linear (thin) kicks are lumped into a single *thin* kick at the beginning of the lattice. A linear flat lattice without coupling can be treated in perturbation theory and the normalization map \mathcal{A}_i at element i is then given as

$$\mathcal{A}_i x = \sqrt{\beta_{x,i}} x + D_{x,i} \delta, \quad \mathcal{A}_i p_x = \frac{-\alpha_{x,i} x + p_x}{\sqrt{\beta_{x,i}}} + D'_{x,i} \delta, \quad (\text{A.73})$$

$$\mathcal{A}_i y = \sqrt{\beta_{y,i}} y, \quad \mathcal{A}_i p_y = \frac{-\alpha_{y,i} y + p_y}{\sqrt{\beta_{y,i}}}, \quad (\text{A.74})$$

where $\beta_{x,i}$ and $\beta_{y,i}$ denote the beta functions at location i and $D_{x,i}$ the dispersion at location i . Then, x and p_x can be represented in the resonance basis h_x^\pm and likewise y and p_y in the basis h_y^\pm , where

$$h_x^\pm \equiv \sqrt{2J_x} e^{\pm j\psi_x} = x \mp jp_x, \quad x = \sqrt{2J_x} \cos \psi_x = \frac{1}{2}(h_x^+ + h_x^-), \quad (\text{A.75})$$

$$h_y^\pm \equiv \sqrt{2J_y} e^{\pm j\psi_y} = y \mp jp_y, \quad y = \sqrt{2J_y} \cos \psi_y = \frac{1}{2}(h_y^+ + h_y^-), \quad (\text{A.76})$$

and J_u, ψ_u are the action-angle variables. In the resonance basis, the operator $\mathcal{R}_{l \rightarrow m}$ is a mere rotation about the phase advance μ between the elements l and m , i.e.

$$\mathcal{R}_{l \rightarrow m} h_x^\pm = \mathcal{R}_{l \rightarrow m} \sqrt{2J_x} e^{\pm j\psi_x} = e^{\pm j\mu_{x,l \rightarrow m}} h_x^\pm, \quad (\text{A.77})$$

where $\mu_{x,l \rightarrow m}$ is the horizontal phase advance between elements l and m . In other words the resonant basis represents the eigenfunctions of the rotation operator \mathcal{R} . Corresponding relations hold for the vertical plane. The vector potential defining the magnetic field around the accelerator lattice can then be represented in the resonance basis. The individual terms will be investigated separately in the following.

Sextupole driving terms

Applying the normalization \mathcal{A}_i and the rotation $\mathcal{R}_{0 \rightarrow i}$ to the sextupole potential at an arbitrary location s_i yields

$$\begin{aligned} \mathcal{R}_{0 \rightarrow i} \mathcal{A}_i \frac{K_2}{6} \frac{x^3 - 3xy^2}{1 + \delta} = & \mathcal{R}_{0 \rightarrow i} \frac{K_2}{6} \left\{ \sqrt{\beta_{x,i}} (\beta_{x,i} x^3 - 3\beta_{y,i} xy^2) (1 - \delta) + 3D_{x,i} (\beta_{x,i} x^2 - \beta_{y,i} y^2) \delta \right. \\ & \left. + 3\sqrt{\beta_{x,i}} x D_{x,i}^2 \delta^2 \right\} + \mathcal{O}(\delta^2). \end{aligned} \quad (\text{A.78})$$

Applying the rotation operator on the different powers of x in the resonance basis yields

$$\mathcal{R}_{0 \rightarrow i} x = \frac{1}{2} \mathcal{R}_{0 \rightarrow i} (h_x^+ + h_x^-) = \frac{1}{2} (h_x^+ e^{j\mu_{x,i}} + c.c.), \quad (\text{A.79})$$

$$\mathcal{R}_{0 \rightarrow i} x^2 = \frac{1}{4} \mathcal{R}_{0 \rightarrow i} (h_x^+ + h_x^-)^2 = \frac{1}{4} (h_x^{+2} e^{j2\mu_{x,i}} + c.c. + 4J_x), \quad (\text{A.80})$$

$$\mathcal{R}_{0 \rightarrow i} x^3 = \frac{1}{8} (h_x^{+3} e^{j3\mu_{x,i}} + 3h_x^{+2} h_x^- e^{j\mu_{x,i}} + c.c.), \quad (\text{A.81})$$

$$\mathcal{R}_{0 \rightarrow i} xy^2 = \frac{1}{8} (h_x^+ h_y^{+2} e^{j(\mu_{x,i} + 2\mu_{y,i})} + h_x^+ h_y^{-2} e^{j(\mu_{x,i} - 2\mu_{y,i})} + 2h_x^+ h_y^+ h_y^- e^{j\mu_{x,i}} + c.c.), \quad (\text{A.82})$$

where $\mu_{x,i}$ denotes the phase advance from $0 \rightarrow i$. It follows from inspecting Eq. (A.78) that the Lie generator $:h:$ has in first order of the potential the general form

$$h^{(1)} = \sum_{|l_1, l_2, l_3, l_4, l_5|=o} h_{l_1, l_2, l_3, l_4, l_5} h_x^{+l_1} h_x^{-l_2} h_y^{+l_3} h_y^{-l_4} \delta^{l_5}, \quad (\text{A.83})$$

where $|l_1, l_2, l_3, l_4, l_5| \equiv l_1 + l_2 + l_3 + l_4 + l_5$. This can be interpreted as a mode expansion of the first order Lie generator $h^{(1)}$, where each mode drives either resonances (terms dependent on the angle variable) or tune shifts (terms independent of angle variable). For the first order resonance driving terms associated with sextupoles $o = 3$, i.e. $l_1 + l_2 + l_3 + l_4 + l_5 = 3$. They contain a contribution from the quadrupole potential, since

$$\mathcal{R}_{0 \rightarrow i} \mathcal{A}_i \frac{K_1}{2} \frac{x^2 - y^2}{(1 + \delta)} = \mathcal{R}_{0 \rightarrow i} \frac{K_1}{2} \left\{ (\beta_{x,i} x^2 - \beta_{y,i} y^2)(1 - \delta) + 2\sqrt{\beta_{x,i} x} D_{x,i} \delta \right\} + \mathcal{O}(\delta^2). \quad (\text{A.84})$$

The first order chromatic terms driving the linear chromaticity are then [152]

$$h_{11001} = + \frac{1}{4} \sum_{i=1}^n [(K_1 L)_i - (K_2 L)_i D_{x,i}] \beta_{x,i} + \mathcal{O}(\delta^2), \quad (\text{A.85})$$

$$h_{00111} = - \frac{1}{4} \sum_{i=1}^n [(K_1 L)_i - (K_2 L)_i D_{x,i}] \beta_{y,i} + \mathcal{O}(\delta^2), \quad (\text{A.86})$$

where $L = L_i$ denotes the length of the element at location i . Since J_u and $2\pi\nu_u$ are conjugate variables the tune-shift is given by

$$\Delta\nu_u = - \frac{1}{2\pi} \frac{\partial h}{\partial J_u}. \quad (\text{A.87})$$

The first order (in δ) chromaticity $\mathcal{C}_u^{(1)} = Q'_u$ is then obtained from

$$\mathcal{C}_x^{(1)} \equiv \frac{\partial(\Delta\nu_x)}{\partial\delta} = - \frac{1}{2\pi} \frac{\partial}{\partial\delta} \frac{\partial h_{11001} h_x^+ h_x^- \delta}{\partial J_x} = - \frac{1}{4\pi} \sum_{i=1}^n [(K_1 L)_i - (K_2 L)_i D_{x,i}] \beta_{x,i} + \mathcal{O}(\delta^2), \quad (\text{A.88})$$

$$\mathcal{C}_y^{(1)} \equiv \frac{\partial(\Delta\nu_y)}{\partial\delta} = - \frac{1}{2\pi} \frac{\partial}{\partial\delta} \frac{\partial h_{00111} h_y^+ h_y^- \delta}{\partial J_y} = + \frac{1}{4\pi} \sum_{i=1}^n [(K_1 L)_i - (K_2 L)_i D_{x,i}] \beta_{y,i} + \mathcal{O}(\delta^2), \quad (\text{A.89})$$

which is exactly what was found already in Eqs. (A.69a) and (A.69b), but in thin lens representation. The remaining first order chromatic sextupole driving terms are

$$h_{20001} = h_{02001}^* = +\frac{1}{8} \sum_{i=1}^n [(K_1 L)_i - (K_2 L)_i D_{x,i}] \beta_{x,i} e^{j2\mu_{x,i}} + \mathcal{O}(\delta^2), \quad (\text{A.90})$$

$$h_{00201} = h_{00021}^* = -\frac{1}{8} \sum_{i=1}^n [(K_1 L)_i - (K_2 L)_i D_{x,i}] \beta_{y,i} e^{j2\mu_{y,i}} + \mathcal{O}(\delta^2), \quad (\text{A.91})$$

$$h_{10002} = h_{01002}^* = +\frac{1}{2} \sum_{i=1}^n [(K_1 L)_i - \frac{1}{2}(K_2 L)_i D_{x,i}] D_{x,i} \sqrt{\beta_{x,i}} e^{j\mu_{x,i}} + \mathcal{O}(\delta^3), \quad (\text{A.92})$$

where h_{20001} and h_{00201} drive synchro-betatron resonances and momentum dependence of the beta function. On the other hand, h_{10002} drives second order dispersion. In addition, the first order Lie generator $h^{(1)}$ contains the five geometric terms

$$h_{21000} = h_{12000}^* = -\frac{1}{16} \sum_{i=1}^n (K_2 L)_i \beta_{x,i}^{3/2} e^{j\mu_{x,i}}, \quad (\text{A.93})$$

$$h_{30000} = h_{03000}^* = -\frac{1}{48} \sum_{i=1}^n (K_2 L)_i \beta_{x,i}^{3/2} e^{j3\mu_{x,i}}, \quad (\text{A.94})$$

$$h_{10110} = h_{01110}^* = +\frac{1}{8} \sum_{i=1}^n (K_2 L)_i \beta_{x,i}^{1/2} \beta_{y,i} e^{j\mu_{x,i}}, \quad (\text{A.95})$$

$$h_{10020} = h_{01200}^* = +\frac{1}{16} \sum_{i=1}^n (K_2 L)_i \beta_{x,i}^{1/2} \beta_{y,i} e^{j(\mu_{x,i}-2\mu_{y,i})}, \quad (\text{A.96})$$

$$h_{10200} = h_{01020}^* = +\frac{1}{16} \sum_{i=1}^n (K_2 L)_i \beta_{x,i}^{1/2} \beta_{y,i} e^{j(\mu_{x,i}+2\mu_{y,i})}, \quad (\text{A.97})$$

which drive the betatron modes with ν_x , $3\nu_x$, $\nu_x - 2\nu_y$ and $\nu_x + 2\nu_y$, respectively.

Sextupoles also induce an amplitude dependent tune shift as defined by the first order anharmonicities a_{xx} , a_{xy} and a_{yy} such that

$$\begin{pmatrix} \Delta\nu_x \\ \Delta\nu_y \end{pmatrix} = \begin{pmatrix} a_{xx} & a_{xy} \\ a_{yx} & a_{yy} \end{pmatrix} \begin{pmatrix} 2J_x \\ 2J_y \end{pmatrix}, \quad (\text{A.98})$$

where $a_{xy} = a_{yx}$. However, sextupoles generate these anharmonicities only in second order (quadratic in their multipole strength K_2). They are [152]

$$\begin{aligned} a_{xx} \equiv \frac{\partial \Delta\nu_x}{2 \partial J_x} &= -\frac{1}{128\pi} \sum_{i=1}^n \sum_{k=1}^n (K_2 L)_i (K_2 L)_k \beta_{x,i}^{3/2} \beta_{x,k}^{3/2} \\ &\times \left[\frac{3 \cos(|\mu_{x,i \rightarrow k}| - \pi\nu_x)}{\sin(\pi\nu_x)} + \frac{\cos(|\mu_{x,i \rightarrow k}| - 3\pi\nu_x)}{\sin(3\pi\nu_x)} \right], \end{aligned} \quad (\text{A.99})$$

$$a_{xy} \equiv \frac{\partial \Delta \nu_x}{2 \partial J_y} = \frac{\partial \Delta \nu_y}{2 \partial J_x} = \frac{1}{64\pi} \sum_{i=1}^n \sum_{k=1}^n (K_2 L)_i (K_2 L)_k \sqrt{\beta_{x,i} \beta_{x,k}} \beta_{y,i} \left[\frac{2\beta_{x,k} \cos(|\mu_{x,i \rightarrow k}| - \pi \nu_x)}{\sin(\pi \nu_x)} \right. \\ \left. - \frac{\beta_{y,k} \cos\{|\mu_{x,i \rightarrow k} + 2\mu_{y,i \rightarrow k}| - \pi(\nu_x + 2\nu_y)\}}{\sin[\pi(\nu_x + 2\nu_y)]} + \frac{\beta_{y,k} \cos\{|\mu_{x,i \rightarrow k} - 2\mu_{y,i \rightarrow k}| - \pi(\nu_x - 2\nu_y)\}}{\sin[\pi(\nu_x - 2\nu_y)]} \right], \quad (\text{A.100})$$

$$a_{yy} \equiv \frac{\partial \Delta \nu_y}{2 \partial J_y} = -\frac{1}{128\pi} \sum_{i=1}^n \sum_{k=1}^n (K_2 L)_i (K_2 L)_k \sqrt{\beta_{x,i} \beta_{x,k}} \beta_{y,i} \beta_{y,k} \left[\frac{4 \cos(|\mu_{x,i \rightarrow k}| - \pi \nu_x)}{\sin(\pi \nu_x)} \right. \\ \left. + \frac{\cos\{|\mu_{x,i \rightarrow k} + 2\mu_{y,i \rightarrow k}| - \pi(\nu_x + 2\nu_y)\}}{\sin[\pi(\nu_x + 2\nu_y)]} + \frac{\cos\{|\mu_{x,i \rightarrow k} - 2\mu_{y,i \rightarrow k}| - \pi(\nu_x - 2\nu_y)\}}{\sin[\pi(\nu_x - 2\nu_y)]} \right]. \quad (\text{A.101})$$

Sextupoles also contribute to second order chromaticity $\mathcal{C}_u^{(2)}$ through the momentum dependence of the optical functions [152], since

$$\mathcal{C}_x^{(2)} = \frac{1}{2} Q_x'' = \frac{1}{2} \frac{\partial^2 \Delta \nu_x(\delta)}{\partial \delta^2} = \frac{1}{2} \frac{\partial}{\partial \delta} \frac{\partial \Delta \nu_x(\delta)}{\partial \delta} \\ = -\frac{1}{2} \mathcal{C}_x^{(1)} + \frac{1}{8\pi} \sum_{i=1}^n \left\{ (K_2 L)_i \frac{\partial D_{x,i}}{\partial \delta} \beta_{x,i} - \left[(K_1 L)_i - (K_2 L)_1 D_{x,i} \right] \frac{\partial \beta_{x,i}}{\partial \delta} \right\}, \quad (\text{A.102})$$

$$\mathcal{C}_y^{(2)} = \frac{1}{2} Q_y'' = \frac{1}{2} \frac{\partial^2 \Delta \nu_y(\delta)}{\partial \delta^2} = \frac{1}{2} \frac{\partial}{\partial \delta} \frac{\partial \Delta \nu_y(\delta)}{\partial \delta} \\ = -\frac{1}{2} \mathcal{C}_y^{(1)} - \frac{1}{8\pi} \sum_{i=1}^n \left\{ (K_2 L)_i \frac{\partial D_{x,i}}{\partial \delta} \beta_{y,i} + \left[(K_1 L)_i - (K_2 L)_1 D_{x,i} \right] \frac{\partial \beta_{y,i}}{\partial \delta} \right\}, \quad (\text{A.103})$$

where

$$\frac{\partial D_{x,k}}{\partial \delta} = -D_{x,k} + \frac{\sqrt{\beta_{x,i}}}{2 \sin(\pi \nu_x)} \sum_{i=1}^n \left[(K_1 L)_i - (K_2 L)_i D_{x,i} \right] D_{x,i} \sqrt{\beta_{x,i}} \cos(|\mu_{x,k \rightarrow i}| - \pi \nu_x), \quad (\text{A.104})$$

and the chromatic beta-variation is

$$\frac{\partial \beta_{x,k}}{\partial \delta} = \frac{\beta_{x,i}}{2 \sin(2\pi \nu_x)} \sum_{i=1}^n \left[(K_1 L)_i - (K_2 L)_i D_{x,i} \right] \beta_{x,i} \cos(|2\mu_{x,k \rightarrow i}| - 2\pi \nu_x), \quad (\text{A.105})$$

$$\frac{\partial \beta_{y,k}}{\partial \delta} = -\frac{\beta_{y,i}}{2 \sin(2\pi \nu_y)} \sum_{i=1}^n \left[(K_1 L)_i - (K_2 L)_i D_{x,i} \right] \beta_{y,i} \cos(|2\mu_{y,k \rightarrow i}| - 2\pi \nu_y). \quad (\text{A.106})$$

Octupole driving terms

The resonance driving terms associated to octupoles can be derived in the same manner as for the sextupoles. The Hamiltonian of an octupole is written as [153]

$$H(x, p_x, y, p_y; s) = \frac{K_3}{24(1 + \delta)} (x^4 - 6x^2 y^2 + y^4) = \frac{K_3}{24} \left[1 - \delta + \delta^2 + \mathcal{O}(\delta^3) \right] (x^4 - 6x^2 y^2 + y^4), \quad (\text{A.107})$$

where $K_3 = B_3/B\rho$ and $B_3 = \partial^3 B_y/\partial x^3$. Applying the normalization operator \mathcal{A}_i and the rotation $\mathcal{R}_{0 \rightarrow i}$ yields

$$\begin{aligned} \mathcal{R}_{0 \rightarrow i} \mathcal{A}_i \frac{K_3}{24(1+\delta)} (x^4 - 6x^2y^2 + y^4) = & \mathcal{R}_{0 \rightarrow i} \frac{K_3}{24} \left\{ [\text{Oct}]_i - \delta \left([\text{Oct}]_i - 4[\text{Sext}]_i D_{x,i} \right) \right. \\ & \left. + \delta^2 \left([\text{Oct}]_i - 4[\text{Sext}]_i D_{x,i} + 6[\text{Quad}]_i D_{x,i}^2 \right) + \mathcal{O}(\delta^3) \right\} \end{aligned} \quad (\text{A.108})$$

where a short notation similar to [153] is used, such that

$$[\text{Oct}]_i = \beta_{x,i}^2 x^4 - 6\beta_{x,i}\beta_{y,i} x^2 y^2 + \beta_{y,i}^2 y^4 \quad (\text{A.109})$$

$$[\text{Sext}]_i = \sqrt{\beta_{x,i}} (\beta_{x,i} x^3 - 3\beta_{y,i} x y^2) \quad (\text{A.110})$$

$$[\text{Quad}]_i = \beta_{x,i} x^2 - \beta_{y,i} y^2 \quad (\text{A.111})$$

The resonance driving terms are then obtained in the same way as done for the sextupole above by representing Eq. (A.123) in the resonance basis. The first order octupole hamiltonian $h^{(1)}$ contains 36 driving terms. Up to second order in momentum deviation, there are five terms which are independent of the angle variable and therefore drive tune shifts. Two of them drive second order chromaticity,

$$h_{11002} = -\frac{1}{8} \sum_{i=1}^n (K_3 L)_i \beta_{x,i} D_{x,i}^2 \quad (\text{A.112})$$

$$h_{00112} = +\frac{1}{8} \sum_{i=1}^n (K_3 L)_i \beta_{x,i} D_{x,i}^2 \quad (\text{A.113})$$

where

$$\mathcal{C}_x^{(2)} = \frac{1}{2} Q_x'' = \frac{1}{2} \frac{\partial^2 \Delta \nu_x}{\partial \delta^2} = -\frac{1}{4\pi} \frac{\partial^2}{\partial \delta^2} \frac{\partial h_{11002} h_x^+ h_x^- \delta^2}{\partial J_x} = +\frac{1}{8\pi} \sum_{i=1}^n (K_3 L)_i \beta_{x,i} D_{x,i}^2, \quad (\text{A.114})$$

$$\mathcal{C}_y^{(2)} = \frac{1}{2} Q_y'' = \frac{1}{2} \frac{\partial^2 \Delta \nu_y}{\partial \delta^2} = -\frac{1}{4\pi} \frac{\partial^2}{\partial \delta^2} \frac{\partial h_{11002} h_y^+ h_y^- \delta^2}{\partial J_y} = -\frac{1}{8\pi} \sum_{i=1}^n (K_3 L)_i \beta_{y,i} D_{x,i}^2. \quad (\text{A.115})$$

The other three are the geometric terms

$$h_{22000} = -\frac{1}{64} \sum_{i=1}^n (K_3 L)_i \beta_{x,i}^2, \quad (\text{A.116})$$

$$h_{11110} = +\frac{1}{16} \sum_{i=1}^n (K_3 L)_i \beta_{x,i} \beta_{y,i}, \quad (\text{A.117})$$

$$h_{00220} = -\frac{1}{64} \sum_{i=1}^n (K_3 L)_i \beta_{y,i}^2, \quad (\text{A.118})$$

driving amplitude dependent tune-shift in first order, such that

$$a_{xx} = \frac{\partial \Delta \nu_x}{2 \partial J_x} = -\frac{1}{4\pi} \frac{\partial^2 h_{22000} h_x^{+2} h_x^{-2}}{\partial J_x^2} = \frac{1}{32\pi} \sum_{i=1}^n (K_3 L)_i \beta_{x,i}^2, \quad (\text{A.119})$$

$$a_{xy} = \frac{\partial \Delta \nu_x}{2 \partial J_y} = \frac{\partial \Delta \nu_y}{2 \partial J_x} = -\frac{1}{4\pi} \frac{\partial \partial h_{11110} h_x^+ h_x^- h_y^+ h_y^-}{\partial J_x \partial J_y} = -\frac{1}{16\pi} \sum_{i=1}^n (K_3 L)_i \beta_{x,i} \beta_{y,i}, \quad (\text{A.120})$$

$$a_{yy} = \frac{\partial \Delta \nu_y}{2 \partial J_y} = -\frac{1}{4\pi} \frac{\partial^2 h_{00220} h_y^{+2} h_y^{-2}}{\partial J_y^2} = \frac{1}{32\pi} \sum_{i=1}^n (K_3 L)_i \beta_{y,i}^2. \quad (\text{A.121})$$

Thus the linear amplitude dependent tune-shift can be controlled with 3 independent octupole magnets. They are preferably installed in a zero dispersion region of the ring. Otherwise they create second order chromaticity. On the other hand, octupoles can be installed on purpose in dispersive locations for correcting second order chromatic effects.

Decapole driving terms

The driving terms associated with decapole magnets are derived in an analogous way as the octupole and septupole driving terms. The Hamiltonian for a decapole magnet is thereby expanded up to δ^3 [153]

$$\begin{aligned} H(x, p_x, y, p_y; s) &= \frac{K_4}{120} (x^5 - 10x^3y^2 + y^5) \\ &= \frac{K_4}{120} \left[1 - \delta + \delta^2 - \delta^3 + \mathcal{O}(\delta^4) \right] (x^5 - 10x^3y^2 + y^5), \end{aligned} \quad (\text{A.122})$$

where $K_4 = B_4/B\rho$ and $B_4 = \partial^4 B_y / \partial x^4$. Applying the normalization operator \mathcal{A}_i and the rotation $\mathcal{R}_{0 \rightarrow i}$ yields

$$\begin{aligned} \mathcal{R}_{0 \rightarrow i} \mathcal{A}_i \frac{K_4}{120} \frac{x^5 - 10x^3y^2 + y^5}{(1+\delta)} &= \mathcal{R}_{0 \rightarrow i} \frac{K_4}{120} \left\{ [\text{Dec}]_i - \delta \left([\text{Dec}] - 5[\text{Oct}]_i D_{x,i} \right) \right. \\ &\quad + \delta^2 \left([\text{Dec}]_i D_{x,i} - 5[\text{Oct}]_i D_{x,i}^2 + 10[\text{Sext}]_i D_{x,i}^3 \right) \\ &\quad - \delta^3 \left([\text{Dec}]_i D_{x,i}^2 - 5[\text{Oct}]_i D_{x,i}^3 + 10[\text{Sext}]_i D_{x,i}^4 - 5[\text{Quad}]_i D_{x,i}^5 \right) \\ &\quad \left. + \mathcal{O}(\delta^4) \right\}, \end{aligned} \quad (\text{A.123})$$

where in addition to the short notations defined in Eqs. (A.109)-(A.111), the definition of $[\text{Dec}]_i$

$$[\text{Dec}]_i = \beta_{x,i}^{5/2} x^5 - 10\beta_{x,i}^{3/2} \beta_{y,i} x^3 y^2 + \beta_{y,i}^{5/2} y^5 \quad (\text{A.124})$$

was introduced. Representing this in the resonance basis allows to identify 65 driving terms associated to decapole magnets in first order $h^{(1)}$, where 60 of them depend on

the angle variable and therefore drive resonances. Two of the remaining terms,

$$h_{11003} = -\frac{1}{24} \sum_{i=1}^n (K_4 L)_i \beta_{x,i} D_{x,i}^3, \quad (\text{A.125})$$

$$h_{00113} = +\frac{1}{24} \sum_{i=1}^n (K_4 L)_i \beta_{y,i} D_{x,i}^3, \quad (\text{A.126})$$

drive third order chromaticity $\mathcal{C}_u^{(3)}$, since

$$\mathcal{C}_x^{(3)} = \frac{1}{6} Q_x''' = \frac{1}{6} \frac{\partial^3 \Delta \nu_x}{\partial \delta^3} = -\frac{1}{12\pi} \frac{\partial^3}{\partial \delta^3} \frac{\partial h_{11003} h_x^+ h_x^- \delta^3}{\partial J_x} = +\frac{1}{24\pi} \sum_{i=1}^n (K_4 L)_i \beta_{x,i} D_{x,i}^3, \quad (\text{A.127})$$

$$\mathcal{C}_y^{(3)} = \frac{1}{6} Q_y''' = \frac{1}{6} \frac{\partial^3 \Delta \nu_y}{\partial \delta^3} = -\frac{1}{12\pi} \frac{\partial^3}{\partial \delta^3} \frac{\partial h_{11003} h_y^+ h_y^- \delta^3}{\partial J_y} = -\frac{1}{24\pi} \sum_{i=1}^n (K_4 L)_i \beta_{y,i} D_{x,i}^3. \quad (\text{A.128})$$

Decapole errors usually present in the field configuration of dipole magnets therefore create third order chromaticity. In addition, there are three terms

$$h_{22001} = -\frac{1}{64} \sum_{i=1}^n (K_4 L)_i \beta_{x,i}^2 D_{x,i}, \quad (\text{A.129})$$

$$h_{11111} = +\frac{1}{16} \sum_{i=1}^n (K_4 L)_i \beta_{x,i} \beta_{y,i} D_{x,i}, \quad (\text{A.130})$$

$$h_{00221} = -\frac{1}{64} \sum_{i=1}^n (K_4 L)_i \beta_{y,i}^2 D_{x,i}, \quad (\text{A.131})$$

driving chromatic amplitude dependent tune shift [153]

$$\frac{\partial \Delta \nu_x}{\partial J_x} = -\frac{1}{2\pi} \frac{\partial^2 h_{22001} h_x^{+2} h_x^{-2} \delta}{\partial J_x^2} = \frac{1}{16\pi} \sum_{i=1}^n (K_4 L)_i \beta_{x,i}^2 D_{x,i} \delta, \quad (\text{A.132})$$

$$\frac{\partial \Delta \nu_x}{\partial J_y} = \frac{\partial \Delta \nu_y}{\partial J_x} = -\frac{1}{2\pi} \frac{\partial \partial h_{11111} h_x^+ h_x^- h_y^+ h_y^- \delta}{\partial J_x \partial J_y} = -\frac{1}{8\pi} \sum_{i=1}^n (K_4 L)_i \beta_{x,i}^2 \beta_{y,i}^2 D_{x,i} \delta, \quad (\text{A.133})$$

$$\frac{\partial \Delta \nu_y}{\partial J_y} = -\frac{1}{2\pi} \frac{\partial^2 h_{22001} h_y^{+2} h_y^{-2} \delta}{\partial J_y^2} = \frac{1}{16\pi} \sum_{i=1}^n (K_4 L)_i \beta_{y,i}^2 D_{x,i} \delta. \quad (\text{A.134})$$

In other words, the feed-down effect of the decapole magnet creates an octupole field for off-momentum particles. Furthermore, decapole components induce non-linear detuning with amplitude in second order (quadratic in their multipole strength $K_4 L$). The corresponding driving terms are not presented here due to their complexity.

B. Longitudinal particle motion

B.1. Acceleration in longitudinal electric field

Charged particles can be accelerated using longitudinal electric fields. In synchrotrons, this electric field is provided by radio frequency (RF) cavities. The longitudinal electric field \mathcal{E} in the RF gap can be described as

$$\mathcal{E} = \mathcal{E}_0 \sin[\varphi_{\text{RF}}(t) + \varphi_s], \quad \varphi_{\text{RF}}(t) = \omega_{\text{RF}}t \quad (\text{B.135})$$

where \mathcal{E}_0 is the amplitude of the electric field and φ_s is the phase angle of the *synchronous* particle with respect to the phase of the RF wave $\varphi_{\text{RF}}(t)$. In particular, the angular frequency of the RF wave ω_{RF} is chosen to be an integer multiple h of the angular revolution frequency of the synchronous particle $\omega_0 = \beta_0 c/R_0$, where β_0 ($\gamma_0 \equiv 1/\sqrt{1-\beta_0^2}$) is the relativistic velocity (mass) factor of the reference particle and R_0 is the average radius of the reference orbit, such that

$$\omega_{\text{RF}} = h\omega_0. \quad (\text{B.136})$$

The harmonic number h defines thus the maximal number of bunches that can be accelerated in a synchrotron. The energy gain ΔE_0 of the synchronous particle passing through an RF cavity with a gap width g is given by

$$\Delta E_s = e \int_{-g/2}^{g/2} \mathcal{E}_0 \sin(\varphi_{\text{RF}} + \varphi_s) ds = e\mathcal{E}_0\beta_0 c \int_{-g/(2\beta_0 c)}^{g/(2\beta_0 c)} \sin(h\omega_0 t + \varphi_s) dt = e\mathcal{E}_0 g \mathcal{T} \sin \varphi_s, \quad (\text{B.137})$$

where it was assumed that the velocity increase of the particle is small compared to its velocity and \mathcal{T} is the transit time factor

$$\mathcal{T} = \frac{\sin(hg/2R_0)}{hg/2R_0}, \quad (\text{B.138})$$

which accounts for the fact that the particle passes through the RF gap within a finite time interval. The effective voltage V seen by the particle is thus given by

$$V = \mathcal{E}_0 g \mathcal{T}. \quad (\text{B.139})$$

In circular accelerators such as synchrotrons, particles will cross the accelerating gap in each revolution. The acceleration rate of the synchronous particle $dE_0/dt \equiv \dot{E}_0$ is then given by

$$\dot{E}_0 = \frac{\omega_0}{2\pi} eV \sin \varphi_s. \quad (\text{B.140})$$

B.2. Momentum compaction and phase-slip factor

As discussed in the context of transverse motion above, the closed orbit of a given particle depends on its momentum offset with respect to the reference particle. To the lowest order in $\delta = \Delta p/p_0$, the path length change around a circular machine ΔC is given by

$$\Delta C = \oint \frac{x}{\rho(s)} ds = \left[\oint \frac{D_x(s)}{\rho(s)} ds \right] \delta, \quad (\text{B.141})$$

where $\rho(s)$ is the bending radius. The momentum compaction factor α_c relates then the change of path length with the momentum offset, such that

$$\alpha_c \equiv \frac{\Delta C/C}{\Delta p/p_0} = \frac{1}{C} \oint \frac{D_x(s)}{\rho(s)} ds, \quad (\text{B.142})$$

where C is the design circumference of the machine. The change of path length will change the revolution frequency depending on the momentum offset of the particle. Since the angular revolution frequency of the reference particle is given as $\omega_0 = 2\pi\beta_0 c/C$, it follows that

$$\frac{\Delta\omega}{\omega_0} = \frac{\Delta\beta}{\beta_0} - \frac{\Delta C}{C}, \quad (\text{B.143})$$

i.e. the revolution frequency change depends on the change of velocity and the change of path length with momentum. Using the relation

$$\frac{dp}{d\beta} = mc \frac{d}{d\beta}(\beta\gamma) = mc\gamma(1 + \beta^2\gamma^2) = p\gamma^2/\beta \Rightarrow \frac{\Delta\beta}{\beta_0} = \frac{1}{\gamma_0^2} \frac{\Delta p}{p_0}, \quad (\text{B.144})$$

where β and $\gamma = 1/\sqrt{1 - \beta^2}$ are the relativistic velocity and mass factors of the non-synchronous particle, respectively, the phase-slip factor or simply slip factor η can be written as

$$\eta \equiv -\frac{\Delta\omega/\omega_0}{\Delta p/p_0} = \alpha_c - \frac{1}{\gamma_0^2} = \frac{1}{\gamma_t^2} - \frac{1}{\gamma_0^2}, \quad (\text{B.145})$$

where $\gamma_t \equiv 1/\sqrt{\alpha_c}$ is called the transition energy. Below transition ($\gamma_0 < \gamma_t$), the time of arrival at a given location in the ring is dominated by the particle velocity. Particles with positive momentum offset have a shorter revolution period than synchronous particles and $\eta < 0$. Above transition ($\gamma_0 > \gamma_t$), the change in path length is more significant than the difference in velocity. Consequently particles with higher momentum have larger revolution period and $\eta > 0$. It should be mentioned that higher order components of the momentum compaction factor with respect to δ can become important during transition crossing, as in this case η depends on the particle's momentum offset and thus particles with different momenta may cross transition at different times.

B.3. Longitudinal equations of motion

Let's consider now a particle with longitudinal parameters which deviate only slightly from the synchronous particle such that

$$\begin{cases} \omega = \omega_0 + \Delta\omega, \\ p = p_0 + \Delta p, \\ \varphi = \varphi_s + \Delta\varphi, \\ E = E_0 + \Delta E. \end{cases} \quad (\text{B.146})$$

Since a particle with a larger revolution frequency will be ahead of the synchronous particle it will have a smaller phase with respect to the RF wave compared to φ_s , i.e. negative $\Delta\varphi$. Thus,

$$\Delta\omega = -\frac{1}{h} \frac{d(\Delta\varphi)}{dt} = -\frac{1}{h} \frac{d\varphi}{dt} \equiv -\frac{1}{h} \dot{\varphi}, \quad (\text{B.147})$$

where it was assumed that the phase angle of the synchronous particle φ_s is changing only slowly in time. This equation can be re-written using the phase-slip factor as defined in Eq. (B.145) and the relation

$$\frac{dp}{dE} = \frac{d(\gamma\beta mc)}{mc^2 d\gamma} = \frac{1}{c} \frac{d}{d\gamma} \left(\gamma \sqrt{1 - 1/\gamma^2} \right) = \frac{1}{\beta c} = \frac{p}{\beta^2 E} \Rightarrow \frac{\Delta p}{p_0} = \frac{1}{\beta_0^2} \frac{\Delta E}{E_0}, \quad (\text{B.148})$$

so that

$$\dot{\varphi} = h\omega_0 \eta \Delta p / p_0 = \frac{h\omega_0^2 \eta}{\beta_0^2 E_0} \left(\frac{\Delta E}{\omega_0} \right), \quad (\text{B.149})$$

which is the first energy phase equation. A second relation is obtained from the acceleration rate as described by Eq. (B.140), which reads for the synchronous particle

$$\dot{E}_0 = \frac{\omega_0}{2\pi} eV \sin \varphi_s. \quad (\text{B.150})$$

Writing the difference between Eq. (B.140) and Eq. (B.150) leads to

$$\frac{\dot{E}}{\omega} - \frac{\dot{E}_0}{\omega_0} = \frac{1}{2\pi} eV (\sin \varphi - \sin \varphi_s), \quad (\text{B.151})$$

which can be approximated by (see for example [14], Chapter 3-I)

$$\frac{d}{dt} \left(\frac{\Delta E}{\omega_0} \right) = \frac{1}{2\pi} eV (\sin \varphi - \sin \varphi_s). \quad (\text{B.152})$$

This is the second energy phase relation. Note that these two energy phase equations can be derived from a Hamiltonian with time t as independent variable and the

conjugate phase-space variables $(\varphi, \Delta E/\omega_0)$

$$H(\varphi, \Delta E/\omega_0; t) = \frac{1}{2} \frac{h\eta\omega_0^2}{\beta_0^2 E_0} \left(\frac{\Delta E}{\omega_0} \right)^2 + \frac{eV}{2\pi} [\cos \varphi - \cos \varphi_s + (\varphi - \varphi_s) \sin \varphi_s], \quad (\text{B.153})$$

with Hamilton's equations

$$\frac{d\varphi}{dt} = \frac{h\omega_0^2\eta}{\beta_0^2 E_0} \left(\frac{\Delta E}{\omega_0} \right), \quad \frac{d}{dt} \left(\frac{\Delta E}{\omega_0} \right) = \frac{eV}{2\pi} (\sin \varphi - \sin \varphi_s). \quad (\text{B.154})$$

They lead to the second order non-linear equation of motion in the longitudinal plane

$$\frac{d}{dt} \left(\frac{\beta_0^2 E_0}{h\omega_0^2\eta} \frac{d\varphi}{dt} \right) = \frac{eV}{2\pi} (\sin \varphi - \sin \varphi_s). \quad (\text{B.155})$$

In the *adiabatic regime*, the parameters of the synchronous particle change slowly with time and thus the equation of motion can be simplified to

$$\ddot{\varphi} = \frac{h\omega_0^2 eV\eta}{2\pi\beta_0^2 E_0} (\sin \varphi - \sin \varphi_s). \quad (\text{B.156})$$

B.4. Small amplitude synchrotron oscillations in the adiabatic regime

For small synchrotron amplitudes, the equation of motion can be expanded around the synchronous phase angle φ_s . In particular, one can write

$$\sin(\varphi_s + \Delta\varphi) - \sin \varphi_s = \sin \varphi_s \cos \Delta\varphi + \sin \Delta\varphi \cos \varphi_s - \sin \varphi_s = \Delta\varphi \cos \varphi_s + \mathcal{O}(\Delta\varphi^2), \quad (\text{B.157})$$

and since in the adiabatic regime φ_s is constant and thus $\frac{d^2}{dt^2} \varphi = \frac{d^2}{dt^2} \Delta\varphi$, the linearized equation of motion for small synchrotron amplitudes is obtained as

$$\frac{d^2}{dt^2} \Delta\varphi = \frac{h\omega_0^2 eV\eta \cos \varphi_s}{2\pi\beta_0^2 E_0} \Delta\varphi. \quad (\text{B.158})$$

For stable synchrotron motion it is thus required that $\eta \cos \varphi_s < 0$. This is also known as the phase stability condition of McMillan and Veksler, and is the fundamental concept of synchrotron oscillations. Below transition $\eta < 0$ and for stability $0 < \varphi_s < \pi/2$. In this case, particles with larger energy will be ahead of the synchronous particle and will receive less energy gain in the RF gap, and vice versa. The RF wave has therefore a focusing effect in the longitudinal plane around the stable fixed point given by φ_s . Above transition, $\eta > 0$ and stability requires $\pi/2 < \varphi_s < \pi$. The synchronous phase has to be shifted to $\pi - \varphi_s$. Approaching transition energy ($\gamma_0 \sim \gamma_t$), the synchrotron frequency ω_s slows down and becomes non-adiabatic eventually. In first order, synchrotron motion is frozen at transition energy.

In small amplitude approximation the longitudinal motion is a harmonic oscilla-

tion. The corresponding angular synchrotron frequency ω_s for small amplitudes can be directly inferred from Eq. (B.157)

$$\omega_s = \omega_0 \sqrt{\frac{heV|\eta \cos \varphi_s|}{2\pi\beta_0^2 E_0}}. \quad (\text{B.159})$$

The synchrotron tune Q_s is then defined as

$$Q_s = \frac{\omega_s}{\omega_0} = \sqrt{\frac{heV|\eta \cos \varphi_s|}{2\pi\beta_0^2 E_0}}. \quad (\text{B.160})$$

For small synchrotron amplitudes the phase-space trajectory is described by an ellipse. Multiplying Eq. (B.157) with $\frac{d}{dt}\Delta\varphi$ and integrating over time t yields the first integral of the equation of longitudinal motion,

$$\frac{\left(\frac{d}{dt}\Delta\varphi\right)^2}{2} - \frac{h\omega_0^2\eta eV \cos \varphi_s}{2\pi\beta_0^2 E_0} \frac{(\Delta\varphi)^2}{2} = \text{constant}. \quad (\text{B.161})$$

Using the fact that in the adiabatic regime $\frac{d}{dt}\Delta\varphi = \frac{d}{dt}\varphi$ and the energy phase relation of Eq. (B.149), the phase-space trajectory in small amplitude approximation is

$$\left(\frac{\Delta E}{\omega_0}\right)^2 - \frac{\beta_0^2 E_0 eV \cos \varphi_s}{2\pi h\omega_0^2 \eta} (\Delta\varphi)^2 = \text{constant}. \quad (\text{B.162})$$

It should be emphasized that this equation indeed describes an ellipse in phase-space centered around the stable phase φ_s , since the stability criterion for synchrotron motion requires that $\eta \cos \varphi_s < 0$ and therefore the second term on the left hand side is positive.

Similar to the transverse plane, the area covered by a particle distribution in longitudinal phase-space is characterized by the longitudinal emittance. The definition of the *invariant* longitudinal emittance ε_l in units eVs used at CERN [1] is

$$\varepsilon_l = 4\pi\sigma_t\sigma_{\frac{\Delta E}{E_0}}E_0, \quad (\text{B.163})$$

where σ_t is the rms bunch length in seconds and $\sigma_{\frac{\Delta E}{E_0}}$ is the relative rms energy spread. Note that at CERN the bunch length is usually quoted as 4σ value, $\tau \equiv 4\sigma_t$. Converting Eq. (B.162) into $(\Delta E/E_0, \Delta t)$ phase-space, where $\Delta t = \Delta\varphi/(\omega_0 h)$ is the time of arrival difference with respect to the synchronous particle, yields

$$\left(\frac{\Delta E}{E_0}\right)^2 - \frac{\omega_0^2\beta_0^2 heV \cos \varphi_s}{2\pi E_0 \eta} (\Delta t)^2 = \text{constant}. \quad (\text{B.164})$$

The longitudinal emittance corresponds then to the phase-space area enclosed by the trajectory which goes through the extremal points $(0, \Delta t = 2\sigma_t)$ and $\left(\frac{\Delta E}{E_0} = 2\sigma_{\frac{\Delta E}{E_0}}, 0\right)$.

It is thus found that in small amplitude approximation (and in absence of radiation damping)

$$\sigma_{\frac{\Delta E}{E_0}} = \sqrt{\frac{\omega_0^2 \beta_0^2 h e V |\cos \varphi_s|}{2\pi E_0 |\eta|}} \sigma_t. \quad (\text{B.165})$$

With the definition of the longitudinal emittance the rms bunch length and the rms energy spread can then be expressed as

$$\sigma_{\frac{\Delta E}{E_0}} = \sqrt{\frac{\varepsilon_l}{4\pi}} \left(\frac{\omega_0^2 \beta_0^2 h e V |\cos \varphi_s|}{2\pi E_0^3 |\eta|} \right)^{1/4}, \quad (\text{B.166a})$$

$$\sigma_t = \sqrt{\frac{\varepsilon_l}{4\pi}} \left(\frac{2\pi |\eta|}{\omega_0^2 \beta_0^2 E_0 h e V |\cos \varphi_s|} \right)^{1/4}. \quad (\text{B.166b})$$

It is interesting to note that for a given longitudinal emittance the bunch length scales like $\sigma_t \propto (|\eta|/V)^{1/4}$ and thus a large increase of the RF voltage is required for adiabatic shortening of bunch length. Another important aspect comes from the fact that for maintaining the bunch length and energy spread for different values of the slip factor η the RF voltage has to be adjusted like $V \propto |\eta|$. It should be emphasized that this observation is not specific to the small amplitude approximation.

B.5. Bucket area

In the discussion about the small amplitude synchrotron motion, it was realized already that the stability condition requires $\eta \cos \varphi_s < 0$. In fact, inspecting the synchrotron Hamiltonian in Eq. (B.153) reveals two fixed points. Synchrotron motion close to the stable fixed point ($\varphi = \varphi_s, \Delta E/\omega_0 = 0$) is described by elliptical trajectories. On the other hand the phase-space point ($\varphi = \pi - \varphi_s, \Delta E/\omega_0 = 0$) is an unstable fixed point and close-by trajectories are hyperbolic. The phase-space trajectory going through the unstable fixed point and thus separating stable and unstable phase-space regions is called the separatrix. The area in phase-space enclosed by the separatrix is called the bucket area \mathcal{B} . Multiplying the adiabatic equation of synchrotron motion derived in Eq. (B.156) with $\dot{\varphi}$ and integrating over time t yields an integral of motion I ,

$$\frac{\dot{\varphi}^2}{2} + \frac{h\omega_0^2 e V \eta}{2\pi \beta_0^2 E_0} (\cos \varphi + \varphi \sin \varphi_s) = I, \quad (\text{B.167})$$

which can be re-written using Eq. (B.149) to obtain

$$\frac{1}{2} \left(\frac{\Delta E}{\omega_0} \right)^2 + \frac{\beta_0^2 E_0 e V}{2\pi h \omega_0^2 \eta} (\cos \varphi + \varphi \sin \varphi_s) = \tilde{I}. \quad (\text{B.168})$$

Since the separatrix goes through the unstable fixed point ($\varphi = \pi - \varphi_s, \Delta E/\omega_0 = 0$), the integration constant is determined as $\tilde{I} = \frac{\beta_0^2 E_0 e V}{2\pi h \omega_0^2 \eta} [\cos(\pi - \varphi_s) + (\pi - \varphi_s) \sin \varphi_s]$. The

separatrix is thus described by the trajectory

$$\left(\frac{\Delta E}{\omega_0}\right)_{\text{sx}} = \pm \sqrt{2 \frac{\beta_0^2 E_0 e V}{2\pi h \omega_0^2 |\eta|} [(\pi - \varphi_s - \varphi) \sin \varphi_s - \cos \varphi_s - \cos \varphi]^{1/2}}. \quad (\text{B.169})$$

The turning point of the separatrix φ_u where $\left(\frac{\Delta E}{\omega_0}\right)_{\text{sx}} = 0$ is defined as

$$(\pi - \varphi_s) \sin \varphi_s - \cos \varphi_s = \cos \varphi_u + \varphi_u \sin \varphi_s, \quad (\text{B.170})$$

and is usually found numerically. The bucket area \mathcal{B} is then obtained by integration of Eq. (B.169) such that

$$\begin{aligned} \mathcal{B} &= \frac{2}{h} \int_{\varphi_u}^{\pi - \varphi_s} \left(\frac{\Delta E}{\omega_0}\right)_{\text{sx}} d\varphi \\ &= \frac{16}{h} \sqrt{\frac{\beta_0^2 E_0 e V}{2\pi h \omega_0^2 |\eta|}} \tilde{\alpha}_{\mathcal{B}}(\varphi_s), \end{aligned} \quad (\text{B.171})$$

where the factor $1/h$ accounts for the fact that the total stable phase-space area is equally distributed among h buckets and the factor 2 for the fact that the energy offset ΔE attains both positive and negative values. The factor $\tilde{\alpha}_{\mathcal{B}}(\varphi_s)$ defined as

$$\tilde{\alpha}_{\mathcal{B}}(\varphi_s) = \left| \frac{1}{4\sqrt{2}} \int_{\varphi_u}^{\pi - \varphi_s} \sqrt{|(\pi - \varphi_s - \varphi) \sin \varphi_s - \cos \varphi_s - \cos \varphi|} d\varphi \right| \leq 1, \quad (\text{B.172})$$

accounts for the reduction of the bucket area of an accelerating bucket with respect to the stationary bucket. The maximal value of $\tilde{\alpha}_{\mathcal{B}} = 1$ is obtained thus for a stationary bucket. The bucket length is simply $|(\pi - \varphi_s) - \varphi_u|$ in phase or $|(\pi - \varphi_s) - \varphi_u|/(h\omega_0)$ expressed in time. The bucket height is the value of $\left(\frac{\Delta E}{\omega_0}\right)_{\text{sx}} = 0$ at $\varphi = \varphi_s$. For practical reasons, the bucket height is usually quoted in terms of relative momentum spread δ . Thus, using Eq. (B.148) the bucket height $\hat{\delta}_{\mathcal{B}}$ is obtained as

$$\hat{\delta}_{\mathcal{B}} = \sqrt{\frac{2eV}{\pi \beta_0^2 E_0 h |\eta|}} \underbrace{\left| (\pi/2 - \varphi_s) \sin \varphi_s - \cos \varphi_s \right|^{1/2}}_{\leq 1}, \quad (\text{B.173})$$

where the expression above the bracket represents the reduction of the bucket height of an accelerating bucket with respect to the stationary bucket, for which it will obtain the maximum value of 1.

C. Collective effects

Up to this point, the dynamics of charged particles in the accelerator have been treated for each particle individually, thus neglecting the Coulomb interaction of particles with each other and with the vacuum chamber. The electromagnetic fields induced by the beam particles depend on the beam intensity and lead to a variety of so-called collective effects. Some basic phenomena of these collective effects are discussed in the following for the case of the transverse plane.

C.1. Transverse plane

Charged particles inside the accelerator will interact not only with the external magnetic fields used to guide the beam, but also with the Coulomb field generated by the beam itself. First, each particle will interact directly with the electromagnetic field generated by the other beam particles. This is called the direct space charge effect. Furthermore, the beam induces surface charges and surface currents in the vacuum chamber and other equipment surrounding the beam trajectory. These electromagnetic fields are commonly known as wake fields. Thus, the particles will interact indirectly with each other through the wake fields. The following derivations follow Ref. [16].

Let the transverse forces coming from the beam induced electromagnetic fields be written as F_u , where u stands again for either x or y . Since $u'' = \frac{1}{\beta_0^2 c^2} \ddot{u}$, the linearized betatron equation of motion perturbed by the force F_u is written as

$$u'' + K_u(s)u = \frac{F_u}{m\gamma_0\beta_0^2 c^2}. \quad (\text{C.174})$$

For small amplitudes u , the beam induced force F_u can be expanded into a Taylor series. In first order, F_u is composed of two terms²⁴ such that

$$F_u \approx \left. \frac{\partial F_u}{\partial u} \right|_{\bar{u}=0} u + \left. \frac{\partial F_u}{\partial \bar{u}} \right|_{u=0} \bar{u}, \quad (\text{C.175})$$

where \bar{u} denotes the average bunch position. The beam induced forces are in first order quadrupole-like errors which therefore induce a betatron tune shift, as discussed in Appendix A.5. By comparison with Eqs. (A.49) and (A.54), it is found that the beam induced force will yield an incoherent tune shift

$$\Delta\nu_u^{\text{inc}} = -\frac{1}{4\pi} \oint \beta_u(s) \frac{1}{m\gamma_0\beta_0^2 c^2} \left. \frac{\partial F_u}{\partial u} \right|_{\bar{u}=0} ds, \quad (\text{C.176})$$

which depends on the individual particle amplitude. The *incoherent* tune shift $\Delta\nu_u^{\text{inc}}$ can thus be calculated by setting $\bar{u} = 0$, i.e. without displacement of the beam center.

²⁴Disregarding terms that do not depend on the beam position or the position of individual particles, as they result merely in a static orbit error.

On the other hand, the perturbed Hill's equation for the average beam position \bar{u}

$$\bar{u}'' + K_u(s)\bar{u} = \frac{F_u}{m\gamma_0\beta_0^2c^2}, \quad (\text{C.177})$$

describes the motion of the center of the beam, or the motion of the bunch as a whole. It follows therefore that the beam induced forces result also in a *coherent* tune shift, which can be written for small amplitudes \bar{u} as

$$\Delta\nu_u^{\text{coh}} = -\frac{1}{4\pi} \oint \beta_u(s) \frac{1}{m\gamma_0\beta_0^2c^2} \left(\left. \frac{\partial F_u}{\partial u} \right|_{\bar{u}=0} + \left. \frac{\partial F_u}{\partial \bar{u}} \right|_{u=0} \right) ds. \quad (\text{C.178})$$

It is important to note that this tune shift may have a nonzero imaginary part and can thus drive the beam unstable. This will be discussed in more detail in the context of the Transverse Mode Coupling instability.

The interaction of the beam with its surrounding environment can be described by wake functions, which for the transverse plane are defined as

$$W_u(x, y, x_0, y_0, z) = -\frac{1}{q_0 q} \int_0^L F_u(x, y, s, x_0, y_0, z) ds, \quad (\text{C.179})$$

where q_0 denotes the charge of a source particle which is located at the coordinates x_0 and y_0 , q is the charge of the test particle at location x and y , and z denotes the distance between the two particles. The wake functions can be expanded into a power series in the offset of the source and the test particle [154]. Considering a symmetric structure and keeping only first order terms, the wake fields can be written as

$$W_x = W_x^{\text{dip}} x_0 + W_x^{\text{quad}} x, \quad (\text{C.180a})$$

$$W_y = W_y^{\text{dip}} y_0 + W_y^{\text{quad}} y, \quad (\text{C.180b})$$

where the dipolar wake W^{dip} and the quadrupolar wake W^{quad} are given by

$$W_x^{\text{dip}}(z) = \left. \frac{W_x(z)}{x_0} \right|_{x=0}, \quad (\text{C.181a})$$

$$W_x^{\text{quad}}(z) = \left. \frac{W_x(z)}{x} \right|_{x_0=0}, \quad (\text{C.181b})$$

$$W_y^{\text{dip}}(z) = \left. \frac{W_y(z)}{y_0} \right|_{y=0}, \quad (\text{C.181c})$$

$$W_y^{\text{quad}}(z) = \left. \frac{W_y(z)}{y} \right|_{y_0=0}. \quad (\text{C.181d})$$

Note that the quadrupolar and dipolar wakes correspond to the two terms of the force in Eq. (C.178). It is often useful to transform the wake functions into frequency domain,

which yields then the beam coupling impedances,

$$Z_u^{\text{dip}}(\omega) = j \int_{-\infty}^{\infty} W_u^{\text{dip}}(z) \exp\left(-\frac{j\omega z}{c\beta}\right) \frac{dz}{c\beta}, \quad (\text{C.182a})$$

$$Z_u^{\text{quad}}(\omega) = j \int_{-\infty}^{\infty} W_u^{\text{quad}}(z) \exp\left(-\frac{j\omega z}{c\beta}\right) \frac{dz}{c\beta}. \quad (\text{C.182b})$$

which have the unit Ω/m . They correspond to the power expansion of the transverse impedance Z_u

$$Z_x = Z_x^{\text{dip}}x_0 + Z_x^{\text{quad}}x, \quad (\text{C.183a})$$

$$Z_y = Z_y^{\text{dip}}y_0 + Z_y^{\text{quad}}y, \quad (\text{C.183b})$$

which has the unit Ω . How the wake functions can drive the beam unstable will be shown in the discussion of the Transverse Mode Coupling instability.

Direct space charge

One of the most basic collective effects is direct space charge, i.e. the interaction of each particle with the Coulomb field generated by the other beam particles. Assuming a circular beam cross section in the transverse plane with a transverse bi-Gaussian particle distribution such that the charge density κ is given by

$$\kappa = \frac{\lambda e}{2\pi\sigma^2} e^{-(x^2+y^2)/(2\sigma^2)}, \quad (\text{C.184})$$

where $e\lambda$ is the line charge density in the longitudinal direction and σ denotes the rms beam size in both planes (circular beam cross section). Let's assume for the moment that the line density λ is constant along the ring circumference, i.e. that the beam is unbunched and the beam current is $I = e\lambda\beta_0 c$. Transforming Eq. (C.184) into polar coordinates (r, ϑ) such that $x = r \cos \vartheta$ and $y = r \sin \vartheta$, the corresponding solution of Maxwell's equations is given by

$$E_r = \frac{e\lambda}{2\pi\epsilon_0} \frac{1}{r} \left[1 - e^{-r^2/(2\sigma^2)}\right], \quad B_\vartheta = \beta_0 c \frac{\mu_0 e\lambda}{2\pi} \frac{1}{r} \left[1 - e^{-r^2/(2\sigma^2)}\right], \quad (\text{C.185})$$

while the azimuthal component of the electrical field $E_\vartheta = 0$ and the radial component of the magnetic field $B_r = 0$ due to symmetry. Since the vacuum permeability μ_0 and the vacuum permittivity ϵ_0 are related by $\mu_0\epsilon_0 = 1/c^2$, the Lorentz force due to the space charge self fields F_r^{SC} is obtained as

$$F_r^{\text{SC}} = e(E_r - \beta_0 c B_\vartheta) = e \frac{e\lambda}{2\pi\epsilon_0\gamma_0^2} \frac{1}{r} \left[1 - e^{-r^2/(2\sigma^2)}\right], \quad (\text{C.186})$$

where it was used that $1 - \beta_0^2 = 1/\gamma_0^2$. Note that this force is nonlinear in the radial position r . Close to the beam center $r \ll \sigma$ and thus F_r^{SC} can be Taylor expanded such that

$$F_r^{\text{SC}} = \frac{e^2 \lambda}{2\pi \epsilon_0 \gamma_0^2} \frac{1}{r} \left[1 - 1 + \frac{r^2}{2\sigma^2} - \dots \right] \approx \frac{e^2 \lambda}{2\pi \epsilon_0 \gamma_0^2} \frac{r}{2\sigma^2}. \quad (\text{C.187})$$

The space charge force close to the beam center in cartesian coordinates is therefore obtained as

$$F_u^{\text{SC}}(u) = \frac{e^2 \lambda}{2\pi \epsilon_0 \gamma_0^2} \frac{u}{2\sigma^2} + \mathcal{O}(u^3). \quad (\text{C.188})$$

Inserting this into Eq. (C.176) yields an expression for the incoherent tune shift due to the space charge self forces

$$\Delta\nu_u^{\text{SC}} = \Delta Q_u^{\text{SC}} = -\frac{1}{4\pi} \oint \frac{e^2 \lambda}{2\pi m c^2 \epsilon_0 \beta_0^2 \gamma_0^3} \frac{\beta_u(s)}{2\sigma^2} ds = -\frac{1}{2\pi} \oint \frac{r_p \lambda}{\beta_0^2 \gamma_0^3} \frac{\beta_u(s)}{2\sigma^2} ds, \quad (\text{C.189})$$

where in the second equation the classical particle radius $r_p = e^2/(4\pi\epsilon_0 m c^2)$ was introduced, which is for protons $r_p = 1.54 \times 10^{-18}$ m. It should be emphasized that in the above derivation of the transverse space charge force a circular beam cross section was assumed. However, the rms beam cross section around the ring depends on the product of the dispersion function with the rms momentum spread $\delta_{\text{rms}} = \left(\frac{\Delta p}{p_0}\right)_{\text{rms}}$ and on the local beta functions. Furthermore, the line density λ of a bunched beam depends on the longitudinal position within the bunch. For a Gaussian distribution in the longitudinal plane the line density in the bunch center is $\hat{\lambda} = N/\sqrt{2\pi}\sigma_l$, where $\sigma_l = \beta_0 c \sigma_t$ is the rms bunch length in meters and N is the number of particles per bunch. Thus, the maximum direct space charge tune shift (Laslett tune shift) is obtained for particles in the core of the beam,

$$\Delta\nu_x^{\text{SC}} = \Delta Q_x^{\text{SC}} = -\frac{r_p}{2\pi\beta_0^2\gamma_0^3} \frac{N}{\sqrt{2\pi}\sigma_l} \oint \frac{\beta_x(s)}{\sigma_x(s) [\sigma_x(s) + \sigma_y(s)]} ds, \quad (\text{C.190a})$$

$$\Delta\nu_y^{\text{SC}} = \Delta Q_y^{\text{SC}} = -\frac{r_p}{2\pi\beta_0^2\gamma_0^3} \frac{N}{\sqrt{2\pi}\sigma_l} \oint \frac{\beta_y(s)}{\sigma_y(s) [\sigma_x(s) + \sigma_y(s)]} ds, \quad (\text{C.190b})$$

where $\sigma_x(s) = \sqrt{\varepsilon_x \beta_x(s) + D_x^2(s) \delta_{\text{rms}}^2}$ and $\sigma_y(s) = \sqrt{\varepsilon_y \beta_y(s) + D_y^2(s) \delta_{\text{rms}}^2}$ are the horizontal and vertical rms beam sizes, respectively, with the physical emittances $\varepsilon_x = \varepsilon_{n,x}/\beta_0 \gamma_0$ and $\varepsilon_y = \varepsilon_{n,y}/\beta_0 \gamma_0$. In rough approximation, the maximal space charge tune shift for round beams with $\varepsilon_{n,x} = \varepsilon_{n,y} = \varepsilon_n$ scales as

$$\Delta Q_u^{\text{SC}} \propto -\frac{NR}{\varepsilon_n \sigma_l \beta_0 \gamma_0^2}. \quad (\text{C.191})$$

It is important to realize that for a beam with non-uniform transverse distribution, i.e. in realistic cases, the space charge self field will lead to a tune spread rather than a tune shift. In particular, particles in the beam core will experience the largest tune spread and particles with larger transverse amplitude will exhibit smaller tune shifts. In addition to that, the space charge tune shift will be largest for particles in the longitudinal center of the beam where the line density reaches its peak value. The space charge tune shifts calculated above correspond exactly to the situation where particles are located in the core of the beam, i.e. exhibit the largest space charge detuning. Note that the overall tune footprint induced by the direct space charge force for realistic beam distributions (e.g. Gaussian distribution) is often referred to as “space charge necktie” due to its typical shape. It should also be emphasized that the incoherent space charge tune spread cannot be measured as a tune shift using turn-by-turn analysis of the beam centroid motion. This method will yield the coherent tune, i.e. the bare machine tune plus the coherent tune shift due to indirect space charge and impedance.

Strong Head Tail Instability - Transverse Mode Coupling

The mechanism of the the fast head tail instability (also called strong head tail instability or transverse mode coupling instability) can be illustrated by a simple two particle model [20, 155]. It is assumed that the beam consists of two macro particles, each having a charge of $Ne/2$. They perform synchrotron oscillations of the same frequency and amplitude, but with opposite phase. During half a synchrotron period $T_s = 2\pi/\omega_s$, particle 1 is leading and thus performing free betatron oscillations while the trailing particle 2 feels the wake field generated by particle 1. Thus, for $0 < s < \pi c/\omega_s$, the equations of motion for the two macro particles can be written as

$$y_1'' + \left(\frac{\omega_\beta}{c}\right)^2 y_1 = 0, \quad (\text{C.192a})$$

$$y_2'' + \left(\frac{\omega_\beta}{c}\right)^2 y_2 = \left(\frac{e^2}{m_0 c^2}\right) \frac{NW_0}{2\gamma C} y_1(s), \quad (\text{C.192b})$$

where y_1 denotes the vertical position of particle 1 and y_2 the position of particle 2, and the focusing term in Hill's equation Eq. (A.15) has been written as $K_y = \left(\frac{\omega_\beta}{c}\right)^2$ with ω_β denoting the (vertical) betatron frequency. Note that it is assumed here that the wake field W_0 (integrated over the machine circumference C) is constant but vanishes before the beam passage in the consecutive turn. This corresponds to the case of a broad band impedance.

The stability of the two particle system is analyzed in the following. The solution for the free betatron oscillation of Eq. (C.192a) can be written as

$$\tilde{y}_1(s) = \tilde{y}_1(0) \exp\left(\frac{-j\omega_\beta s}{c}\right), \quad (\text{C.193})$$

where the complex phasor $\tilde{y}_1(s)$

$$\tilde{y}_1(s) = y_1(s) + j \frac{c}{\omega_\beta} y_1'(s) \quad (\text{C.194})$$

has been introduced. Inserting the solution for $\tilde{y}_1(s)$ into Eq. (C.192b) leads to the solution for $\tilde{y}_2(s)$

$$\tilde{y}_2(s) = \tilde{y}_2(0) \exp\left(-\frac{j\omega_\beta s}{c}\right) + j \frac{Ne^2 W_0}{4m_0 \gamma c C \omega_\beta} \left[\frac{c}{\omega_\beta} \tilde{y}_1^*(0) \sin\left(\frac{\omega_\beta s}{c}\right) + \tilde{y}_1(0) s \exp\left(-\frac{j\omega_\beta s}{c}\right) \right], \quad (\text{C.195})$$

which consists of the free betatron oscillation term and a driven oscillation term. For the further analysis, the position of the two particles is evaluated at $s = \pi c/\omega_s$, i.e. after half the synchrotron period. Since the betatron frequency is typically much larger than the synchrotron frequency, i.e. $\omega_\beta \gg \omega_s$, the second term on the right hand side of Eq. (C.195) is small compared to the last term. Thus the solutions of the equations of motion can be written in matrix form such that

$$\begin{pmatrix} \tilde{y}_1 \\ \tilde{y}_2 \end{pmatrix}_{s=\pi c/\omega_s} = \exp\left(-\frac{j\pi\omega_\beta}{\omega_s}\right) \cdot \begin{pmatrix} 1 & 0 \\ j\Upsilon & 1 \end{pmatrix} \cdot \begin{pmatrix} \tilde{y}_1 \\ \tilde{y}_2 \end{pmatrix}_{s=0}, \quad (\text{C.196})$$

where the positive dimensionless parameter Υ has been defined,

$$\Upsilon = \frac{\pi Ne^2 W_0}{4m_0 \gamma C \omega_\beta \omega_s}. \quad (\text{C.197})$$

During the second half of the synchrotron period, i.e. $\pi c/\omega_s < s < 2\pi c/\omega_s$, the two particles exchange their roles and now particle 2 is leading while particle 1 is feeling the wake field. Thus the equations of motion have to be exchanged and the transformation matrix for the full synchrotron period is obtained as

$$\begin{pmatrix} \tilde{y}_1 \\ \tilde{y}_2 \end{pmatrix}_{s=2\pi c/\omega_s} = \exp\left(-\frac{j2\pi\omega_\beta}{\omega_s}\right) \cdot \begin{pmatrix} 1 & j\Upsilon \\ 0 & 1 \end{pmatrix} \cdot \begin{pmatrix} 1 & 0 \\ j\Upsilon & 1 \end{pmatrix} \cdot \begin{pmatrix} \tilde{y}_1 \\ \tilde{y}_2 \end{pmatrix}_{s=0} \quad (\text{C.198a})$$

$$= \exp\left(-\frac{j2\pi\omega_\beta}{\omega_s}\right) \cdot \begin{pmatrix} 1 - \Upsilon^2 & j\Upsilon \\ j\Upsilon & 1 \end{pmatrix} \cdot \begin{pmatrix} \tilde{y}_1 \\ \tilde{y}_2 \end{pmatrix}_{s=0}. \quad (\text{C.198b})$$

Stability of the system is determined by the eigenvalues of the transformation matrix. The characteristic equation for the two eigenvalues λ_\pm yields

$$\lambda_\pm = (1 - \Upsilon^2/2) \pm \sqrt{(1 - \Upsilon^2/2)^2 - 1}. \quad (\text{C.199})$$

Since the product of the two eigenvalues is equal to 1, the condition for stability requires

that they are purely imaginary exponentials, i.e.

$$\lambda_+ \cdot \lambda_- = 1 \Rightarrow \lambda_{1,2} = \exp(\pm jv). \quad (\text{C.200})$$

Inserting this back into Eq. (C.199) yields finally

$$\lambda_+ + \lambda_- = 2 - \Upsilon^2 \Rightarrow \sin\left(\frac{v}{2}\right) = \frac{\Upsilon}{2}. \quad (\text{C.201})$$

Stability requires that v is real, which in turn is satisfied only if $\Upsilon \leq 2$,

$$\Upsilon = \frac{\pi N e^2 W_0}{4m_0 \gamma C \omega_\beta \omega_s} \leq 2. \quad (\text{C.202})$$

The threshold intensity for the onset of the Fast Head Tail instability in the two particle model is thus obtained as

$$N_{\text{thr}} = \frac{8}{\pi e^2} \frac{p_0 \omega_s}{\beta_y} \left(\frac{C}{W_0} \right). \quad (\text{C.203})$$

The main features of this instability are: the intensity threshold is proportional to p_o , i.e. bunches with higher energy are more stable. The threshold scales with the synchrotron frequency ω_s , i.e. faster synchrotron motion helps damping the instability. Furthermore the threshold is inversely proportional to the beta function at the location of the impedance source and inversely proportional to the integrated wake field around the ring per unit length W_0/C .

The evolution of the center of charge of the beam in the two particle model is obtained by the sum of $\tilde{y}_1 + \tilde{y}_2$, which is found as

$$\begin{aligned} (\tilde{y}_1 + \tilde{y}_2)(s) &= \exp\left[-j\left(\omega_\beta \mp \frac{v\omega_s}{2\pi}\right)\frac{s}{c}\right] \sum_{m=-\infty}^{\infty} C_m \exp\left(-\frac{jm\omega_s s}{c}\right), \\ C_m &= 2j\Upsilon \frac{1 \pm (-1)^m}{(2\pi m \mp v)^2} (1 \mp e^{\pm jv/2}) \end{aligned} \quad (\text{C.204})$$

with the amplitude coefficients C_m for the oscillation modes with the mode number m . The oscillation frequencies of these modes are given by

$$\begin{cases} \Omega_+ = \omega_\beta + m\omega_s + v\omega_s/2\pi, & m \text{ even,} \\ \Omega_- = \omega_\beta + m\omega_s - v\omega_s/2\pi, & m \text{ odd.} \end{cases} \quad (\text{C.205})$$

Thus, as a function of the beam intensity the modes are shifting in frequency through the dependence on v . Figure C.2 shows the frequencies of these modes for $m = 0$ and $m = -1$ as function of Υ . The two modes merge at $\Upsilon = 2$ and the oscillation frequency becomes imaginary, i.e. the beam becomes unstable and exhibits exponential growth. This is illustrated by plotting also the imaginary part of the oscillation frequencies.

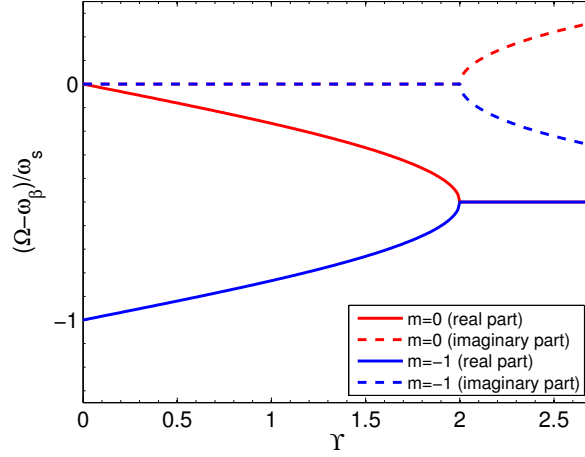


Figure C.2: Frequency spectrum of the center of charge motion as a function of the parameter Υ as predicted by the two particle model.

The fast head tail instability is therefore also called transverse mode coupling (TMC) instability.

Beyond the two-particle model, several analytical formalisms have been developed for describing the transverse mode coupling instability, as summarized in [75]. Good agreement between the different approaches is obtained when assuming a broadband resonator Z_y^{BB} as driving impedance,

$$Z_y^{\text{BB}}(\omega) = \frac{\omega_r}{\omega} \frac{R_s}{1 + jQ \left(\frac{\omega}{\omega_r} - \frac{\omega_r}{\omega} \right)}, \quad (\text{C.206})$$

where ω_r is the resonance angular frequency, Q is the resonator quality factor and R_s is the resonator shunt impedance (in Ω/m). In the long bunch regime, i.e. $\tau > \pi/\omega_r$, the TMCI threshold can be obtained for example from the quasi coasting beam approach using the peak values of bunch current and momentum spread [156], which yields [75]

$$N_{\text{thr}}^{\text{TMC}} = \frac{16\sqrt{2}}{3\pi} \frac{R|\eta|\varepsilon_l}{\beta_y e \beta^2 c} \frac{\omega_r}{|Z_y^{\text{BB}}|} \left(1 + \frac{Q'_y \omega_0}{\eta \omega_r} \right), \quad (\text{C.207})$$

where R is the machine circumference, $|Z_y^{\text{BB}}|$ is the peak value of the broadband resonator impedance and ω_0 is the angular revolution frequency. Note that in comparison to the instability threshold obtained with the two particle model in Eq. (C.203), the TMCI intensity threshold depends here in addition to the synchrotron tune (through the slip factor η) also on the longitudinal emittance ε_l . Furthermore, the threshold can be raised by operating the machine with positive (negative) chromaticity above (below) transition.

Bibliography

- [1] O. S. Brüning, P. Collier, P. Lebrun *et al.*, editors, *LHC Design Report Vol. I: The LHC Main Ring*, CERN-2004-003-V-1, CERN, Geneva, Switzerland (2004).
- [2] ATLAS collaboration, *Observation of a new particle in the search for the Standard Model Higgs boson with the ATLAS detector at the LHC*, Physics Letters B, 716(1), 1 – 29 (2012).
- [3] CMS collaboration, *Observation of a new boson at a mass of 125 GeV with the CMS experiment at the LHC*, Physics Letters B, 716(1), 30 – 61 (2012).
- [4] O. S. Brüning, R. Cappi, R. Garoby *et al.*, *LHC Luminosity and energy upgrade: A Feasibility Study*, LHC-Project-Report-626, CERN, Geneva, Switzerland (2002).
- [5] M. Benedikt, K. Cornelis, R. Garoby *et al.*, *Report of the High Intensity Protons Working Group*, CERN-AB-2004-022-OP-RF, CERN, Geneva, Switzerland (2004).
- [6] M. Benedikt, R. Garoby, F. Ruggiero *et al.*, *Preliminary accelerator plans for maximizing the integrated LHC luminosity*, CERN-AB-2006-018-PAF, CERN, Geneva, Switzerland (2006).
- [7] L. Arnaudon, P. Baudrenghien, M. Baylac *et al.*, *Linac4 Technical Design Report*, CERN-AB-2006-084, CERN, Geneva, Switzerland (2006).
- [8] R. Garoby, *Upgrade Issues for the CERN Accelerator Complex*, in *Proceedings of the 11th European Particle Accelerator Conference (EPAC'08)*, Genoa, Italy (2008).
- [9] G. I. Budker, G. I. Dimov, and V. G. Dudnikov, *Experiments on producing intensive proton beams by means of the method of charge-exchange injection*, Soviet Atomic Energy, 22(5), 441–448 (1967).
- [10] W. Bartmann, *Design of Injection and Extraction Systems with Optimisation of Lattice and Layout for the CERN PS2 Synchrotron*, Ph.D. thesis, Vienna, Technical University, Vienna (2009).
- [11] S. Myers and F. Zimmermann, *Chamonix'10 Summary*, in *Proceedings of the Chamonix 2010 LHC Performance Workshop*, Chamonix, France (2010).

-
- [12] L. Rossi, *LHC Upgrade Plans: Options and Strategy*, in *Proceedings of the 2nd International Particle Accelerator Conference (IPAC'11)*, San Sebastian, Spain (2011).
- [13] R. Garoby, S. Gilardoni, B. Goddard *et al.*, *Plans for the upgrade of the LHC injectors*, in *Proceedings of the 2nd International Particle Accelerator Conference (IPAC'11)*, San Sebastian, Spain (2011).
- [14] S. Y. Lee, *Accelerator physics*, World Scientific (2004), ISBN 9789812562005.
- [15] A. Chao, K. Mess, M. Tigner, and F. Zimmermann, *Handbook of Accelerator Physics and Engineering (2nd Edition)*, World Scientific Publishing Company Incorporated, Singapore (2013), ISBN 9789814415842.
- [16] K. Y. Ng, *Physics of Intensity Dependent Instabilities*, Lecture notes of the United States Particle Accelerator School (USPAS), Los Angeles, CA, USA (2002).
- [17] K. Y. Ng, *Higher-order momentum compaction for a simplified FODO lattice and comparison with SYNCH*, FERMILAB-FN-578, FERMILAB, Batavia, IL (1991).
- [18] D. Möhl, *Compensation of space-charge effects at transition by an asymmetric Q-jump: a theoretical study*, CERN-ISR-300-GS-69-62, CERN, Geneva, Switzerland (1969).
- [19] W. W. Lee and L. C. Teng, *Beam Bunch Length Matching at Transition Crossing with Space-Charge Forces*, in *Proceedings of the 4th Particle Accelerator Conference (PAC'71)*, Chicago, IL, USA (1971).
- [20] A. Chao, *Physics of collective beam instabilities in high energy accelerators*, Wiley series in beam physics and accelerator technology, Wiley (1993), ISBN 9780471551843.
- [21] T. Risselada, *Gamma transition jump schemes. Design of quadrupole schemes to modify gamma transition*, CERN-PS-90-51-PA, CERN, Geneva, Switzerland (1990).
- [22] W. Hardt and D. Möhl, *Q-jump at transition*, CERN-ISR-300-GS-69-16, CERN, Geneva, Switzerland (1969).
- [23] W. Hardt, *Gamma-transition-jump scheme of the CPS*, in *Proceedings of the 9th International Conference on High-energy Accelerators*, Stanford, CA, USA (1974).
- [24] J.-P. Burnet, C. Carli, M. Chanel *et al.*, *Fifty years of the CERN Proton Synchrotron: Volume 1*, CERN-2011-004, CERN, Geneva, Switzerland (2011).

- [25] S. Aumon, *High Intensity Beam Issues in the CERN Proton Synchrotron*, Ph.D. thesis, École Polytechnique Fédérale de Lausanne, CERN-THESIS-2012-261 (2012).
- [26] L. C. Teng, *Infinite Transition Energy Synchrotron Lattice Using Pi straight Sections*, Part. Accel., 4, 81–85 (1972).
- [27] Y. Yamazaki, K. Hasegawa, M. Ikegami *et al.*, editors, *Accelerator Technical Design Report for J-PARC*, KEK-2002-13, High Energy Accelerator Research Organization, KEK (2003).
- [28] Methodical Accelerator Design (MADX), <http://madx.web.cern.ch>.
- [29] D. Trbojevic, D. Finley, R. Gerig, and S. Holmes, *Design Method for High Energy Accelerator without Transition Energy*, in *Proceedings of the 2nd European Particle Accelerator Conference (EPAC'90)*, Nice, France (1990).
- [30] S. Y. Lee, K. Y. Ng, and D. Trbojevic, *Minimizing dispersion in flexible-momentum-compact lattices*, Phys. Rev. E, 48, 3040–3048 (1993).
- [31] O. Brunner, S. Calatroni, E. Ciapala *et al.*, *Plans for a Superconducting H⁻ LINAC (SPL) at CERN*, in *Proceedings of the 24th International Linear Accelerator Conference (LINAC'08)*, Victoria, BC, Canada (2008).
- [32] E. Shaponshnikova, *SPS Challenges*, in *Proceedings of the CARE-HHH-APD Workshop on Finalizing the Roadmap for the Upgrade of the CERN and GSI Accelerator Complex (BEAM'07)*, Geneva, Switzerland (2007).
- [33] M. Benedikt, *What will LP-SPL and PS2 provide for the LHC*, in *Proceedings of the Chamonix 2010 LHC Performance Workshop*, Chamonix, France (2010).
- [34] R. Garoby, *RF Constraints on the size of PS2*, CERN-AB-Note-2007-020, CERN, Geneva, Switzerland (2007).
- [35] M. Benedikt and B. Goddard, *Design Optimization of PS2*, in *Proceedings of the 23rd Particle Accelerator Conference (PAC'09)*, Vancouver, BC, Canada (2009).
- [36] W. Bartmann, M. Benedikt, C. Carli *et al.*, *Optics Considerations for the PS2*, in *Proceedings of the 22nd Particle Accelerator Conference (PAC'07)*, Albuquerque, NM, USA (2007).
- [37] W. Bartmann, M. Benedikt, E. Métral, D. Möhl, and S. Peggs, *Gamma Transition Jump for PS2*, in *Proceedings of the 11th European Particle Accelerator Conference (EPAC'08)*, Genoa, Italy (2008).
- [38] D. Trbojevic, R. de Maria, Y. Papaphilippou, and S. Peggs, *Lattice without Transition Energy for the Future PS2*, in *Proceedings of the 11th European Particle Accelerator Conference (EPAC'08)*, Genoa, Italy (2008).

- [39] Y. Papaphilippou, J. Barranco, W. Bartmann *et al.*, *Linear optics design of negative momentum compaction lattices for PS2*, in *Proceedings of the 23rd Particle Accelerator Conference (PAC'09)*, Vancouver, BC, Canada (2009).
- [40] Y. Papaphilippou, J. Barranco, W. Bartmann *et al.*, *Orbit, optics and chromaticity correction for PS2 negative momentum compaction lattices*, in *Proceedings of the 23rd Particle Accelerator Conference (PAC'09)*, Vancouver, BC, Canada (2009).
- [41] W. Bartmann, B. Goddard, and C. Hessler, *A doublet-based injection-extraction straight section for PS2*, in *Proceedings of the 1st International Particle Accelerator Conference (IPAC'10)*, Kyoto, Japan (2010).
- [42] H. Bartosik, W. Bartmann, M. Benedikt, B. Goddard, and Y. Papaphilippou, *Linear optimization and tunability of the PS2 Lattice*, in *Proceedings of the 1st International Particle Accelerator Conference (IPAC'10)*, Kyoto, Japan (2010).
- [43] H. Bartosik, A. Lachaize, Y. Papaphilippou *et al.*, *Comparison of PS2 Lattices with different geometries*, in *Proceedings of the 1st International Particle Accelerator Conference (IPAC'10)*, Kyoto, Japan (2010).
- [44] E. Mahner, *Requirements, Challenges, Design, and Functional Specification for the CERN PS2 Vacuum System*, CERN-ATS-Note-2010-040 TECH, CERN, Geneva, Switzerland (2010).
- [45] V. Lebedev, *Impedance Estimates and Requirements for the PS2*, in *Proceedings of the CARE-HHH-APD Workshop on Finalizing the Roadmap for the Upgrade of the CERN and GSI Accelerator Complex (BEAM'07)*, Geneva, Switzerland (2007).
- [46] K. L. F. Bane, G. Stupakov, U. Wienands *et al.*, *Impedance Considerations for the Design of the Vacuum System of the CERN PS2 Proton Synchrotron*, in *Proceedings of the 1st International Particle Accelerator Conference (IPAC'10)*, Kyoto, Japan (2010).
- [47] D. S. Robin, W. Wan, F. Sannibale, and V. P. Suller, *Global analysis of all linear stable settings of a storage ring lattice*, *Phys. Rev. ST Accel. Beams*, 11, 024002 (2008).
- [48] K. Niki, K. Ishii, Y. Nemoto, E. Yanaoka, and M. M., *Results of field measurements for J-PARC Main Ring Magnets*, in *Proceedings of the 10th European Particle Accelerator Conference (EPAC'06)*, Edinburgh, UK (2006).
- [49] J. Laskar, *Secular evolution of the solar system over 10 million years*, *Astronomy and Astrophysics*, 198, 341–362 (1988).

- [50] J. Laskar and D. Robin, *Application of frequency map analysis to the ALS*, Part. Accel., 54(LBL-38241. LSAP-210-G), 183–192. 9 p (1996).
- [51] D. Robin, C. Steier, J. Laskar, and L. Nadolski, *Global Dynamics of the Advanced Light Source Revealed through Experimental Frequency Map Analysis*, Phys. Rev. Lett., 85, 558–561 (2000).
- [52] Y. Papaphilippou, *Frequency maps of LHC models*, in *Proceedings of the 18th Biennial Particle Accelerator Conference (PAC'99)*, New York, NY, USA (1999).
- [53] J. Laskar, *Introduction to frequency map analysis*, C. Simó, NATO Advanced Study Institutes (Kluwer Academic Publishers, Dordrecht, The Netherlands, 1999) (1999).
- [54] R. Bartolini and F. Schmidt, *SUSSIX: A Computer Code for Frequency Analysis of Non-Linear Betatron Motion*, SL-Note-98-017-AP, CERN, Geneva, Switzerland (1998).
- [55] Y. Senichev, *A "resonant" lattice for a synchrotron with a low or negative momentum compaction factor*, , KEK, Tsukuba, Japan (1997).
- [56] Y. Senichev, *The Lattice with Imaginary γ -transition for the CERN Proton Synchrotron PS2*, in *Proceedings of the CARE-HHH-APD Workshop on Finalizing the Roadmap for the Upgrade of the CERN and GSI Accelerator Complex (BEAM'07)*, Geneva, Switzerland (2007).
- [57] E. Shaposhnikova, *SPS upgrade possibilities*, in *Proceedings of the Chamonix 2010 LHC Performance Workshop*, CERN, Chamonix, France (2010).
- [58] G. Rumolo, G. Arduini, E. Métral *et al.*, *Dependence of the Electron-Cloud Instability on the Beam Energy*, Phys. Rev. Lett., 100, 144801 (2008).
- [59] G. Arduini, J. Borburgh, J.-P. Burnet *et al.*, *Possible Improvements to the Existing Pre-Injector Complex in the frame of Continued Consolidation*, in *Proceedings of the Chamonix 2010 LHC Performance Workshop*, Chamonix, France (2010).
- [60] K. Hanke, O. Aberle, A. Blas *et al.*, *PS Booster Energy Upgrade Feasibility Study First Report*, CERN-EDMS-1082646, CERN, Geneva, Switzerland (2010).
- [61] R. Garoby, S. Hancock, and J. L. Vallet, *Demonstration of Bunch Triple Splitting in the CERN PS*, in *Proceedings of the 7th European Particle Accelerator Conference (EPAC'00)*, Vienna, Austria (2000).
- [62] M. Benedikt, P. Collier, V. Mertens, J. Poole, and K. Schindl, editors, *LHC Design Report Vol. III: The LHC Injector Chain*, CERN-2004-003-V-3, CERN, Geneva, Switzerland (2004).

- [63] B. Goddard, H. Bartosik, C. Bracco *et al.*, *Can the proton injectors meet the HL-LHC requirements after LS2?*, in *Proceedings of the Chamonix 2012 LHC Performance Workshop*, Chamonix, France (2012).
- [64] J. M. Jiménez, G. Arduini, K. Cornelis *et al.*, *Electron cloud: SPS vacuum observations with LHC type beams*, in *Proceedings of the 10th Chamonix LEP and SPS Performance Workshop*, Chamonix, France (2000).
- [65] M. Jiménez, G. Arduini, and K. Weiss, *SPS vacuum observations and electron scrubbing with LHC beams*, in *Proceedings of the 11th Chamonix LHC Workshop*, Chamonix, France (2001).
- [66] J. M. Jiménez, *SPS: Scrubbing or coating?*, in *Proceedings of the Chamonix 2012 LHC Performance Workshop*, Chamonix, France (2012).
- [67] G. Arduini, E. Benedetto, H. Burkhardt, E. Métral, and G. Rumolo, *Observation of a Fast Single-Bunch Transverse Instability on Protons in the SPS*, in *Proceedings of the 9th European Particle Accelerator Conference (EPAC'04)*, Lucerne, Switzerland (2004).
- [68] B. Salvant, *Impedance model of the CERN SPS and aspects of LHC single-bunch stability*, Ph.D. thesis, Ecole Polytechnique, Lausanne, Switzerland (2010).
- [69] B. Salvant, G. Arduini, R. Calaga *et al.*, *Transverse Mode-Coupling Instability in the CERN SPS: Comparing Moses Analytical Calculations and Headtail Simulations with experiments in the SPS*, in *Proceedings of the 11th European Particle Accelerator Conference (EPAC'08)*, Genoa, Italy (2008).
- [70] G. Adrian, D. Allen, O. Andujar *et al.*, *Probing intensity limits of LHC-Type bunches in the CERN SPS with nominal optics*, in *Proceedings of the 2nd International Particle Accelerator Conference (IPAC'11)*, San Sebastian, Spain (2011).
- [71] E. Shaposhnikova, *Longitudinal stability of the LHC beam in the SPS*, SL-Note-2001-031-HRF, CERN, Geneva (2001).
- [72] G. Papotti, T. Bohl, T. Linnecar, E. Shaposhnikova, and J. Tückmantel, *Study of Controlled Longitudinal Emittance Blow-up for High Intensity LHC Beams in the CERN SPS*, in *Proceedings of the 11th European Particle Accelerator Conference (EPAC'08)*, Genoa, Italy (2008).
- [73] E. Shaposhnikova, E. Ciapala, and E. Montesinos, *Upgrade of the 200 MHz RF System in the CERN SPS*, in *Proceedings of the 2nd International Particle Accelerator Conference (IPAC'11)*, San Sebastian, Spain (2011).
- [74] B. Goddard, T. Argyropoulos, H. Bartosik *et al.*, *Progress with the upgrade of the SPS for the HL-LHC era*, in *Proceedings of the 4th International Particle Accelerator Conference (IPAC'13)*, Shanghai, China (2013).

- [75] E. Métral, *Overview of Single-Beam Coherent Instabilities in Circular Accelerators*, in *Proceedings of the 1st CARE-HHH-APD Workshop on Beam Dynamics in Future Hadron Colliders and Rapidly Cycling High-Intensity Synchrotrons*, Geneva, Switzerland (2004).
- [76] H. Timko, T. Argyropoulos, T. Bohl *et al.*, *Experimental and simulation studies of the PS-to-SPS beam transfer efficiency*, CERN-ATS-Note-2012-059 PERF (2012).
- [77] K. Ohmi, F. Zimmermann, and E. Perevedentsev, *Wake-field and fast head-tail instability caused by an electron cloud*, Phys. Rev. E, 65, 016502 (2001).
- [78] K. Ohmi, T. Toyama, and C. Ohmori, *Electron cloud instability in high intensity proton rings*, Phys. Rev. ST Accel. Beams, 5, 114402 (2002).
- [79] T. Bohl, M. Lamont, T. P. R. Linnecar, W. Scandale, and E. Shaposhnikova, *Measurement of the Effect on Single Bunch Stability of Changing Transition Energy in the CERN SPS*, in *Proceedings of the 6th European Particle Accelerator Conference (EPAC'98)*, Stockholm, Sweden (1998).
- [80] P. Collier and B. Goddard, *The SPS as LHC Injector*, in *Proceedings of the 19th Particle Accelerator Conference (PAC'01)*, Chicago, IL, USA (2001).
- [81] D. Boussard, L. R. Evans, P. Faugeras *et al.*, *The working point $Q_H = 15.38$, $Q_V = 15.42$ and single bunch acceleration.*, CERN-SPS-Improvement-Report-147, CERN, Geneva (1978).
- [82] K. Cornelis, *Additional quadrupoles in the SPS, what can they be used for?*, in *Proceedings of the 9th Chamonix LEP and SPS Performance Workshop*, Chamonix, France (1999).
- [83] Y. Papaphilippou, *Possible reduction of transition energy in SPS*, Presentation at the SPSU-BD working group, CERN, Geneva, Switzerland (2010).
- [84] G. Arduini, C. Arimatea, C. Despas *et al.*, *Test of a low gamma transition optics*, SL-Note-98-001-MD, CERN, Geneva (1998).
- [85] *The 300 GeV programme*, CERN-1050-E, CERN, Geneva, Switzerland (1972).
- [86] E. Shaposhnikova, *Lessons from SPS studies in 2010*, in *Proceedings of the Chamonix 2011 LHC Performance Workshop*, Chamonix, France (2011).
- [87] J. Uythoven, *The New SPS Injection Channel*, in *Proceedings of the 9th Chamonix LEP and SPS Performance Workshop*, Chamonix, France (1999).
- [88] J. Bauche, *private communication*.

-
- [89] *CERN optics repository*, <http://cern-accelerators-optics.web.cern.ch>.
- [90] P. J. Bryant, *Beam transfer lines*, CAS - CERN accelerator school, Jyväskylä, Finland (1993).
- [91] G. Arduini and P. Raimondi, *Transverse emittance blow-up due to injection errors*, SL-Note-99-022-SLI, CERN, Geneva (1999).
- [92] J. Bonthond, L. Ducimetière, G. Schröder *et al.*, *The future of the SPS injection channel*, in *Proceedings of the 18th Biennial Particle Accelerator Conference (PAC'99)*, New York, NY, USA (1999).
- [93] J. Uythoven, *private communication*.
- [94] E. Gianfelice-Wendt, *Matching of TI2 and TI8 for Q20 SPS Optics*, CERN-ATS-Note-2012-095 TECH, CERN, Geneva, Switzerland (2012).
- [95] W. Bartmann, H. Bartosik, C. Bracco *et al.*, *Injection MD*, CERN-ATS-Note-2012-090 MD, CERN, Geneva, Switzerland (2012).
- [96] A. Ijspeert, R. Bellone, and P. Sievers, *The New Internal Beam Dump at the SPS. Temperature and Stress Calculations and Its Design*, Nuclear Science, IEEE Transactions on, 28(3), 3062–3064 (1981).
- [97] F. Velotti, O. Aberle, C. Bracco *et al.*, *Performance Improvements of the SPS Internal Beam Dump for the HL-LHC beam*, in *Proceedings of the 4th International Particle Accelerator Conference (IPAC'13)*, Shanghai, China (2013).
- [98] T. Kramer, G. Arduini, O. Berrig *et al.*, *Studies of Beam Losses from Failures of SPS Beam Dump Kickers*, in *Proceedings of the 22nd Particle Accelerator Conference (PAC'07)*, Albuquerque, NM, USA (2007).
- [99] G. Arduini, A. Faus-Golfe, and F. Zimmermann, *Measurements and Modelling of Nonlinear Chromaticity and Detuning with Amplitude at 26 GeV*, SL-Note-2001-030-MD, CERN, Geneva, Switzerland (2001).
- [100] G. Arduini, F. Zimmermann, A. Faus-Golfe, N. Iida, and R. Tomás, *2002 Non-linear Optics Measurements and Modelling for the SPS at 26 GeV*, AB-Note-2003-025-MD, CERN, Geneva, Switzerland (2003).
- [101] R. Tomás, G. Arduini, R. Calaga *et al.*, *Improved Algorithms to determine the Non-Linear Optics Model of the SPS from Non-Linear Chromaticity*, in *Proceedings of the 22nd Particle Accelerator Conference (PAC'07)*, Albuquerque, NM, USA (2007).
- [102] W. H. Press, S. A. Teukolsky, W. T. Vetterling, and B. P. Flannery, *Numerical Recipes 3rd Edition: The Art of Scientific Computing*, Cambridge University Press, New York, NY, USA, 3 edition (2007), ISBN 0521880688, 9780521880688.

-
- [103] J. Wenninger, *Dynamic Effects on Chromaticity for the LHC beam cycle in the SPS*, SL-Note-2002-041-OP, CERN, Geneva (2003).
- [104] G. Arduini, P. Collier, F. Zimmermann, and A. Faus-Golfe, *2001 SPS Measurements and Modelling of Nonlinear Chromaticity and Detuning with Amplitude at 26 GeV*, SL-Note-2001-049-MD, CERN, Geneva (2002).
- [105] M. Cornacchia, *Correction of half-integer resonances at injection*, CERN-SPS-COMMISSIONING-REPORT-27, CERN, Geneva (1976).
- [106] P. Collier and H. Schmickler, *Systematic studies of the LEP working point*, in *Proceedings of the 16th Particle Accelerator Conference (PAC'95)*, Dallas, TX, USA (1995).
- [107] F. Roncarolo, G. Arduini, C. Arimatea *et al.*, *SPS Working Point Studies*, CERN-AB-Note-2006-008-ABP-MD, CERN, Geneva, Switzerland (2006).
- [108] G. Franchetti, B. Franczak, and P. Schütt, *A benchmarking experiment in SIS for dynamic aperture induced beam loss*, GSI-Acc-Note-2004-05-001, GSI, Darmstadt, Germany (2004).
- [109] G. Franchetti, P. Schütt, I. Hofmann, G. Rumolo, and A. Franchi, *Mapping of the resonances in SIS18*, GSI-Acc-Note-2005-02-001, GSI, Darmstadt, Germany (2005).
- [110] A. Huschauer, *Working point and resonance studies at the CERN Proton Synchrotron*, Ph.D. thesis, Vienna University of Technology, Vienna, Austria (2012).
- [111] G. Arduini, H. Burkhardt, and E. Métral, *Observation of a fast single bunch transverse instability on protons in the SPS*, AB-Note-2003-093-MD, CERN, Geneva, Switzerland (2003).
- [112] M. Gasior and R. Jones, *High Sensitivity Tune Measurement by Direct Diode Detection*, in *Proceedings of the 7th European Workshop on Beam Diagnostics and Instrumentation for Particle Accelerators*, CERN-AB-2005-060, Lyons, France (2005).
- [113] R. Jones and H. Schmickler, *The measurement of Q' and Q'' in the CERN-SPS by head-tail phase shift analysis*, in *5th European Workshop on Diagnostics and Beam Instrumentation (DIPAC'01)*, CERN-SL-2001-020-BI, Grenoble, France (2001).
- [114] T. Kroyer, F. Caspers, and E. Gaxiola, *Longitudinal and Transverse Wire Measurements for the Evaluation of Impedance Reduction Measures on the MKE Extraction Kickers*, CERN-AB-Note-2007-028, CERN, Geneva, Switzerland (2007).

-
- [115] C. Zannini, *Electromagnetic Simulation of CERN Accelerator Components and Experimental Applications*, Ph.D. thesis, Ecole Polytechnique, Lausanne, Switzerland (2013).
- [116] G. Rumolo and F. Zimmermann, *Electron cloud simulations: beam instabilities and wakefields*, Phys. Rev. ST Accel. Beams, 5, 121002 (2002).
- [117] E. Shaposhnikova, T. Argyropoulos, T. Bohl, J. Esteban Müller, and H. Timko, *Longitudinal Instabilities in the SPS and Beam Dynamics Issues with High Harmonic RF Systems*, in *Proceedings of the 52nd ICFA Advanced Beam Dynamics Workshop on High-Intensity and High-Brightness Hadron Beams (HB 2012)*, Beijing, China (2012).
- [118] T. Bohl, T. P. R. Linnecar, E. Shaposhnikova, and J. Tückmantel, *Study of Different Operating Modes of the 4th RF Harmonic Landau Damping System in the CERN SPS*, 6th European Particle Accelerator Conference, Stockholm, Sweden, (CERN-SL-98-026-RF) (1998).
- [119] F. J. Sacherer, *A longitudinal stability criterion for bunched beams*, IEEE Trans. Nucl. Sci. NS-20 (1973).
- [120] T. Argyropoulos, *Longitudinal Beam Stability in Single and Double RF Systems in the CERN SPS*, Ph.D. thesis, Physics Department of the National Technical University of Athens (2013).
- [121] T. Argyropoulos, T. Bohl, T. Linnecar, E. Shaposhnikova, and J. Tückmantel, *Controlled Longitudinal Emittance Blow-up in a Double Harmonic RF System at CERN SPS*, in *Proceedings of the 46th ICFA Advanced Beam Dynamics Workshop on High-Intensity and High-Brightness Hadron Beams (HB 2010)*, Morschach, Switzerland (2010).
- [122] H. Timko, T. Argyropoulos, T. Bohl *et al.*, *Longitudinal Beam Loss Studies of the CERN PS-to-SPS Transfer*, in *Proceedings of the 52nd ICFA Advanced Beam Dynamics Workshop on High-Intensity and High-Brightness Hadron Beams (HB 2012)*, Beijing, China (2012).
- [123] G. Vanbavinckhove, W. Bartmann, H. Bartosik *et al.*, *Beam transfer to LHC with the low gamma-transition SPS optics*, in *Proceedings of the 4th International Particle Accelerator Conference (IPAC'13)*, Shanghai, China (2013).
- [124] T. Bohl, *private communication*.
- [125] M. Kuhn, G. Arduini, J. Emery *et al.*, *LHC Emittance preservation during the 2012 run*, in *Proceedings of the Evian 2012 LHC beam operation workshop*, Evian, France (2012).

- [126] G. Franchetti, I. Hofmann, M. Giovannozzi, M. Martini, and E. Métral, *Space charge and octupole driven resonance trapping observed at the CERN Proton Synchrotron*, Phys. Rev. ST Accel. Beams, 6, 124201 (2003).
- [127] G. Franchetti, O. Chorniy, I. Hofmann *et al.*, *Experiment on space charge driven nonlinear resonance crossing in an ion synchrotron*, Phys. Rev. ST Accel. Beams, 13, 114203 (2010).
- [128] H. Damerau, A. Findlay, S. Gilardoni, and S. Hancock, *RF manipulations for higher beam brightness LHC-type beams*, in *Proceedings of the 4th International Particle Accelerator Conference (IPAC'13)*, Shanghai, China (2013).
- [129] F. Zimmermann, *A simulation study of electron-cloud instability and beam-induced multipacting in the LHC*, CERN-LHC-Project-Report-95, CERN, Geneva (1997).
- [130] R. Cimino, I. R. Collins, M. A. Furman *et al.*, *Can Low-Energy Electrons Affect High-Energy Physics Accelerators?*, Phys. Rev. Lett., 93, 014801 (2004).
- [131] K. Ohmi, *Beam-Photoelectron Interactions in Positron Storage Rings*, Phys. Rev. Lett., 75, 1526–1529 (1995).
- [132] K. Ohmi and F. Zimmermann, *Head-Tail Instability Caused by Electron Clouds in Positron Storage Rings*, Phys. Rev. Lett., 85, 3821–3824 (2000).
- [133] G. Arduini, *Observations in the SPS: beam emittance, instabilities*, in *Proceedings of the 10th Chamonix LEP and SPS Performance Workshop*, Chamonix, France (2000).
- [134] G. Arduini, K. Cornelis, G. Ferioli, L. Jensen, and F. Zimmermann, *Transverse Instabilities of the LHC Proton Beam in the SPS*, in *Proceedings of the 7th European Particle Accelerator Conference (EPAC'00)*, Vienna, Austria (2000).
- [135] G. Arduini, *Observations on Transverse Instabilities*, in *Proceedings of the 11th Chamonix LHC workshop*, Chamonix, France (2001).
- [136] K. Cornelis, *The Electron Cloud Instability in the SPS*, in *Proceedings of the Mini Workshop on Electron Cloud Simulations for Proton and Positron Beams (E-CLOUD'02)*, Geneva, Switzerland (2002).
- [137] G. Arduini, T. Bohl, K. Cornelis *et al.*, *Beam observations with electron cloud in the CERN PS and SPS complex*, in *Proceedings of the 31st ICFA Advanced Beam Dynamics Workshop on Electron-Cloud Effects (E-CLOUD'04)*, Napa, CA, USA (2004).
- [138] H. Bartosik, G. Iadarola, G. Rumolo *et al.*, *Electron Cloud and Scrubbing Studies for the SPS in 2012*, CERN-ATS-Note-2013-019 MD, CERN, Geneva (2013).

- [139] G. Arduini, K. Cornelis, W. Höfle, G. Rumolo, and F. Zimmermann, *The Electron Cloud Instability of the LHC Beam in the CERN SPS*, in *Proceedings of the 20th Particle Accelerator Conference (PAC'03)*, Portland, OR, USA (2003).
- [140] C. Yin Vallgren, G. Arduini, J. Bauche *et al.*, *Amorphous carbon coatings for the mitigation of electron cloud in the CERN Super Proton Synchrotron*, *Phys. Rev. ST Accel. Beams*, 14 (2011).
- [141] G. Iadarola and G. Rumolo, *Py-Ecloud and Build Up Simulations at CERN*, in *Proceedings of the 5th Electron Cloud workshop (ELOUD'12)*, Isola d'Elba, Italy (2012).
- [142] G. Iadarola, H. Bartosik, M. Mensi *et al.*, *Recent electron cloud studies in the SPS*, in *Proceedings of the 4th International Particle Accelerator Conference (IPAC'13)*, Shanghai, China (2013).
- [143] H. Bartosik, W. Höfle, G. Iadarola, Y. Papaphilippou, and G. Rumolo, *Benchmarking HEADTAIL with electron cloud instabilities observed in the LHC*, in *Proceedings of the 5th Electron-Cloud workshop (ELOUD'12)*, Isola d'Elba, Italy (2012).
- [144] Y. Papaphilippou, H. Bartosik, T. Bohl, and G. Vanbavinckhove, *SPS operation with Q20 optics*, Presentation at the MSWG meeting, CERN, Geneva, Switzerland (2012).
- [145] T. Mastoridis, P. Baudrenghien, A. Butterworth, M. Jaussi, and J. Molendijk, *Batch By Batch Longitudinal Emittance Blowup MD*, CERN-ATS-Note-2012-050 MD, CERN, Geneva, Switzerland (2012).
- [146] M. Kuhn, G. Arduini, P. Baudrenghien *et al.*, *Investigations of the LHC emittance blow-up during the 2012 proton run*, in *Proceedings of the 4th International Particle Accelerator Conference (IPAC'13)*, Shanghai, China (2013).
- [147] Y. Papaphilippou, G. Arduini, T. Argyropoulos *et al.*, *Operational performance of the LHC proton beams with the SPS low transition energy optics*, in *Proceedings of the 4th International Particle Accelerator Conference (IPAC'13)*, Shanghai, China (2013).
- [148] L. Drosdal, W. Bartmann, H. Bartosik *et al.*, *Analysis of LHC transfer line trajectory drifts*, in *Proceedings of the 4th International Particle Accelerator Conference (IPAC'13)*, Shanghai, China (2013).
- [149] B. Mikulec, H. Bartosik, C. Carli *et al.*, *Performance Reach of LHC Beams in the PSB*, Presentation at the LIU Beam Studies Review Day, CERN, Geneva, Switzerland (2012).

- [150] F. Antoniou, G. Arduini, H. Bartosik *et al.*, *Performance of SPS low transition energy optics for LHC ion beams*, in *Proceedings of the 4th International Particle Accelerator Conference (IPAC'13)*, Shanghai, China, Shanghai, China (2013).
- [151] J. M. Jowett, R. Alemany-Fernandez, P. Baudrengnien *et al.*, *Proton-Nucleus collisions in the LHC*, in *Proceedings of the 4th International Particle Accelerator Conference (IPAC'13)*, Shanghai, China (2013).
- [152] J. Bengtsson, *The Sextupole Scheme for the Swiss Light Source (SLS): An Analytical Approach*, , SLS, Villigen, Switzerland (1997).
- [153] S. C. Leemann and A. Streun, *Perspectives for future light source lattices incorporating yet uncommon magnets*, *Phys. Rev. ST Accel. Beams*, 14, 030701 (2011).
- [154] S. Heifets, A. Wagner, and B. Zotter, *Generalized Impedances and Wakes in Asymmetric Structures*, SLAC/AP110, SLAC, Stanford, CA, USA (1998).
- [155] G. Rumolo, *Beam Instabilities II*, Lecture at the CERN Accelerator School - Advanced Accelerator Physics Course, Trondheim, Norway (2013).
- [156] J. L. Laclare, *Introduction to Coherent Instabilities - Coasting Beam Case*, CAS - CERN accelerator school, Paris, France, (CERN 85-19) (1985).

Nomenclature

α_c	momentum compaction factor
$\tilde{\alpha}_B$	bucket reduction factor for accelerating bucket
α_u	alpha function (Courant Snyder parameter), where u stands for x or y
$a_u(s)$	available aperture (in units of rms beam size) around the ring, where u stands for x or y
β	relativistic beta
β_0	relativistic beta of the reference particle
β_u	beta function (Courant Snyder parameters), where u stands for x or y
\mathcal{B}	longitudinal bucket area
ζ	Courant Snyder invariant
C	circumference of circular accelerator
\mathcal{C}	chromaticity
δ_{rms}	rms momentum spread
$\hat{\delta}_B$	bucket height
$\Delta\hat{u}_{co}$	maximum closed orbit error, where u stands for x or y
$\Delta\nu^{\text{SC}}$	space charge tune shift
d_ν	tune diffusion rate
D_u	dispersion function, where u stands for x or y
$D_{n,x}$	normalized dispersion phase space coordinate
$D_{n,u}$	normalized dispersion phase space coordinate, where u stands for x or y
$D'_{n,x}$	normalized dispersion phase space coordinate
$D'_{n,u}$	normalized dispersion phase space coordinate, where u stands for x or y
\mathcal{D}_u	parametric dispersion, where u stands for x or y

ε	physical transverse emittance
ε'	transverse emittance after filamentation
ϵ_0	Vacuum permittivity
ε_l	longitudinal emittance
ε_n	normalized transverse emittance
$\varepsilon_{n,x}$	horizontal normalized emittance, $\varepsilon_{n,x} = \beta_0 \gamma_0 \varepsilon_x$
$\varepsilon_{n,y}$	vertical normalized emittance, $\varepsilon_{n,y} = \beta_0 \gamma_0 \varepsilon_y$
ε_x	horizontal physical emittance
ε_y	vertical physical emittance
E	total energy
E_0	energy of the reference (synchronous) particle
E_{thr}	Energy at the onset of the longitudinal instabilities in the SPS
f_0	revolution frequency
F	force
\mathcal{F}	blow-up factor due to betatron mismatch
γ	relativistic gamma
γ_0	relativistic gamma of the reference particle
γ_t	gamma at transition
γ_u	gamma function (Courant Snyder parameter), where u stands for x or y
η	phase slip factor
h	harmonic number
H	Hamiltonian
J_u	betatron action, where u stands for x or y
\mathcal{J}	blow-up factor due to dispersion mismatch
κ	transverse charge density
k_β	beta-beat factor

k_D	parasitic dispersion factor
λ	line charge density
μ	betatron phase advance (alternative symbol)
ν	betatron tune (alternative symbol)
n_A	global available aperture (in units of rms beam size)
n_b	number of bunches per beam in a collider
N	number of particles per bunch
$N_{\text{thr}}^{\text{LLD}}$	intensity threshold for loss of Landau damping
$N_{\text{thr}}^{\text{TMC}}$	intensity threshold for transverse mode coupling instability
ψ	betatron phase advance
ϕ	betatron phase advance in periodic structure
φ	longitudinal phase angle
φ_s	longitudinal synchronous phase
Q	resonator quality factor
Q_s	synchrotron tune
Q_u	betatron tune, where u stands for x or y
ρ	bending radius
ρ_e	electron density
$\rho_{e,\text{thr}}$	electron density at the instability threshold
r_p	classical particle radius of a proton, $r_p = e^2/(4\pi\epsilon_0 mc^2) = 1.54 \times 10^{-18}$ m
R	radius of circular accelerator
R_s	resonator shunt impedance
σ_{FT}	rms beam size of the fixed target beam
σ_l	bunch length (in meters)
σ_t	bunch length (in seconds)
σ_u	rms beam size, where u stands for x or y

τ	4σ bunch length (CERN convention, c.f. [1])
θ	bending angle
V	Voltage of an RF cavity for longitudinal focusing and acceleration
ω_0	angular revolution frequency
ω_r	resonator frequency
ω_s	synchrotron frequency
W	wake function
ξ_u	specific chromaticity, $\xi_u \equiv Q'_u/Q_u$, where u stands for x or y
Z_y^{BB}	vertical broadband impedance

Acknowledgements

First of all I would like to thank my supervisor Yannis Papaphilippou. Not only that he introduced me to the field of nonlinear dynamics at the USPAS course in 2008, but he also gave me the chance to become a doctoral student at CERN. Working with Yannis during the last years was a great pleasure. Developing ideas on a common basis of mutual understanding and respect made this time truly exceptional for me. Thank you Yannis for the unforgettable and countless hours we spent in the control room working on the SPS and the interesting studies we did together.

I would like to thank my supervisor at the Technical University of Vienna, Michael Benedikt, for having accepted me as doctoral student, for his advice and suggestions during my studies on the PS2 design and for all the support during my PhD.

I really appreciated working with Gianluigi Arduini as section leader. His suggestions and ideas were always of great help. He triggered many interesting thoughts and studies by putting the focus on the crucial points.

Special thanks I would like to address to Fanouria Antoniou for helping me getting started efficiently in the early phase of my work at CERN and her warm support as a friend throughout the years.

It was a great pleasure working together with the Giovannis, Giovanni Rumolo and Gianni Iadarola. Studying the electron cloud effects in the SPS and the LHC with you guys is very exciting. Not to mention all the sleepless nights we shared in the control room for taking measurements and maximally exploiting the machine time, for example for studying the TMCI instability during the last days before the long shutdown! Thanks for all the help and support, the invaluable contribution to this work, and the many scientific and less-scientific discussions we had. I learned a lot.

Furthermore I would like to mention Benoit Salvant, who was of great help during the early days of the machine studies with the Q20 optics and the measurements on the TMCI. Thank you for the good collaboration and in particular the help on the analysis of the TMCI measurements. In this context I would like to thank also Carlo Zannini, who provided me with the present SPS impedance model data for the HEADTAIL simulations, Niccolò Biancacci who helped during the TMCI measurements, and Elias Métral and Nicolas Mounet for discussions.

I am very grateful to Elena Shaposhnikova and Thomas Bohl for the very nice and productive collaboration we are having since the last few years and their advice on different matters. I would like to thank them, together with the rest of the SPS RF team, Theodoros Argyropoulos, Juan Esteban Müller and Helga Timko, for the longitudinal optimization and measurements they performed in the SPS and the data they provided me with for this thesis.

I would like to thank Frank Schmidt and Alexander Molodozhentsev for their contributions to the space charge measurements and help with simulations. Furthermore I would like to thank Kevin Li for his help and contribution to the HEADTAIL simulations for the electron cloud instability as well as Elena Benedetto for the discussions about electron cloud effects.

I would like to point out the great support of Karel Cornelis and Jörg Wenninger during measurements with the Q20 optics and in particular for the implementation of the new optics in the machine. Together with them, I would like to thank Stephane Cettour-Cavé and Fabio Follin for their help during machine studies, Wolfgang Höfle and Daniel Valuch for their support with the SPS transverse feedback and Ana Guerrero for her help with the wire scanner measurements.

For setting up the SPS extraction from the Q20 optics and rematching the transfer lines to the LHC, I would like to express my gratitude to Wolfgang Bartmann, Eliana Gianfelice-Wendt, Brennan Goddard, Verena Kain and Glenn Vanbavinckhove.

For proofreading parts of the manuscript I would like to thank Yannis Pappalippou, Giovanni Rumolo, Elena Shaposhnikova, Gianni Iadarola, Benoit Salvant, Matthias Karacson, Lutz Hein, and Alexander Huschauer.

Nun möchte ich noch meiner Familie danken, meinen Eltern, Gertrude und Heinrich, die mich immer unterstützt haben und sich um viele Dinge in Österreich gekümmert haben während ich im Ausland war, und meinem Bruder, mit dem ich eine ganz besondere Verbindung habe. Mein innigster Dank gilt meiner Lebensgefährtin Christine, die mich nun schon so lange an meiner Seite begleitet. Christine, Du hast mich immer so herzlich, tatkräftig und selbstlos unterstützt, dafür kann ich Dir gar nicht genug danken. Ich habe höchsten Respekt vor Deiner mutigen Entscheidung mit mir ins Ausland zu ziehen und somit Deine wohlbehütete Umgebung in Wien zu verlassen. Ich weiss, dass Du es oft nicht leicht hast mit mir. Aber gemeinsam können wir alles schaffen.

Hannes Bartosik, October 2013

Hannes Bartosik

CURRICULUM VITÆ

19, chemin du Château
01170 Echenevex, France
0041 / 76 504 85 39
hannes.bartosik@gmail.com

Personal information

Date of birth 05/10/1982
Place of birth Vienna
Nationality Austrian

Education

2009 – 2013 **Vienna University of Technology**, doctoral studies. Title of doctoral thesis: “Beam dynamics and optics studies for the LHC injectors upgrade”. Supervisors Dr. Y. Papaphilippou and Priv. Doz. Dr. Michael Benedikt.

2000 – 2009 **Vienna University of Technology**, Studies of technical physics. Master (Diplom Ingenieur) in atomic physics. Title of diploma thesis: “Experimental test of quantum contextuality with neutron interferometry”.

Research appointments

2012 – now **CERN Accelerators and Beam Physics Group** (Geneva), fellow. Studies for future high-intensity and high brightness LHC beams in the SPS, including space charge, transverse instabilities due to impedance and due to electron cloud effects, and the SPS non-linear optics model.

2009 – 2012 **CERN Accelerators and Beam Physics Group** (Geneva), doctoral student. Lattice optimization for the PS2 design study and mitigation of performance limitations for LHC beams in the SPS by means of optics manipulations.

2007 (2 months) **Lawrence Berkeley National Lab** (Berkeley), student assistant. Development of a test bench for measuring magnetic fields of several T pulsed in a few ns using Faraday rotation in optical fibers.

2006 (3 months) **CERN Physics Department** (Geneva), summer student. Development of a beam monitoring system for measuring the phase of the incoming bunches with respect to the reference clock of the ATLAS level 1 trigger.

Languages and other skills

Languages German (mother tongue)
English (fluent)
French (conversational)

Simulation tools MADX, MADX-PTC, PTC-ORBIT, HEADTAIL

Programming C, C++, Matlab, Mathematica, LabView, Python

Interests

Sports sailing, skiing, tennis
Others drums, radio-controlled aircrafts